THE UNIVERSITY OF WARWICK

Library Declaration and Deposit Agreement

1. STUDENT DETAILS

Please complete the following:

Full name: ……

University ID number: ……

2. THESIS DEPOSIT

2.1 I understand that under my registration at the University, I am required to deposit my thesis with the University in BOTH hard copy and in digital format. The digital version should normally be saved as a single pdf file.

2.2 The hard copy will be housed in the University Library. The digital version will be deposited in the University's Institutional Repository (WRAP). Unless otherwise indicated (see 2.3 below) this will be made openly accessible on the Internet and will be supplied to the British Library to be made available online via its Electronic Theses Online Service (EThOS) service.
[At present, theses submitted for a Master's degree by Research (MA, MSc, LLM, MS or MMedSci) are not being deposited in WRAP and not being made available via EthOS. This may change in future.]

2.3 In exceptional circumstances, the Chair of the Board of Graduate Studies may grant permission for an embargo to be placed on public access to the hard copy thesis for a limited period. It is also possible to apply separately for an embargo on the digital version. (Further information is available in the *Guide to Examinations for Higher Degrees by Research*.)

2.4 *If you are depositing a thesis for a Master's degree by Research, please complete section (a) below. For all other research degrees, please complete both sections (a) and (b) below:*

(a) Hard Copy

I hereby deposit a hard copy of my thesis in the University Library to be made publicly available to readers (please delete as appropriate) EITHER immediately OR after an embargo period of ……..... months/years as agreed by the Chair of the Board of Graduate Studies.

I agree that my thesis may be photocopied. YES / NO (*Please delete as appropriate*)

(b) Digital Copy

I hereby deposit a digital copy of my thesis to be held in WRAP and made available via EThOS.

Please choose one of the following options:

EITHER My thesis can be made publicly available online. YES / NO (*Please delete as appropriate*)

OR My thesis can be made publicly available only after…..[date] (Please give date)
YES / NO (*Please delete as appropriate*)

OR My full thesis cannot be made publicly available online but I am submitting a separately identified additional, abridged version that can be made available online.
YES / NO (*Please delete as appropriate*)

OR My thesis cannot be made publicly available online. YES / NO (*Please delete as appropriate*)

3. GRANTING OF NON-EXCLUSIVE RIGHTS

Whether I deposit my Work personally or through an assistant or other agent, I agree to the following:

Rights granted to the University of Warwick and the British Library and the user of the thesis through this agreement are non-exclusive. I retain all rights in the thesis in its present version or future versions. I agree that the institutional repository administrators and the British Library or their agents may, without changing content, digitise and migrate the thesis to any medium or format for the purpose of future preservation and accessibility.

4. DECLARATIONS

(a) I DECLARE THAT:

- I am the author and owner of the copyright in the thesis and/or I have the authority of the authors and owners of the copyright in the thesis to make this agreement. Reproduction of any part of this thesis for teaching or in academic or other forms of publication is subject to the normal limitations on the use of copyrighted materials and to the proper and full acknowledgement of its source.

- The digital version of the thesis I am supplying is the same version as the final, hard-bound copy submitted in completion of my degree, once any minor corrections have been completed.

- I have exercised reasonable care to ensure that the thesis is original, and does not to the best of my knowledge break any UK law or other Intellectual Property Right, or contain any confidential material.

- I understand that, through the medium of the Internet, files will be available to automated agents, and may be searched and copied by, for example, text mining and plagiarism detection software.

(b) IF I HAVE AGREED (in Section 2 above) TO MAKE MY THESIS PUBLICLY AVAILABLE DIGITALLY, I ALSO DECLARE THAT:

- I grant the University of Warwick and the British Library a licence to make available on the Internet the thesis in digitised format through the Institutional Repository and through the British Library via the EThOS service.

- If my thesis does include any substantial subsidiary material owned by third-party copyright holders, I have sought and obtained permission to include it in any version of my thesis available in digital format and that this permission encompasses the rights that I have granted to the University of Warwick and to the British Library.

5. LEGAL INFRINGEMENTS

I understand that neither the University of Warwick nor the British Library have any obligation to take legal action on behalf of myself, or other rights holders, in the event of infringement of intellectual property rights, breach of contract or of any other right, in the thesis.

Please sign this agreement and return it to the Graduate School Office when you submit your thesis.

Student's signature: .....…… Date: .....

Pulsatile electrical stimulation of Auditory nerve fibres: A modelling approach

By

Xisha Chen

A thesis submitted in partial fulfilment of the requirements for the degree of Doctor of Philosophy

School of Engineering

THE UNIVERSITY OF WARWICK

April. 2012

Table of Contents

Table of Contents I

List of Figures VI

List of Tables XII

Abbreviations XV

Acknowledgement XVI

Declaration XVII

Abstract XVIII

Chapter 1. Introduction 1

1.1 Background 1

1.1.1 Anatomy and physiology of the ear 1

1.1.2 Coding of sound in the normal ear 4

1.1.3 Cochlear implants 7

1.2 Computational modelling approach 10

1.3 Aims and objectives 12

1.4 Thesis Outline 13

Chapter2. Literature Review 15

2.1 Introduction 15

2.2 Conductance-based models 16

2.3 The stochastic ion channel gating model 22

2.4 Phenomenological models 26

2.4.1 The LIFDT model 29

2.5 Summary 30

Chapter3. Methodology 31

3.1 Introduction 31

3.2 A stochastic AN model 32

3.3 The LIFDT model 38

3.3.1 Response to suprathreshold stimulus: Refractory effects 42

3.3.2 Response to subthreshold stimulus: Accommodation effects 44

3.4 Experimental data 45

3.4.1 Experimental procedure 45

3.4.2 Electrophysiological experimental data 47

3.4.3 Data considerations 52

3.5 Summary 52

Chapter4. Fitting the LIFDT model to experimental data 53

4.1 Introduction 53

4.2 Analysis of experimental data 54

4.3 Theoretical calculation of I/O functions for the LIFDT model with simplified threshold 56

4.3.1 I/O at the first pulse 57

4.3.2 I/O at the second pulse 61

4.3.3 Calculation of firing probability at the *i*'th pulse 64

4.3.4 The accuracy of the theoretical calculation....64
4.4 Fitting results of the theoretical calculations....65
4.4.1 Analysis of the suppression in experimental data....68
4.5 Conclusion....74
Chapter5. Analytical approximation of the LIFDT model....78
5.1 Introduction....78
5.2 Analytical approximation of LIFDT model: linear approximation....79
5.2.1 Analytical approximation of LIFDT model to a single-pulse stimulus....80
5.2.2 Analytical approximation of LIFDT model to a subthreshold pulse-train stimulus....91
5.3 Predictions by the analytical version of LIFDT model....94
5.3.1 Predictions of single-pulse response....95
5.3.2 Predictions of pulse-train response....96
5.4 The maximum accommodation effects in the LIFDT model....100
5.4.1 Analytical approximation of the modified LIFDT model: step function approximation....106
5.4.2 Maximum accommodation effects in the modified LIFDT model with step function approximation....115
5.5 Conclusion....127
Chapter6. Markov Statistical Model....130
6.1 Introduction....130

6.2 A general Markov renewal process model 133

6.2.1 A stationary first order Markov model 136

6.2.2 A stationary second order Markov model 138

6.2.3 A stationary third order Markov model 140

6.3 Fitting the stationary Markov model to the neurophysiological data .. 142

6.3.1 The least-squares fitting 142

6.3.2 Uniqueness of the solution 144

6.3.3 Least-squares fitting with constraints 145

6.4 Results of stationary Markov model 146

6.4.1 Fitting gradient data set 148

6.4.2 Fitting the whole data set 155

6.4.3 The shifting *k* 157

6.5 Non-stationary Markov renewal process model 165

6.6 Fitting the full history Markov model to the neurophysiological data 168

6.6.1 Fitting the full history Markov model by the trust-region dogleg algorithm 169

6.6.2 Validation of the trust-region dogleg algorithm: noise effects 171

6.6.3 Validation of the trust-region dogleg algorithm: convergence time effects 174

6.7 Results of the full history Markov renewal process model 176

6.8 Conclusion 180

Chapter7. Conclusion 181

7.1 Summary 181

7.2 Implications for computational modelling of auditory neurons 183

7.2.1 Accommodation effects on auditory nerve response 183

7.3 Future work 185

Appendix A Code for LIFDT model with two –step Heun scheme: 187

Appendix B Proofs for Chapter 5 188

References 196

List of Figures

Figure 1-1 The central partition of the cochlea, which is depicted as if it had been unrolled. 3

Figure 2-1 Potassium conductance compared with the H-H voltage clamp data [89].. 18

Figure 2-2 Kinetic diagram of the sodium channel 23

Figure 2-3 Kinetic diagram of the potassium channel 23

Figure 3-1 A stochastic AN model of: Single pulse [47] 33

Figure 3-2 Probability density function of noise with mean of zero and variance of $\sigma 2$. 35

Figure 3-3 I/O function for stochastic AN model [47]: single pulse 36

Figure 3-4 A stochastic AN model: Pulse-train [46]. 37

Figure 3-5 The mechanisms of the LIFDT model 40

Figure 3-6 The relationship between the asymptotic value of the inactivation of sodium permeability and the membrane potential (Eq.(3.3.3)) 41

Figure 3-7 Neural response of the LIFDT model: Refractory Effects. 43

Figure 3-8 Neural response of the LIFDT model: Accommodation Effects. 44

Figure 3-9 Experimental recording setup[16] 46

Figure 3-10 A single pulse of 200pps pulse Train 46

Figure 3-11 200pps Pulse Train 47

Figure 3-12 I/O Function for the 200 pps pulse train from neurophysiological data [16] 47

Figure 3-13 Definition of the spike density in PST Histograms as an average over several runs of [116] 49

Figure 3-14 Normalised data and Original data at $FE = 0.5$ 51

Figure 3-15 Firing probability in response to a 200 pps pulse train stimulation, FE varies from 0.02 to 1.0 51

Figure 4-1 Discharge probability versus stimulus amplitude at each pulse: the experimental data 55

Figure 4-2 Single Biphasic pulse train (50 μs/phase, 10 μs interphase gap, anodic phase first) applied to the LIFDT model.. 58

Figure 4-3 Comparison of the membrane potential V(t) at the first pulse and the second pulse 62

Figure 4-4 I/O curves of the theoretical calculations Eq.(4.3.20) to the experimental data. 66

Figure 4-5 Firing probabilities against stimulus amplitude (I/O curve) for the first pulse of 200pps pulse train. 68

Figure 4-6 All the possible responses of the neuron to two biphasic pulses.. 69

Figure 4-7 The maximum suppression of firing probability due to refractory effects only 70

Figure 4-8 Fitted I/O curves of the theoretical calculation Eq. (4.3.19) at the second pulse by different fitting methods 73

Figure 4-9 Simulation results of the LIFDT model: “fitting by hand” 77

Figure 5-1 Single-pulse stimulus or the first pulse of pulse-train stimulus 200pps. 81

Figure 5-2 Membrane potential $\boldsymbol{V(t)}$ response to a single-pulse stimulus, Eq.(4.3.6)..... 83

Figure 5-3 Linear approximation for $\boldsymbol{h}_{\infty}$(V) , Eq.(4.3.28), ... 84

Figure 5-4 $\boldsymbol{h}_{\infty}(\boldsymbol{t})$ response to a single-pulse stimulus,..... 85

Figure 5-5 $\boldsymbol{h(t)}$ response to a single-pulse stimulus, Eq.(4.3.36)..... 87

Figure 5-6 Threshold $\boldsymbol{\theta(t)}$ response to a single-pulse stimulus, Eq.(3.2.12) 87

Figure 5-7 First two pulses of the 200pps pulse-train $\boldsymbol{S(t)}$ 92

Figure 5-8 I/O curves to a single-pulse stimulus or the first pulse of a pulse-train stimulus.. 96

Figure 5-9 I/O curves to a two-pulse stimulus by the theoretical version of LIFDT model. 97

Figure 5-10 I/O curves to the second pulse of a two-pulse stimulus. 100

Figure 5-11 $\Delta \boldsymbol{h}$ as a function of the time constant $\boldsymbol{\tau h}$ 103

Figure 5-12 Modified function of $\boldsymbol{h}\infty(\boldsymbol{V})$. 105

Figure 5-13 Membrane potential $\boldsymbol{V}(\boldsymbol{t})$ response to a single-pulse stimulus, ... 107

Figure 5-14 Step function approximation of $\boldsymbol{h}\infty$ to a single-pulse stimulus 108

Figure 5-15 Modified h(t) response to a single-pulse stimulus..... 109

Figure 5-16 Threshold response to a single-pulse stimulus with modified $\boldsymbol{h}\infty(\boldsymbol{t})$ 110

Figure 5-17 The membrane potential $\boldsymbol{V}(\boldsymbol{t})$ response to the second pulse.. 111

Figure 5-18 Step function approximation of $\boldsymbol{h}\infty$ to the second pulse..... 112

Figure 5-19 Response of $\boldsymbol{h}(\boldsymbol{t})$ in the modified LIFDT model to the second pulse 113

Figure 5-20 Response of $\boldsymbol{\theta}(\boldsymbol{t})$ in the modified LIFDT model to the second pulse 113

Figure 5-21 Comparing $\Delta \boldsymbol{h}$ in the original LIFDT model to the modified LIFDT model 116

Figure 5-22 I/O curves to a two-pulse stimulus by the theoretical version of the modified LIFDT model. 119

Figure 5-23 I/O curves of the modified LIFDT model to 1st pulse of a two-pulse stimulus..... 120

Figure 5-24 I/O curves of the modified LIFDT model to 2nd pulse of a two-pulse stimulus..... 121

Figure 5-25 $\Delta \boldsymbol{P}$ due to accommodation effects against stimulus amplitude.. 123

Figure 5-26 $\Delta \boldsymbol{P}$ due to refractory effects against stimulus amplitude. 124

Figure 6-1 Increment of the firing probability histogram from fitting the second order Markov model..... 151

Figure 6-10 Firing probability histogram from fitting results for the second order Markov model to gradient data..... 153

Figure 6-19 The dynamic of $\boldsymbol{kn}$ in the second order Markov model at FE of 0.05..... 158

Figure 6-20 Comparing PST histograms constructed with different $\boldsymbol{k}$..... 160

Figure 6-21 The drifting in *k* from the LIFDT model with each modulated threshold at FE=0.05. 163

Figure 6-22 Fitting the noise free test data $\boldsymbol{Tn1}$ by the trust-region dogleg algorithm 173

Figure 6-23 Fitting the 5% noise test data $\boldsymbol{Tn2}$ by the trust-region dogleg algorithm 173

Figure 6-24 Fitting the 10% noise test data $\boldsymbol{Tn3}$ by the trust-region dogleg algorithm 173

Figure 6-25 PST histogram calculated by the fitted full history Markov renewal process model.. 176

Figure 6-28 Fitted conditional probability of Eq.(6.5.7) at FE 0.1 177

Figure 6-29 Fitted conditional probability of Eq.(6.5.7) at FE 0.2 177

Figure 6-31 Fitted conditional probability of Eq.(6.5.7) at FE 0.4 177

Figure 6-32 Fitted conditional probability of Eq.(6.5.7) at FE 0.5 178

List of Tables

Table 3-1 Parameter values of the LIFDT model [104]..... 39

Table 4-1 Comparison of the theoretical calculations of Eq.(4.3.13) and simulation results of the LIFDT model at the first pulse 65

Table 4-2 Fitting results of the theoretical calculations Eq.(4.3.20) to the experimental data 66

Table 4-3 Fitting the variables in LIFDT model by I/O curve for the 1st pulse 67

Table 4-4 Fitting results of the theoretical calculation Eq. (4.3.19) by different fitting methods for the first two pulses..... 73

Table 5-1 Fitted parameter values of LIFDT model to the I/O curve on the first pulse..... 94

Table 5-2 Fitted parameter values of the modified LIFDT model to the I/O curve on the first pulse 118

Table 6-1 The relationship between firing at the *n*'th pulse to the firing status of previous pulses.. 134

Table 6-2 Firing status of the first order Markov model (discharge at the *n*'th pulse) 137

Table 6-3 Firing status of the second order Markov model (discharge at the *n*'th pulse) 139

Table 6-4 Firing status of the third order Markov model (discharge at the *n*'th pulse) 141

Table 6-5 *SSE* of fitting the gradient data with constraints..... 148

Table 6-6 R Squared of fitting the gradient data with constraints 148

Table 6-7 Adjusted R Squared of fitting the gradient of the data with constraints 150

Table 6-8 Fitting the gradient data to the second order Markov model with constraints 153

Table 6-9 Fitting the whole data to first order Markov model with constraints ($\alpha 1 \leq 0$ $0 \leq k \leq 1$) 155

Table 6-10 Fitting the whole data to the second order Markov model with constraints 156

Table 6-11 Fitting the whole data to the third order Markov model with constraints ($\alpha 1 \leq 0$ $\alpha 2 \leq 0$ $\alpha 3 \leq 0$ $0 \leq k \leq 1$) 156

Table 6-12 Comparing the statistics of kn 159

Table 6-13 Statistics of the shifting *k* with original threshold, modulated threshold θ_1 and modulated threshold θ_2. 164

Table 6-14 The permitted histories at the fifth pulse 167

Table 6-15 Parameter values of the test data 172

Table 6-16 Fitting results of the test data with different noise intensity by the trust-region dogleg algorithm 173

Table 6-17 Fitting results of the test data to Eq.(6.5.7) with different convergence time by the trust-region dogleg algorithm 175

Abbreviations

Auditory Nerve	AN
Absolute Refractory Period	ARP
Cumulative Distribution Function	CDF
Channel-number-tracking	CNT
Channel-state-tracking	CST
Firing Efficiency	FE
Frankenhaeuser-Huxley model	F-H
Hodgkin-Huxley model	H-H
Input-Output	I/O
Interspike interval histogram	ISIH
Leaky integrate-and-fire model with dynamic threshold	LIFDT
Probability density function	PDF
Peristimulus time	PST
Relative Refractory Period	RRP
Relative Spread	RS
Pulses per Second	PPS

Acknowledgement

First, I would like to express my special thanks to my supervisor, Professor Nigel G Stocks, for his academic guidance, constant encouragement, constructive advice and extremely valuable support throughout my study. Special thanks are due to my colleagues in Engineering for their fruitful discussions and valuable advices.

I would like to thank my parents for their financial and moral support which made possible of my PhD study.

Declaration

This thesis is submitted in partial fulfilment for the degree of Doctor of Philosophy under the regulations set out by the Graduate School at the University of Warwick. The work described in this thesis was conducted by Xisha Chen, except where stated otherwise, under the supervision of Prof. Nigel G. Stocks in the School of Engineering, University of Warwick between the dates of Oct 2006 and Feb 2012. No part of this work has been previously submitted to any institution for admission to a higher degree.

Abstract

A stochastic leaky integrate-and-fire nerve model with a dynamical threshold (LIFDT) has been derived for the neural response to sinusoidal electrical stimulation. The LIFDT model incorporates both the refractory effects and the accommodation effects in the interpulse interactions. In this thesis, this phenomenological nerve model is extended for the neural response to pulsatile electrical stimulation, which is widely used in cochlear implants as it reduces inter channel interference.

Neurophysiological data from adult guinea pigs were fitted to the LIFDT model. First, the parameters were constrained by the Input/output (I/O) curve analysis. Analysis of the data showed strong accommodation effects. The figures of I/O function for each pulse were plotted according to the physiological data. Fitting the I/O function of the data constrained the value of four variables of LIFDT model. The other five parameters were “optimised by eye”. Although the LIFDT is built with stimulus-dependent threshold, the response of short duration biphasic pulsatile stimuli exhibits weak accommodation effects.

Then, in order to avoid the complication of full optimization, analytical approximation of the LIFDT model was derived for pulsatile electrical stimulation. It improves computational efficiency and provides information on how the parameters of the LIFDT model affect the accommodation effects. Theoretical predictions indicate that the LIFDT model could not capture the strong accommodation effects in the neurophysiological data due to structural problems.

Alternatively, a Markov renewal process model was utilized to track the pulse-train response. The stationary and non-stationary Markov renewal process models were fitted to the neurophysiological data. Both models can interpret the conventional PST histograms into conditional probabilities, which are directly related to the interpulse intervals. The consistent results from those two models provide a qualitative analysis of the accommodation characteristics.

Chapter 1. *Introduction*

Hearing loss refers to a disruption in the transduction of sound waves into neural activity in the auditory nerve. In most individuals suffering deafness due to loss of sensory hair cells in the cochlea, hearing can be partly restored by direct stimulation of the remaining auditory nerves using a cochlear implant. A typical cochlear implant consists of a sound processor, an electrode array and a means of transmitting signals across the skin to the electrodes [1]. The sound processor extracts features of acoustic signals and transfers them into spatiotemporal patterns of electrical currents. The electrical currents are delivered to electrodes near the cochlear nerve fibres. These excite the higher centres in the central auditory nervous system. The aim of the cochlear implant is to mimic the action of a healthy ear.

The aim of this thesis is to develop an accurate model for the response of auditory nerve fibres to electrical pulsatile stimuli from physiological data. These models can then be integrated into models of cochlear implantation and the differences between natural acoustic stimuli and electrical stimulation studied.

Before an overview of specific modelling issues addressed in this thesis, a brief summary is provided of how the normal ear may be coding sound features, and how cochlear implants function.

1.1 Background

1.1.1 Anatomy and physiology of the ear

In the human auditory system, the function of the ear is to convert sound waves into nerve impulses, which leads to the perception of sound. The transduction

process can be described as the coding of sound features in the patterns of activity in the auditory nerve.

A summary of the anatomy and physiology of the ear is presented in this section based on the Oxford Handbook of Auditory Science [2], which is relevant to this thesis.

The ear is composed of three parts: the outer, middle and inner ears. The outer ear comprises the pinna, external auditory meatus and the tympanic membrane. The outer ear is constructed to capture sound waves, provide frequency filtering of the sound and increase the sound pressure amplitude. The middle ear consists of an air-filled cavity with three ossicles: the malleus, the incus and the stapes. The main mechanics of the middle ear are transferring the sound energy from air to water and matching the different impedances between the auditory meatus and the cochlear fluids. The inner ear, the cochlear, essentially consists of a coiled tube formed three fluid-filled scalae (the scala vestibuli, the scala media and the scala tympani). The structure of the inner ear is shown schematically in Figure 1-1 as it would look unwound and cut lengthwise. Within this outer tube is an interior tube (called the scala media), which divides the outer tube (cochlear) into two separated parts (called the scala vestibuli and scala tympani). The scala vestibule and scala tympani are joined at the apical end through a small hole (called the helicotrema) in the dividing membrane. The scala media forms a closed inner compartment, which is separated from the scala vestibule by Reissner's membrane on one side and from the scala tympany by the basilar membrane on the other side. At the basal end, the membrane is narrow and stiff; at the apical end it is both wider and considerably more flaccid.

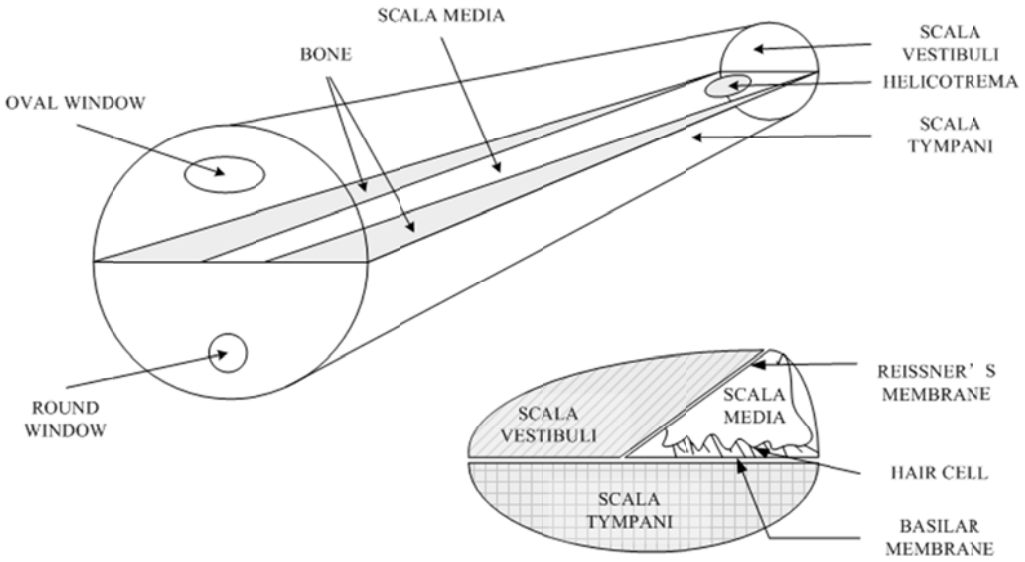

Figure 1-1 The central partition of the cochlea, which is depicted as if it had been unrolled.

The footplate of the stapes is attached to the oval window. Movement of the oval window produces a displacement of the cochlear fluids to the round window. The flow of the cochlea fluids results in a wavelike displacement of the basilar membrane, referred to as the travelling wave. The basilar membrane can roughly be described as a continuous series of band-pass filters, with the centre frequency of each filter decreasing monotonically with distance from the base. The travelling wave propagates from the base of the basilar membrane to its apex, where the action is in the inner ear and wave motions are transduced into neural electrical activity. Specifically, the transduction of the sound energy conveyed by the travelling wave into neural activity within the auditory nerve is achieved by the inner hair cells and auditory nerve synapses.

Auditory nerve fibres connect the hair cells with a direct synaptic link and head towards the brain. A fibre's axons and cell body are effectively a continuous myelinated membrane, with regular breaks in the myelin referred to as the nodes of *Ranvier*. Ionic fluids fill and surround the nerve membrane, with differing

concentrations of ions in the internal and external fluid. The difference in potential between the internal and the external fluids leads to a change of the excitatory postsynaptic potential. Specifically, the reception of the neurotransmitters by an auditory nerve synapse causes ions to flow through the membrane from the interior to the exterior of the fibre and vice versa. If the postsynaptic potential is of sufficient magnitude, it is propagated along the auditory nerve fibre to the brain. Such a response is called an action potential, discharge, firing or spike. This neural activity is then processed by the brain to give the perception of sound.

1.1.2 Coding of sound in the normal ear

There are a number of different forms of neural processing that form the perception of sound. In general, the information of sound may be coded in the site of the activity (spatial coding), in the timing of the activity (temporal coding), or in some combination of the two (spatiotemporal coding) [1].

In the theory of spatial coding, it is hypothesised that acoustical stimuli are coded by which auditory nerve fibres respond. The spatial arrangement of the nerve cells and their best frequencies of response are more important than whether the nerve cells have fired in time with the electrical stimulation. The hearing receptors in the inner ear and the cells and fibres in the central nervous systems are arranged in a tonotopic way so that they will respond to only a limited range of frequencies along a scale from low to high. Frequencies may be coded by which fibres represent the maximum mean discharge rate [3]. Also, Kim *et al*., showed that frequency is coded by the fibres representing the greatest difference in mean discharge rate with respect to their spontaneous rate [4], or with respect to the local population of fibres [5].

In the theory of temporal coding, it is proposed that acoustical stimuli are coded by the timing of auditory nerve fibre responses. In the firing sequences, the firing state of the current stimuli is dependent on the firing state of previous stimuli. Such dependencies are normally referred to as interpulse interactions. The interpulse interactions observed from physiological data are mainly the refractory effects and accommodation effects.

Refractory effects refer to the phenomenon that the neuron is unable or less able to generate a discharge after a previous discharge. The ionic basis of refractory effects by electrical stimuli is described below. By injecting electrical current through a microelectrode, sodium ions enter the cell of a neuron [6]. When entry of Na^+depolarizes the membrane beyond a threshold, a discharge is generated. After a discharge, the neuron enters a refractory period. The refractory period consists of an absolute refractory period (ARP) and a relative refractory period (RRP). The neuron enters the absolute refractory period instantaneously after the discharge. During this period, sodium channels inactivate. The neuron is unable to fire regardless of the stimulus level. Then the neuron enters the relative refractory period. During this period, the membrane potential stays hyperpolarized until the potassium channels close. Thus, more current is required to depolarize the membrane across the threshold; it is more difficult to fire than when it is outside the refractory period.

Accommodation effects refer to the phenomenon that subthreshold stimuli cause the nerve to become less excitable [7]. For example, when a slowly increasing and long lasting current is delivered to a neuron, the threshold rises gradually [7]. The more slowly current rises, the stronger the current required to attain the threshold. The threshold seems to “accommodate” the stimulus. Accommodation

effects disappear when the neuron is allowed to return to its resting state. Hill demonstrated that the Ca ion has a large effect in increasing the speed of accommodation [8]. Observations from animal models of myelinated nerve fibres [9-12] indicate that the inactivation of the sodium ion channel, and the activation of the slow potassium ion channel contribute to the accommodation mechanisms.

As refractoriness is the major form of the interpulse interactions, previous studies have been focused on the refractory effects. The stimuli intensity could be coded not only by the spread of discharge, but also by the average discharge rates in single fibres or in populations of fibres[13]. Frequencies may be coded by interspike intervals in both single fibres and in populations of fibres [14] [15]. All the above studies concerned the refractory effects exclusively. Recently, it has been indicated that accommodation effects are also a fundamental factor in the temporal neural response of auditory nerve fibres [16-19]. For sinusoidal stimuli, accommodation behaviour was observed from the tuning curve below approximately 100 Hz [19]. For pulsatile stimuli, accommodation behaviour was evident from poststimulus time (PST) histograms at lower discharge probabilities [16-18]. Accommodation behaviour was also observed from psychophysical data [20]. Psychophysical data showed that as long as the number of stimulus pulses was held constant, as the time interval between pulses was decreased, behavioural threshold current decreased and perceived loudness increased. Thus, in developing cochlear implants, it is important to understand the accommodation effects in temporal coding. In this thesis, mathematic models are developed to investigate the accommodation behaviour in the neural response of single auditory nerve fibres to electrical stimulation.

1.1.3 Cochlear implants

Researchers indicated that the most common cause of deafness is the loss of hair cells, rather than the loss of auditory neurons [21, 22]. The hair cells and the basilar membrane are responsible for translating mechanical information into neural activity. Therefore, cochlear implants are designed to bypass the normal hearing mechanism (outer, middle, and part of the inner ear including the hair cells) and stimulate directly surviving neurons in the auditory nerve. Normally, implant devices have a microphone that picks up the sound, a signal processor that converts the sound into electrical signals, a transmission system that transmits the electrical signals to the implanted electrodes, and an electrode or an electrode array that is implanted into the cochlea. The present generation of cochlear implants utilises an array of up to 24 electrodes, which is implanted into the basal turns of the scala tympani of the cochlea through the round window. Injection of current by means of a cochlear implant can cause a sudden depolarisation in the nerve membrane, similar to an excitatory postsynaptic potential produced by a healthy hair cell [23].

To date, cochlear implant technology is still unable to perform such advanced processing of sound as the human ear. Action potentials in the normal cochlea are generated by the mechanical transduction action of hair cells. However, action potentials evoked by cochlear implants are caused by direct electrical stimulation. The response of the auditory nerve to electrical stimulation is very different from its response to acoustical stimulation [24]. Under electrical stimulation, the neuron usually responds quite synchronously and the dynamic range is narrow. Under acoustical stimulation, the neuron behaves more stochastically. These dissimilarities contribute to the lack of speech perception.

Consequently, it is desirable to understand what patterns of response are produced by electrical stimulation.

Since the 1950s, there have been studies of direct stimulation of the auditory nerve by single electrodes [24]. The studies of electrical stimulation on single electrodes assessed the possibility of reproducing the coding of frequency [25, 26]. It is proposed that the frequency of a sound could also be conveyed to the brain on the basis of the spatial coding [27]. This led to stimulating the auditory nerve with multiple electrodes [28, 29]. The electrodes were placed with the aim of stimulating nerve fibres representing different frequencies selectively. In the 1970s, appropriate multiple-electrode interfaces with the auditory nervous system were investigated for psychophysical and speech research in patients. It has been discovered that voicing could be transmitted by varying the rate of stimulation on different electrodes independently of the place of stimulation [28-31]. Thus voicing was perceived by varying the rate of stimulation across different nerve populations. Also a preliminary psychophysical study with a multi-electrode implant indicated that either the site of stimulation or the rate of the stimulation could be varied to change the pitch (psychological percept of frequency) [32]. Temporal and spatial information provided two components to the pitch of an electrical stimulus. Both spatial coding and temporal coding schemes have been implemented in speech processors for multi-electrode cochlear implants [32-34].

In the discrimination of complex sounds such as speech and music, temporal coding is more important than spatial coding [1]. Physiological studies demonstrated that the temporal properties of vowels are accurately represented in the firing pattern of single fibres of the auditory nerve [35]. It is also supported

by pathological observations on the impairment of frequency discrimination and pitch perception [36]. It was found that injuries to the auditory nerve, which impair temporal coherence of the discharges of auditory nerve fibres, are associated with serious impairments in speech discrimination. Therefore, it is crucial to accurately understand temporal response of auditory nerve fibres to improve speech-processing strategies in cochlear implants. In this thesis, only the temporal responses of single auditory nerve fibres to electrical stimulation are investigated.

Direct observation of individual nerve fibres within the human cochlea is hard to make for both ethical and experimental reasons. Therefore, physiological models are widely used in place of the human cochlear nerve. The auditory nerve system in other animals could resemble the human auditory system [31]. The human auditory nerve is a myelinated nerve. In principle, any mammalian myelinated auditory nerve could be used in place of the human auditory nerve. Experimental data have been taken from toads [37, 38], rats [39] , rabbits [40] , cats [41] , guinea pigs [26] and monkeys [42], which are all used as physiological models of the electrically stimulated human cochlear nerve.

Based on the physiological data, computational models have been developed to predict the human auditory nerve response to electrical stimulation. It would be advantageous for directing physiological and psychophysical experimental design if the temporal response could be predicted via computer simulations or theoretical analyses.

1.2 Computational modelling approach

The temporal response of auditory nerve fibres to electrical stimulation has been widely studied via computational models [23, 27, 37, 38, 43-54]. Conductance-based models are based on a system of equations and parameters derived from voltage-clamp experiments on nerves from a specific animal species. The first conductance-based model of the electrical activity of the nerve was developed by Hodgkin and Huxley [43]. They studied the response from an unmyelinated squid axon and built a neural model with conductance-based nonlinear differential equations. Frijns *et al*., [55] extended Frankenhaeuser and Huxley's myelinated nerve model of the toad sciatic nerve for electrical prosthesis design. The conductance-based model is designed to accurately describe the kinetics of ion channels, particularly sodium and potassium. Although all nerves have similar ion channels with similar kinetics, the distribution and density of ion channels differs between species [56]. Consequently, the system of equations and parameters for different species vary. Ideally, voltage-clamp experiments should be performed on specific mammalian cochlear nerves. However, dissection of a sufficient length of the cochlear nerve from a guinea pig or a cat for voltage-clamp experiments is not currently possible, nor is maintenance of the nerve in good physiological conditions. Alternatively, microelectrode data can be fitted to a standard conductance model. The problem is conductance-based models have over forty parameters and require an enormous amount of data to constrain each parameter.

Interest in the modelling of large populations of nerves has increased as electrical nerve stimulation is widely used in practice [57]. Avoiding the complex electrophysiological process modelling, phenomenological models are developed

as simplified neuron models compared to conductance-based models. Moreover, the parameters of a phenomenological model are usually characterised by neuron physiological properties, such as refractory time, membrane potential or threshold. Thus it is easier to visualize the outcome of a phenomenological model when fitting the parameters to experimental data.

In phenomenological models, the temporal response of auditory nerve fibres to electrical stimulation is usually described by two characterizations [1, 45, 46, 58-65]. One is the excitation of the auditory nerve fibres, another is the interpulse interactions. Historically, the excitation to electrical stimulation has been modelled via deterministic descriptions [23, 55, 65]. Recently, it has been widely studied that incorporating stochastic activity in a neural model is a fundamental factor to produce accurate predictions of physiological and psychophysical phenomena [46, 47, 51, 66-70]. In the phenomenological models, normally refractoriness is expressed by a simple refractory function, which is obtained directly from the observed interspike interval (ISI) statistics [46, 60, 69]. Accommodation effects has not been fully investigated. To date, none of the phenomenological models of auditory nerve fibres were built with accommodation effects, except the leaky integrate-and-fire model with dynamic threshold (LIFDT) [19]. The LIFDT model was derived from the response of the sciatic nerve of the toad to sinusoidal electrical stimulation. It is the first electrical stimulated phenomenological model incorporating accommodation effects. The accommodation behaviour in the neural response to sinusoidal analogue electrical stimulation has been successfully predicted by the LIFDT model [19]. Therefore, only the neural response to pulsatile electrical stimulation is investigated in this thesis.

1.3 Aims and objectives

In this thesis, the aim is to further develop the phenomenological modelling approach incorporating accommodation effects for use in cochlear implant simulation.

In cochlear implant devices, information is presented either in analogue electrical stimulation or pulsatile electrical stimulation [71]. In analogue stimulation, a sum of sinusoids with time-varying amplitudes and fixed frequencies is presented to the electrode as an electrical analogue of the acoustic waveform. Due to its simultaneous stimulation, the analogue stimulation may cause channel interaction. The channel interaction affects the salience of spectral cues, which is crucial for speech understanding [72]. In pulsatile stimulation, a set of narrow pulses is delivered to the electrode. The advantage of the pulsatile stimulation is that the pulses can be delivered non-simultaneously, thereby minimizing the possibility of electrical interactions

The primary objective of this work is to investigate whether the LIFDT model is applicable for pulsatile stimuli and whether incorporating accommodation mechanisms can improve the prediction of neural response.

As the LIFDT model incorporates stochastic, refractory and accommodation properties of auditory nerve fibres, it is time consuming and computationally laborious to directly fit this model to neurophysiological data from a guinea pig model of the electrically stimulated cochlea [16, 17]. The methodology used is first to derive a theoretical expression for the response of the LIFDT model, and then to evaluate how parameters in the LIFDT model affect accommodation effects, and finally to reproduce the neurophysiological data. Therefore, the

thesis will explore the approximated analytical result for the firing probability of the LIFDT model to pulsatile stimulation.

The thesis also aims to explore the accommodation characteristics of auditory nerve fibres. Neurophysiological data under accommodation conditions are quite limited. Normally, accommodation effects are not measured directly like refractory effects, but observed from PST histograms, in which both accommodation effects and refractory effects affect the firing probabilities. This thesis will conduct separate evaluations of those two interpulse interactions using different modelling approaches.

1.4 Thesis Outline

Chapter one gives a brief overview of the coding in cochlear implants, including its development history, its challenges and tasks. The research objective and overall structure of the thesis are also listed in this chapter.

Chapter two reviews the existing electrically simulated computational models. Three types of computational models are compared, including conductance-based models, stochastic ion channel gating models and phenomenological models.

Chapter three introduces the phenomenological models which will be used in the following chapters. The LIFDT model consists of a refractory LIF model, a stimulus-dependent threshold and a stochastically-varying membrane potential. The stochastic part of the LIFDT model is extended from the stochastic auditory nerve model proposed by Bruce *et al*., [46, 47]. Detailed descriptions of this stochastic auditory nerve model and the LIFDT model are presented. Also a set

of neurophysiological data to pulsatile stimulation from adult guinea pigs is presented in this chapter.

The LIFDT model has nine variables. The optimization of all variables requires a considerable amount of data. As the neurophysiological data are limited, an initial assessment of the neurophysiological data is made in chapter four. An I/O curve model is derived based on the stochastic auditory nerve model. It quantifies the size of accommodation effects in the data and provides constraints on some parameter values of the LIFDT model. Then predictions of the firing probabilities are constructed by Monte Carlo simulation of the LIFDT model.

In chapter five, theoretical expressions for the response of the LIFDT model to single pulse and pulse-train stimulation are derived. Accommodation effects in the LIFDT model are studied by the theoretical predictions and simulations. Moreover, the maximum accommodation effects in the LIFDT model are explored. It shows that the LIFDT model is insufficient to achieve the strong accommodation effects in the experimental data due to structural problems.

Alternatively, a Markov renewal process model is developed in chapter six. This statistical model provides an estimation of the conditional probability related to refractory effects or accommodation effects and separates those two interpulse interactions. The conditional probabilities in the Markov renewal process model are assumed stationary at first, and then extended to non-stationary. Both methods provide a consistent qualitative description of accommodation effects in the experimental data.

Chapter seven presents the conclusions and examines the implications for computational modelling.

Chapter2. *Literature Review*

2.1 Introduction

In order to further develop the phenomenological modelling approach incorporating accommodation effects, it is advantageous to review existing computational models of the auditory nerve fibres and how accommodation effects are modelled.

The excitation and accommodation in nerves were reviewed by Hill [7] based on experimental work on various nerves from frog, cat, dog, cuttle-fish, and spider-crab. A mathematical model was built to describe two time-factors in electrical excitation: one is the "excitatory disturbance" or "local potential"; another is the "accommodation" or change of "threshold". In general, the "accommodation" is of the same general nature as "excitation", but a gradual process with a time-constant of its own, depending upon the value of the current at all moments up to "excitation". Since the nature of those two time-factors was not specified, this mathematical model cannot be directly used in auditory nerve fibres. However, it provides a theoretical analysis of accommodation behaviour.

In the study of temporal response of auditory nerve fibres, three types of computational models are frequently used: conductance-based models, ion channel gating models, and phenomenological models. This chapter will provide a theoretical background of computational models of each type and investigate how the temporal spike firing patterns are coded.

2.2 Conductance-based models

Conductance-based models are derived from voltage-clamp experiments of single nerve fibre. In principle, conductance-based models consist of a system of time-dependent differential equations with conductance variables, which is designed to accurately describe the kinetics of ion channels.

The Hodgkin-Huxley (H-H) model [40, 43, 52, 73-84] is the starting point of the conductance-based neuron model. It describes how action potentials in neurons are initiated and propagated in axons via voltage-gated ion channels. Hodgkin and Huxley's work were based on an extensive series of experiments on the unmyelinated giant axon of squid. The model is a set of nonlinear ordinary differential equations that approximates the conductance of three voltage-dependent ion channels: a sodium channel with index *Na*, a potassium channel with index *K* and unspecific leakage channel which accounts for other channel types. The current *I* through the membrane is related to the time change of the potential across the membrane *V,* membrane capacity *C,* and the ionic current I_i,

$$I = C\dot{V} + \sum_i I_i \tag{2.2.1}$$

The leakage channel is described by a voltage-independent conductance g_L, other ion channels are voltage and time dependent. The probability that a channel is open is described by additional gating variables *m*, *n* and *h*. The combined action of *m* and *h* controls the Na^+ channels. The K^+ channels are controlled by *n*. The parameters V_{Na}, V_K and V_L are the reversal potentials through conductance g_{Na}, g_k and g_L. The ionic current is given by,

$$\sum_{i} I_i = g_{Na} m^3 h (V - E_{Na}) + g_K n^4 (V - E_K) + g_L (V - E_L) \qquad (2.2.2)$$

In addition, probabilities *m*, *n* and *h* vary according to equations in the form with a voltage-dependent relaxation time $\tau_x(V)$ and the steady state value $x_\infty(V)$, where *x* stands for *m*, *n* and *h*.

$$\frac{\partial x}{\partial t} = \frac{x_\infty(V) - x}{\tau_x(V)} \qquad (2.2.3)$$

Linear cable theory is applied to the propagation of an action potential. The H-H model provides a good description of the electrophysiological properties of the giant axon including the passive and active local responses, the threshold phenomenon, the subthreshold oscillations, the action potential, refractoriness and stochastic activity. It succeeds in describing the generation and propagation of action potentials at the level of ion channels and ion current flow.

When the H-H model is applied to human auditory nerve fibres, substantial adjustment should be made. The H-H model was derived from experiments at 6.3°C. For human auditory nerve fibres the normal temperature is 37°C. At higher temperatures, the membrane kinetics become faster as the gating mechanism reacts more quickly. Thus, the amplitude of action potentials is smaller and refractory time is shorter. Hodgkin and Huxley introduced a special constant to accelerate the membrane behaviour [43, 85]. With the correction of temperature, the H-H model can predict the auditory nerve response both in timing and multiple spiking. Thus the H-H model is an important reference computational model of auditory nerve fibres [40, 52, 54, 74, 76-84, 86-88].

The H-H model has some accommodation properties for step currents below some certain value [73, 89]. However, an inhibitory effects of large stimulus currents on discharge was observed from experimental data of the space-clamped squid giant axon [90]. To reproduce such accommodation behaviour by the H-H model, Fohlmeister [89] modified the potassium conductance equation by adding an inactivation channel of the potassium conductance and a kinetically separate potassium channel with longer time constant compared with τ_n in H-H model. With these modifications, Eq.(2.2.2) can be reformed as,

$$\sum_i I_i = g_{Na} m^3 h (V - E_{Na}) + g_K [n^4 (1 - ak) + k] \cdot (V - E_K) + g_L (V - E_L) \quad (2.2.4)$$

Hence the potassium conductance is directly dependent on the potassium current, and predictions of this modified H-H model show a good agreement with the experimental data of the H-H voltage clamp data for potassium as shown in Figure 2-1.

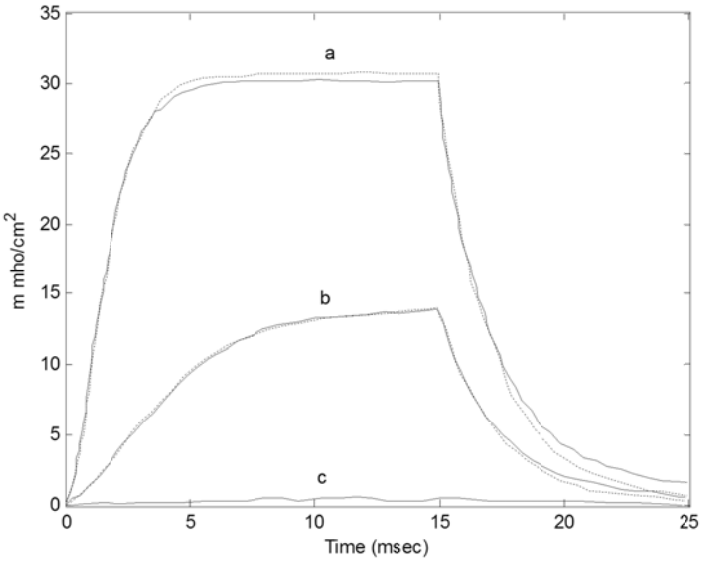

Figure 2-1 Potassium conductance compared with the H-H voltage clamp data [89]. Potassium conductance under conditions of voltage clamp stepped from V=0 (rest) at time t=0 to (a) 100mV, (b) 38mV, (c) 6mV. At time t=15 msec the potential is again stepped to

zero. The dashed curves are for the H-H model. The solid curves are with the k-variable formulation included.

The Frankenhaeuser-Huxley (F-H) model [37] is another classic conductance-based model, which was derived from voltage clamp experiments on myelinated nerve fibres of *Xenopus laevis*. The F-H model was extended from the H-H model with more variables and differential equations to capture the response of myelinated nerve fibres. For myelinated fibres, the myelin sheet is interrupted at regular intervals along the axon by the nodes of *Ranvier*. Typically the length of a node is very small compared to the length of the intermodal segment. Potassium channels are present under the myelin sheet along the intermodal section. Spike generation essentially only takes place at the node. Thus conduction does not proceed continuously along the cable, but jumps from one node of *Ranvier* to the next.

Although the unmyelinated axon (squid giant axon) and the myelinated vertebrate fibre are quite different in detail, their currents are mainly carried by sodium and potassium. Thus the outlines of their mechanisms of impulse conduction are similar. In the F-H model, a second sodium current, I_P, is added to Eq.(2.2.1). Thus Eq.(2.2.1) is replaced by

$$I_i = I_{Na} + I_K + I_L + I_P \tag{2.2.5}$$

The F-H model uses ionic permeabilities instead of membrane conductances in the H-H model. The currents in the F-H model are given by,

$$
\begin{aligned}
I_{Na} &= P_{Na} h m^2 \frac{EF^2}{RT} \frac{(Na)_0 - (Na)_i e^{EF/RT}}{1 - e^{EF/RT}} \\
I_K &= P_K n^2 \frac{EF^2}{RT} \frac{(K)_0 - (K)_i e^{EF/RT}}{1 - e^{EF/RT}} \\
I_P &= P_P p^2 \frac{EF^2}{RT} \frac{(Na)_0 - (Na)_i e^{EF/RT}}{1 - e^{EF/RT}} \\
I_L &= g_L (V - V_L)
\end{aligned}
\tag{2.2.6}
$$

where $E = V - V_R \ \ (mV)$, F is Faraday's constant (J/mol) , R is the gas constant $(J/mol \cdot K)$, T is the temperature (K) , the suffixes "0" and "*i*" denote outer and inner concentrations $\left(mol/m^3\right)$, P denote the permeability constant $\left(\mu m/s\right)$.

Frankenhaeuser and Moore published thermal effects of the F-H model below 20°C [91]. To apply the F-H model to auditory nerve fibres, correction of temperature to 37°C was made by Rattay *et al*. [85] by adding a time scale factor *k* of gating variable *m*, to give

$$
\dot{m} = \left[-\left(\alpha_m + \beta_m \right) \cdot m + \alpha_m \right] \cdot k \tag{2.2.7}
$$

where k is a thermic coefficient $k = 3^{0.1T - 0.63}$, α, β are the opening and closing rates of the gates *m*, as

$$
\alpha_m = \frac{m_\infty}{\tau_m} \tag{2.2.8}
$$

$$
\beta_m = \frac{1 - m_\infty}{\tau_m} \tag{2.2.9}
$$

The thermal effects corrected F-H model could successfully predict the temporal response observed from experimental data [85].

Accommodation mechanisms in the F-H model were studied by Frankenhaeuser *et al.* [92, 93]. The predictions by the F-H model qualitatively agreed with the experimental data of myelinated nerve fibres from *Xenopus laevis*. It was concluded that the accommodation is mainly manipulated by the inactivation of the sodium permeability, which is consistent with the modifications of accommodation mechanisms in the H-H model discussed previously [89].

The accommodation mechanisms in both the original H-H model and the F-H model were investigated by Motz *et al*. [76, 85]. Both models were adjusted to warm-blooded conditions, and applied with the analogue sinusoidal signals and pulsatile electrical signals.

When applying sinusoidal signals at low frequencies, the H-H model produced two or more discharges during a half-period; and the F-H model only produced one discharge during each period [76]. According to the subthreshold activity observed from feline experiments [94], the H-H model is more adequate. However, it is argued that the H-H model exaggerates multiple discharges and presents a poor dynamic range compared to experimental data.

For pulsatile stimulation, a signal of double pulses was applied to both models to investigate subthreshold effects [85]. The method is based on a double pulse eletrostimulation experiment on the human cochlear implants [95]: The first pulse is set just at the threshold value. If a second pulse is smaller than the first pulse and can still distinguished by patients, then a subthreshold effects is observed. The subthreshold effects was obtained from both the F-H model and

the H-H model. The H-H model requires a small second stimulus and produces a long flat part between the stimulating pulse and the spike. And the F-H model requires a much higher second stimulus as the subthreshold activity decreases quickly after the first stimulus. Therefore, both conductance-based models can model accommodation effects. The suitability of the two models depends on the accommodation behaviour observed.

2.3 The stochastic ion channel gating model

The above conductance-based models are designed with a deterministic threshold. However, deterministic models fail to accurately represent probabilistic firing. It is well known that the natural stochasticity of the neural response is important for auditory signal processing [47, 96]. It is demonstrated that the addition of noise would result in a more acoustic-like neural response, which in turn results in improved auditory perception by cochlear implants listeners.

To address this limitation, recent physiological results based on the F-H model suggest that utilizing stochastic resonance may enhance information transformation, where the noise term is added into the single channel of the simulated cochlear implant [67, 97]. However, membrane noise and axonal excitability change with the state of ion channels [98]. As the nodes of *Ranvier* in auditory nerve fibres have a relatively small number of ion channels, the stochastic nature of voltage-dependent ion channel gating is known to be physiologically significant in auditory nerve fibres [48, 49, 74, 98, 99].

To accurately model the stochastic property of ion channels, the stochastic ion channel gating model have been developed based on the H-H model [83, 98, 100]. The deterministic voltage dependent conductances in the H-H model

(g_{Na}, g_K) are replaced by individual stochastic ion channel particles. Specifically, the sodium channel has three independent activation particles m and one inactivation particle h; the potassium channel has four independent activation particles n. Each individual particle only has two states: open and closed. The Markov kinetics for gating of sodium and potassium channels are given by Figure 2-2 and Figure 2-3

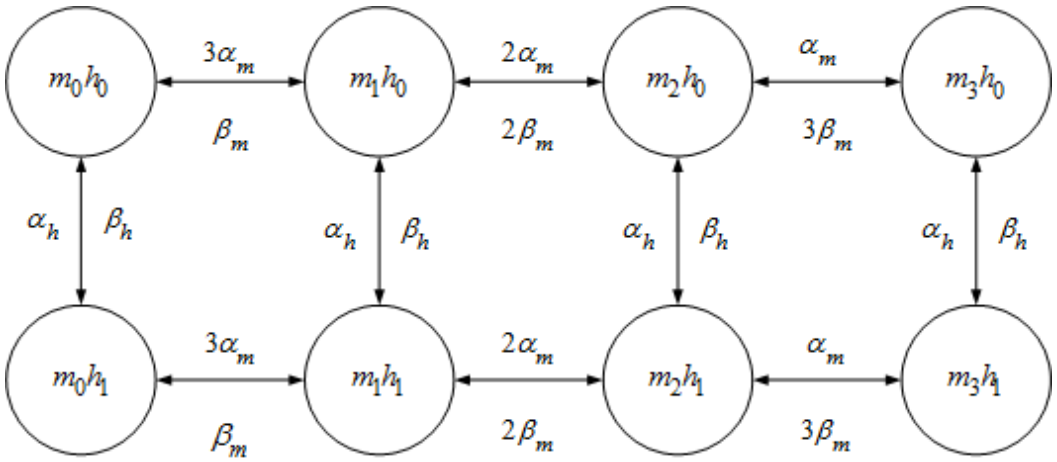

Figure 2-2 Kinetic diagram of the sodium channel

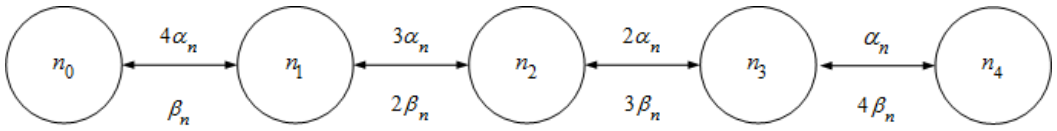

Figure 2-3 Kinetic diagram of the potassium channel

where α_x is the average rate at which the x particle switches from closed to open, β_x is the average rate at which the x particle switches from open to closed, and x_i represents that i particles of type x are currently open in the channel. In order for the sodium channel to be in its conductive state, all three m particles as well as the inactivating h particle need to be in their open position, which is represented by the state m_3h_1.

There are several different numerical techniques for simulating Markov kinetics. Fox and Lu [83, 101] utilized a stochastic differential equation to approximate the Markov process. Another way of building this stochastic ion channel gating model is using a continuous-time, discrete-state Markov jumping process to describe the kinetics of the ion channel [102, 103]. The algorithm could be subdivided into a channel-state-tracking (CST) algorithm and channel-number-tracking (CNT) algorithm.

The CST algorithm tracks the states of each channel. Rubinstein kept track of the gating particle states of every ion channel [98]. It is demonstrated that the microscopic fluctuations of single voltage-sensitive sodium channels in the nodes of Ranvier are sufficient to account for the macroscopic fluctuation of the threshold to electrical stimulation. The CST algorithm is simple in principle, but computationally intensive.

The CNT algorithm tracks the number of channels in each state assuming that multichannel systems are independent and memoryless [81]. The CNT algorithm renews the states of sodium channels only at each sampled time without tracking the state transitions between the sampled times. Thus the CNT algorithm is much more computational efficient.

Mino *et al* [100] compared the above four stochastic ion channel gating models with simulations of a patch of membrane with 1000 sodium channels to investigate the fundamental statistical parameters. It is suggested that the firing efficiency, latency and jitter are identical among Markov jumping process models (including Rubinstein and Chow & White) [100]. Fox and Lu [83, 101] produced quite different action potential statistics. The inaccuracy of the Fox and

Lu model might be the inappropriate Langevin approach to solving the nonlinear, internally generated noise. It also concludes that the CNT algorithm is the most computationally efficient.

Imennov and Rubinstein [104] developed a stochastic population model with gating particles of both sodium and potassium channels. The parameters are optimized for feline AN fibres. The model could predict the relative spread, spike latency, jitter, chronaxie, relative refractory period and conduction velocity of felines. It also matched the response characteristics of a population of fibres. However, the time constant of the model is not long enough to encompass short-term neural adaptation that occurs within first 100 to 300 ms of continuous stimulation.

Woo *et al*. [88] developed an adaptation model based on the stochastic ion channel gating model [105]. It incorporates potassium ion (K^+) channel, sodium ion (${N_a}^+$) channel and the external potassium ion K^+ concentration ($[K_{ext}^+]$). The relatively efficient Fox altorithm [83] is used in the ion channel gating model. The adaptation (accommodation) is mainly achieved by a leaky integrator based on external potassium ion K^+ concentration.

Miller *et al*. [106] further developed the adaptation model [88] by adding low-threshold potassium ion channel (Klt) and high-threshold potassium ion channel (Kht). Simulation results of this model demonstrate that forward-masker pulse trains can enhance the neural response to subsequent stimuli, which is also observed from the neural response of cat auditory nerve fibres. It indicates that Klt channel activation is largely responsible for sub-threshold accommodation effects.

Since stochastic ion channel gating models only consist of the voltage-dependent ion channels, leakage conductance and membrane capacitance, it is not able to predict the temporal properties of real neurons in detail, such as the adaptation recovery and ARP. To obtain the PST histogram and input-output (I/O) function, numerical stimulations need to be performed with large numbers of ion channels. Consequently, it needs enormous amounts of experimental data to constrain all the parameters.

2.4 Phenomenological models

The leaky integrator used in the stochastic ion channel gating model is actually a simple phenomenological model. Such simple phenomenological models are widely used for studies of neural temporal coding.

Phenomenological models are derived from experimental results and aim to describe the trends in the data. Phenomenological models have fewer parameters compared to conductance-based models or ion channel gating models. The required amount of data to constrain parameters is reduced as well. Furthermore, the phenomenological models with less equations speed up the computation time, which is more crucial when simulating a large population of nerve fibres or using Monte Carlo methods. Moreover, the parameters in the phenomenological model are directly related to experimental measurements, such as the membrane constant, absolute refractory period, relative refractory period, etc. Consequently, the temporal response can be visualized more easily. Hence, phenomenological models seem appropriate for our work as stated in chapter one.

A simple phenomenological model of neural excitation is a threshold-crossing model of firing. The model generates an action potential when the membrane

potential crosses the threshold [7]. As the spike is an all-or-none phenomenon, they are fully characterized by their firing sequences. There are different ways of defining the membrane potential, threshold, refractory effects and accommodation effects in the phenomenological models.

The integrate-and-fire model is one of earliest threshold models [107]. The moment of membrane voltage V_m crossing a fixed threshold defines the firing time and the membrane voltage V_m is calculated using Eq.(2.4.1),

$$I(t) = C_m \cdot \frac{dV_m}{dt} \tag{2.4.1}$$

where C_m is the membrane capacity. This simple model is memoryless which could be modified with a refractory period. During the refractory period, firing is prohibited. However, under subthreshold stimulus, the model remains memoryless which cannot capture the neural behaviour of time-dependent memory.

The leaky-integrate-and-fire (LIF) model is one of the best known formal phenomenological models. In the LIF model, the memory problem is solved by introducing a "leak" term to the membrane potential. Thus the model is modified as

$$I(t) - \frac{V(t)}{R} = C\frac{dV(t)}{dt} \tag{2.4.2}$$

Multiplying Eq.(2.4.2) by R and introducing the time constant, τ_m,

$$\tau_m = R \cdot C \tag{2.4.3}$$

Eq.(2.4.2) yields the standard LIF form

$$\tau_m \frac{dV(t)}{dt} = -V(t) + R \cdot I(t) \tag{2.4.4}$$

Furthermore, a refractory period can be added to the standard LIF model. After an action potential, the neuron enters the refractory period instantaneously. During absolute refractory time, firing is prohibited, and the integration is restarted after ARP with a new initial condition. For simplicity, the initial condition is usually set to zero.

Bruce *et al.* [46, 47] avoided the use of complex biophysical modelling, only considering the single-fibre rate-level function. Based on the physiological data from cat auditory nerve fibres, Bruce *et al.* developed a simplified, but stochastic, model of the auditory nerve (AN) by introducing Gaussian noise. Analytical expressions are derived for both single-pulse responses and pulse-train responses [51]. Thus, predictions can be simply computed and multiple iterations are not required. Bruce *et al.* [46, 47] successfully predicted the steady state of neural responses from cat auditory nerve fibres. Furthermore, predictions of psychophysical measures such as uncomfortable loudness, and the dynamic range were improved [66]. Therefore, stochastic activity is important in the design of a phenomenological model. This model will be used in this thesis, a detailed description is provided in chapter three.

Collins *et al*. [108] investigated the ISI histogram of a single fibre using the Bruce *et al.* stochastic AN model [46, 47] and showed that the presence of noise reduced neural synchrony, which resulted in a more acoustic-like neural response. Yifang Xu *et al.* [69] adopted the same model with refractory function presented

by conditional probability using recursive method. The model is used to predict the threshold of noise-modulated pulse-train electrical stimuli, dynamic range and intensity discrimination. It is demonstrated that the dynamic range for noise-modulated pulse-train stimuli should increase with additive noise. However, intensity discrimination under additive noise degrades. Predictions of the threshold match the psychophysical data derived from monkeys [109].

As stated in chapter one, accommodation has significant effects on the neural representation of stimuli in the auditory nerve fibres. However, none of the above phenomenological models can predict accommodation behaviour.

2.4.1 The LIFDT model

A leaky integrate-and-fire model with dynamic threshold (LIFDT) is proposed by Allingham*, et al*. [19] on the basis of the standard LIF model. The standard LIF model is extended to have a stochastic membrane potential and a dynamic threshold which accounts for both refractory effects and accommodation effects. The noise term also enables the LIFDT model to produce stochastic activity.

The dynamic threshold in the LIFDT model is not designed to capture accommodation effects at first, but to accurately predict the refractory period to sinusoidal stimuli across different frequencies. The dynamics of the LIFDT model are validated with extensive physiological data to sinusoidal electrical stimuli [19, 53, 110]. The dynamic threshold is built with the inactivation of sodium permeability from the F-H model [37], which also contributes to accommodation effects [10, 11, 92]. It enables the LIFDT model to incorporate accommodation mechanism and its predictions agreed with accommodation behaviour in the experimental data [19]. It is the first phenomenological model of

the auditory nerve that includes accommodation effects. A detailed description of this LIFDT model is presented in chapter three.

2.5 Summary

The current chapter has briefly reviewed some computational auditory nerve fibre models including the conductance-based H-H model, F-H model; stochastic ion channel gating models and phenomenological models. Previous studies of auditory nerve modelling provide different approaches of temporal coding. Conductance-based models and ion channel gating models are derived by the description of each ion channel state. Although the time of firing is illustrated, the threshold, interpulse interactions have to be further calculated. On the contrary, parameters of phenomenological models are directly related to experimental measurements, such as the membrane constant, ARP, RRP and the threshold. Therefore, it is more convenient to investigate the temporal response of phenomenological models.

Neurophysiological data (presented in chapter three), that obtained from the auditory nerve of adult guinea pigs by Sly, *et al*.[16], were used. Only ten sets of data were available. Each set has ten data points. For such limited data, it is impractical to constrain forty parameters in conductance-based models and stochastic ion channel models. Therefore, phenomenological models with less ten parameters seem the most appropriate model for the analysis performed and presented in this thesis.

Chapter3. *Methodology*

3.1 Introduction

Accommodation has a significant effect on the neural representation of stimuli by auditory nerve fibres. The lagged computational modelling is in part due to the historic lack of systematic auditory nerve fibre data. Recently neural response from animal models to both analogue electrical stimulation and pulsatile electrical stimulation were obtained, which reveal accommodation behaviour [16, 17, 19]. It motivates us to further build a phenomenological model incorporating accommodation effects.

As the LIFDT model successfully captured the accommodation behaviour to analogue stimulation, the thesis will investigate whether accommodation behaviour can be obtained from the LIFDT model subject to pulsatile stimulation.

In this chapter, two phenomenological models are presented with the detailed temporal response, which will be used in this thesis. One is the LIFDT model in section 3.3; the other is the stochastic AN model of Bruce, *et al.* [46, 47, 51] in section 3.2. Bruce, *et al.*[51] proposed a theoretical analysis of the stochastic AN model. This theoretical approach is utilized to conduct the analytical approximation of the LIFDT model in chapter five.

The neural response [16] to pulsatile stimulation from guinea pig auditory nerve fibres, a model of the electrically stimulated human auditory nerve, is also introduced in this chapter. The electrical stimuli were biphasic pulse trains. Extracellular recordings were made via a dorsal approach. The experiments are described in detail in section 3.4. The neural responses are presented in the form

of I/O curves and peristimulus time histogram (PST histogram) plots (defined in Figure 3-13). The I/O curve is generated to illustrate how single auditory nerve fibres' firing efficiency varies against stimulus amplitude. The PST histogram plots are utilized to illustrate how single auditory nerve fibres' excitability varies across pulse number. Analysis of the experimental data is demonstrated in chapter four.

3.2 A stochastic AN model

Bruce *et al*. developed a stochastic AN model of auditory nerve response to electrical stimulation [46, 47]. The model is a simple phenomenological threshold model and includes several neural parameters which controls the generation of spikes.

For a single pulse stimulus, the mechanism is to compare the amplitude of the stimulus V_{stim} and threshold V_{thr} , shown in Figure 3-1. If the stimulus V_{stim} crosses the threshold V_{thr}, a spike is generated. As only one pulse is delivered to the model, the refractory effects is not considered. The threshold consists of a fixed threshold potential V_{thr} and the membrane noise V_{noise}. The membrane noise, which represents the membrane potential fluctuations, has been characterized by Verveen *et al*, [96, 99, 111, 112]. The noise has a Gaussian amplitude distribution and a $1/f$ spectrum.

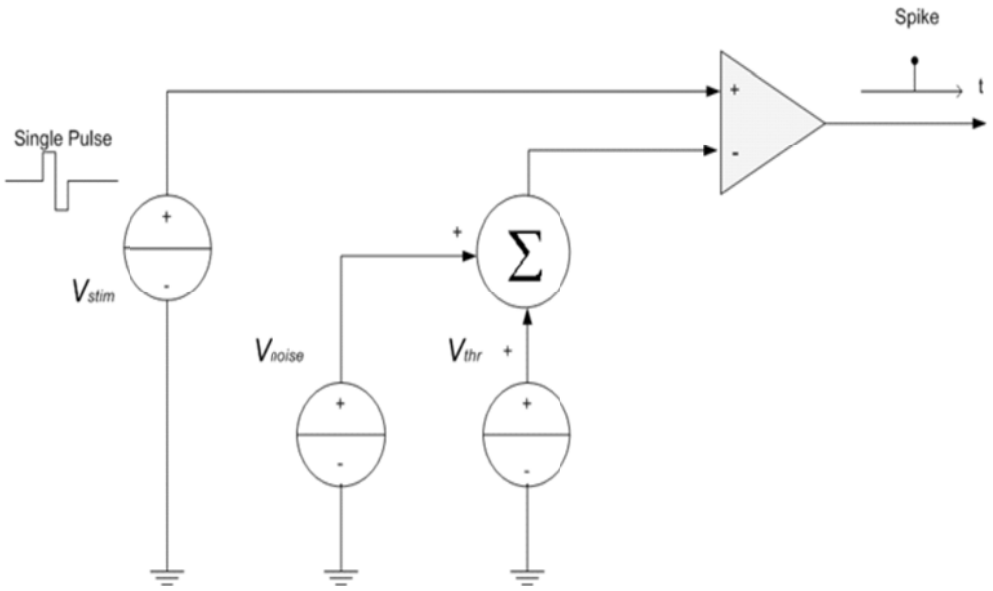

Figure 3-1 A stochastic AN model of: Single pulse [47]

Bruce *et al*. made several approximations to simplify the AN model. First, for biphasic current pulses, discharges only occur in response to the onset of the cathodic phases, because the threshold for the onset of a cathodic phase is lower than the onset of an anodic phase [7]. No discharge is generated between pulses. Second, changes of threshold with the stimulating current (accommodation effects) are ignored. Third, accurate simulation of noise with a $1/f$ frequency spectrum is laborious. The noise term in the AN model is approximated by a Gaussian distribution with a mean of zero and variance σ^2.

With these approximations, Monte Carlo simulation of the model is quite simple. Furthermore, the simulation is actually a Bernoulli process. An analytical expression of this model is derived for a single pulse stimulus. The Bernoulli random variable $p(n)$ is the discharge probability during pulse n.

$$p(n) \triangleq \Pr\{\text{discharge during pulse } n\} \qquad (3.2.1)$$

Discharge is considered to be a success (expressed as "1") and no discharge is considered to be a failure (expressed as "0"). Then an analytical expression for the discharge probability for any single pulse *n* is developed as follows,

$$p(n)=\begin{cases}0 & for\, V_{stim}(n) < V_{thr}(n)+V_{noise}(n)\\ 1 & for\, V_{stim}(n) \geq V_{thr}(n)+V_{noise}(n)\end{cases} \qquad (3.2.2)$$

As $V_{stim}(n)$ and $V_{thr}(n)$ are fixed within the pulse, we can rearrange the inequality in Eq.(3.2.2) as,

$$p(n)=\begin{cases}0 & for\, V_{noise}(n) > V_{stim}(n)-V_{thr}(n)\\ 1 & for\, V_{noise}(n) \leq V_{stim}(n)-V_{thr}(n)\end{cases} \qquad (3.2.3)$$

As the noise is normally distributed with a mean of zero and variance of σ^2, the probability density function (PDF) of the noise is plotted in Figure 3-2. Discharge occurs when the noise falls in the interval $(-\infty, V_{stim}(n) - V_{thr}(n)]$. The grey area represents the probability of discharge $p(n)$, which is the integral of the noise PDF over the interval $(-\infty, V_{stim}(n) - V_{thr}(n)]$. Thus the probability of discharge is related to an integrated Gaussian function given by Eq.(3.2.4).

The discharge probability versus stimulus intensity (I/O function) is

$$\begin{aligned} p(n) &= \int_{-\infty}^{V_{stim}(n)-V_{thr}(n)} f(x)dx \\ &= \int_{-\infty}^{V_{stim}(n)-V_{thr}(n)} \frac{1}{\sqrt{2\pi\sigma^2}} e^{-\frac{x^2}{2\sigma^2}} dx \end{aligned} \qquad (3.2.4)$$

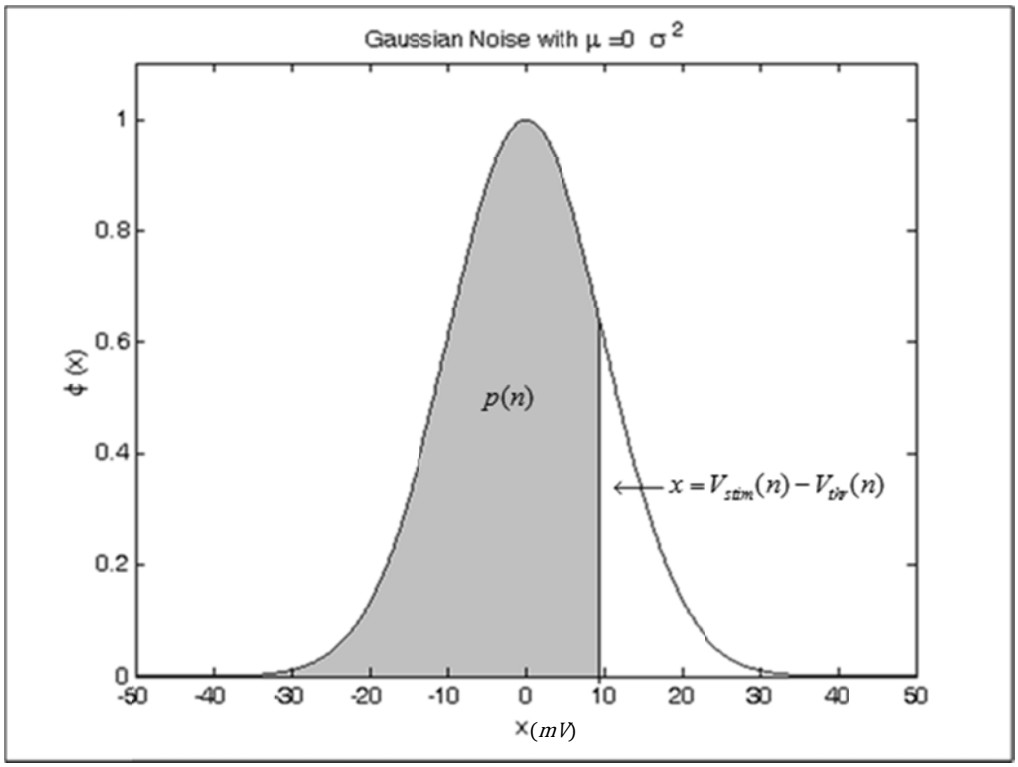

Figure 3-2 Probability density function of noise with mean of zero and variance of σ^2. The grey area represents the probability of discharge *p(n)*, which is the integral of the noise PDF over the interval $(-\infty, \boldsymbol{V_{stim}(n) - V_{thr}(n)}]$

The integrated Gaussian function can be written as an error function,

$$p(n) = \frac{1}{2}(1 + erf(\frac{V_{stim}(n) - V_{thr}(n)}{\sqrt{2}\sigma})) \tag{3.2.5}$$

where $V_{thr}(n)$ is referred to the stimulus amplitude required for the fibre to fire with mean probability of 0.5, σ controls the slope of the I/O function. Relative spread (RS) is referred to the normalized form of σ.

$$\text{RS} \triangleq \frac{\sigma}{V_{thr}} \tag{3.2.6}$$

The greater the value of RS, the shallower the slope of the I/O function (see Figure 3-3).

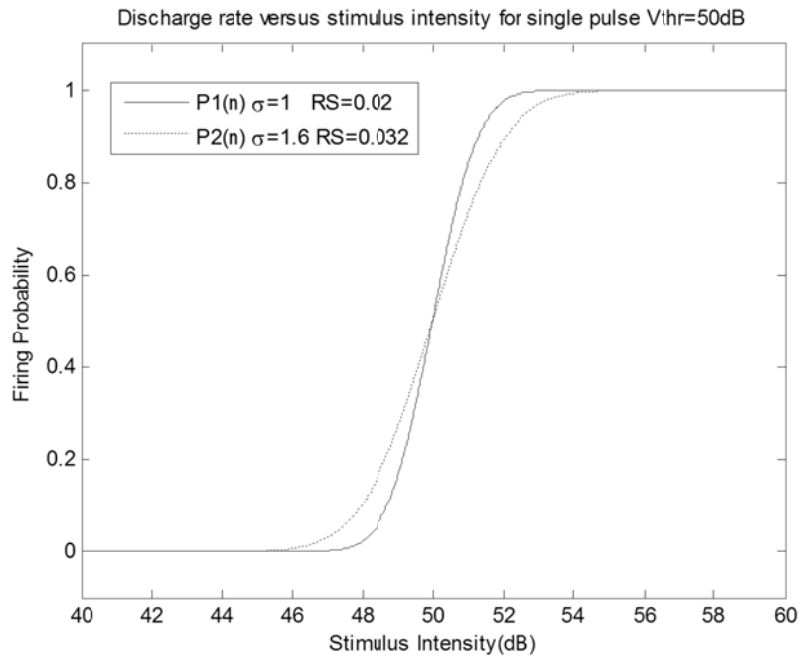

Figure 3-3 I/O function for stochastic AN model [47]: single pulse

For pulse-train stimuli, the neural response to any pulse in the train is dependent on whether the neuron has fired or not in the previous pulses in the pulse train. In the stochastic AN model [46], only refractory effects are considered. Based on the single-pulse model Eq.(3.2.5), a refractory function (V_{ref}) (defined in Eq.(3.2.8)) is added to "the threshold potential" (V_{thr}) after a spike (shown in Figure 3-4).

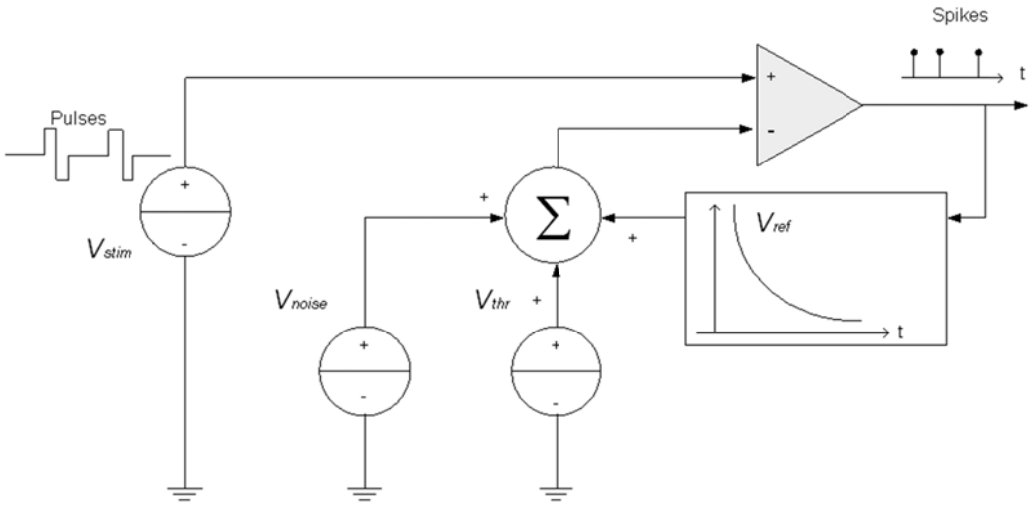

Figure 3-4 A stochastic AN model: Pulse-train [46]. Details are explained in the following text.

After a spike, the neuron is in its refractory period. The discharge probability to the single-pulse occurring in refractory period is defined as

$$p_{ref}(n)=\begin{cases}1 & V_{stim}(n)\geq V_{thr}(n)+V_{noise}(n)+V_{ref}\\ 0 & V_{stim}(n)<V_{thr}(n)+V_{noise}(n)+V_{ref}\end{cases} \tag{3.2.7}$$

The refractory function is set to infinity during ARP. Thus, no discharge occurs during that time. During the RRP, the refractory function, which is defined by an exponential function, falls monotonically to zero. Thus after the RRP, the neuron recovers to its resting state. The general refractory function is given by

$$V_{ref}(t)=\begin{cases}\infty & 0\leq t\leq 0.7ms\\ 0.97V_{thr}\cdot e^{-\frac{t-0.7ms}{1.32ms}} & 0.7ms<t\leq 20ms\\ 0 & t>20ms\end{cases} \tag{3.2.8}$$

where t refers to the time after the action potential, the ARP lasts 0.7 ms, the RRP starts from 0.7 ms to 20 ms with a time-constant of 1.32ms. This model can be implemented by Monte Carlo simulation.

The stochastic AN model of a pulse-train stimulus can be described as a renewal process. In a renewal process, the waiting times between successive occurrences of an event are mutually independent random variables having the same distribution [113]. For the stochastic AN model, the neuron begins the refractory period anew after each discharge. All the "memory" of previous discharge is lost. With the renewal process theory, analytical expressions for the mean and variance of the total discharge rate are derived under a noise-free pulse train of

evenly timed, uniform pulses. The theoretical analysis only studies stable state probability. It did not provide the neural response to each pulse. The stochastic AN model demonstrates that it is fundamental to include a stochastic component in auditory nerve models [46, 47, 51]. Furthermore, analytical expressions for other stochastic models can be derived based on the stochastic AN model for a single pulse stimulus.

3.3 The LIFDT model

The LIFDT model [19] is developed based on standard LIF model [114]. An action potential is generated when the membrane potential V crosses the threshold θ.

The membrane potential V is defined by

$$\tau_m \dot{V}(t) = -V(t) + S(t) + \sqrt{2D}\xi(t) \tag{3.3.1}$$

where $V(t)$ represents the membrane potential of the neuron at time t, τ_m is the membrane time constant, which controls how quickly the nerve responds to the stimulation, $S(t)$ is the input stimulus, D is the noise intensity, $\xi(t)$ is Gaussian noise with $\langle \xi(t)\xi(t') \rangle = \delta(t-t')$ and $\langle \xi(t) \rangle = 0$,where $\delta(t-t')$ is the Dirac delta function.

The dynamic threshold θ is defined by

$$\tau_h \dot{h}(t) = -h(t) + h_\infty(t) \tag{3.3.2}$$

$$h_\infty(t) = (1 + e^{\frac{V(t)-\mu_\infty}{\sigma_\infty}})^{-1} \tag{3.3.3}$$

$$\theta(t) = \frac{\theta_m}{h(t)^p} + \theta_0 \tag{3.3.4}$$

where h is the voltage-gated variable for inactivation of sodium permeability, τ_h is the recovery time constant of h, h_∞ is the asymptotic value of h, μ_∞ is the offset for h_∞, σ_∞ is the standard deviation of h_∞, θ_0 is the base value of the threshold and does not have physiological meaning, θ_m is the threshold multiplier and p is the multiplier of h. One set of parameter values of Eq.(3.3.1) -(3.3.4) are given in Table 3-1, which are fitted to cat data [53].

Table 3-1 Fitted parameter values of the LIFDT model [53]

SIMBOLS & UNIT	D	τ_m[ms]	τ_h[ms]	μ_∞ [mV]	σ_∞ [mV]
FITTED VALUE	0.01	0.7	1.9	-4.5	100
SIMBOLS &UNIT	θm [mV]	θ_0 [mV]	p	τ_{abs} [ms]	
FITTED VALUE	3	50	1.3	0.284	

The mechanisms of the LIFDT model are shown in Figure 3-5. Unlike the stochastic AN, the noise term is added to the membrane potential. The noise term originates from the fluctuations in the opening and closing of the ion channels [47, 112]. The *Leaky integrator block* represents the stochastic differential Eq.(3.3.1) for the membrane potential V. It takes the integrator of *Stimulus* and *Noise* by the membrane time constant τ_m. A dynamic threshold θ is derived based on the inactivation of sodium permeability variables h from the F-H model [37], for which there is a strong relationship between inactivation of sodium permeability h and the instantaneous stimulus amplitude required to invoke a spike [19]. The parameters from Eq.(3.3.4) are obtained by fitting

threshold behaviour curve of the F-H model. This feature enables refractory effects and accommodation effects to be incorporated in the LIFDT model.

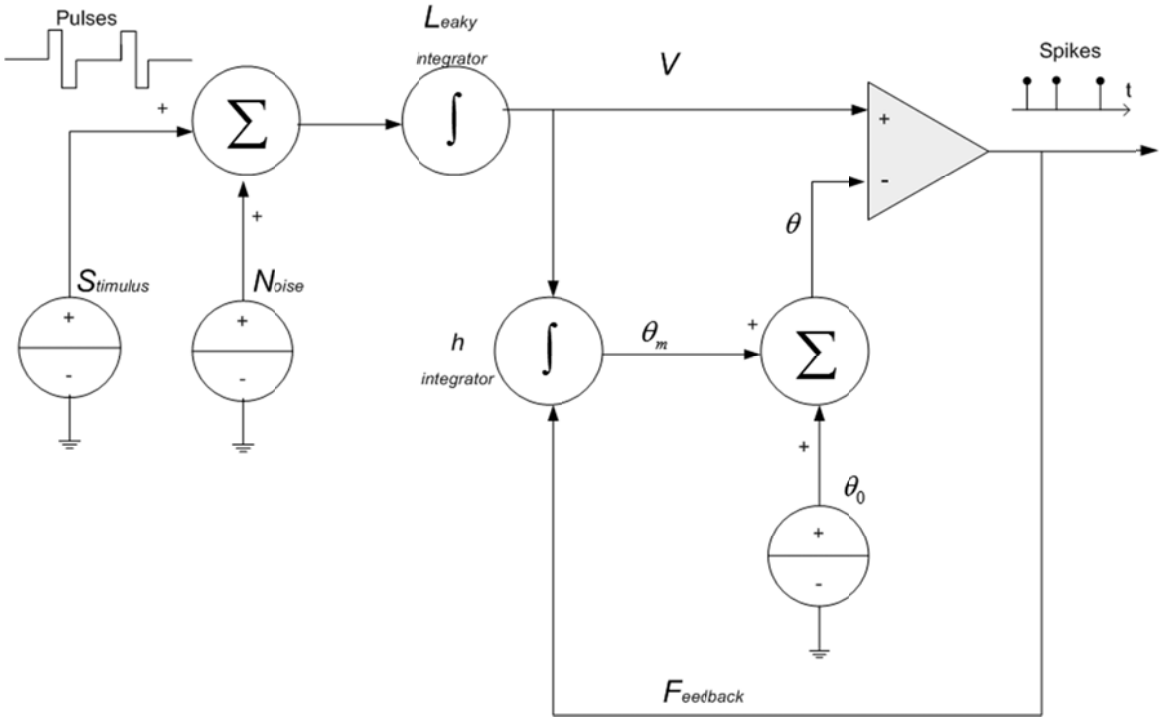

Figure 3-5 The mechanisms of the LIFDT model

The threshold θ consists of a constant part θ_0 and a dynamic part which is dependent on h. The *h integrator block* represents the differential equation Eq.(3.3.2) and equilibrium equation Eq.(3.3.3) of h. Those two equations are modified from the F-H model. The relevant equation for h in the F-H model contains six parameters, which is quite complex and requires substantial experimental data. In this LIFDT model, the equation for h_∞ is approximated by a sigmoid function Eq.(3.3.3) with fixed τ_h, where μ_∞ controls at what value of membrane voltage h_∞ is 0.5 and σ_∞ controls the slope of h_∞.

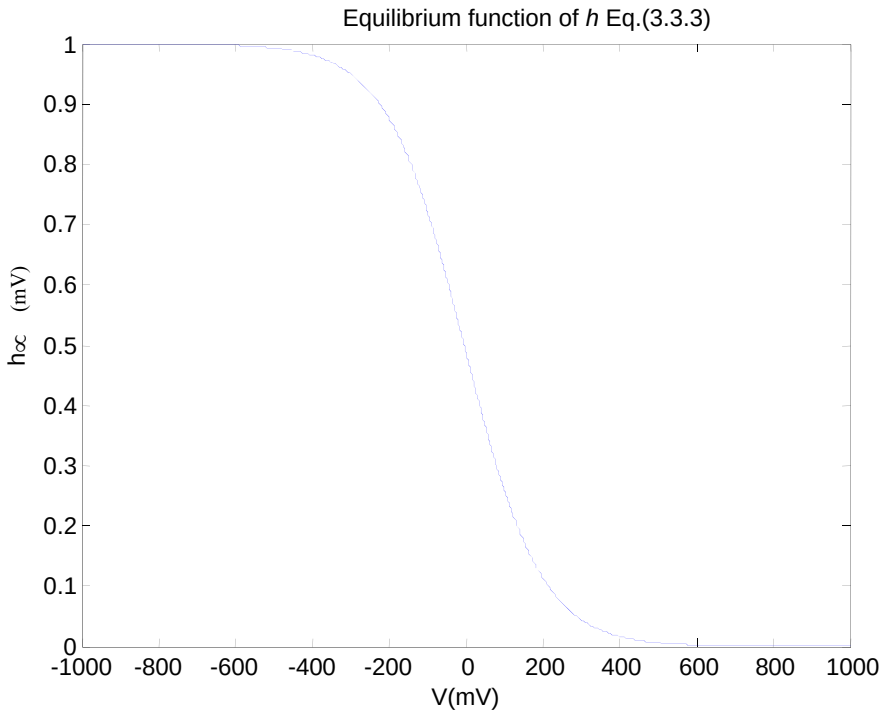

Figure 3-6 The relationship between the asymptotic value of the inactivation of sodium permeability and the membrane potential (Eq.(3.3.3))

The relationship between V and h_∞ is shown in Figure 3-6. For fixed stimulus $\bar{V}$, the variable h approaches the asymptotic value $h_\infty(\bar{V})$ with the time constant τ_h.Therefore, the threshold θ is stimulus-dependent at all times.

For a particular electrical stimulus, the membrane potential V and threshold θ can be calculated at any given time, t, according to Eq.(3.3.1)-(3.3.4). In this thesis the model is integrated using a two-step Heun scheme, as it is more accurate for integrating stochastic differential equations with Gaussian noise [115]. The code is presented in Appendix A.

Unlike other phenomenological models [46, 69], both the membrane potential V and threshold θ are dependent on the stimulus. Therefore, this model can respond to a suprathreshold stimulus and even to a subthreshold stimulus.

Consequently, it is suitable for investigating the accommodation effects. The neural responses of suprathreshold and subthreshold stimuli are presented in the following sections.

3.3.1 Response to suprathreshold stimulus: Refractory effects

When the membrane potential V crosses the threshold θ, an action potential or spike is generated, then the neuron enters the refractory period instantaneously. In the model of Bruce, *et al.,*[46] refractoriness is defined separately. For ARP, the threshold is set to infinity. For RRP, an exponential function is used to describe the decreasing threshold. In the LIFDT model, refractoriness is defined implicitly, because h and θ are calculated during the refractory period. After a discharge, the membrane potential V and gating variable h are reset to zero, but not held constant for any period, and integration continues during ARP. The neuron's "memory" is refreshed by resetting the membrane potential V to zero. The threshold θ is set to infinity when h equals zero. As integration continues, h approaches $h_{\infty}(V)$. The threshold θ decreases smoothly to its resting value afterwards. An explicit ARP τ_{abs} is added to this model. Within the time of τ_{abs}, firing is prohibited even when the stimulus potential crosses the threshold.

To demonstrate the refractory phenomenon more clearly, noise-free pulsatile stimuli are applied to the LIFDT model. The electrical stimuli are two biphasic pulses (50 μs/phase, 10 μs interphase gap, anodic phase first, at rates of 200 pulses per second (pps)), which were also used in neurophysiological experiments discussed in section 3.4. The chosen stimulus amplitude only evokes an action potential at the first pulse but not the second. Figure 3-7 shows the refractory effects of the LIFDT model. The dashed line represents the membrane

potential V in Eq.(3.3.1) and the solid line represents the threshold θ in Eq.(3.3.4). In Figure 3-7, the membrane potential V follows the stimulus with the membrane constant τ_m.

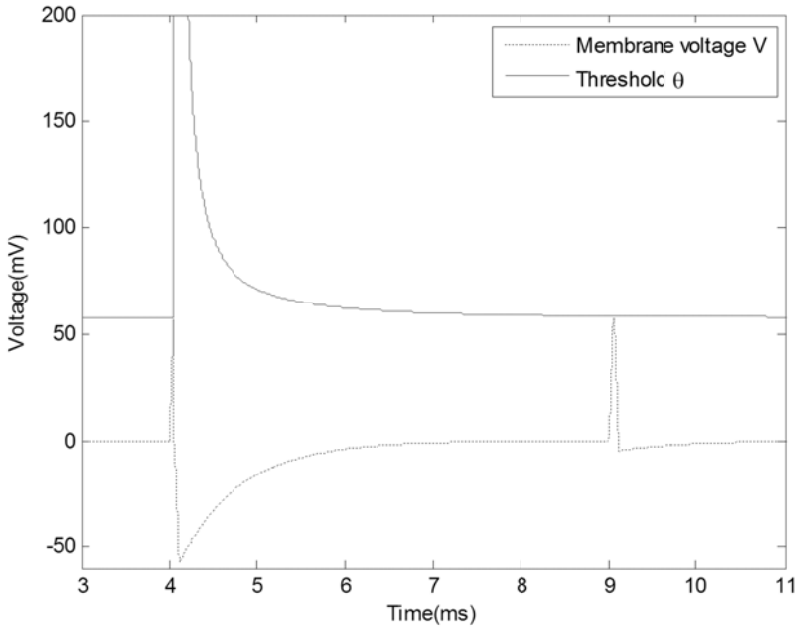

Figure 3-7 Neural response of the LIFDT model: Refractory Effects. The dashed line is the membrane potential V in Eq.(3.3.1) and the solid line is the threshold θ in Eq.(3.3.4) .

An action potential is generated at the first pulse, then the neuron enters the refractory period. Although refractory effects are defined implicitly, the shape of the threshold function $\theta(t)$ is similar to the separately defined refractory function Eq.(3.2.8) in the stochastic AN model. After an action potential, the threshold θ is too large for another action potential to be evoked. This period lasts a few milliseconds. Then the threshold θ decreases monotonically to its resting value. In the LIFDT model, the RRP is not explictly defined.

3.3.2 Response to subthreshold stimulus: Accommodation effects

The LIFDT model is able to capture accommodation effects when presented with low frequency sinusoidal stimulation [19]. Accommodation effects were observed from the tuning curve (onset-of-firing amplitude against frequency). It demonstrated that the onset-of-firing amplitude monotonically increases when frequency increases. Accommodation effects in the LIFDT model can be observed directly from the plot of threshold θ. Two-pulse stimuli with subthreshold amplitude are applied to the LIFDT model.

Figure 3-8 presents the neural response of the LIFDT model to subthreshold stimulus.

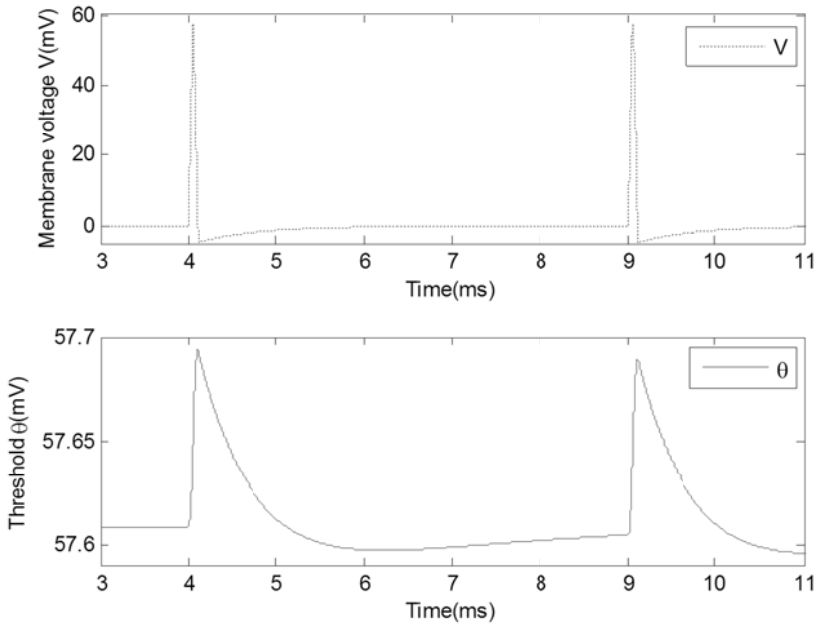

Figure 3-8 Neural response of the LIFDT model: Accommodation Effects. The dashed line represents the membrane potential V in Eq. (3.3.1) and the solid line represents the threshold θ in Eq.(3.3.4)

The dashed line represents the membrane potential V in Eq.(3.3.1) and the solid line represents the threshold θ in Eq.(3.3.4). For a noise-free subthreshold

stimulus, no action potential is generated. The membrane potential V "follows" the stimulus. The threshold θ also responds to the stimulus. Firstly, it shifts then recovers to its resting value. Accommodation effects in the LIFDT model are further studied in chapter five.

3.4 Experimental data

Neurophysiological data was obtained from the auditory nerve of adult guinea pigs by Sly, *et al*.[16], which is a physiological model of the cochlear nerve. Extracellular recordings were made from the central axon of a single auditory nerve from adult guinea pigs.

3.4.1 Experimental procedure

The experimental details are described in [17]. The experimental set up is presented in Figure 3-9. In brief, the cochlear stimulating electrode was inserted into the scala tympani of the cochlea via a dorsal approach. Quartz glass recording electrodes were inserted into the cochlear nucleus toward the underlying auditory nerve. The stimulating electrode delivered the stimulus to the auditory nerve and the recording electrode measured the electrical activity of the auditory nerve. The electrical stimuli in the experiment were charge-balanced biphasic pulse trains (50 μs/phase, 10 μs interphase gap, cathodic phase first). With short duration charge-balanced biphasic pulsatile stimuli, the localized electrochemical reactions were reversed during the second phase of the biphasic current pulse. No net electrochemical products were formed. A single biphasic pulse is shown in Figure 3-10. Pulse trains at either 200 pps or 800 pps were presented for 100 ms within each trial. Thus, for a pulse train at 200 pps, 20 pulses were delivered to the auditory nerve fibres. Likewise, 80 pulses were

delivered for the 800 pps pulse train. The interval between each trial was 100 ms. 50 trials were delivered to each auditory nerve fibre (shown in Figure 3-11).

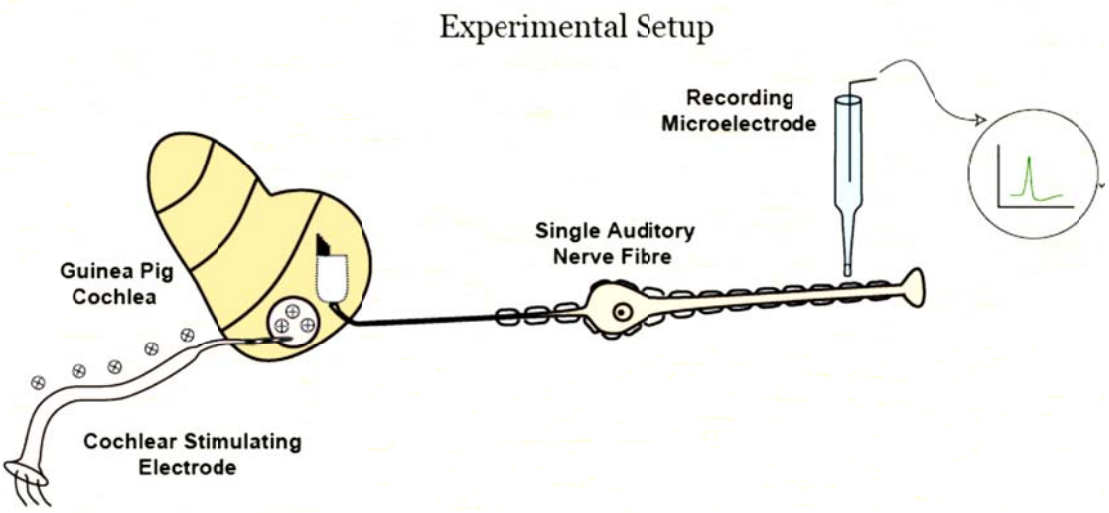

Figure 3-9 Experimental recording setup[16]

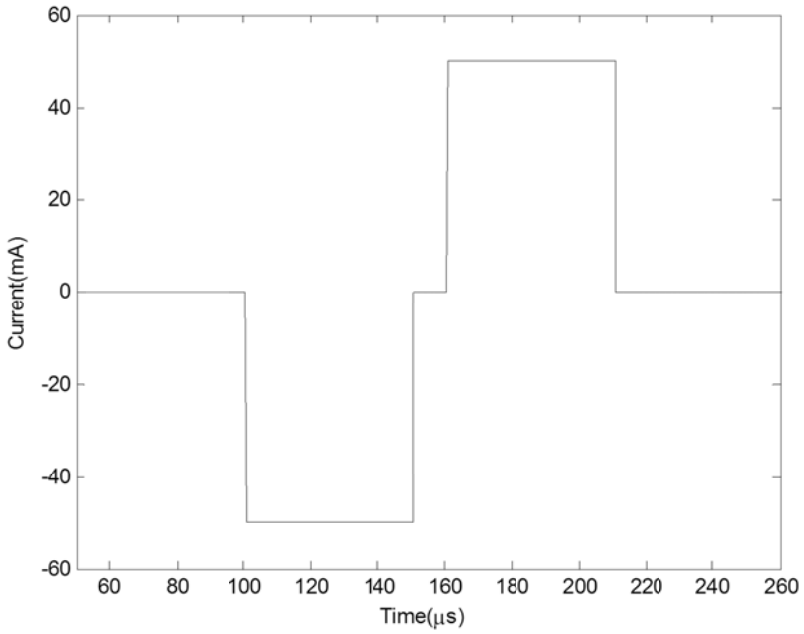

Figure 3-10 A single pulse of 200pps pulse Train

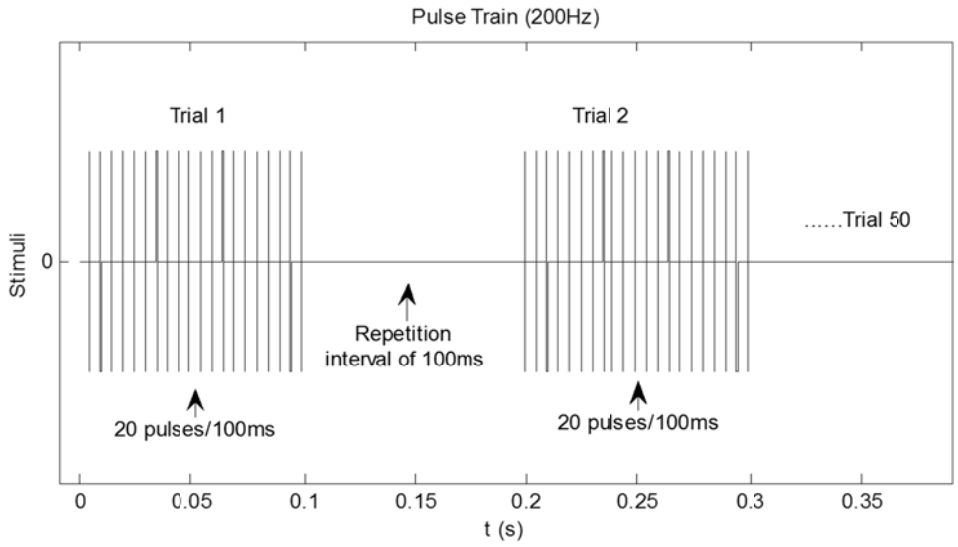

Figure 3-11 200pps Pulse Train

3.4.2 Electrophysiological experimental data

A total of 518 auditory nerve fibres among 40 animals were studied in the experiment. The neural responses of pulse train stimuli were presented in an I/O curve and PST Histograms for mean firing efficiencies (FE) from 0.02 to 1. For each auditory nerve fibre, an I/O curve was constructed by plotting FE against stimulus current for the 200 pps pulse train (as shown in Figure 3-12).

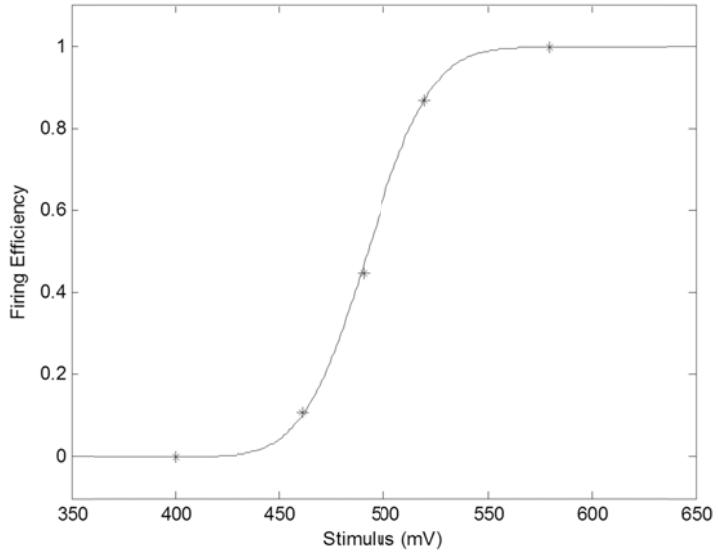

Figure 3-12 I/O Function for the 200 pps pulse train from neurophysiological data [16]

Normally, firing efficiency (FE) is defined as the average firing rate over one trial (see Figure 3-11). Counting the spikes in one trial, which consists of N pulses, the summed spike number is n_{sp}. Then the FE is given by

$$\mathrm{FE} \triangleq \frac{n_{sp}}{N} \tag{3.4.1}$$

The PST Histogram presents the spike density of the neural response. In principle, it is defined as an average over several repetitions of the experiment [116, 117]. The same stimulation sequence is repeated several times. The spike number n_K is summed over all repetitions with a time window Δt, which is typically about one or a few milliseconds. The neural response was recorded while the pulse trains are applied K times. Then the spike density is given by

$$\rho = \frac{1}{\Delta t} \cdot \frac{1}{K} n_K(t; t + \Delta t) \tag{3.4.1}$$

For these experimental data, because a significant number of firing probabilities is required to demonstrate how the nerve responses, each PST Histogram is calculated by a small population of auditory nerve fibres with a narrow range of FE. For example, the PST Histogram of FE 0.5 is constructed by averaging the response of all the auditory nerve fibres with FE of 0.5±0.1. In other words, FE is referred to as the mean firing probability of several fibres within the data pool.

Furthermore, as the stimulus is a biphasic pulse train with very short duration (110 μs), the neuron can only fire once within each pulse. Therefore, there is no need to sum the spike number over all repetitions with a time window Δt. Moreover, only fibres with response latencies smaller than 800 μs were categorized as direct neural responses and fibres outside this criterion were

excluded. Thus, the spike number n_i is summed from the start of the cathodic phase of the applied *i*'th pulse to the time line, which is 800 μs after the end of the anodic phase of the *i*'th pulse. An example of a constructed PST Histogram [16, 17] is shown in Figure 3-13. Assume the total number of auditory nerve fibres within specific range of FE (e.g. FE= 0.5 ± 0.1) is *M*. For each single auditory nerve fibre, the same trial is repeated 50 times. Then the firing probability p_i at the *i*'th pulse is defined as,

$$p_i = \frac{1}{M} \cdot \frac{1}{50} \cdot n_i \left(pulse \quad i \right) \tag{3.4.2}$$

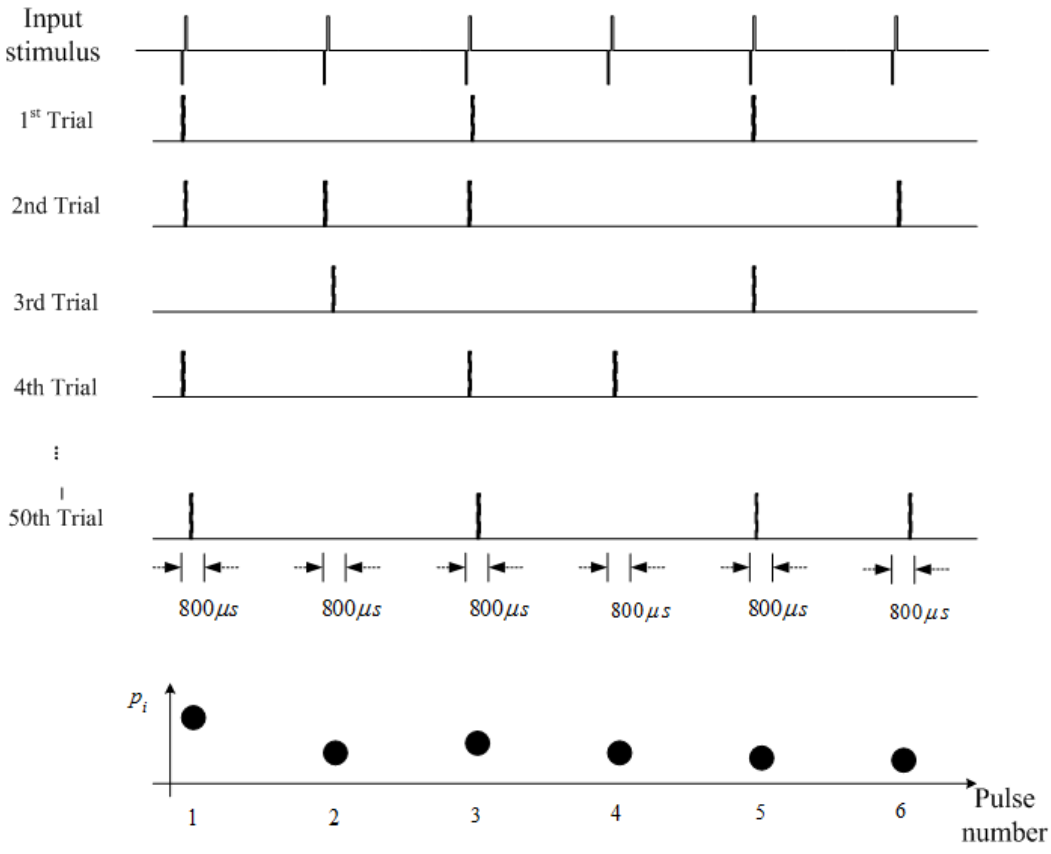

Figure 3-13 Definition of the spike density in PST Histograms as an average over several runs of [116]

In other words, the constructed PST Histogram is not a continuous-time plot, but a discreet-time plot. Each PST Histogram was labelled by its firing efficiency FE, and the presented plot was normalized by the firing probability at the first pulse,

$$p_i^n = \frac{p_i}{p_1} \tag{3.4.3}$$

where p_i^n is the normalized firing probability at the *i'th* pulse.

Thus each curve was plotted with the first pulse firing probability equal to one (shown in Figure 3-14). Rewriting Eq.(3.4.3), the original firing probability p_i at the i 'th pulse can be calculated given the value of FE and p_i^n as,

$$p_i = p_i^n \cdot p_1 \tag{3.4.4}$$

where

$$p_1 = \frac{\mathrm{FE}}{\frac{1}{20}\sum_{i=1}^{20} p_i^n} \tag{3.4.5}$$

Thus the experimental data are transformed to their original version as shown in Figure 3-14. All the original PST histograms in response to a 200pps pulse train are presented in Figure 3-15. There was a drop in the firing probability after the first pulse. The suppression not only occurred at high FE, but also at low FE. For low FE (FE <0.4), the firing probability at the first pulse was about three times greater than the firing probability at subsequent pulses. For $\mathrm{FE} = 0.05$, the auditory nerve fibres fired on average once every twenty pulses. It is unlikely that the suppression of firing is due to refractoriness as the nerve fibres rarely

fired. It is hypothothesised that accommodation results in this suppression. The experimental data will be further analysed in chapter four.

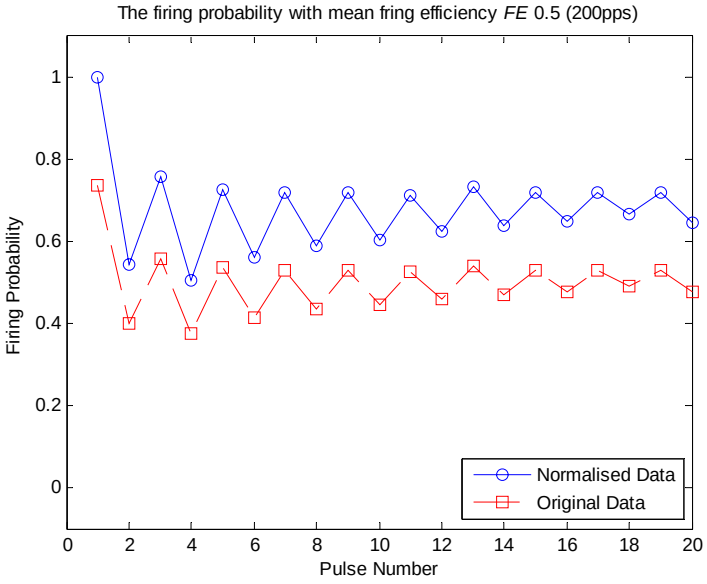

Figure 3-14 Normalised data and Original data at FE = 0.5 **.**

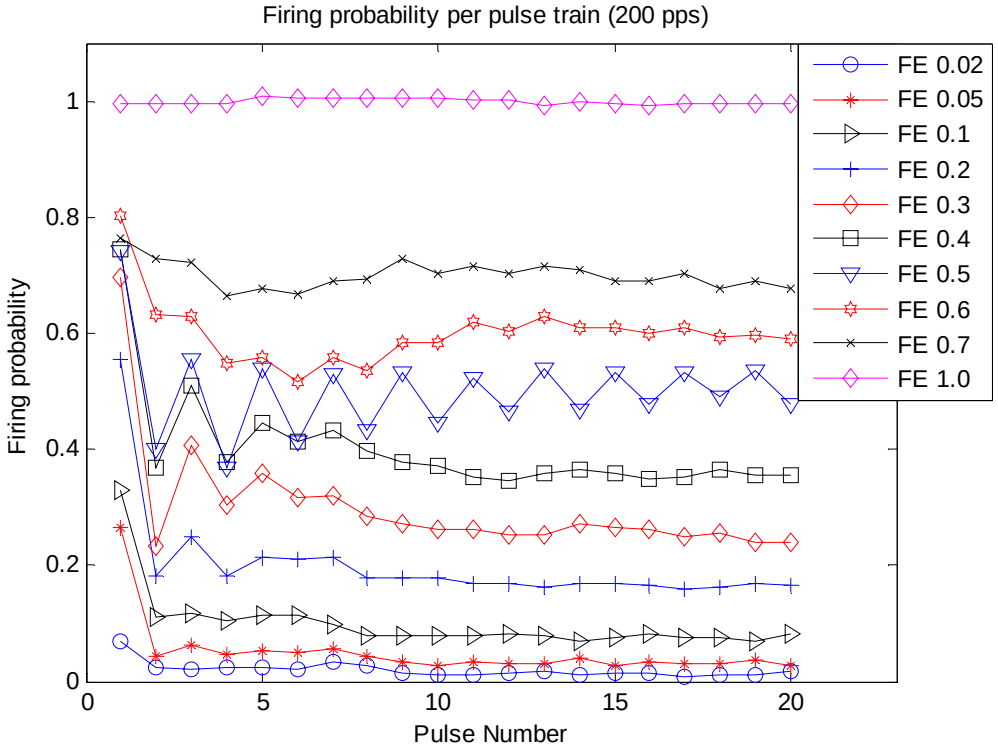

Figure 3-15 Firing probability in response to a 200 pps pulse train stimulation, FE varies from 0.02 to 1.0

3.4.3 Data considerations

There are some methodological factors that should be considered for the neurophysiological data..

First, stable recordings from single auditory nerve fibres are viable for short periods of time. The firing probability from one trial of 200-pps pulse train was different from other trial. The firing stability of one nerve fibre was examined by dividing the total number of spikes that occurred during the first 25 trials by the number that occurred during the last 25 trials [17]. This ratio was 1.54 ± 0.45 at a FE of 0.1; 1.27 ± 0.26 at a FE of 0.5 and 1.27 ± 0.26 at a FE of 0.9. It suggested that the error of measurement is greater at low FE.

Second, to overcome the firing stability of one nerve fibre, the data were pooled across the auditory nerve fibres within defined ranges of FE. For example, the PST histogram of 0.5 FE was calculated by averaging responses of all auditory nerve fibres within a mean firing efficiency of 0.5 ± 0.1. For FE s of 0.02 and 0.05, ranges of pooling were not specified, but one datum could only contribute to one histogram.

3.5 Summary

Two phenomenological models are compared in this chapter. The LIFDT model is the first phenomenological model that incorporates both refractory effects and accommodation effects. Since the acquired experimental data show some accommodation behaviour, we choose the LIFDT model to investigate the interpulse interactions in the experimental data. The accommodation effects in will be studied in chapter four by using the LIFDT model and Chapter 6 by using the Markov model.

Chapter4. *Fitting the LIFDT model to experimental data*

4.1 Introduction

The LIFDT model and experimental data have been presented in previous chapter. The LIFDT model was developed using analogue sinusoidal stimuli [1] and hence has not been validated with pulsatile stimuli. The main objective in this chapter is to investigate whether the LIFDT model is applicable for pulsatile stimuli.

The optimization of the LIFDT model with experimental data involves nine parameters as shown in Table 3-1. Previous optimization of the LIFDT model with sinusoidal stimulation was only based on steady state firing efficiencies [19]. However, the experimental data for pulsatile stimulation indicates the firing probability at the first pulse is significantly larger than that for the subsequent pulses, which does not seem attributable to refractory effects. After ten pulses, the firing probability becomes almost constant. In order to model this phenomenon by the LIFDT model, investigation of how the average firing efficiency across the whole pulse train varies on different values of the parameters is clearly insufficient. To take into account the non-stationary effects that accommodation introduces, the optimization should be constructed based on the firing probability at each pulse.

The experimental data contain ten curves with $\overline{FE}$ ranging from 0.02 to 1.0. Each curve has twenty data points. Hence, there are two hundred experimental data points in total.

The goodness function for the optimization was the sum of errors between two hundred experimental data points and simulation results from the LIFDT model. Monte Carlo simulations of the LIFDT model were performed using one thousand iterations. Consequently this full optimization is time consuming and computational laborious. Moreover, the main difficultly was that the formulated goodness function actually calculates the error in the firing probabilities, which was not continuous as a function of each parameter.

To avoid massive computational calculations, the experimental data are first analysed to provide approximate ranges of the parameters for the LIFDT model in section 4.2. From the experimental data, the I/O function for 200pps pulse train was generated by plotting FE against stimulus amplitude. To investigate the response at each pulse, new I/O curves were generated by plotting the firing probabilities at each pulse against stimulus amplitude. A simplified I/O curve analysis for the LIFDT model is derived in section 4.3 based on the stochastic AN model [51]. Then the experimental data were fitted to this simplified I/O curve in section 4.4. The fitting results provide approximate ranges for some parameters of the LIFDT model. Given the range of parameter values, initial assessment of fitting the LIFDT model is achieved in section 4.5.

4.2 Analysis of experimental data

From experimental data, the I/O function for electrical stimuli at 200pps was generated in Figure 3-12, which only presented the relationship between the average firing probability (FE) over all pulses and the stimulus amplitude. Since we are interested in the firing probability for the first few pulses, a new I/O function at each individual pulse is constructed.

Taking the I/O function at the first pulse as an example: For each FE, the firing probability at the first pulse , p_1, is obtained from its PST histogram. Instead of the FE s, p_1s are plotted against the stimulus amplitude. Then, the I/O function at the first pulse includes ten data points.

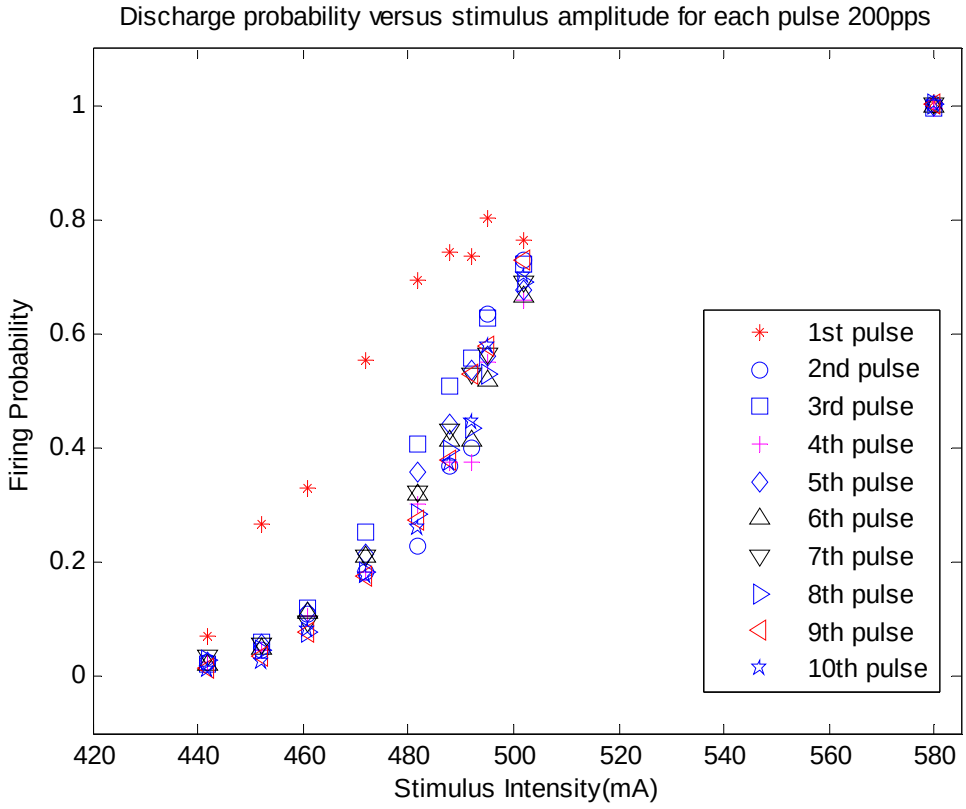

Figure 4-1 Discharge probability versus stimulus amplitude at each pulse: the experimental data

The same process was repeated from the second pulse to the tenth pulse. The observation from the PST histogram indicates that the neural response after nine pulses is almost constant (except for $\mathrm{FE} = 0.5$). The auditory nerve fibre achieves its steady state. Therefore, the I/O functions of the eleventh pulse and subsequent pulses are not generated. All the acquired data are plotted in Figure 4-1.

In Figure 4-1, the data points of the firing probabilities for the 1st pulse are all above those of the firing probabilities for the subsequent pulses. There is an

obvious suppression of the firing probabilities at the second pulse (compared to the firing at the first pulse).

4.3 Theoretical calculation of I/O functions for the LIFDT model with simplified threshold

The I/O data points at each individual pulse is shown in Figure 4-1. Usually an integrated Gaussian curve was used to fit the I/O function [17, 47, 69]. The integrated Gaussian curve has two parameters, the mean μ and the standard deveiation σ. The RS at each pulse can be calculated according to Eq.(3.2.6). Additionally, Bruce *et al*. [51] proposed a theoretical calculation of the I/O curve of the stochastic AN model based on a PDF function of the noise term. Since the LIFDT model has the same noise term, this section will derive a theoretical calculation of the I/O curve for the LIFDT model. This theoretical calculation will provide information directly related to the parameters in the LIFDT model, in this section a theoretical calculation of I/O functions for the LIFDT model is developed. Fitting the I/O data points at each pulse can constrain some of the parameters in LIFDT model.

Before the calculation of the theoretical I/O function for LIFDT model, an approximation of the threshold and the application of the stimulus is made as follows:

As refractory effects in the LIFDT model are achieved by resetting the variable h to zero, analytical approximation of the threshold is complicated. Hence, the threshold θ will be simplified in the following sections.

The electrical stimuli used in the experimental data were charge-balanced, biphasic current (cathodic phase first) shown in Figure 3-10. The resting

potential of a neuron is usually in the range from -70 to -80mV [114]. During the cathodic phase of a biphasic pulse, the membrane potential of the neuron rises towards the threshold [7]. When the membrane potential crosses the threshold, an action potential is generated. Then anodic phase of the biphasic pulse is applied, and the electrochemical reactions are reversed. In previous study of the LIFDT model, the resting potential is set at around 53 mV. The membrane potential V rises with anodic current, falls with cathodic current, which is in the opposite direction to real neuron response. Therefore, when applying the biphasic pulse to the LIFDT model, the anodic phase should come first then the cathodic phase. In this way, the neural response is in accordance with the real neuron response. A single pulse from a pulse train, applied to the LIFDT model, is plotted in Figure 4-2 .

4.3.1 I/O at the first pulse

First, an analytical expression for the LIFDT model to the first pulse of the 200pps pulse train is developed. This analysis is straightforward because there is no refractoriness to take into account. The response of the membrane potential and the threshold to a single pulse is calculated by solving the differential equations Eq.(3.3.1)-(3.3.4). Then the stochastic AN model for a single pulse (presented in section 3.2) is utilized to calculate the firing probability at the first pulse.

In order to solve the differential equations, the biphasic pulse train is approximated by a combination of a positive Dirac Delta and a negative Dirac Delta function with an interval of τ, (shown in Figure 4-2). Each Dirac Delta function is applied in the middle of the anodic/cathodic phase. The origin is horizontally shifted along the x axis bu 25 μs. The stimulus function is written as

$$S(t) = \delta(t) - \delta(t - \tau) \tag{4.3.1}$$

where τ =60 μs.

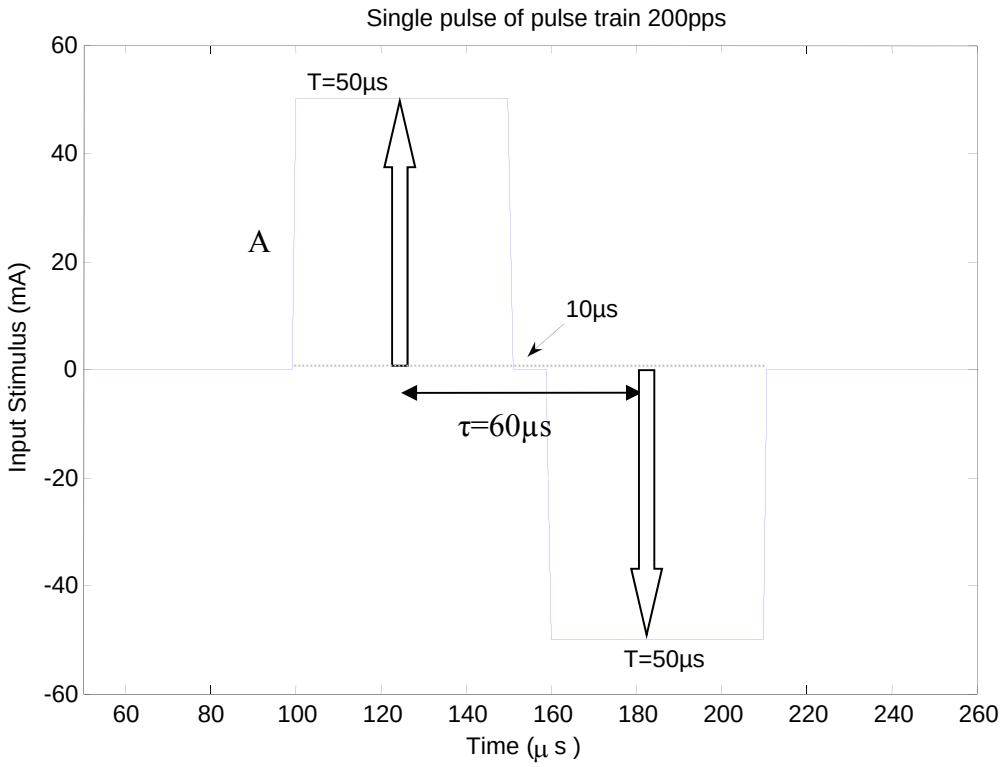

Figure 4-2 Single Biphasic pulse train (50 μs/phase, 10 μs interphase gap, anodic phase first) applied to the LIFDT model. It is approximated to a positive Dirac Delta and negative Dirac Delta function with an interval of 60 μs.

In the LIFDT model, the membrane potential V is defined by an ordinary differential equation, Eq.(3.3.1). As the noise is calculated separately by an integrated Gaussian function, the noise intensity is set to zero in Eq.(3.3.1). Thus Eq.(3.2.9) is changed into a noise free deterministic version,

$$\tau_m \dot{V}(t) = -V(t) + S(t) \tag{4.3.2}$$

To solve the differential Eq.(4.3.2), the Laplace transform was applied to both sides of Eq.(4.3.2), to give,

$$\tau_m\left(\bar{V}(s)s - V(t)|_{t=0}\right) = -\bar{V}(s) + \mathcal{L}\left(\delta(t) - \delta(t-\tau)\right) \qquad (4.3.3)$$

where the standard 'over bar' is used to denote Laplace transform and $V(t)|_{t=0} = 0$.

The Laplace transform of a unit impulse (Dirac Delta function) is 1. However, the weighting of the delta function is obtained by calculating the distributed area under one part of the biphasic pulse. As seen in Figure 4-2 the distributed area of a positive impulse and a negative impulse are the same. It is equal to the amplitude of the impulse amplitude *A* multiplied by the duration of the impulse *T* (*T*=50 μs). Thus

$$\tau_m\left(\bar{V}(s)s - V(t)|_{t=0}\right) = -\bar{V}(s) + AT\left(1 - e^{-\tau s}\right) \qquad (4.3.4)$$

Solving for $\bar{V}(S)$ gives,

$$\bar{V}(s) = AT \cdot \left(\frac{1/\tau_m}{s + 1/\tau_m} - \frac{1/\tau_m}{s + 1/\tau_m} e^{-\tau s} \right) \qquad (4.3.5)$$

Then, taking the inverse Laplace transform to get the general solution

$$V(t \mid 1^{st}\ pulse) = \frac{A \cdot T}{\tau_m} \cdot \left(e^{\frac{-t}{\tau_m}} \cdot u(t) - e^{\frac{-(t-\tau)}{\tau_m}} \cdot u\left(t - \tau\right) \right) \qquad (4.3.6)$$

where $u(t)$ is a unit step function,

$$u(t) = \begin{cases} 0 & t < 0 \\ 1 & t \geq 0 \end{cases} \qquad (4.3.7)$$

The maximum amplitude of the membrane potential during the first pulse is

$$V_{\max}(1^{st}\ pulse)=\frac{A\cdot T}{\tau_m} \tag{4.3.8}$$

The threshold of the LIFDT model is approximated as an average threshold U_i at the $i'th$ pulse. In the LIFDT model, an action potential is generated when the membrane potential crosses the threshold. The noise term is added to the membrane potential, hence for a given membrane potential, threshold and noise distribution, the firing probability can be derived according to the stochastic auditory nerve model [47] as follows.

Assume an action potential only occurs when the membrane potential reaches its maximum value during a pulse period. (This assumption will be validated in section 4.4). Then a spike is generated at the first pulse when

$$V_{\max}(1^{st}\ pulse)+V_{noise}>U_1 \tag{4.3.9}$$

Substituting (4.3.8) into (4.3.9) and rearranging the inequality gives,

$$V_{noise}>U_1-\frac{AT}{\tau_m} \tag{4.3.10}$$

The noise is defined by a Gaussian distribution. As the noise factor is involved in the differential equation Eq.(3.3.1) with density D and time constant τ_m, the variance of the noise is D/τ_m. The PDF of the Gaussian distribution is given by,

$$f(x)=\frac{1}{\sqrt{2\pi\sigma_1^{\,2}}}e^{-\frac{(x-\mu)^2}{2\sigma_1^{\,2}}} \tag{4.3.11}$$

where $\mu=0$ and $\sigma_1^{\,2}=\frac{D}{\tau_m}$

The probability of discharge is related to the cumulative distribution function (CDF) of the noise. According to Eq.(4.3.10), discharge occurs when the noise probability falls within the interval $\left[U_1 - \frac{AT}{\tau_m}, \infty\right)$. Thus

$$p_1 = \int_{U_1 - \frac{AT}{\tau_m}}^{\infty} f(x)dx \tag{4.3.12}$$

Substituting Eq.(4.3.11) into Eq.(4.3.12) gives,

$$p_1 = \int_{U_1 - \frac{AT}{\tau_m}}^{\infty} \frac{1}{\sqrt{2\pi\sigma_1^2}} e^{-\frac{x^2}{2\sigma_1^2}} dx \tag{4.3.13}$$

where

$$\sigma_1^2 = \frac{D}{\tau_m} \tag{4.3.14}$$

Thus the relationship of the firing probability at the first pulse against stimulus amplitude is established by Eq.(4.3.13) and (4.3.14). p_1 is only dependent on the amplitude of the stimulus with two variables: U_1 and σ_1^2.

4.3.2 I/O at the second pulse

For the second pulse, the dynamic of the neuron is more complicated. The neuron response is influenced by noise, accommodation effects and also refractory effects.

For the 200pps pulse train, the second pulse is applied 5ms after the first pulse. The stimulus is

$$S(t)\Big|_{2^{nd}\ pulse} = \delta(t) - \delta(t-\tau) + \delta(t-t_2) - \delta(t-t_2-\tau) \tag{4.3.15}$$

where t_2 is the interval between pulses, $t_2 = 5(ms)$.

Take Eq.(4.3.15) into Eq.(4.3.2) and solve for $V(t)$,

$$V(t\,|\,2^{nd}\ pulse) = \frac{A\cdot T}{\tau_m}\left[e^{\frac{-t}{\tau_m}}\cdot u(t) - e^{\frac{-(t-\tau)}{\tau_m}}\cdot u(t-\tau) + e^{\frac{-(t-t_2)}{\tau_m}}\cdot u(t-t_2) - e^{\frac{-(t-t_2-\tau)}{\tau_m}}\cdot u(t-t_2-\tau) \right] \tag{4.3.16}$$

As shown in Eq.(4.3.16), before the second pulse it is the same as Eq.(4.3.6). After the second pulse two shifting exponential terms are added to the equation. To evaluate the difference between the membrane potential at each pulse, Eq.(4.3.16) is plotted in Figure 4-3 with the comparison with the simulation result of the LIFDT model using a parameter values from a previous study [19] presented Table 3-1. The simulation result is plotted in the dashed line with star markers. The theoretical result is plotted in the solid line.

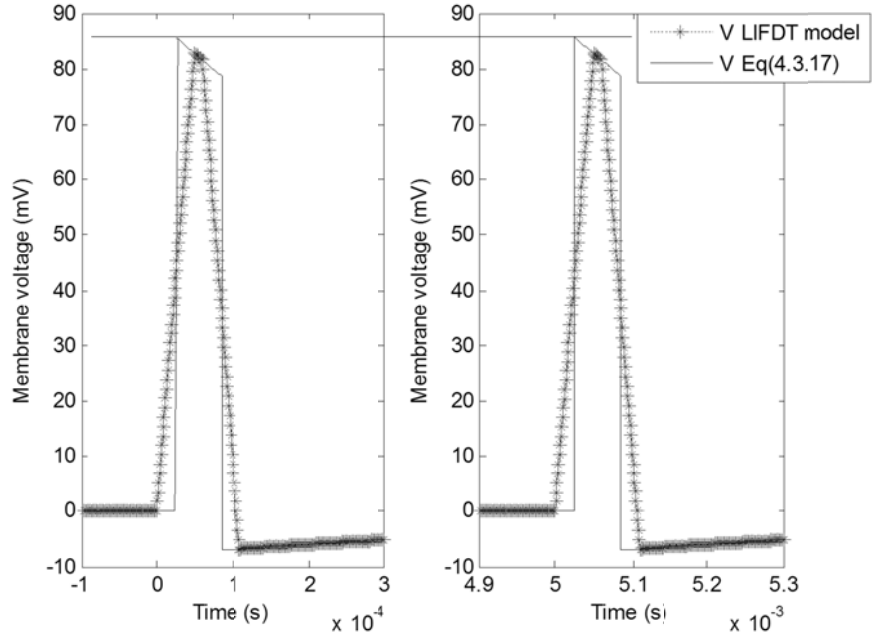

Figure 4-3 Comparison of the membrane potential V(t) at the first pulse and the second pulse

$$V(t \mid 2^{nd}\ pulse)_{\max} = V(t_2) = \frac{A \cdot T}{\tau_m}\left[e^{\frac{-t_2}{\tau_m}} - e^{\frac{-(t_2-\tau)}{\tau_m}} + 1 \right] \qquad (4.3.17)$$

The simulation results demonstrate that the difference between the maximum value of the membrane potential at the first pulse and second pulse is 0.19% of its value. The maximum value of the membrane potential at the tenth pulse is the same as that at the second pulse. The shifted response in the membrane potential only affects the second pulse, and does not build up in subsequent pulses.

It seems that after 5 ms the first pulse's influence on the membrane potential dies away. Therefore, the maximum membrane potential at the second pulse is simplified as,

$$V_{\max}(2^{nd}\ pulse) = \frac{A \cdot T}{\tau_m} \qquad (4.3.18)$$

For the second pulse, refractory effects are taken into account. The overall threshold is denoted by U_2. Due to refractory effects, the threshold is raised and firing is suppressed. Moreover, refractory effects may change the behaviour of the membrane noise[47]. It is not clear whether refractory effects will change the slope of the I/O curve. Thus the variance of the noise is not necessarily related to noise intensity for the second pulse. It is simply denoted by $\sigma_2{}^2$.

The relationship of the firing probability at the second pulse against stimulus amplitude is established by an integrated Gaussian function as,

$$p_2 = \int_{U_2 - \frac{AT}{\tau_m}}^{\infty} \frac{1}{\sqrt{2\pi\sigma_2{}^2}} e^{-\frac{x^2}{2\sigma_2{}^2}} dx \qquad (4.3.19)$$

4.3.3 Calculation of firing probability at the *i*'th pulse

Finally, an analytical expression for the LIFDT model to each pulse of a 200pps pulse train is derived. Based on previous analysis, the maximum membrane potential is approximated to $\frac{AT}{\tau_m}$ for each pulse. However, threshold and noise variance change between pulses. The I/O function for the $i^{'th}$ pulse can therefore be written as

$$p_i = \int_{U_i - \frac{AT}{\tau_m}}^{\infty} \frac{1}{\sqrt{2\pi\sigma_i^2}} e^{-\frac{x^2}{2\sigma_i^2}} dx \qquad (4.3.20)$$

where U_i is the threshold for the $i^{'th}$ pulse, σ_i^2 is the noise variance of the $i^{'th}$ pulse.

4.3.4 The accuracy of the theoretical calculation

This theoretical calculation Eq.(4.3.20) is derived with several approximations and assumptions. The most important assumption is that action potential only occurs at the maximum value of the membrane potential during a pulse period.

In order to investigate the accuracy of this assumption, the theoretical calculation Eq.(4.3.13) is compared with the simulation result of the LIFDT model to a single pulse stimulus. The parameter values are taken from Table 3-1. Monte Carlo simulation of the LIFDT model is performed with one thousand iterations. U_1 is set by Eq.(3.3.4), where t =25 μs. That is the threshold of the LIFDT model when the membrane voltage reaches its maximum amplitude. The results are shown in Table 4-1.

The results of the theoretical calculation Eq.(4.3.13) are consistent with simulation results of the LIFDT model, even at low FE. The prediction of Eq.(4.3.13) is not degraded. This suggests that the assumption on the firing time is correct. Therefore, it is appropriate to apply these theoretical calculations to study the experimental data.

Table 4-1 Comparison of the theoretical calculations of Eq.(4.3.13) and simulation results of the LIFDT model at the first pulse

Stimulus(mA)		420	435	447	456	465	471	480	496
p_1	theoretical	0.05	0.10	0.20	0.30	0.41	0.50	0.62	0.80
	simulations	0.04± 0.01	0.11± 0.03	0.20± 0.09	0.30± 0.13	0.41± 0.18	0.51± 0.19	0.61± 0.20	0.79± 0.23

4.4 Fitting results of the theoretical calculations

Thus, the theoretical calculation Eq.(4.3.20) is fitted to the experimental data (shown in Figure 4-1) using the Levenberg-Marquardt Method [118]. Ten integrated Gaussian curves are fitted to the experimental data. The fitting results are plotted in Figure 4-4.

Each integrated Gaussian curve is presented with a specific markers and line style as shown in the legend. The markers represent the fitted points, not the experimental data point, and are included to improve clarity. The result of fitting is given in Table 4-2. The goodness of fit is presented by the sum of squares due to error (SSE).

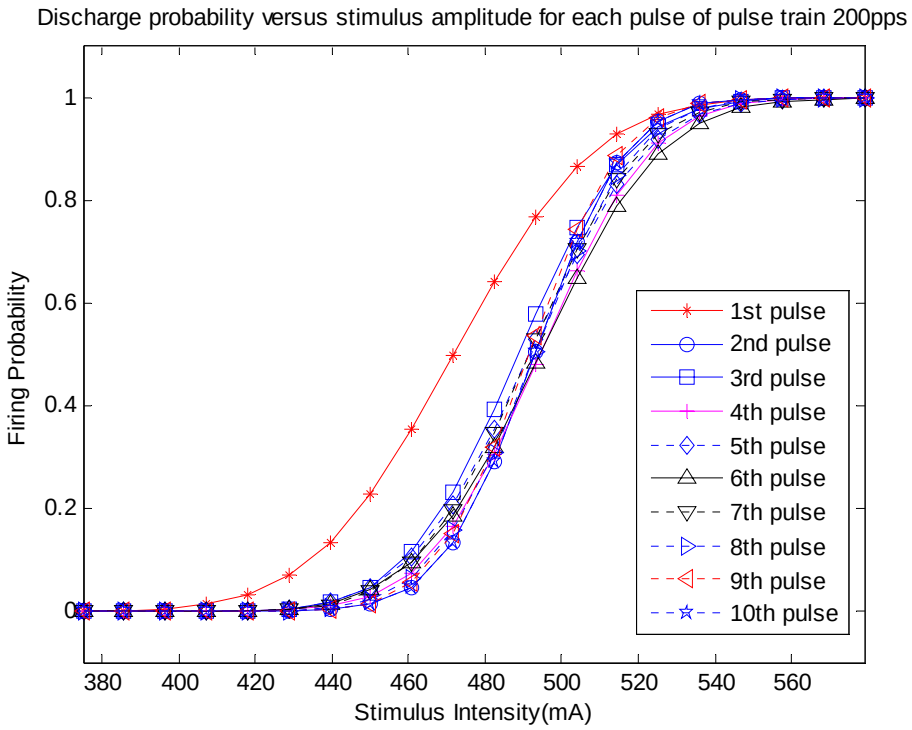

Figure 4-4 I/O curves of the theoretical calculations Eq.(4.3.20) to the experimental data. Only the firing probabilities (I/O curves) from the theoretical calculations are plotted. The markers do not stand for the experimental data points, but are used to distinguish different line types.

Table 4-2 Fitting results of the theoretical calculations Eq.(4.3.20) to the experimental data

i^{th}pulse	1	2	3	4	5
U_i (mV)	33.68	35.19	34.84	35.32	35.06
σ_i^2	4.012	1.749	2.779	2.902	3.015
RS	0.0595	0.0376	0.0478	0.0482	0.0495
SSE	0.1634	0.0708	0.0506	0.1673	0.1607
i^{th}pulse	6	7	8	9	10
U_i (mV)	35.27	35.08	35.24	35.11	35.21
σ_i^2	3.320	2.688	2.416	1.793	1.960
RS	0.0517	0.0467	0.0441	0.0381	0.0398
SSE	0.1287	0.1066	0.1020	0.0099	0.0001

From Figure 4-4, it is apparent that the firing probabilities at the first pulse (solid line with asterisk markers) are higher than those of subsequent pulses for most stimulus intensities. This occurs because U_1 is smaller than $U_i|_{i>1}$ for subsequent

pulses. The I/O curves for the second pulse and subsequent pulses have similar values of threshold, $U_{i,}$ and hence approximately align. Also the variance and RS at the first pulse are biggest compared to those of subsequent pulses. RS, which is defined in Eq.(3.2.6), controls the slope of the I/O curve. The RS value varies in a narrow range but has the highest value at the first pulse. The neural response at the second pulse is suppressed for all stimulus intensity. The threshold U_2 is 4.45% bigger than U_1. The variance σ_2^2 is 56.41% less than σ_1^2. From the second pulse to the tenth pulse, changes in the slopes of the I/O curves and the amplitudes of the threshold U_i are quite small.

To analyse the data in detail, the fitted I/O curves are now plotted with the original experimental data. According to Eq.(4.3.14), as σ_1^2 is fixed, the ratio of D/τ_m is then fixed. The membrane time constant is set from a previous study [19], as it well captures the temporal response of feline auditory nerve fibres. Thus, D is calculated according to Eq.(4.3.11). The fitted parameters of the LIFDT model are demonstrated in Table 4-3.

Table 4-3 Fitting the parameters in LIFDT model by I/O curve for the 1st pulse

τ_m (ms)	D
0.7	0.0028

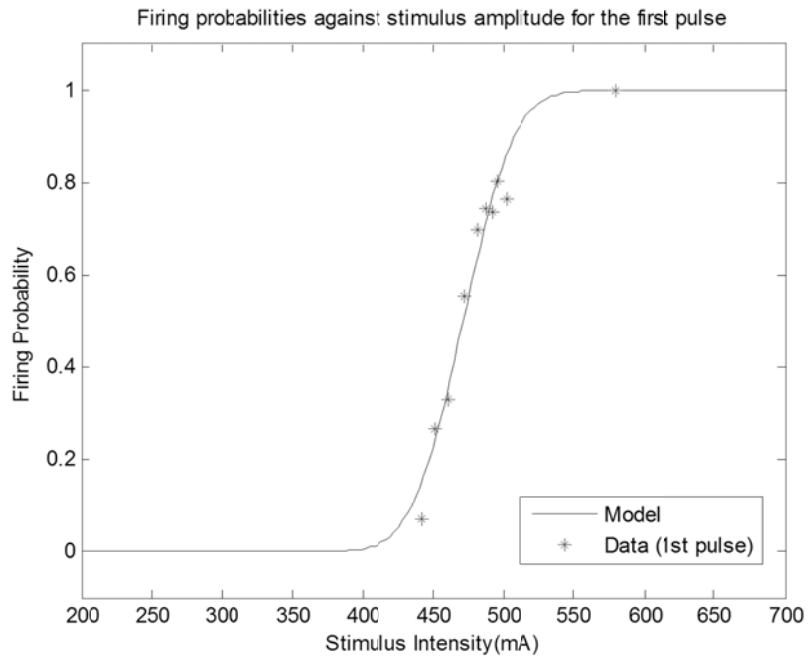

Figure 4-5 Firing probabilities against stimulus amplitude (I/O curve) for the first pulse of 200pps pulse train. The solid line represents the prediction from the theoretical calculation Eq.(4.3.13). The experimental data at the first pulse are plotted using asterisk markers.

4.4.1 Analysis of the suppression in experimental data

The suppression phenomenon at $\overline{FE} = 0.02$ is discussed in chapter 3. As the neuron rarely fired at the first pulse, the suppression of firing at the second pulse can probably be attributed to accommodation effects. It is not clear whether accommodation effects have the same influence for higher $\overline{FE}$ value.

To find out the cause of the suppression of firing, assume that in the experimental data there is no accommodation effects but only refractory effects. To investigate the maximum suppression of firing that refractory effects can achieve, assume that the ARP is longer than 5ms. Thus if the neuron fires at the first pulse, it cannot definitely fire at the second pulse. For the first two pulses of a pulse train, all the possible responses of the neuron are shown in Figure 4-6. Here, "1" represents the neuron firing and "0" represents the neuron not firing. Before the stimulus is applied, the neuron is at its resting potential. No discharge

is generated. After the first pulse, the probability of firing is denoted as "p_1". Therefore, the probability of not firing at the first pulse is $1-p_1$. It is now necessary to calculate the probability of firing at the second pulse, which is denoted as "$\tilde{p}_2$". Under our assumption, those neurons that fired at the first pulse cannot fire at the second pulse. Only those that did not fire at the first pulse can generate a spike at the second pulse. As it is assumed no accommodation effects are present, the probability of firing at the second pulse on condition that it did not fire at the first pulse is the same as the probability of firing at the first pulse.

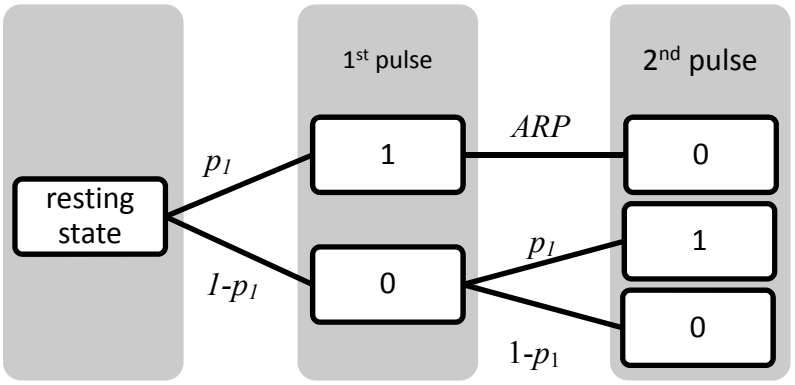

Figure 4-6 All the possible responses of the neuron to two biphasic pulses. Detail is explained in the text.

According to Figure 4-6, the firing probability at the second pulse $\tilde{p}_2$ can be calculated as

$$\tilde{p}_2 = p_1 \times 0 + [1 - p_1] \cdot p_1 \tag{4.3.21}$$

where p_1 is taken from the fitted I/O curve of the first pulse, $\tilde{p}_2$ represents the firing probability due to ARP.

The results are plotted in Figure 4-7. The solid line is the fitted I/O curve of the 1st pulse. The star markers represent the experimental data of the first pulse. The

circle markers represent the data of the second pulse. The dash-dot line with right-pointing triangle markers is $\tilde{p}_2$, calculated from Eq.(4.3.21). $\tilde{p}_2$ is only calculated for $\mathrm{FE} < 0.3$. For higher FE, $\tilde{p}_2$ is not calculated because the probability is underestimated by the assumption that the ARP is longer than 5ms.

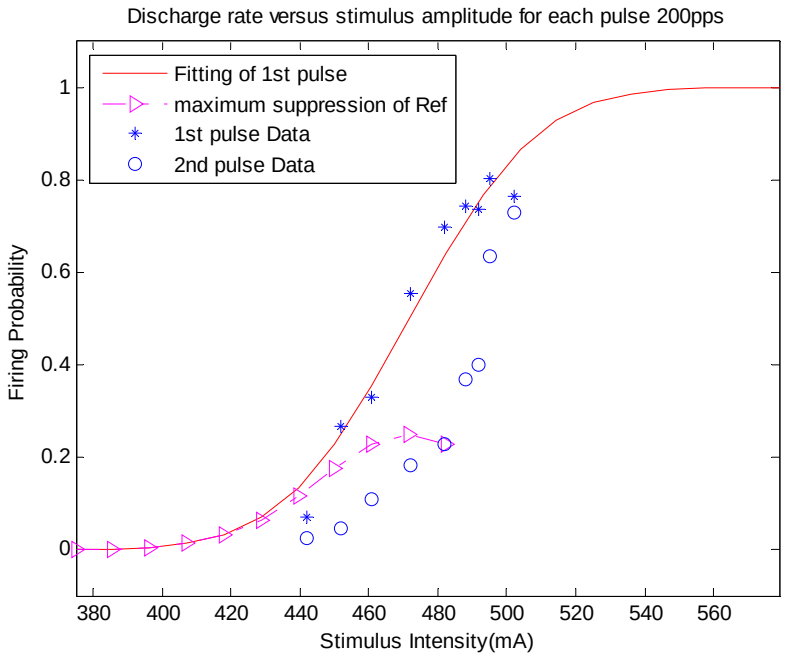

Figure 4-7 The maximum suppression of firing probability due to refractory effects only

For low FE (0.02, 0.05, 0.1 and 0.2), $\tilde{p}_2$ is above the original experimental data p_2. It is demonstrated that even a hypothesised maximum suppression of firing due to refractory effects is not enough to result in the suppressed firing rates in the experimental data at the 2nd pulse. Therefore, the suppression phenomenon must be due to non-refractory effects; accommodation effects are the most likely candidate to explain the enhanced suppression of the firing rate.

From the analysis in the previous section, both accommodative mechanisms and refractory mechanisms contribute to the suppression after the first pulse. Consequently the overall threshold is influenced by both mechanisms.

Refractoriness is commonly defined by an exponential function which is independent on stimulus intensity. However, for high stimulus intensity, most neurons will fire at the first pulse and enter the refractory period. If the refractory period of the neuron is longer than 5 ms, then the threshold of the second pulse is increased. Therefore, the overall threshold of the second pulse for high stimulus intensity is increased. For fixed high stimulus intensity, as the overall threshold U_i is increased after the first pulse due to refractoriness, the firing probability under the same stimulus intensity should decrease.

The increase in the overall threshold U_i was observed from Table 4-2, and the decreasing of the firing probability at high stimulus intensity was observed in Figure 4-4 as well. What interests us is that the same size of decreasing in the firing probability under fixed stimulus intensity was observed at low stimulus intensities, which must result mainly from accommodation effects. It implies that accommodation effects may have the same size of suppression on firing for low stimulus intensities as refractory effects have in high stimulus intensity. As the firing in low stimulus intensities is relatively smaller than in high stimulus intensities, the accommodation may have a severe suppression of firing compared to the refractoriness.

The accommodative mechanism is not fully understood from the presented PST histograms (Figure 3-15). As the I/O curve for a single pulse were not obtained experimentally, it is not clear how long it will take accommodation effects to fully recover. Other physiological data from guinea pigs [16] indicate that the accommodative mechanism starts about 1 ms after a subthreshold pulse and takes full effects about 5 ms after the pulse.

This is consistent with the presented experimental data: For all FEs, the firing probabilities at the second pulse (applied 5 ms after the first pulse) are maximumally suppressed. The firing probabilities of the neuron on the application of the third pulse are not further suppressed compared to those observed when a second pulse is applied.

In the stochastic AN model [47], the variance of the noise is a random variable, which itself is normally distributed. To simplify the analysis, it is assumed fixed during simulation [47]. The impact of this simplification is studied by Xu and Collins [69]. Xu and Collins demonstrated that the model with fixed parameters and the model with random parameters provide identical statistics. They proposed another method to fit the I/O curve at individual pulse: set the variance of noise as constant (σ_1^2), and fit the overall threshold only. A least squares method (Gauss-Newton algorithm) is used for this fitting. Figure 4-8 shows the fitting of the firing probability at the second pulse with different parameters. The firing probabilities corresponding to the first pulse are marked by the star markers and by the circle markers for those corresponding to the 2nd pulse. The solid line (1st pulse) and dotted line (2nd pulse) were both fitted with two parameters U_i and σ_i^2 . The dashed line represents the result when fitted to only one parameter U_i . The value of the parameters is given in Table 4-4.

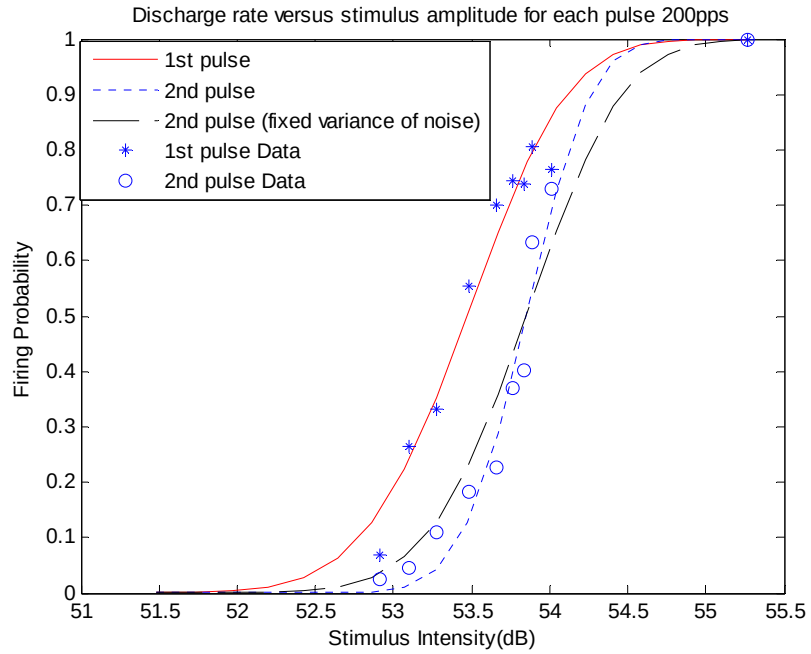

Figure 4-8 Fitted I/O curves of the theoretical calculation Eq. (4.3.19) at the second pulse by different fitting methods

Table 4-4 Fitting results of the theoretical calculation Eq. (4.3.19) by different fitting methods for the first two pulses

	$U_i\,(mV)$	σ_i^2	$R.S$	SSE
Fitted I/O curve of 1st pulse	33.68	4.012	0.0595	0.1634
Fitted I/O curve of 2nd pulse	35.19	1.749	0.0376	0.0708
Fitted I/O curve of 2nd pulse with fixed σ_i^2	35.19	4.012	0.0567	0.1459

The SSE in Table 4-4 indicates that fitting with two parameters provides a better fit. Although the SSE in the third row doubled the SSE in the second row, in Figure 4-8, the I/O curves of the second pulse fitted with different variable intersect at the point where the firing probability is 0.5. Although it has been discussed that the overall threshold U_2 varies with stimulus intensities, the identical fitting result for U_2 still provides an approximate threshold for the

second pulse. Therefore we can conclude that the threshold of the neuron shifted by about 1.51mV from the first pulse to the second pulse.

4.5 Conclusion

The theoretical calculation at the first pulse Eq.(4.3.13) is validated by the simulation result. The fitting results in Table 4-3 provide the value of the overall threshold U_1 and the variance of the noise σ_1^2, the noise intensity D and the membrane time constant τ_m. The threshold shifting between the first pulse and the second pulse is qualitatively studied.

Based on the parameter values given in Table 4-3, fitting is applied to the LIFDT model. The remaining unknown LIFDT model parameters are adjusted to the data 'by hand'. Monte Carlo simulations of the LIFDT model were performed using one thousand iterations. The results are plotted in Figure 4-9. The solid line represents the simulation result of the LIFDT model, and the asterisks represent the experimental data.

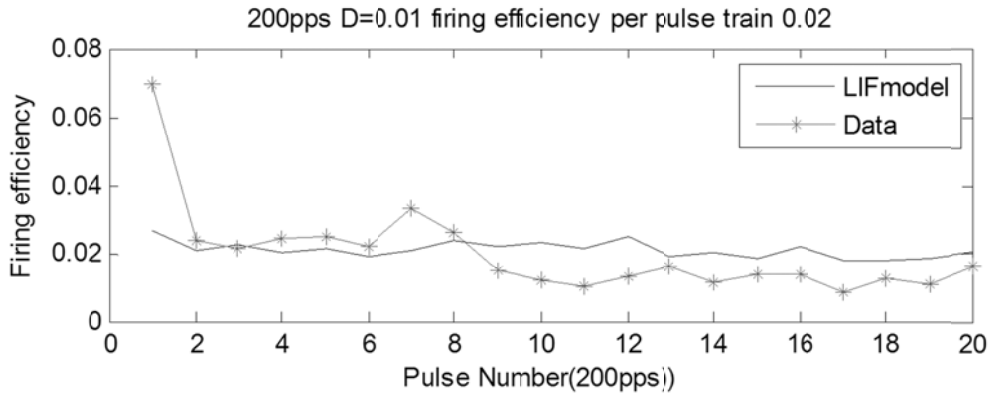

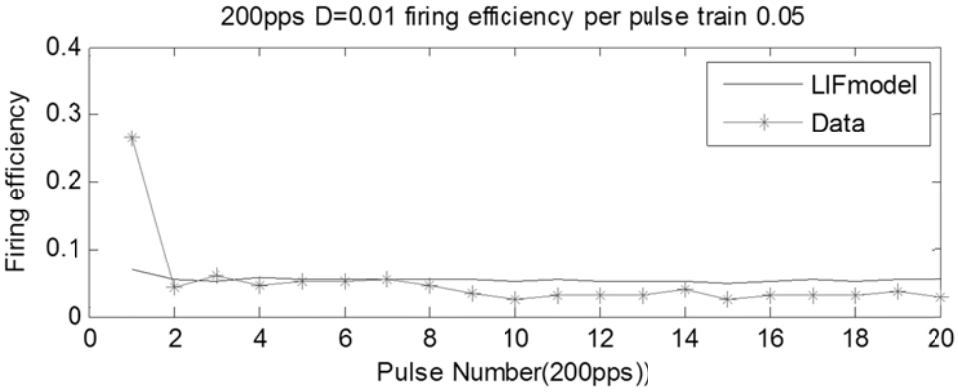
200pps D=0.01 firing efficiency per pulse train 0.05
Firing efficiency
Pulse Number(200pps))
LIFmodel
Data

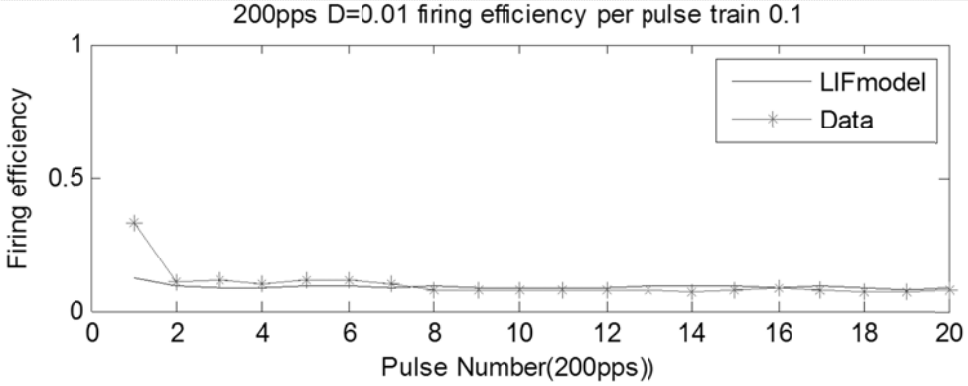
200pps D=0.01 firing efficiency per pulse train 0.1
Firing efficiency
Pulse Number(200pps))
LIFmodel
Data

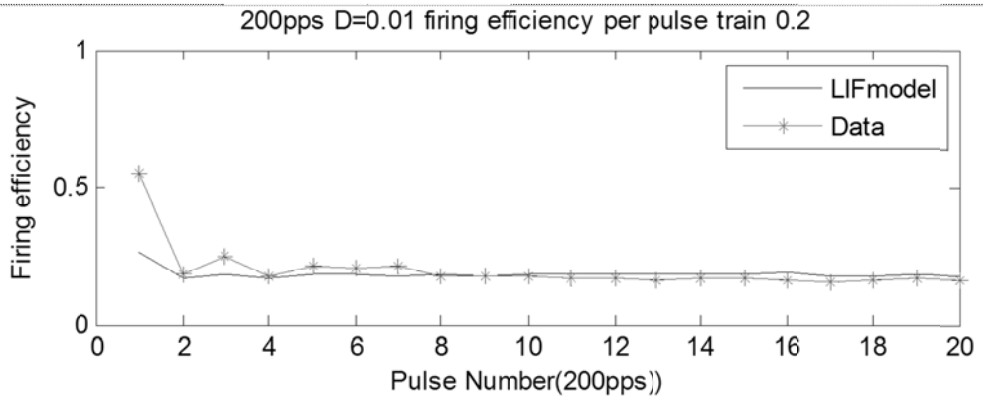
200pps D=0.01 firing efficiency per pulse train 0.2
Firing efficiency
Pulse Number(200pps))
LIFmodel
Data

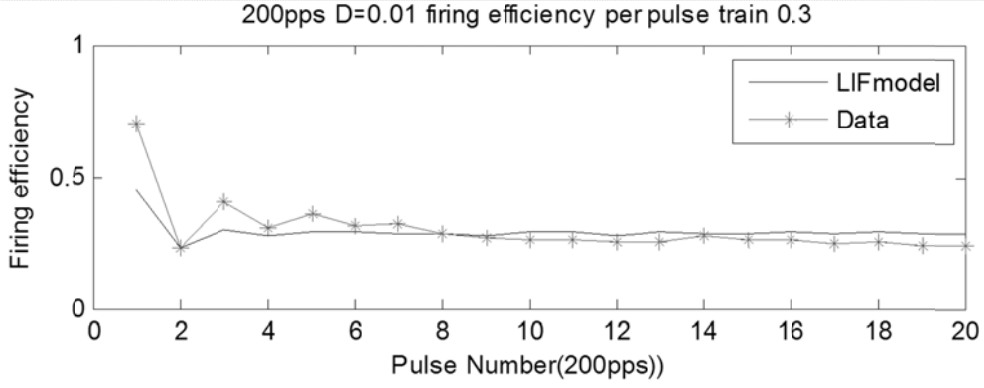
200pps D=0.01 firing efficiency per pulse train 0.3
Firing efficiency
Pulse Number(200pps))
LIFmodel
Data

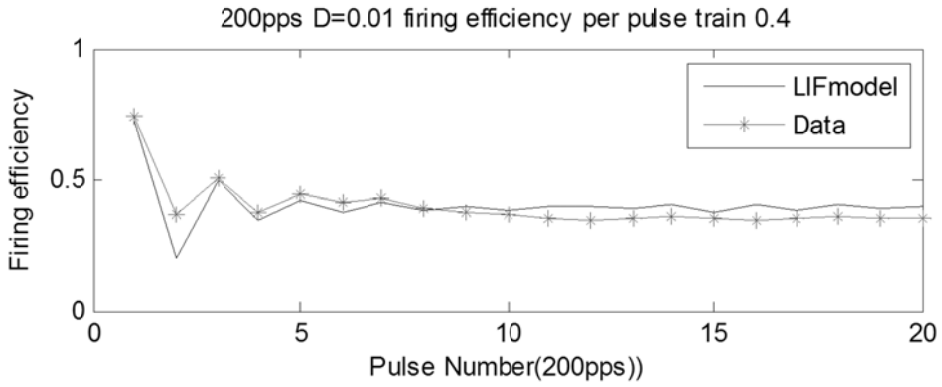
200pps D=0.01 firing efficiency per pulse train 0.4
Firing efficiency
Pulse Number(200pps))
LIFmodel
Data
0
0.5
1
0
5
10
15
20

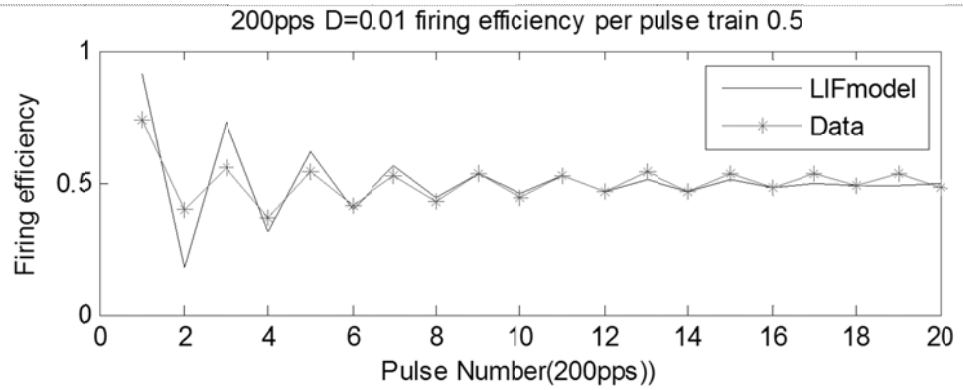
200pps D=0.01 firing efficiency per pulse train 0.5
Firing efficiency
Pulse Number(200pps))
LIFmodel
Data
0
0.5
1
0
2
4
6
8
10
12
14
16
18
20

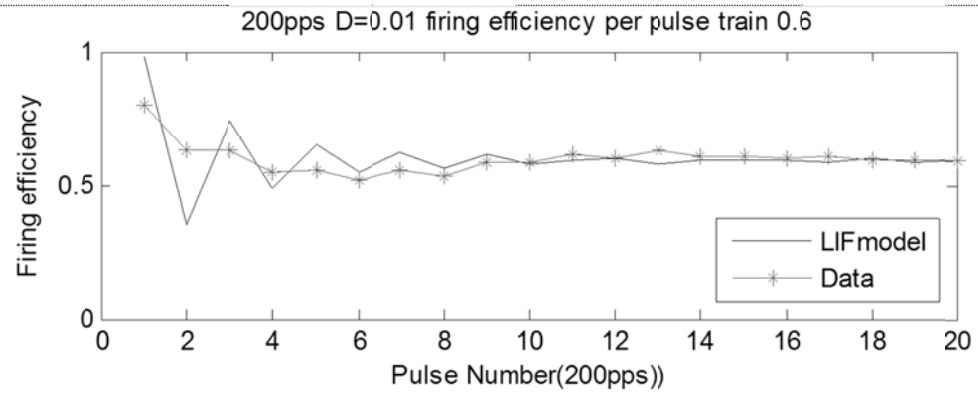
200pps D=0.01 firing efficiency per pulse train 0.6
Firing efficiency
Pulse Number(200pps))
LIFmodel
Data
0
0.5
1
0
2
4
6
8
10
12
14
16
18
20

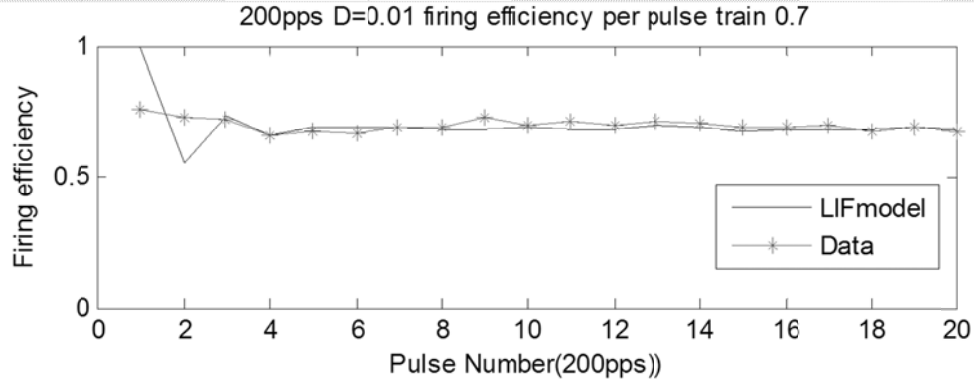
200pps D=0.01 firing efficiency per pulse train 0.7
Firing efficiency
Pulse Number(200pps))
LIFmodel
Data
0
0.5
1
0
2
4
6
8
10
12
14
16
18
20

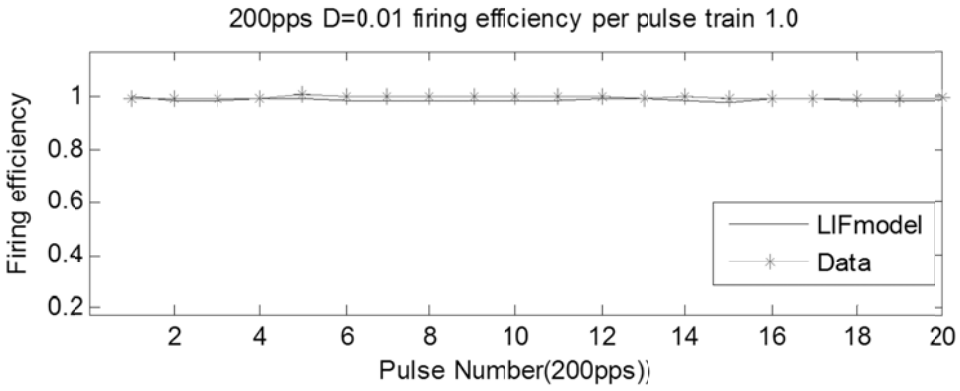

Figure 4-9 Simulation results of the LIFDT model: "fitting by hand"

The fitting was optimized by hand. The fitting involves a trade-off between the firing probability at the first pulse and the steady state probability. When fitting to the firing probability at the first pulse, firing probabilites from the simulation results converge at a rate significantly higher than the experimental data. When fitting the firing probability at the steady state, the dynamics of experimental data in the first few pulses was well captured. Figure 4-9 presents the latter case. At each $\overline{FE}$, the simulation results of the LIFDT model successfully predicted the steady state of firing rate. Also for $\overline{FE} = 0.5$, it successfully predicts oscillations in the neural response. However, p_1 at low $\overline{FE}$ is lower than the experimental data and p_1 at high $\overline{FE}$ is higher than the experimental data. It indicates that in the LIFDT model accommodation effects should be enlarged, at the same time refractory effects should be decreased.

As the fitting is accomplished "by hand", it is not clear whether the failure of the fitting is due to inappropriate parameter values or structural problems in the LIFDT model. This problem is studied in chapter five.

Chapter5. *Analytical approximation of the LIFDT model*

5.1 Introduction

The initial fit to the LIFDT model failed to represent the strong accommodation effects in neurophysiological data. As stated in section 4.1, the full optimization of the LIFDT model is quite challenging. It is therefore advantageous to derive an analytical approximation of the LIFDT model and investigate how the parameters of the model affect the accommodation effects. The analytical approximation can provide a theoretical expression of the firing probability instead of relying on simulations of the model. Additionally, this theoretical model can improve computational efficiency, which is crucial when simulating a large population of nerve fibres.

A simplified I/O function of the LIFDT model is developed previously in chapter four section 4.3, in which the threshold is assumed fixed. The value of the threshold is determined from the measured neurophysiological data [16]. Although this simplification makes the analysis more straightforward, the simplified analytical model is only valid for a single-pulse stimulus; it is therefore unable to accurately describe the firing probabilities due to subsequent pulses.

In section 5.2.1, a full analytical model is derived by extending the simplified model with analytical expressions of the threshold response, $\theta(t)$, for a single-pulse stimulus. Then it is extended to describe the response to a pulse-train stimulus in section 5.2.2. The difference between predicting the neural response

to a single-pulse stimulus and the pulse-train stimulus relies on whether previous discharge has influence on the current pulse. In the LIFDT model, both accommodative mechanisms and refractory mechanisms are included when predicting the response to a pulse train, as shown in Chapter 3 with noise-free stimulus. For a noise-modulated pulse-train stimulus, it is complicated to calculate the firing probability theoretically concerning both accommodation effects and refractory effects, because each auditory nerve fibre responds independently from other fibres according to the stochastic noise term. As the initial fitting of the LIFDT model cannot capture the strong accommodation effects in neurophysiological data, first we try to predict the neural response concerning the accommodative mechanism only. In other words, if the neuron has fired, it is assumed to be fully recovered when the next pulse applied. The validation of the full analytical model is presented in section 5.3. The theoretical model is validated by Monte Carlo simulation results of the LIFDT model to both single-pulse and pulse-train stimuli.

Although the LIFDT model is built with an accommodative mechanism, it is not affected by the parameters of Table 3-1. The maximum accommodation effects in the LIFDT model are theoretically investigated in section 5.4. Also, we study the impact of different parameter selection on neural responses. Both theoretical analysis and Monte Carlo simulations perform these predictions. Discussions and conclusions are drawn in section 5.5.

5.2 Analytical approximation of LIFDT model: linear approximation

The LIFDT model has been presented in section 3.3. The values of all parameters from the LIFDT model are taken from Table 3-1. The pulsatile stimulus was

described in section 4.3. First, an analytical approximation of the LIFDT model is derived in section 5.2.1 for simulation of a single-pulse response, because it avoids the complicated interpulse interactions. The single-pulse result is valid for any pulse whose response properties are not dependent on any previous pulses.

Second, the theoretical model is extended to a subthreshold pulse-train response in section 5.2.2. The response to the first pulse in the pulse-train is identical to the response to a single-pulse stimulus. The theoretical analysis of a single-pulse response is used as the basis for an extension to describe the pulse-train response.

5.2.1 Analytical approximation of LIFDT model to a single-pulse stimulus

The LIFDT model is a stochastic model with Gaussian white noise. In order to derive the analytical expression of the LIFDT model to a single-pulse stimulus, it is necessary to investigate the responses of $V(t)$ and $\theta(t)$ to a single-pulse stimulus without noise first.

The single-pulse stimulus has been presented in Figure 4-2 where the single-pulse stimulus is approximated by the combination of a positive and a negative Dirac Delta function. To increase the accuracy, the single biphasic pulse stimulus (plotted in Figure 5-1) is defined by a rectangular function,

$$\begin{aligned} S(t) &= \begin{Bmatrix} A & 0 < t < T_1 \\ 0 & T_1 \le t \le T_1 + T_2 \\ -A & T_1 + T_2 < t < 2T_1 + T_2 \\ 0 & t \ge 2T_1 + T_2 \end{Bmatrix} \\ &= A \cdot [u(t) - u(t - T_1) - u(t - T_1 - T_2) + u(t - 2T_1 - T_2)] \end{aligned} \tag{4.3.22}$$

where A is the amplitude of the stimulus, $T_1 = 50\ \mu s$ is the duration of the step function, $T_2 = 10\ \mu s$ is the interphase gap and $u(t)$ is the unit step function.

Thus the anodic phase starts at $t = 0$, and ends at $t = T_1$. The cathodic phase starts at $t = T_1 + T_2$ and ends at $t = 2T_1 + T_2$. To analyse the response to different phases, three time lines, $t = T_1$, $t = T_1 + T_2$ and $t = 2T_1 + T_2$, are plotted in the following figures.

Rewrite the membrane potential function Eq. (3.3.1) without the noise term gives,

$$\tau_m \dot{V}(t) = -V(t) + S(t) \tag{4.3.23}$$

Substituting Eq.(4.3.22) into Eq.(4.3.23) gives,

$$\tau_m \dot{V}(t) = -V(t) + A \cdot [u(t) - u(t - T_1) - u(t - T_1 - T_2) + u(t - 2T_1 - T_2)] \tag{4.3.24}$$

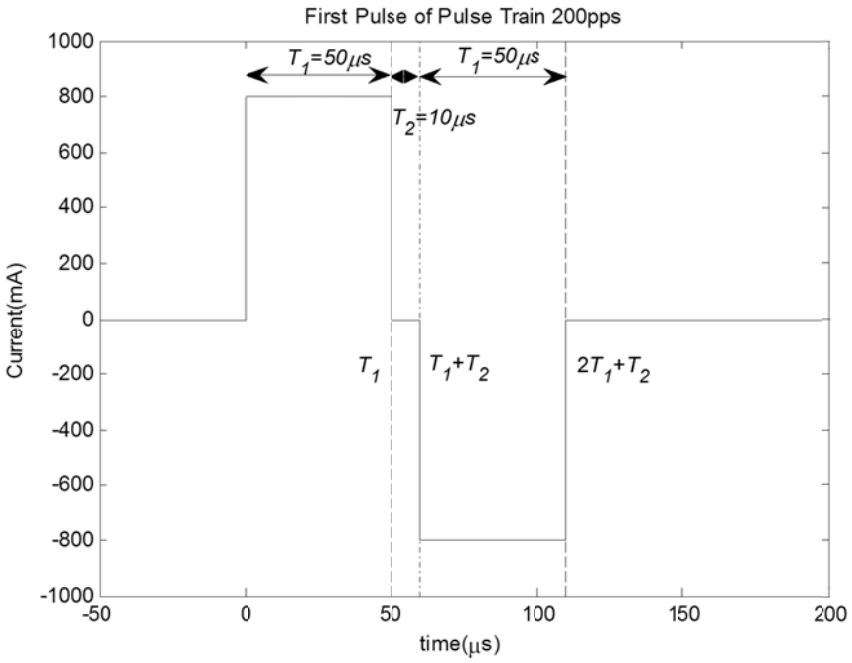

Figure 5-1 Single-pulse stimulus or the first pulse of pulse-train stimulus 200pps, T_1 is the duration of the step function, 50 μs, T_2 is the interphase gap 10 μs, the dashed lines and dash-dot line display the time t= T_1, t= T_2 and t= $2T_1 + T_2$.

To calculate the membrane potential, the Laplace transform is applied to both sides of the differential equation Eq.(4.3.24). The standard over bar is used to denote Laplace Transform. Using standard transforms leads to;

$$\tau_m\left(\bar{V}(s)\cdot s - V(0)\right) = -\bar{V}(s) + A\cdot[\frac{1}{s} - \frac{e^{-T_1 s}}{s} - \frac{e^{-(T_1+T_2)s}}{s} + \frac{e^{-(2T_1+T_2)s}}{s}] \quad (4.3.25)$$

where the initial condition is $V(0) = 0$. Solving for $\bar{V}(s)$ yields,

$$\bar{V}(s) = \frac{A}{s(s\tau_m + 1)}\cdot[1 - e^{-T_1 s} - e^{-(T_1+T_2)s} + e^{-(2T_1+T_2)s}] \quad (4.3.26)$$

Then, take the inverse Laplace transform to get the general solution yields,

$$\begin{aligned} V(t) &= \mathcal{L}^{-1}\left\{\frac{A}{s(s\tau_m+1)}(1 - e^{-T_1 s} - e^{-(T_1+T_2)s} + e^{-(2T_1+T_2)s})\right\} \\ &= A(1-e^{-t/\tau_m})\cdot u(t) \\ &\quad -A(1-e^{-(t-T_1)/\tau_m})\cdot u(t-T_1) \\ &\quad -A(1-e^{-(t-T_1-T_2)/\tau_m})\cdot u(t-T_1-T_2) \\ &\quad +A(1-e^{-(t-2T_1-T_2)/\tau_m})\cdot u(t-2T_1-T_2) \end{aligned} \quad (4.3.27)$$

The theoretical solution of the membrane potential, Eq.(4.3.6), is compared with the simulation results of LIFDT model in Figure 5-2. As noise is not included in the calculation, the LIFDT model was executed once with a two-step Heun scheme [115]. The time step for integration was 0.1 μs. The amplitude of the stimulus, *A*, was 800 mA. The simulation is also performed to derive responses of $h_\infty(t), h(t)$ and $\theta(t)$: these results are presented in the following figures. The theoretical solutions are plotted in solid lines with square markers and the simulation results are plotted in dotted lines with asterisk markers.

In Chapter3, Eq.(3.3.3) is plotted in Figure 3-6. It is demonstrated that the steady state h_∞ is a monotonically decreasing function of V. In Figure 5-2, the membrane potential varies in the range $[-5, 60]mV$, when the single-pulse stimulus applied. Within the small range of the membrane potential, Eq.(3.3.3) can be replaced by a linear equation. The linear equation for $h_\infty(V)$ is derived by the Taylor series expression of Eq.(3.3.3) around the point $V(t = 0)$.

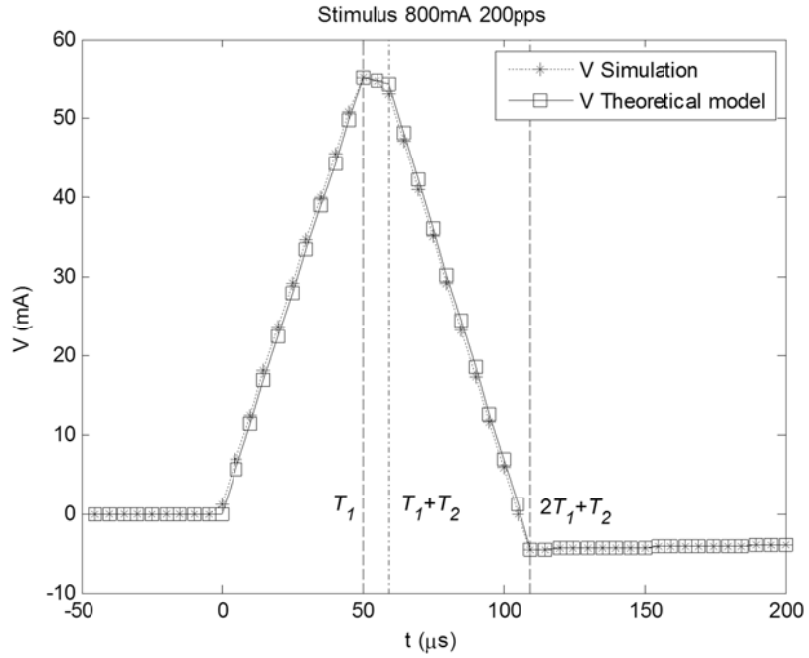

Figure 5-2 Membrane potential $V(t)$ response to a single-pulse stimulus, Eq.(4.3.6)

$$\begin{aligned} h_\infty(t) &= h_\infty(0) + h'_\infty(0)\cdot(V(t)-0) \\ &= (1+e^{\frac{V(0)-\mu_\infty}{\sigma_\infty}})^{-1} - (1+e^{\frac{V(0)-\mu_\infty}{\sigma_\infty}})^{-2}\cdot e^{\frac{V(0)-\mu_\infty}{\sigma_\infty}}\cdot\frac{1}{\sigma_\infty}\cdot(V(t)-0) \quad (4.3.28) \\ &= b\cdot V(t) + c \end{aligned}$$

where $b = -(1+e^{\frac{-\mu_\infty}{\sigma_\infty}})^{-2}\cdot e^{\frac{-\mu_\infty}{\sigma_\infty}}\cdot\frac{1}{\sigma_\infty}$ and $c = (1+e^{\frac{-\mu_\infty}{\sigma_\infty}})^{-1}$.

The linear equation, Eq.(4.3.28), is compared with Eq.(3.3.3) in Figure 5-3.The dotted line with asterisk markers represents Eq.(3.3.3) in the LIFDT model. The solid line with square markers represents the linear approximation.

Then substituting Eq.(4.3.6) into Eq.(4.3.28) the response of $h_\infty(t)$ to the single-pulse stimulus can be calculated theoretically. Comparison is made between the approximated $h_\infty(t)$ and the simulation result of $h_\infty(t)$ in Figure 5-4, where the dotted line with asterisk markers represents the simulation result and the solid line with square markers represents the theoretical approximation result.

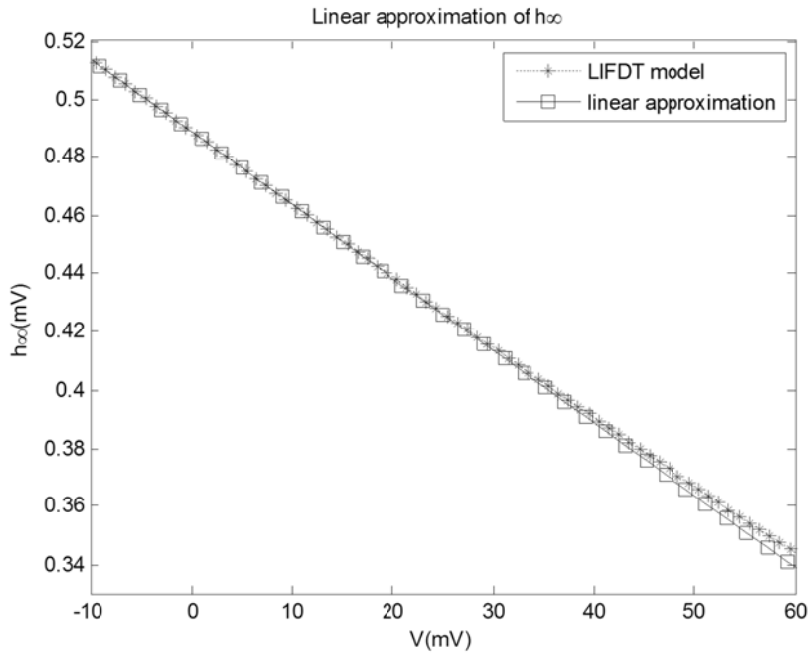

Figure 5-3 Linear approximation for h_∞(V) , Eq.(4.3.28),

Substituting the linear equation, Eq.(4.3.28), into Eq.(3.3.2) to give,

$$\tau_h \dot{h}(t) = -h(t) + b \cdot V(t) + c \tag{4.3.29}$$

and applying Laplace transforms to both sides of Eq.(4.3.29), still using the standard over bar to denote the Laplace Transform, yields

$$\tau_h \cdot \mathcal{L}\left\{\dot{h}(t)\right\} = -\mathcal{L}\left\{h(t)\right\} + b \cdot \mathcal{L}\left\{V(t)\right\} + \mathcal{L}\left\{c\right\} \tag{4.3.30}$$

which implies that

$$\tau_h \cdot [s \cdot \bar{h}(s) - h(0)] = -\bar{h}(s) + b \cdot \bar{V}(s) + \frac{c}{s} \tag{4.3.31}$$

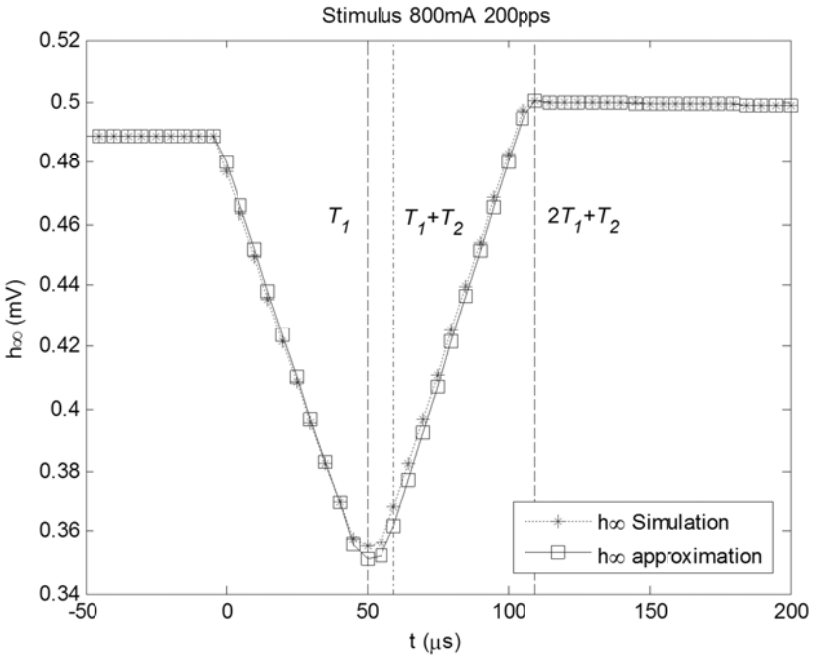

Figure 5-4 $h_\infty(t)$ response to a single-pulse stimulus,

Solving for $\bar{h}(s)$ gives

$$\bar{h}(s) = \frac{h(0)}{s + 1/\tau_h} + \frac{b \cdot \bar{V}(s)/\tau_h}{s + 1/\tau_h} + \frac{c/\tau_h}{s^2 + s/\tau_h} \tag{4.3.32}$$

The second part of Eq.(4.3.32) is in the form of the product of two known Laplace Transforms which are

$$\mathcal{L}^{-1}\left\{\frac{b/\tau_h}{s + 1/\tau_h}\right\} = \frac{b}{\tau_h} \cdot e^{-t/\tau_h} \cdot u(t) \tag{4.3.33}$$

$$\mathcal{L}^{-1}\left\{\overline{V}(s)\right\} = V(t) \tag{4.3.34}$$

According to the convolution theorem,

$$\mathcal{L}^{-1}\left\{\overline{V}(s)\cdot\frac{b/\tau_h}{s+1/\tau_h}\right\} = V(t)\otimes\frac{b}{\tau_h}\cdot e^{-t/\tau_h} = \frac{Ab}{\tau_h}\int_0^t V(q)\cdot e^{-(t-q)/\tau_h}dq \tag{4.3.35}$$

Taking the inverse Laplace transform of Eq.(4.3.32) to get the general solution,

$$\begin{aligned}
h(t) &= \mathcal{L}^{-1}\left\{\frac{h(0)}{s+1/\tau_h}\right\} + \mathcal{L}^{-1}\left\{\frac{b\cdot\overline{V}(s)/\tau_h}{s+1/\tau_h}\right\} + \mathcal{L}^{-1}\left\{\frac{c/\tau_h}{s^2+s/\tau_h}\right\} \\
&= h(0)\cdot e^{-t/\tau_h} + \frac{Ab}{\tau_h}\int_0^t V(q)\cdot e^{-(t-q)/\tau_h}dq + h(0)\cdot[1-e^{-t/\tau_h}] \\
&= h(0) + Ab\cdot(1-e^{-t/\tau_h} - \frac{\tau_m}{\tau_m-\tau_h}e^{-t/\tau_m} + \frac{\tau_m}{\tau_m-\tau_h}e^{-t/\tau_h})\cdot u(t) \\
&\quad -Ab\cdot(1-e^{-(t-T_1)/\tau_h} - \frac{\tau_m}{\tau_m-\tau_h}e^{-(t-T_1)/\tau_m} + \frac{\tau_m}{\tau_m-\tau_h}e^{-(t-T_1)/\tau_h})\cdot u(t-T_1) \\
&\quad -Ab\cdot(1-e^{-(t-T_1-T_2)/\tau_h} - \frac{\tau_m}{\tau_m-\tau_h}e^{-(t-T_1-T_2)/\tau_m} + \frac{\tau_m}{\tau_m-\tau_h}e^{-(t-T_1-T_2)/\tau_h})\cdot u(t-T_1-T_2) \\
&\quad +Ab\cdot(1-e^{-(t-2T_1-T_2)/\tau_h} - \frac{\tau_m}{\tau_m-\tau_h}e^{-(t-2T_1-T_2)/\tau_m} + \frac{\tau_m}{\tau_m-\tau_h}e^{-(t-2T_1-T_2)/\tau_h})\cdot u(t-2T_1-T_2)
\end{aligned} \tag{4.3.36}$$

Then substituting Eq.(4.3.36) into Eq.(3.3.4), the threshold $\theta(t)$ can be calculated theoretically. The theoretical solutions of $h(t)$ and $\theta(t)$ are compared separately with the simulation results in Figure 5-5 and Figure 5-6.

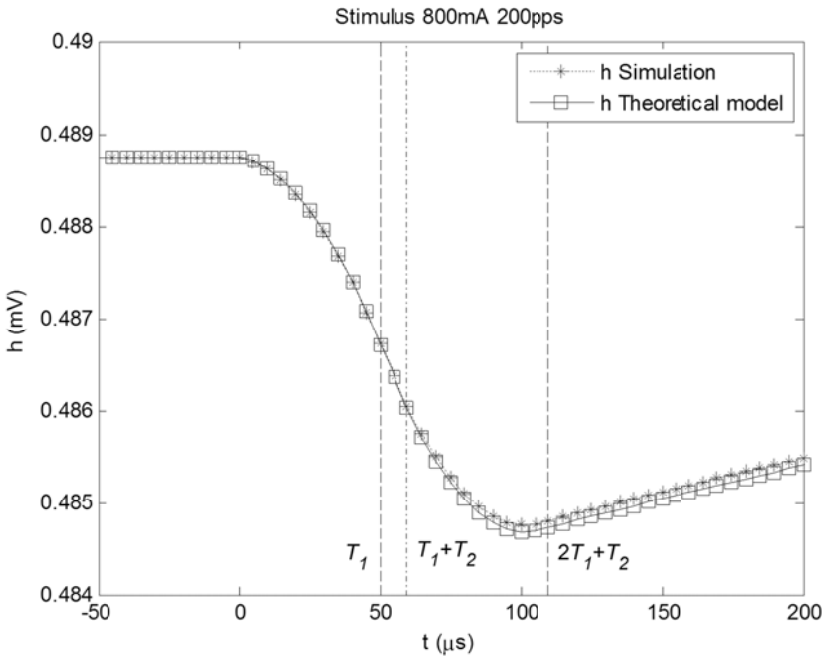

Figure 5-5 $h(t)$ response to a single-pulse stimulus, Eq.(4.3.36)

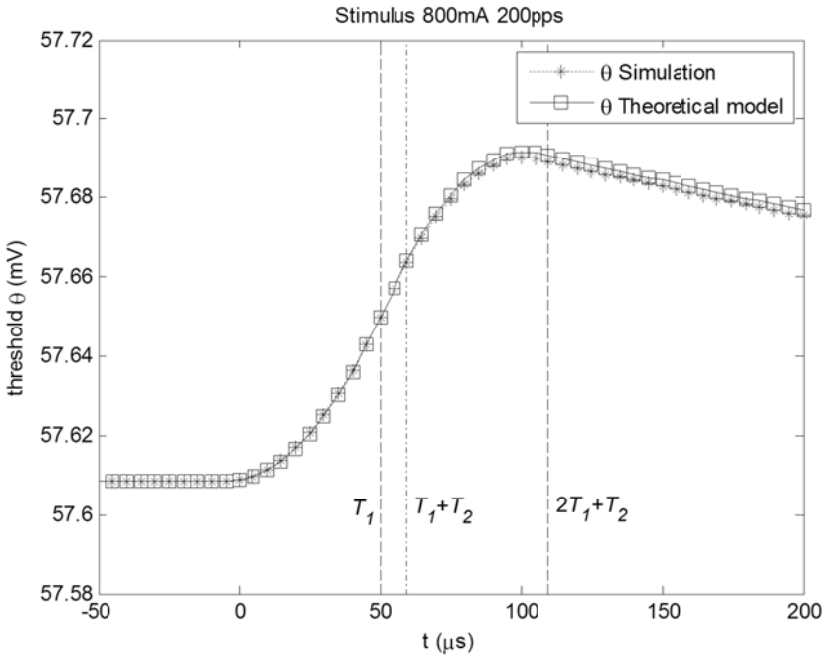

Figure 5-6 Threshold $\theta(t)$ response to a single-pulse stimulus, Eq.(3.2.12)

In Figure 5-3, it is suggested that, for a stimulus amplitude above 50 mV, the response of $h_\infty(t)$ is underestimated by the linear equation Eq.(4.3.28). The linear approximation of h_∞ degrades the theoretical prediction of the dynamics.

However, as seen in Figure 5-2, the membrane potential $V(t)$ only exceeds 50 mV in an approximate interval $[T_1, T_1 + T_2]$. The duration of this interval is around 10 μs, which is only 10% of the total duration of the anodic phase and the cathodic phase. Thus, the theoretical model can still successfully predict the response of $h(t)$and $\theta(t)$ (as shown in Figure 5-5 and Figure 5-6). For larger stimulus amplitude, the duration of $V(t)$ exceeding 50 mV gets longer. Predictions of neural response may be further degraded. Validation of the theoretical model is presented in section 5.3.

The theoretical solution to the noise free single-pulse stimulus is built with four algebraic equations, Eq.(4.3.6), Eq.(4.3.28), Eq.(4.3.36) and Eq.(3.3.4). It provides a simplified expression of the LIFDT model. In Figure 5-2, the membrane potential $V(t)$ increases monotonically during the anodic phase of the single-pulse stimulus. It reaches the maximum voltage at the end of the anodic phase $(t = T_1)$. $V(t)$ decreases monotonically afterwards. In Figure 5-6, the threshold $\theta(t)$ increases monotonically during the single-pulse stimulus. It reaches the maximum voltage just before the end of the cathodic phase $(t = 2T_1 + T_2)$. $\theta(t)$ decreases after the stimulus. Therefore without the noise, when the single-pulse stimulus is delivered, the only chance of firing depends on whether the maximum membrane potential,$V(T_1)$, crosses the threshold, $\theta(T_1)$.

With the knowledge of the neural response to the noise free single-pulse stimulus, the theoretical model is expanded to capture the behaviour of noise. The noise used in the LIFDT model is Gaussian white noise, which is applied to the membrane potential, Eq.(3.3.1). The same Gaussian white noise is used in the stochastic auditory nerve model (presented in section 3.2, [47]). Therefore, the

stochastic auditory nerve model, Eq.(3.2.4) and Eq.(3.2.5), is modified to obtain the analytical approximation of the LIFDT model.

In the LIFDT model, a spike is generated when the membrane potential crosses the threshold. So the two parameters to be compared are $V(t)$ and $\theta(t)$. According to Eq.(4.3.6) and Eq.(3.3.4), $V(t)$ and $\theta(t)$ follow the biphasic pulse instantaneously. $V(t)$ varies in the interval [-5, 60]mV (as shown in Figure 5-2) and $\theta(t)$ varies in the interval [57.6, 57.7]mV (as shown in Figure 5-6). To utilize the stochastic auditory nerve model, several approximations have to be made.

- Based on previous analysis of noise-free neural response, assume a spike is generated only in response to the maximum membrane potential during a pulse, $V_{\max}^{n}$.
- The threshold $\theta(t)$ is assumed constant during the anodic phase of the pulse n. It is denoted as θ^{n}. The value of θ^{n} is calculated by $V_{\max}^{n}$ accordingly.

Therefore, for any single pulse n, the membrane potential and the threshold are compared only at the time, T_1, when the membrane potential reaches its maximum amplitude. The noise is denoted as V_{noise}, which has a Gaussian amplitude distribution. Following these approximations, the LIFDT model is in effects a Bernoulli process according to the stochastic auditory nerve model (presented in section3.2). The probability of firing during pulse n is denoted as $p(n)$. The Bernoulli random variable, discharge probability $p(n)$ is given by

$$p(n)=\begin{Bmatrix}0 & for\, V_{\max}^{n}+V_{noise}(n)<\theta^{n}\\ 1 & for\, V_{\max}^{n}+V_{noise}(n)\geq\theta^{n}\end{Bmatrix} \tag{4.3.37}$$

Rearrange the inequality

$$p(n)=\begin{Bmatrix}0 & for\, V_{noise}(n)<\theta^{n}-V_{\max}^{n}\\ 1 & for\, V_{noise}(n)\geq\theta^{n}-V_{\max}^{n}\end{Bmatrix} \tag{4.3.38}$$

The discharge occurs when the noise falls in the interval $[\theta^n - V_{max}^n, \infty)$. The noise is a Gaussian distribution with mean zero and variance σ^2, which is also used in the stochastic AN model. Thus the discharge probability versus stimulus intensity (input/output function) is given by

$$\begin{aligned} p(n) &= \int_{\theta^{n}-V_{\max}^{n}}^{\infty} f(x)dx \\ &= \int_{\theta^{n}-V_{\max}^{n}}^{\infty} \frac{1}{\sqrt{2\pi\sigma^{2}}} e^{-\frac{x^{2}}{2\sigma^{2}}} dx \end{aligned} \tag{4.3.39}$$

The integrated-Gaussian can be written as an error function,

$$p(n)=\frac{1}{2}(1+erf(\frac{V_{\max}^{n}-\theta^{n}}{\sqrt{2}\sigma})) \tag{4.3.40}$$

According to Eq.(4.3.6), the maximum membrane potential V_{max}^n is given by

$$V_{\max}^{n}=V(T_1)=A(1-e^{-T_1/\tau_m}) \tag{4.3.41}$$

and $h(T_1)$ and $\theta(T_1)$ are calculated accordingly as,

$$h(T_1)=h(0)+Ab\cdot(1-e^{-T_1/\tau_h}-\frac{\tau_m}{\tau_m-\tau_h}e^{-T_1/\tau_m}+\frac{\tau_m}{\tau_m-\tau_h}e^{-T_1/\tau_h}) \tag{4.3.42}$$

$$\theta^n = \theta(T_1) = \frac{\theta_m}{h(T_1)^p} + \theta_0 \tag{4.3.43}$$

Therefore, Eq.(4.3.40) can be written as

$$p(n) = \frac{1}{2}(1 + erf(\frac{V(T_1) - \theta(T_1)}{\sqrt{2}\sigma})) \tag{4.3.44}$$

where $V(T_1)$ is calculated by Eq.(4.3.43) and $\theta(T_1)$ is calculated by Eq.(4.3.42) and Eq.(4.3.43).This gives the approximated analytical result for the firing probability of the LIFDT model to a single-pulse stimulus. The function $p(n)$ is dependent on the stimulus amplitude A with six independent parameters: $\tau_m, \tau_h, p, \theta_m, \theta_0$ and σ. Predictions of a single-pulse response can be computed simply using Eq.(4.3.44). It is more efficient than Monte Carlo simulations of the LIFDT model, because it does not require multiple iterations. The results are presented in section 5.3. As the membrane potential $V(t)$ and the threshold $\theta(t)$ both have complex dynamics, it is difficult to conduct an analysis of the error introduced by all the assumptions and approximations. However, predictions of the neural response to a single-pulse stimulus by the theoretical model, Eq.(4.3.44), are compared with simulation results for the LIFDT model in section 5.3.

5.2.2 Analytical approximation of LIFDT model to a subthreshold pulse-train stimulus

The analytical approximation of the LIFDT model to a single-pulse stimulus was established in previous section. It speeds up the calculation of large-scale population responses. However, pulse-train stimuli are typically used in designing speech processing strategies for cochlear implants. Therefore, the

theoretical model must accurately predict the neural response to a pulse-train stimulus. The LIFDT model is developed with refractory effects and accommodation effects (presented in section 3.3.1 and 3.3.2). The analysis of the neurophysiological data in low FE revealed that accommodation effects mainly contribute to the initial drop of firing probability on the second pulse. In order to fit the strong initial drop observed in the experimental data by the LIFDT model, only the response to a subthreshold stimulus is studied in this section. In particular, the analytical approximation of the firing probability on the second pulse in the 200pps pulse train is developed.

Two pulses of the pulse-train 200pps were applied to the LIFFDT model (shown in Figure 5-7).

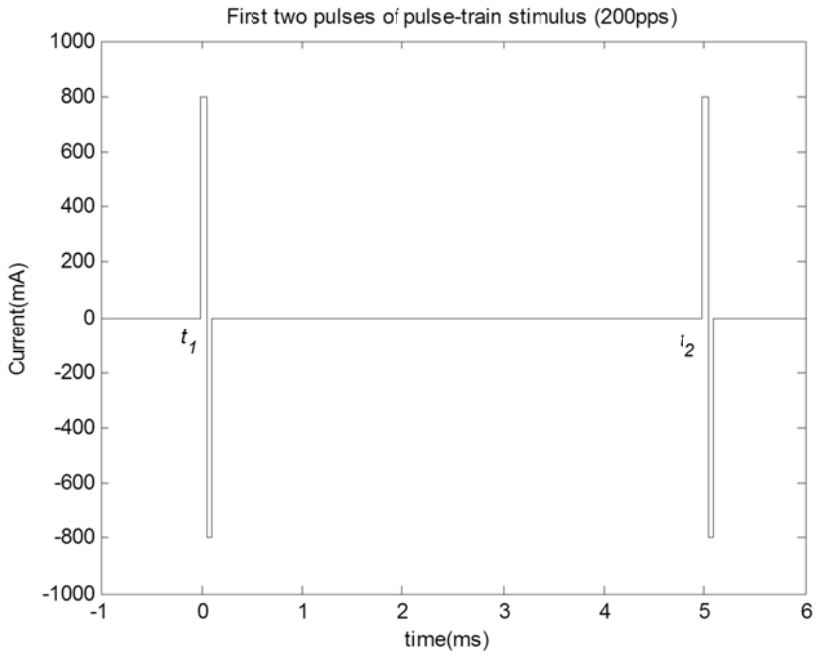

Figure 5-7 First two pulses of the 200pps pulse-train $S(t)$, the start time of the first pulse is denoted as t_1 , $t_1 = 0$; the start time of the second pulse is denoted as t_2, $t_2 = 5ms$.

The response to the first pulse of a two-pulse stimulus ($0 < t \le t_2$) is identical to the response to a single-pulse stimulus. It is calculated according to Eq.(4.3.44),

$$p(1) = \frac{1}{2}(1 + erf(\frac{V(T_1) - \theta(T_1)}{\sqrt{2}\sigma})) \tag{4.3.45}$$

For 200pps pulse-train stimulus, the second pulse is delivered 5ms after the first pulse. The same process (section 5.2.1) is applied to the LIFDT model to get the general solution (Proof: see Appendix B). The only chance of firing on the second pulse is still at the end of the anodic phase. It depends on whether the maximum membrane potential, $V(t_2 + T_1)$, crosses the threshold, $\theta(t_2 + T_1)$.

The probability of firing on the second pulse,$p(2)$, can be expressed as,

$$p(2) = \int_{\theta\big|_{t=t_2+T_1} - V\big|_{t=t_2+T_1}}^{\infty} \frac{1}{\sqrt{2\pi\sigma^2}} e^{-\frac{x^2}{2\sigma^2}} dx \tag{4.3.46}$$

where σ^2 is variance of the noise, value of threshold and membrane potential at the end of anodic phase ($t = t_2 + T_1$) can be calculated according to Eq(10,13,14) in Appendix B.

Thus, Eq.(4.3.46) can be written as

$$p(2) = \frac{1}{2}(1 + erf\frac{V(t_2 + T_1) - \theta(t_2 + T_1)}{\sqrt{2}\sigma}) \tag{4.3.47}$$

This gives the approximated analytical result for the firing probability of the LIFDT model to the second pulse of a two-pulse stimulus on condition that the nerve fibre does not fire on the first pulse. The function $p(2)$ is developed based on the theoretical model to a single-pulse stimulus, Eq.(4.3.44). It is dependent on stimulus amplitude A with six independent parameters: $\tau_m, \tau_h, p, \theta_m, \theta_0$ and σ. However, it only predicts accommodation effects in the pulse-train response. The refractory effects, the major part observed in interpulse interactions, are not

included in Eq.(4.3.47). A statistical model developed in Chapter 6 describes the refractory effects. In this chapter, only accommodation effects are theoretically studied. This analytical version of the LIFDT model provides a fitting approach to the experimental data [16], which separates the interpulse interactions. In order to achieve the large accommodation effects observed in the data, the analytical version of the LIFDT model is investigated in section 5.4 avoiding numerical integration.

5.3 Predictions by the analytical version of LIFDT model

The analytical version of the LIFDT model is derived under the assumption that a spike is only generated in response to the maximum membrane potential within the pulse. Also the equation of $h_{\infty}(t)$ is replaced by the linear equation Eq.(4.3.28). It is important to assess the impact of these assumptions and approximations. A Monte Carlo simulation of the LIFDT model was conducted to investigate the accuracy of analytical version of the LIFDT model. The values of the parameters used in the simulation are given in Table 5-1. The values of parameters in the analytical version of the LIFDT model are the same. The values of D and τ_m are given by the initial assessment of fitting the neurophysiological data (Table 4-3). Because there is no refractory effects or accommodation effects on the first pulse, it is not clear how to fit the other seven parameters in LIFDT model accordingly. At this stage, the LIFDT model fit is achieved by only adjusting the value of θ_0 according to the fitted I/O curve for the first pulse with ten data points (presented in Figure 4-4). The values of $\tau_h, \mu_{\infty}, \sigma_{\infty}, \theta_m, p$ and τ_{abs} are taken from Table 3-1 and Table 4-3.

Table 5-1 Fitted parameter values of LIFDT model to the I/O curve on the first pulse

D	$\tau_m\,(ms)$	$\tau_h\,(ms)$	$\mu_\infty\,(mV)$	$\sigma_\infty\,(mV)$
0.0028	0.7	1.9	-4.5	100
$\theta_m\,(mV)$	$\theta_0(mV)$	P	$\tau_{abs}\,(ms)$	
3	25	1.3	0.284	

The LIFDT model (Eq.(3.3.1)-Eq.(3.3.4)) was simulated over a thousand iterations for a two-pulse stimulus (shown in Figure 5-7), but with different noise at each iteration. For Monte Carlo simulation with iterations of N, the standard error of the sample mean reduces at the rate of $\sqrt{N}$, and the standard error of the sample variance reduces at the rate of $\sqrt{(N+1)/2}$ [119]. As N is very large in this simulation, it is assumed that the sample mean and sample variance have converged completely after ten thousand iterations. Predictions from the LIFDT model and the analytical version of the LIFDT model are compared in the following sections.

5.3.1 Predictions of single-pulse response

The discharge probabilities on the first pulse against stimulus amplitudes, also referred as I/O curves to the first pulse of pulse-train stimulus, are presented in Figure 5-8. The analytical result of the theoretical model is consistent with both the simulation result of the LIFDT model and the fitted simplified analytical model. Thus both the stochastic LIFDT model and the analytical version of the LIFDT model successfully predicted the physiological data in response to the single-pulse stimulus or the first pulse of pulse-train stimulus. The analytical version of the LIFDT model provides an almost exact description of the stochastic LIFDT model. Even at low stimulus amplitudes, the neural responses predicted by the theoretical model are not degraded by the approximation and

simplification. It indicates that discharge occurs mostly at the maximum membrane potential within the single pulse. The approximation and linear simplification appear to be accurate and appropriate.

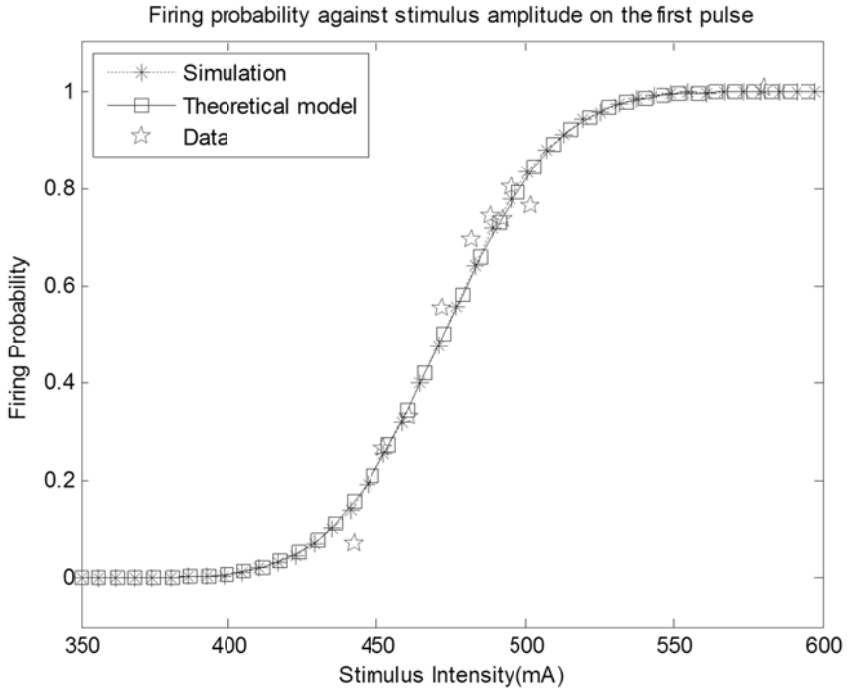

Figure 5-8 I/O curves to a single-pulse stimulus or the first pulse of a pulse-train stimulus. Stars represent the neurophysiological data, the dotted line with asterisk markers presents the simulation result by LIFDT model, the solid line with square markers represents the predictions of the theoretical model, Eq.(4.3.44).

5.3.2 Predictions of pulse-train response

Then, we investigate the neural responses to a two-pulse stimulus. The neural responses to the first pulse have been studied in section 5.3.1. The neural responses to the second pulse is calculated by Eq.(4.3.47). The results are presented in Figure 5-9. In order to investigate the accuracy of this prediction, simulations to the second pulse are also conducted. As the theoretical model only considers accommodation effects, comparisons are only made for low firing

probabilities in which most neurons did not fire at the first pulse and refractory effects have little influence.

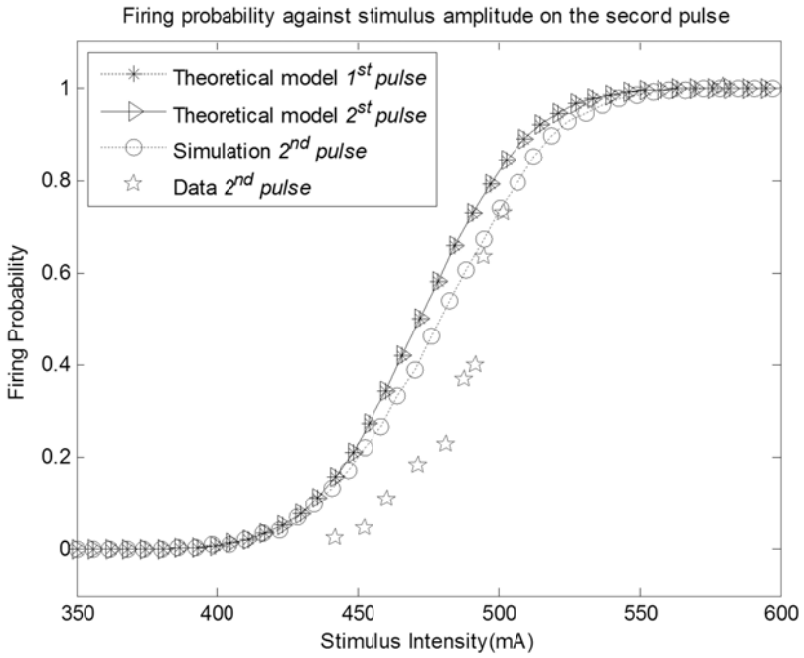

Figure 5-9 I/O curves to a two-pulse stimulus by the theoretical version of LIFDT model. The dotted line with asterisk markers represents the predictions by theoretical model on the first pulse Eq.(4.3.45), the solid line with right-pointing triangle markers represents the predictions by theoretical model Eq.(4.3.47) the dotted line with circle markers represents the simulation results on the second pulse, stars represent the neurophysiological data on the second pulse.

The goodness of fit of predictions from the theoretical model to the simulation results are given in Table 5-2.

Table 5-2 Goodness fit of theoretical model to simulation results at the 1st pulse and 2nd pulse

Goodness of fit	SSE	R-Square
1st pulse	0.004	1.000
2nd pulse	0.122	0.959

The R-Squared value for the theoretical predictions at the first pulse is 1.0, which demonstrates that the theoretical model successfully fits to the simulation results.

At the second pulse, although R-Squared value is 0.959, the SSE increases enormously. Because the theoretical model does not include the refractory effects, predictions at high stimulus amplitudes are higher than stimulation results. We focus on the results at low stimulus amplitudes. In Figure 5-9, the theoretical model approximates the neural responses to the second pulse accurately for firing probabilities between 0 and 0.2. The theoretical model provides an almost exact description of the LIFDT model for low firing probabilities. It successfully quantifies accommodation effects in the LIFDT model. For firing probabilities higher than 0.2, the theoretical predictions overestimate the neural responses. Refractory effects constitute the difference between the predictions by the theoretical model (solid line with right-pointing triangle markers) and simulation results (dotted line with circle markers). It indicates that the accuracy of this theoretical model is relatively sensitive to refractory effects in the model.

Given the values of the parameters in Table 5-1 from fits to the first pulse, the simulation result to the second pulse does not reach the slope of the neurophysiological data and the shape of the curve is inaccurate. In chapter 4, the neurophysiological data have been evaluated and analysed. The suppression in the firing probability to the second pulse is due to both accommodation effects and refractory effects. In order to achieve the suppression in the neurophysiological data, accommodation effects or refractory effects or both effects in the LIFDT model have to be modified.

In physiological experiments, the refractory function is usually measured by applying a pair of suprathreshold pulses to the nerve [38, 60]. The amplitude of the first pulse is fixed, and an action potential is generated in response to the first pulse. For a range of amplitudes of the second pulse, the minimum interpulse

intervals between those two pulses are recorded, at which the second pulse is just able to evoke an action potential. With the limited neurophysiological data presented in section 3.4, it is infeasible to estimate the refractory function directly. For one I/O curve, there is only ten data points. Also as the data points are taken from the pool of neurons, not from one single neuron. The quality of the data is low and there is a lot of noise for low FE. For accommodation effects, it is the same case.

In Figure 5-9, the simulation results could predict the neurophysiological data for the second pulse for $FE > 0.7$. The main difference between the simulation results and the neurophysiological data relies on the part for FE between 0 and 0.7. It is suggested that accommodation effects have to be enlarged to reach the neurophysiological data, as accommodation effects dominate the interpulse intervals for low FE .

In order to prove this observation, neural responses are predicted with maximum refractory effects as the same approach in section 4.4. In Figure 5-10, the predictions with the maximum refractory effects cannot reach the neurophysiological data. It is suggested that accommodation effects in the LIFDT model are not large enough. Therefore, we compare the predictions to the first pulse and the second pulse obtained from the theoretical model in Figure 5-9. Predictions on the second pulse by Eq.(4.3.47) are identical to the theoretical predictions to the first pulse by Eq.(4.3.45). It indicates that inclusion of accommodation mechanism with parameter values given in Table 5-1 did not improve the predictions of pulse-train response.

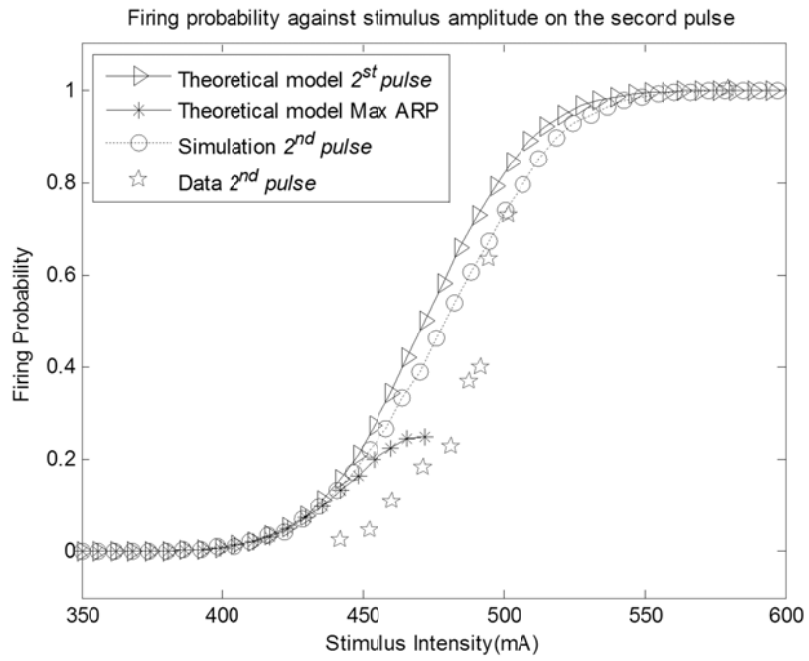

Figure 5-10 I/O curves to the second pulse of a two-pulse stimulus. The solid line with right-pointing triangle markers represents the predictions by theoretical model Eq.(4.3.47), the solid line with asterisk markers represents the predictions by theoretical model with maximum refractory effects, the dotted line with circle markers represents the simulation results, pentagrams represent the neurophysiological data.

5.4 The maximum accommodation effects in the LIFDT model

To improve the fit of the LIFDT model to the experimental data, accommodation effects have to be increased. More specifically, the difference between the firing probabilities on the first pulse and the second pulse has to be increased. In this section we investigate whether the small accommodation effects result from a structural problem with the LIFDT model or from an incorrect selection of parameters. Therefore, previous fitted parameter values are abandoned. In this section, the parameter values are optimized to achieve the maximum accommodation effects.

Accommodation effects in this section are defined as follows. According to the analytical theory (presented in section 5.2), the difference between firing probabilities is calculated as

$$\Delta p = p(1) - p(2) \tag{4.5.1}$$

Substituing Eq.(4.3.45) and Eq.(4.3.47) into Eq.(4.5.1) gives,

$$\Delta p = \frac{1}{2}(1 + erf\frac{V(T_1) - \theta(T_1)}{\sqrt{2}\sigma}) - \frac{1}{2}(1 + erf\frac{V(t_2 + T_1) - \theta(t_2 + T_1)}{\sqrt{2}\sigma}) \tag{4.5.2}$$

Writing in the form of Gaussian integral gives

$$\Delta p = \int_{\theta(T_1)-V(T_1)}^{\infty} \frac{1}{\sqrt{2\pi\sigma^2}} e^{-\frac{x^2}{2\sigma^2}} dx - \int_{\theta(t_2+T_1)-V(t_2+T_1)}^{\infty} \frac{1}{\sqrt{2\pi\sigma^2}} e^{-\frac{x^2}{2\sigma^2}} dx \tag{4.5.3}$$

According to the data, $p(1)$ is no smaller than $p(2)$. Thus $\Delta p \geq 0$, and the integral area of $p(1) \leq p(2)$, thus,

$$\Delta p = \int_{\theta(T_1)-V(T_1)}^{\theta(t_2+T_1)-V(t_2+T_1)} \frac{1}{\sqrt{2\pi\sigma^2}} e^{-\frac{x^2}{2\sigma^2}} dx \tag{4.5.4}$$

The lower limit and upper limit are dependent on stimulus amplitude A. The independent parameters: τ_m, θ_0 and σ are fitted by the neurophysiological data to the first pulse. Only the interval of the integration can be modified to increase Δp. The length of the interval,L, can be calculated as

$$\begin{aligned} L &= \left[\theta(t_2 + T_1) - V(t_2 + T_1)\right] - \left[\theta(T_1) - V(T_1)\right] \\ &= \left[\theta(t_2 + T_1) - \theta(T_1)\right] - \left[V(t_2 + T_1) - V(T_1)\right] \end{aligned} \tag{4.5.5}$$

As stated in Appendix B, the difference between $V(t_2 + T_1)$ and $V(T_1)$ is only 0.1% of its value. This leads to a modification of the first two parts of the equation, which represent the difference between $\theta(t_2 + T_1)$ and $\theta(T_1)$. The threshold θ is monotonically decreasing with regard to the variable h. The values of $h(t_2 + T_1)$ and $h(T_1)$ are calculated according to the value in Table 5-1.

$$h(T_1) = 0.4888$$
$$h(t_2 + T_1) = 0.4886$$

There is no apparent difference between the value of $h(t_2 + T_1)$ and $h(T_1)$, which contributes to the failure of predicting accommodation effects. Even setting θ_m forty times larger than its original value, the difference between $\theta(t_2 + T_1)$ and $\theta(T_1)$ is still only about 0.07. Therefore, it is crucial to enlarge the difference between $h(T_1)$ and $h(t_2 + T_1)$, which is

$$\Delta h = h(T_1) - h(t_2 + T_1) \tag{4.5.6}$$

$$\begin{aligned}\Delta h = -Ab \cdot e^{-T_1/\tau_h} \cdot [&(1 - e^{-t_2/\tau_h} - \frac{\tau_m}{\tau_m - \tau_h} e^{-t_2/\tau_m} + \frac{\tau_m}{\tau_m - \tau_h} e^{-t_2/\tau_h}) \\ &-(1 - e^{-(t_2 - T_1)/\tau_h} - \frac{\tau_m}{\tau_m - \tau_h} e^{-(t_2 - T_1)/\tau_m} + \frac{\tau_m}{\tau_m - \tau_h} e^{-(t_2 - T_1)/\tau_h}) \\ &-(1 - e^{-(t_2 - T_1 - T_2)/\tau_h} - \frac{\tau_m}{\tau_m - \tau_h} e^{-(t_2 - T_1 - T_2)/\tau_m} + \frac{\tau_m}{\tau_m - \tau_h} e^{-(t_2 - T_1 - T_2)/\tau_h}) \\ &+(1 - e^{-(t_2 - 2T_1 - T_2)/\tau_h} - \frac{\tau_m}{\tau_m - \tau_h} e^{-(t_2 - 2T_1 - T_2)/\tau_m} + \frac{\tau_m}{\tau_m - \tau_h} e^{-(t_2 - 2T_1 - T_2)/\tau_h})]\end{aligned} \tag{4.5.7}$$

In Eq.(4.3.21), Δh is dependent on the stimulus amplitude,A. Only independent parameters, b and τ_h, are available to be optimized. Δh is proportional to the absolute value of the slope of the linear equation Eq.(4.3.28),$|b|$. The relationship

between Δh and τ_h is more complicated. For different values of τ_h, Δh is calculated according to Eq.(4.3.21), in which other parameters are fixed; the stimulus amplitude is 800 mA, τ_m is 0.7ms and b is calculated from Eq.(4.3.28). The results are plotted in Figure 5-11. In physiology, the time constant of sodium permeability,τ_h, is always bigger than the membrane time constant, τ_m[37]. Thus the value of τ_h is taken in the interval $[0.7ms, 10ms]$.

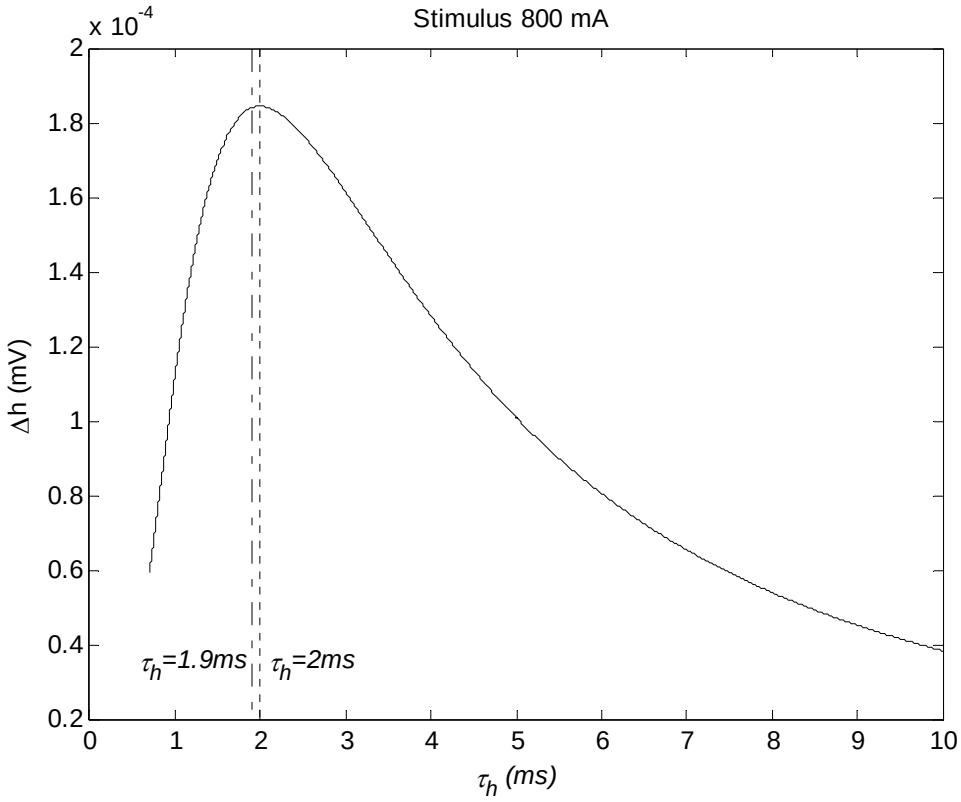

Figure 5-11 Δh as a function of the time constant τ_h

In Figure 5-11, the maximum value of Δh is obtained when τ_h equals 2ms (dotted line), which is close to its current value given in Table 5-1, 1.9ms (dash-dotted line).

In order to increase Δh, one approach is to set τ_h to 2ms. However, it cannot significantly improve the model (shown in Figure 5-11). Another approach is to

change the slope of the linear equation Eq.(4.3.28),b. The linear equation is a simplification of the sigmoid equation Eq.(3.3.3). In Figure 5-3, when a stimulus is applied, h_∞ changes from 0.49 to 0.35, approximately, under the current sigmoid equation. Then the variable h approaches the asymptotic value h_∞ for the time constant τ_h within the pulse duration. By increasing the absolute value of the slope of the linear equation Eq.(4.3.28), the impact on h_∞ is extended, therefore, Δh increases. The extreme value of Δh is attained when the linear equation is a vertical line. Although the linear approximation is not appropriate in this extreme condition, it is suggested that a sigmoid function Eq.(3.2.11) with very sharp slope will increase the value of Δh. In this case, h_∞ quickly switches from one to zero when the stimulus is applied. Therefore, unlike the linear approximation by Eq.(4.3.28), the function of h_∞ should be modified to behave like a step function.

In Eq.(3.2.11), the sigmoid function of h_∞ is dependent on the membrane voltage V with two independent parameters: μ_∞ and σ_∞. σ_∞ is the standard deviation of h_∞, and it controls the slope of h_∞. The smaller the value of σ_∞, the sharper the slope of the sigmoid function. μ_∞ is the offset of h_∞, and it defines the value of V that produces h_∞ the value of 0.5. To mimic the behaviour of a step function, we use a small σ_∞. Next we try to find an appropriate value for μ_∞. For small σ_∞, μ_∞ is approximately equivalent to the switching point. For a membrane voltage $V \geq \mu_\infty$, h_∞ switches to zero. Figure 5-2 presents the dynamics of the membrane potential to a single-pulse stimulus without noise. The equilibrium value for the membrane potential is zero. It monotonically increases to the level of $A(1 - e^{-T_1/\tau_m})$ and then decreases to zero in response to the stimulus. The switching point should be in the interval $[V(S = 0), V_{max}]$. Given small σ_∞, the

sigmoid function of h_∞ is changed to its opposite state. It cannot slowly vary in the interval [0, 1], but only has two states '0' or '1'. The equilibrium value of both h_∞ and h are one. Only after the switching point, h_∞ changes to zero and then h begins to move towards zero. To extend the influence on h, it is better to make the switching point close to zero. Then as soon as the stimulus has been applied to the membrane potential, h can start moving accordingly. However, in the LIFDT model, the Gaussian noise with intensity D is added to the membrane potential (defined in Eq.(3.3.1)). The membrane potential changes stochastically. To avoid h_∞ accidently switching by noise, the switching point should be above the level of the noise. Therefore, new parameter values are given below

- $\mu_\infty = 8\,mV;\ \sigma_\infty = 0.1$

The modified sigmoid function of h_∞ is plotted in Figure 5-12.

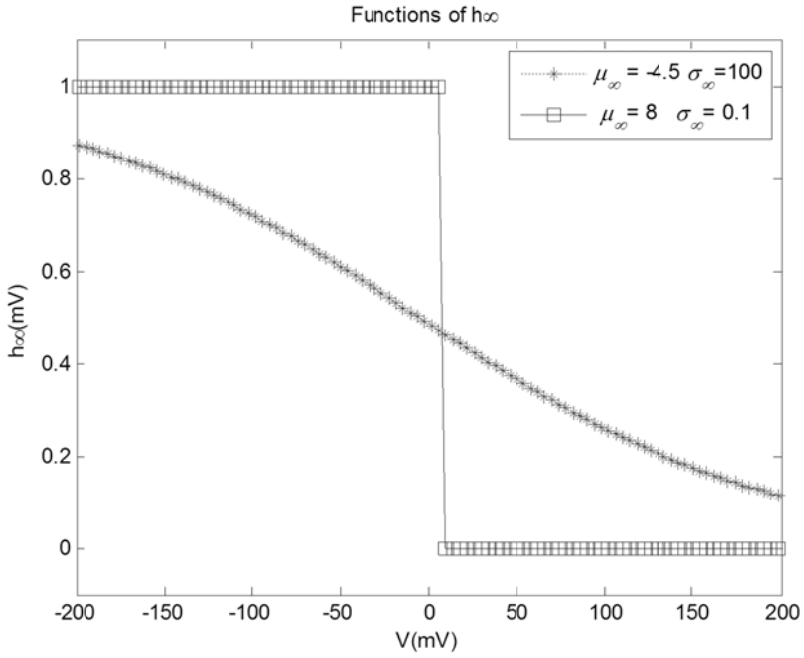

Figure 5-12 Modified function of $h_\infty(V)$. The dotted line with asterisk markers presents the sigmoid function with former values. The solid line with square markers presents the sigmoid function with modified values.

5.4.1 Analytical approximation of the modified LIFDT model: step function approximation

As $h_\infty(V)$ is modified as a step function, the analytical approximation of the LIFDT model derived previously is not appropriate to use. A new analytical approximation of the modified LIFDT model with the step function approximation is derived in this section.

In this section, an analytical approximation of the modified LIFDT model is only developed for a two-pulse stimulus. First the responses of $V(t)$ and $\theta(t)$ to the two-pulse stimulus (shown in Figure 5-7) without noise are investigated. In the following figures, predictions by the theoretical calculations are plotted in solid lines with square markers, and simulation results are plotted in dotted lines with asterisk makers.

The first pulse of the stimulus is defined by Eq.(4.3.22). The analytical approximation of the membrane potential (Eq.(4.3.6)) remains the same. To ease the difficulty in calculation, the modified sigmoid function of h_∞ can be approximated by a step function of V,

$$h_\infty(V) = \begin{cases} 1 & V \geq \mu_\infty \\ 0 & V < \mu_\infty \end{cases} \tag{4.5.8}$$

where $\mu_\infty = 8\, mV$.

The response of the membrane potential to the first pulse is plotted in Figure 5-13, which is identical to Figure 5-2 except the stimulus amplitude is $600mV$, since a stimulus of $800mV$ is suprathreshold in the modified LIFDT model.

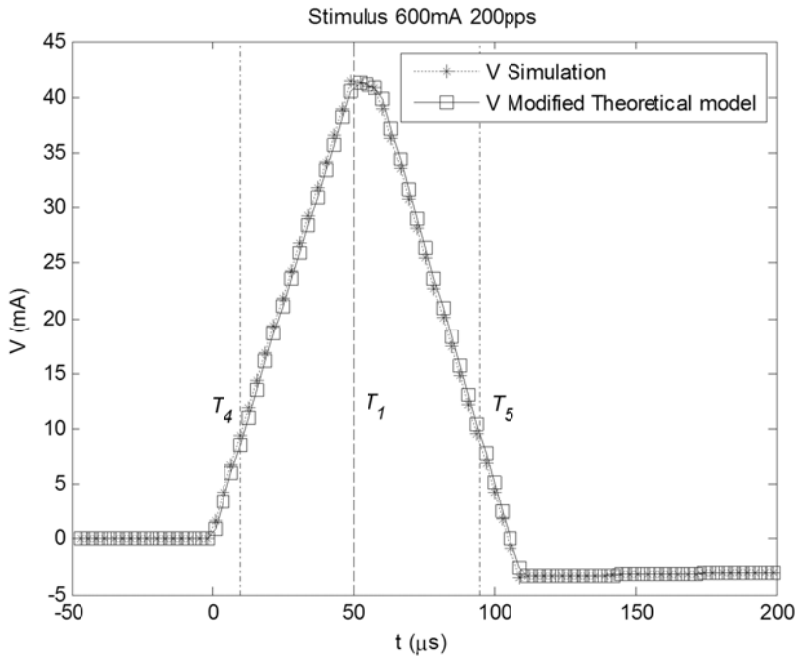

Figure 5-13 Membrane potential $V(t)$ response to a single-pulse stimulus, the dash-dot lines, denoted as T_4 and T_5, display the time when the membrane potential crosses the switching point μ_∞, the dashed line, denoted as T_1, displays the time when the membrane potential reaches its maximum amplitude.

When the first pulse is delivered to the neuron, the membrane potential V monotonically increases and crosses the switching point μ_∞ at the time $(t = T_4)$, and it attains its maximum amplitude at the end of anodic phase $(t = T_1)$. Then it begins to monotonically decrease and crosses the switching point μ_∞ at the time $(t = T_5)$. According to Eq.(4.5.8), the function $h_\infty(t)$ is actually a rectangular function,

$$h_\infty(t) = \begin{cases} 1 & 0 \le t \le T_4 \\ 0 & T_4 < t < T_5 \\ 1 & t \ge T_5 \end{cases} \tag{4.5.9}$$

which can be written in the terms of the unit step function

$$h_\infty(t) = 1 - u(t - T_4) + u(t - T_5) \tag{4.5.10}$$

The approximated $h_\infty(t)$ is compared with simulation results in Figure 5-14. This result shows the validity of the approximation since the simulation curve matches the prediction of the simplified unit step function.

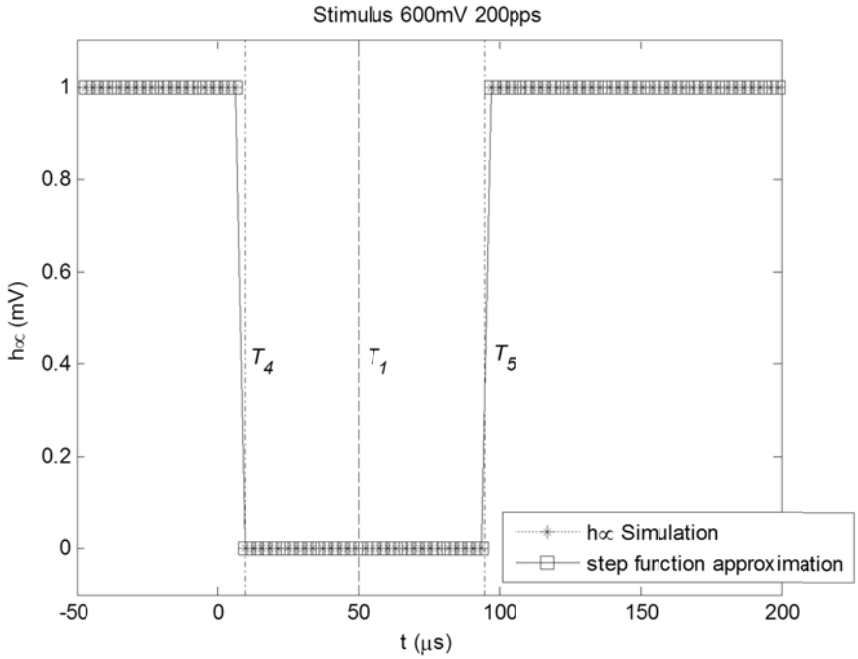

Figure 5-14 Step function approximation of h_∞ to a single-pulse stimulus

Then substituting the simplified function of h_∞ Eq.(4.5.10) into Eq.(3.3.2) yields,

$$\tau_h \dot{h}(t) = -h(t) + 1 - u(t - T_4) + u(t - T_5) \tag{4.5.11}$$

Taking Laplace transforms on both sides of Eq.(4.5.11), using the standard overbar to denote Laplace Transform gives,

$$\tau_h \cdot \mathcal{L}\{\dot{h}(t)\} = -\mathcal{L}\{h(t)\} + \mathcal{L}\{1 - u(t - T_4) + u(t - T_5)\} \tag{4.5.12}$$

which implies

$$\tau_h \cdot [s \cdot \bar{h}(s) - h(0)] = -\mathcal{L}\{\bar{h}(s)\} + \frac{1}{s} - \frac{e^{-T_4 s}}{s} + \frac{e^{-T_5 s}}{s} \tag{4.5.13}$$

Solving for $\bar{h}(s)$ gives

$$\bar{h}(s) = \frac{h(0)}{s+1/\tau_h} + \frac{1/\tau_h}{s^2+s/\tau_h} - \frac{e^{-T_4 s}/\tau_h}{s^2+s/\tau_h} + \frac{e^{-T_5 s}/\tau_h}{s^2+s/\tau_h} \qquad (4.5.14)$$

where the initial condition for the modified h is 1.

Thus taking the inverse Laplace transform of Eq.(4.5.14) to get the general solution,

$$\begin{aligned} h(t) &= \mathcal{L}^{-1}\left\{ \frac{h(0)}{s+1/\tau_h} + \frac{1/\tau_h}{s^2+s/\tau_h} - \frac{e^{-T_4 s}/\tau_h}{s^2+s/\tau_h} + \frac{e^{-T_5 s}/\tau_h}{s^2+s/\tau_h} \right\} \\ &= h(0)\cdot e^{-t/\tau_h}\cdot u(t) + [1-e^{-t/\tau_h}]u(t) - [1-e^{-(t-T_4)/\tau_h}]u(t-T_4) \\ &+ [1-e^{-(t-T_5)/\tau_h}]u(t-T_5) \\ &= 1-[1-e^{-(t-T_4)/\tau_h}]u(t-T_4) + [1-e^{-(t-T_5)/\tau_h}]u(t-T_5) \end{aligned} \qquad (4.5.15)$$

Then the threshold could be calculated by Eq.(3.3.3). The response of $h(t)$ and $\theta(t)$ for the first pulse are presented in Figure 5-15 and Figure 5-16.

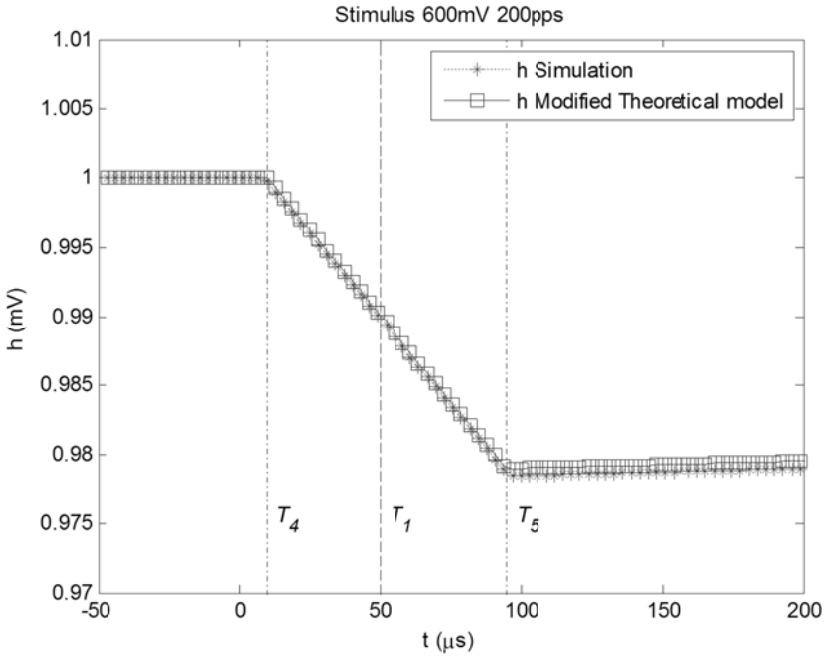

Figure 5-15 Modified h(t) response to a single-pulse stimulus

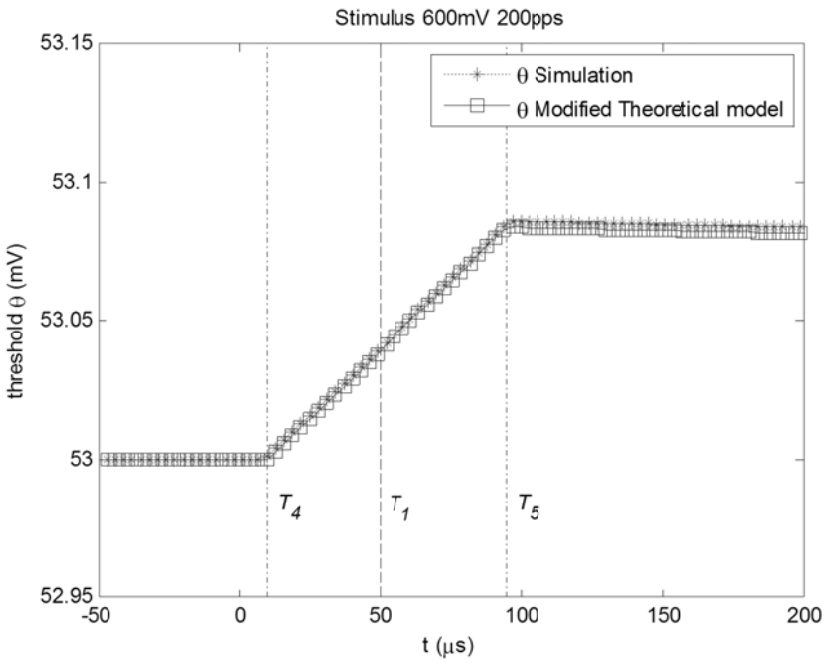

Figure 5-16 Threshold response to a single-pulse stimulus with modified $h_\infty(t)$

For the second pulse, the analytical approximation of the membrane potential is given by

$$\begin{aligned} V(t) = {} & A(1-e^{-t/\tau_m})\cdot u(t) \\ & -A(1-e^{-(t-T_1)/\tau_m})\cdot u(t-T_1) \\ & -A(1-e^{-(t-T_1-T_2)/\tau_m})\cdot u(t-T_1-T_2) \\ & +A(1-e^{-(t-2T_1-T_2)/\tau_m})\cdot u(t-2T_1-T_2) \\ & +A(1-e^{-(t-t_2)/\tau_m})]\cdot u(t-t_2) \\ & -A(1-e^{-(t-T_1-t_2)/\tau_m})\cdot u(t-T_1-t_2) \\ & -A(1-e^{-(t-T_1-T_2-t_2)/\tau_m})\cdot u(t-T_1-T_2-t_2) \\ & +A(1-e^{-(t-2T_1-T_2-t_2)/\tau_m})\cdot u(t-2T_1-T_2-t_2) \end{aligned} \tag{4.5.16}$$

To simplify the calculation, assume the neuron has fully recovered to zero before the second pulse. Thus the two switching points for the second pulse are at $t = t_2 + T_4$ and $t = t_2 + T_5$, and $h_\infty(t)$ can be approximated by a time-delayed function of Eq.(4.5.10),

$$h_{\infty}(t) = u(t - t_2) - u(t - T_4 - t_2) + u(t - T_5 - t_2) \qquad (4.5.17)$$

Predictions of the modified theoretical model (solid lines with square markers) are compared with simulation results (dotted lines with asterisk markers) in the following figures (Figure 5-17-Figure 5-20). Like the figures of the neural response to the first pulse, three time lines are plotted in the following figures to further analyse the response to the second pulse. Two dash-dotted lines are denoted as the approximated switching time lines and one dashed line is denoted as the maximum amplitude time line.

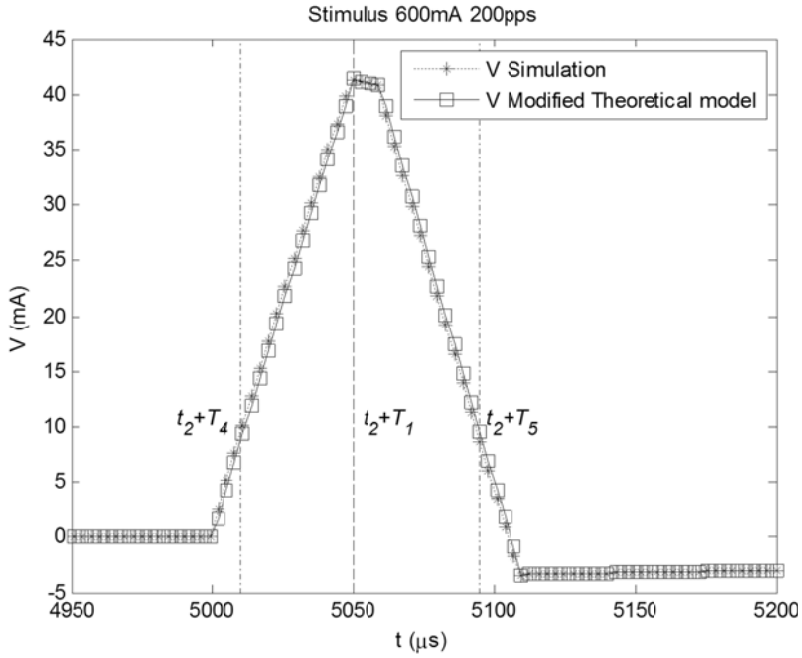

Figure 5-17 The membrane potential $V(t)$ response to the second pulse, the dash-dot lines, denoted as $t_2 + T_4$ and $t_2 + T_5$, display the approximated time when the membrane potential crosses the switching point μ_∞, the dashed line, denoted as $t_2 + T_1$, displays the time when the membrane potential reaches its maximum amplitude.

In Figure 5-18, the approximated step function captures the first switching point. The second switching point in the approximated step function Eq.(4.5.17) is about 4 μs later than the simulation result.

Then the differential equation of $h(t)$, Eq.(3.2.10), is

$$h(t) = [(e^{-(t_2-T_4)/\tau_h} + 1 - e^{-(t_2-T_5)/\tau_h}) \cdot e^{-(t-t_2)/\tau_h} + (1 - e^{-(t-t_2)/\tau_h})] \cdot u(t-t_2)$$
$$-[1 - e^{-(t-T_4-t_2)/\tau_h}] \cdot u(t-T_4-t_2) + [1 - e^{-(t-T_5-t_2)/\tau_h}] \cdot u(t-T_5-t_2) \quad (4.5.18)$$

and the threshold is calculated according to Eq.(3.3.4).

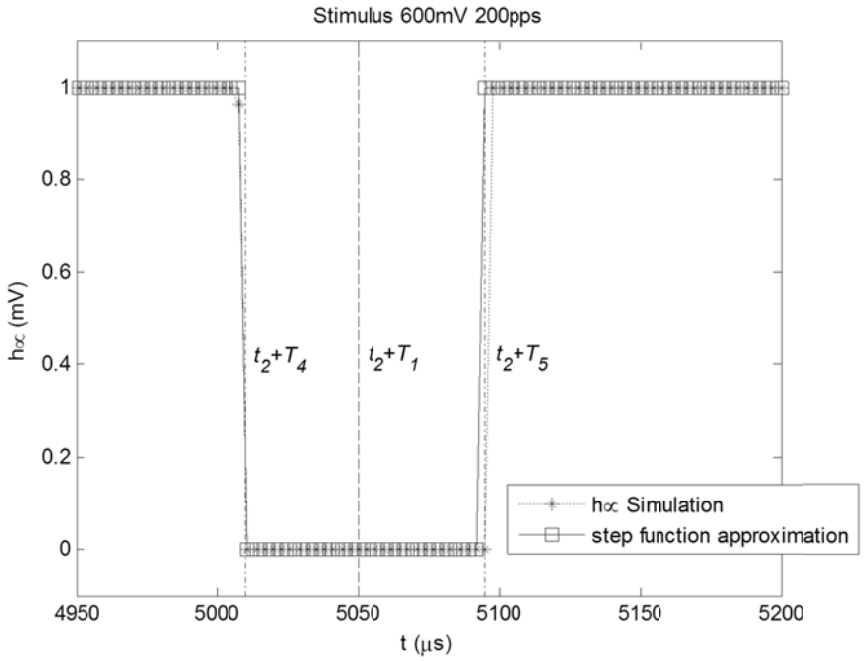

Figure 5-18 Step function approximation of h_∞ to the second pulse

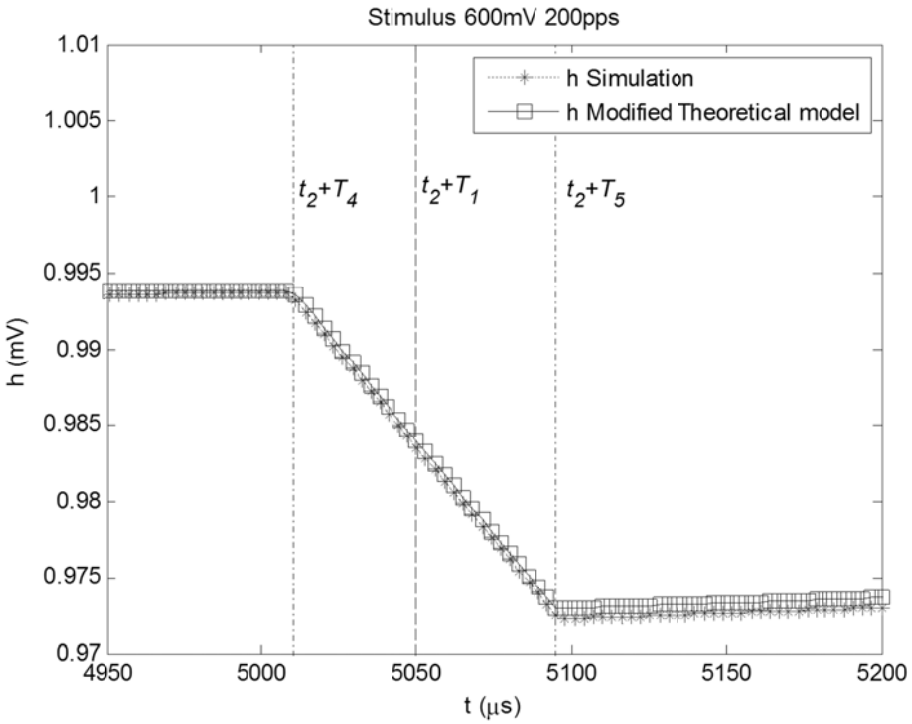

Figure 5-19 Response of $h(t)$ in the modified LIFDT model to the second pulse

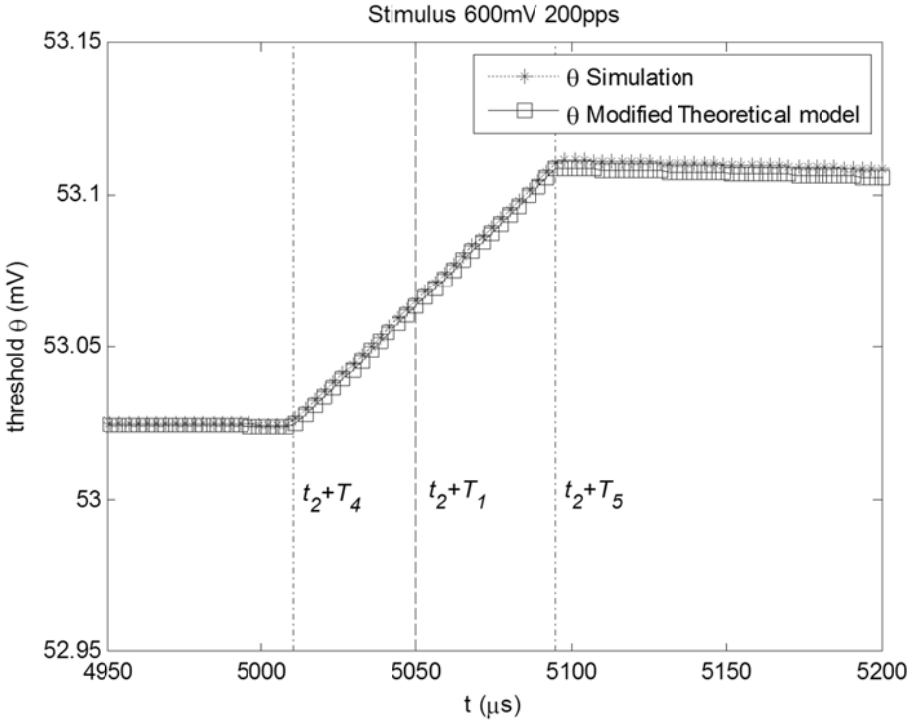

Figure 5-20 Response of $\theta(t)$ in the modified LIFDT model to the second pulse

Predictions by Eq.(4.5.18) are plotted in Figure 5-19, and predictions of the threshold accordingly are plotted in Figure 5-20. Although prediction accuracy is

degraded by the approximated step function, the analytical results of the first pulse and the second pulse are consistent with the simulation results of the modified LIFDT model. The trends of the $\theta(t)$ curve remain like those of the original LIFDT model. Changes in $V(t)$ are about fifty times bigger than changes in $\theta(t)$. Thus firing still depends on whether the maximum amplitude of the membrane potential will cross the threshold for each pulse. For the first pulse, $V(T_1)$ is compared to $\theta(T_1)$. For the second pulse, $V(t_2+T_1)$ is compared to $\theta(t_2+T_1)$.

Second add the noise to the deterministic theoretical model. Based on previous analysis, the discharge probability of modified LIFDT model for the first pulse can still be expressed by Eq.(4.3.44) but with a different $\theta(T_1)$,

$$p(1) = \frac{1}{2}(1 + erf(\frac{V(T_1) - \theta(T_1)}{\sqrt{2}\sigma})) \tag{4.5.19}$$

where $V(T_1)$ is calculated by Eq.(4.3.41) and $\theta(T_1)$ is calculated as follows.

According to Eq.(4.5.15),

$$h(T_1) = e^{-(T_1 - T_4)/\tau_h} \tag{4.5.20}$$

$$\theta(T_1) = \frac{\theta_m}{h(T_1)^p} + \theta_0 \tag{4.5.21}$$

and the discharge probability of the modified LIFDT model for the second pulse can be expressed by Eq.(4.3.47) but with a different $\theta(t_2 + T_1)$,

$$p(2) = \frac{1}{2}(1 + erf\frac{V(t_2 + T_1) - \theta(t_2 + T_1)}{\sqrt{2}\sigma}) \tag{4.5.22}$$

where $V(t_2 + T_1)$ is calculated by Eq.(4.5.16) and $\theta(t_2 + T_1)$ is calculated as follows.

According to Eq.(4.5.18)

$$h(t_2 + T_1) = h(t_2) \cdot e^{-T_1/\tau_h} - e^{-T_1/\tau_h} + e^{-(T_1 - T_4)/\tau_h} \tag{4.5.23}$$

$$\theta(t_2 + T_1) = \frac{\theta_m}{h(t_2 + T_1)^p} + \theta_0 \tag{4.5.24}$$

5.4.2 Maximum accommodation effects in the modified LIFDT model with step function approximation

The function of h_∞ is altered by a step function to increase the difference between $h(t_2 + T_1)$ and $h(T_1)$. Then the theoretical expression of accommodation effects must change consequently. In the beginning of section 5.4, the difference in the firing probabilities is related to the interval of integration, L. According to Eq.(4.5.5), the interval L is affected by $\tau_m, h(T_1), h(T_1 + t_2), P$ and θ_m.

First, τ_m is fixed by fitting the neurophysiological data for the first pulse.

Second, the difference of $h(T_1)$ and $h(T_1 + t_2)$ should be enlarged. For the modified LIFDT model, Δh is calculated by taking Eq.(4.5.20) and Eq.(4.5.23) into Eq.(4.5.6),

$$\begin{aligned} \Delta h &= [1 - h(t_2)] \cdot e^{-T_1/\tau_h} \\ &= e^{-(t_2 + T_1 - T_5)/\tau_h} - e^{-(t_2 + T_1 - T_4)/\tau_h} \end{aligned} \tag{4.5.25}$$

Unlike Eq.(4.3.21), Δh in the modified LIDT model is not dependent on the stimulus amplitude, A. Δh of the modified LIFDT model, Eq.(4.5.25), is plotted

in Figure 5-21 compared with Δh of the original LIFDT model, Eq.(4.3.21). Figure 5-21(a) plots Δh for fixed $\tau_h(1.9\ ms)$ for different stimulus amplitudes, and Figure 5-21(b) plots Δh for fixed stimulus amplitude $(800\ mA)$ for different values of τ_h. The results of the original LIFDT model are presented in solid lines with circle markers and the results of the modified LIFDT model are presented in solid lines with square markers.

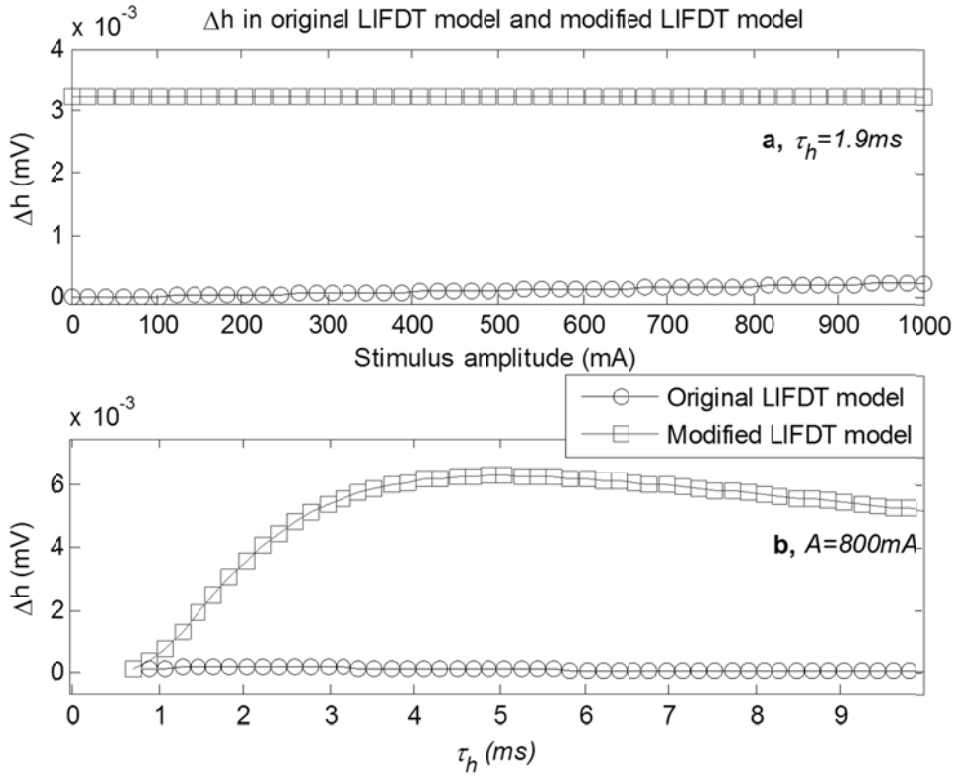

Figure 5-21 Comparing Δh in the original LIFDT model to the modified LIFDT model

In Figure 5-21(a), the modified LIFDT model has increased the value of Δh by ten times that of its original value. Figure 5-21(b) demonstrates that the maximum value of Δh is obtained when τ_h equals $5ms$. The obtained maximum value of Δh is twenty times larger than its original value. However, increasing the value of τ_h is actually extending the recovery time for h. Both refractory effects and accommodation effects are controlled by τ_h. For large τ_h, it also

takes more time for h to recover from zero after an action potential. Consequently, the refractory period may extend. To determine whether changing the value of τ_h provides a better fit to the neurophysiological data, predictions by two sets of parameter values are performed in the following part.

Third, the parameter P, power of h in Eq.(3.2.12), was chosen to be 1.3 from many fits of experimental data[19]. As the data in Chapter 3 are limited, here this value is preferred.

Fourth, L is a monotonically increasing function of the last variable, θ_m. In order to get the maximum value of the interval, L, θ_m is chosen by its maximum value. According to Eq.(3.2.12), θ_m varies in the interval $(0, \theta]$, where θ is dependent on the variable h. θ_m gets its maximum value, θ, when θ_0 is zero. Thus,

- $\theta_0 = 0$

Then θ_m can be calculated by Eq.(4.3.43), where $\theta(T_1)$ can be fitted by comparing the neurophysiological data for the first pulse to the analytical model Eq.(4.3.44).

Therefore, three sets of parameter values are generated in Table 5-3 to investigate the maximum accommodation effects in the LIFDT model: the values of D and τ_m are fitted in Chapter 4; P and τ_{abs} are taken from previous work [19]. For *Set A* and *Set B*, μ_∞ and σ_∞ are given by the analysis at the beginning of section 5.4, which change $h_\infty(V)$ into a step function. The differences between those two sets rely on the value of τ_h. In *set A*, the value of τ_h is taken from previous work. And in *set B*, the value of τ_h is optimized to approach the maximum Δh in Figure 5-21. For each set, the value of θ_m is fitted to the

neurophysiological data for the first pulse with given value of τ_h. In order to investigate the impact of the maximum θ_m and the minimum θ_0, *set C* is generated for comparison. In *set C*, all the parameter values remain the same as Table 5-1 except for θ_m and θ_0. The value set of Table 5-1 is denoted as the Original Set.

Table 5-3 Fitted parameter values of the modified LIFDT model to the I/O curve for the first pulse

	$\tau_h(ms)$	μ_∞ (mV)	σ_∞ (mV)	θ_m (mV)
Set A	1.9	8	0.1	31.70
Set B	5.0	8	0.1	32.25
Set C	1.9	-4.5	100	12.8

Other parameter values are $D = 0.0028$, $p = 1.3$, $\tau_m = 0.7[ms]$, $\theta_0 = 0[mV]$ and $\tau_{abs} = 0.284[ms]$.

With parameter values in Table 5-3, predictions are made by the theoretical model of a pulse-train response for *Set A* and *Set B* (Eq.(4.5.19) and Eq.(4.5.22)) in Figure 5-22. In Figure 5-22, predictions for the first pulse made by value *Set A* and *Set B* are both consistent with the neurophysiological data. We are interested in the predictions for the second pulse. Predictions made by the original value of the LIFDT model for the second pulse are almost identical to the predictions for the first pulse (shown in Figure 5-9).

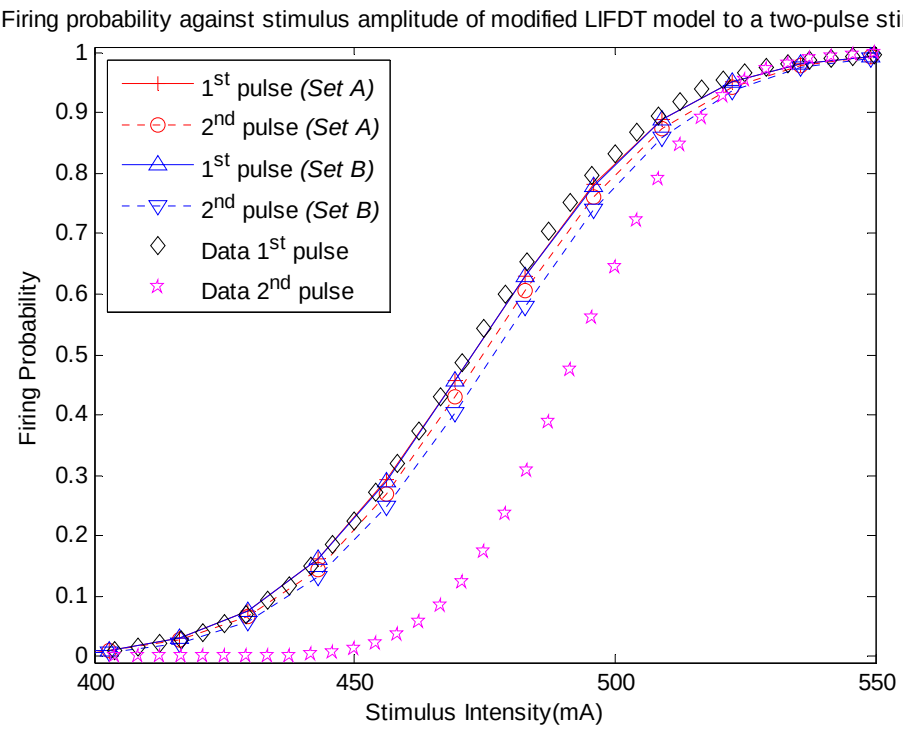

Figure 5-22 I/O curves to a two-pulse stimulus by the theoretical version of the modified LIFDT model. The solid line with plus sign markers represents the predictions by the theoretical model for the first pulse Eq.(4.5.19) with parameter values of *set A*. The dotted line with circle markers represents the theoretical model for the second pulse Eq.(4.5.22) with parameter values of *set A*. The solid line with Upward-pointing triangle markers represents the predictions by the theoretical model for the first pulse Eq.(4.5.19) with parameter values of *set B*. The dotted line with Upward-pointing triangle markers represents the theoretical model for the second pulse Eq. (4.5.22) with parameter values of *set B*. The experimental data[16] for the first pulse are presented in diamond markers. And the experimental data for the second pulse are presented in pentagram markers.

For the value *Set A*, which has increased Δh by ten times, firing probabilities for the second pulse are suppressed by 6.9% on average compared to the firing probabilities for the first pulse. For the value *Set B*, which has increased Δh by twenty times, firing probabilities for the second pulse are suppressed by 12.3% on average compared to the firing probabilities for the first pulse. However, neither *Set A* nor *Set B* can capture the experimental data, in which the firing probabilities for the second pulse were suppressed by 47.17% on average.

On the other hand, the theoretical model (Eq.(4.5.19) and Eq.(4.5.22)) only concerns accommodation effects in interpulse interactions. For high stimulus intensity, predictions made by the theoretical model will overestimate the firing probabilities for the second pulse. The accuracy of the analytical approximation of the LIFDT model has been demonstrated in section 5.3. To test the accuracy of the analytical approximation of the modified LIFDT (section 5.4.1), the modified LIFDT model was executed ten thousand times for parameter value from *Set A* and *Set B*, but with different noise each time. Simulations of data *Set C* and the *Original Set* are also conducted in order to compare the influence on the neural responses by each parameter. Both theoretical predictions and simulations results are presented for those four data sets in Figure 5-23 and Figure 5-24.

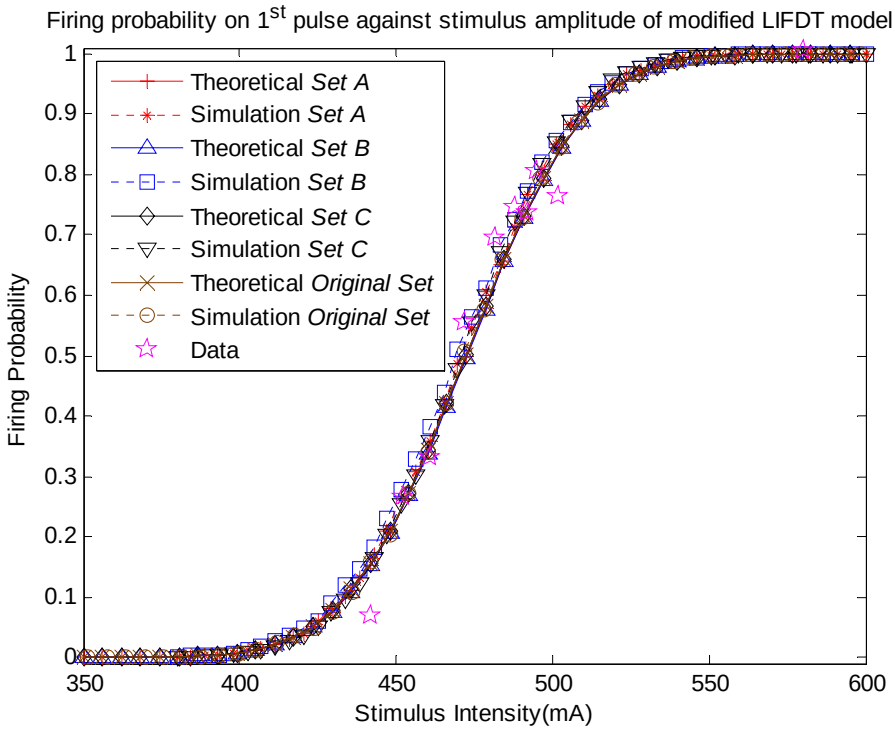

Figure 5-23 I/O curves of the modified LIFDT model to 1st pulse of a two-pulse stimulus. For *Set A*, the solid line with plus sign markers represents the predictions by the theoretical model Eq.(4.5.19); the dotted line with asterisk markers represents the simulation results.

For *Set B*, the solid line with upward-pointing triangle markers represents the predictions by the theoretical model Eq.(4.5.19); the dotted line with square markers represents the simulation results. For *Set C*, the solid line with diamond markers represents the predictions by the theoretical model Eq.(4.3.45); the dotted line with downward-pointing triangle markers represents the simulation results. For *Original Set*, the solid line with cross markers represents the predictions by the theoretical model Eq.(4.3.45); the dotted line with circle markers represents the simulation results. The experimental data for the first pulse are presented in stars.

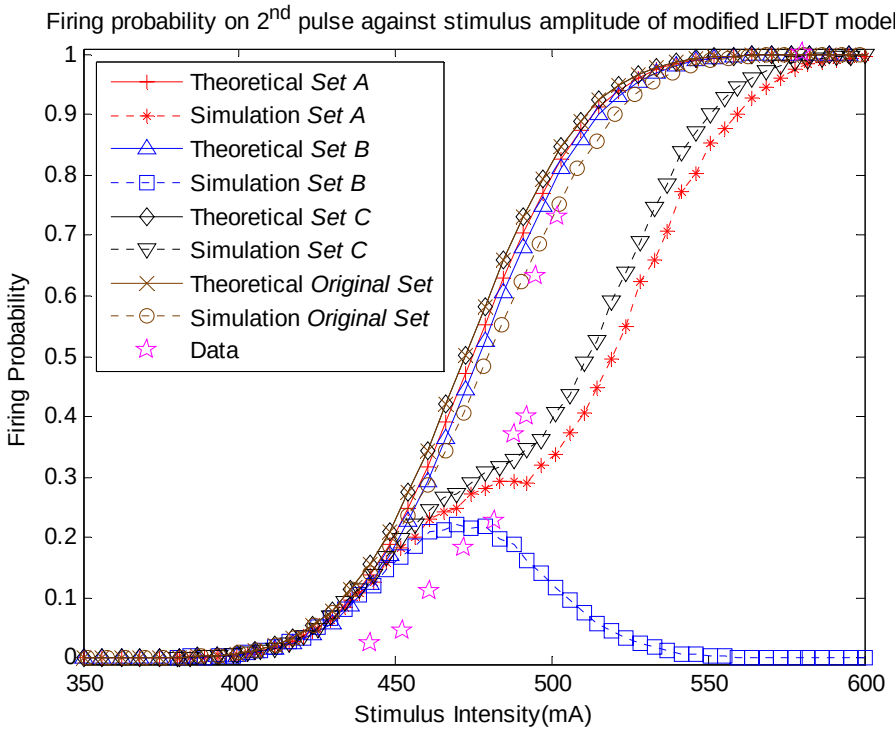

Figure 5-24 I/O curves of the modified LIFDT model to 2nd pulse of a two-pulse stimulus. For *Set A*, the solid line with plus sign markers represents the predictions by the theoretical model Eq.(4.5.22); the dotted line with asterisk markers represents the simulation results. For *Set B*, the solid line with upward-pointing triangle markers represents the predictions by the theoretical model Eq.(4.5.22); the dotted line with square markers represents the simulation results. For *Set C*, the solid line with diamond markers represents the predictions by the theoretical model Eq.(4.3.47); the dotted line with downward-pointing triangle represents the simulation results. For *Original Set*, the solid line with cross markers represents the predictions by the theoretical model Eq.(4.3.45); the dotted line with circle markers represents the simulation results. The experimental data for the second pulse are presented in stars.

The results for the first pulse (in Figure 5-23) show consistent firing probabilities between theoretical predictions and simulation results for all data sets. The

theoretical model (Eq.(4.5.19)) accurately predicts the neural responses of the modified LIFDT model to the first pulse.

For the second pulse (in Figure 5-24), the theoretical model (Eq.(4.5.22)) accurately predicts the slope over lower stimulus amplitudes ($A < 450mA$) for *Set A*, *Set B* and *Set C*. This indicates that Eq.(4.5.22) successfully predicts accommodation effects in the modified LIFDT model. However, it does not predict a suppressed trend in the simulation results over higher stimulus amplitudes ($A > 480mA$).

Refractory effects constitute the difference between the theoretical predictions and the simulation results. Specifically, for *Set A* and *Set C*, the simulation results demonstrate that firing probabilities are suppressed due to refractory effects for stimulus amplitudes between 450 *mA* and 580 *mA*. For *Set B*, refractory effects inhibit firing even further so that the neuron rarely fires for stimulus amplitudes between 500 *mA* and 600 *mA*.

Moreover, it suggests that refractory effects can be quantified by comparing the theoretical predictions and simulation results. Then the differences of firing probabilities between the first pulse and the second pulse can be divided into two categories; one is caused by accommodation effects, another one is caused by refractory effects. Those caused by accommodation effects, denoted as Δp_{acc}, can be calculated theoretically by

$$\Delta p_{acc} = p(1) - p(2) \tag{4.5.26}$$

where $p(1)$ is the prediction of firing for the first pulse by theoretical model Eq.(4.5.19) and $p(2)$ is the prediction of firing for the second pulse by

theoretical model Eq.(4.5.22) or Eq.(4.3.47). Those firing differences caused by refractory effects, denoted as Δp_{ref}, can be calculated by

$$\Delta p_{ref} = p(2) - \bar{p}(2) \tag{4.5.27}$$

where $\bar{p}(2)$ is the simulation result for the second pulse. By this approach, we can investigate refractory effects and accommodation effects separately. The results of Δp_{acc} and Δp_{ref} for all the data sets are plotted in Figure 5-25 and Figure 5-26. The differences of firing probabilities observed from neurophysiological data are also plotted for comparison, which were caused by both accommodation effects and refractory effects.

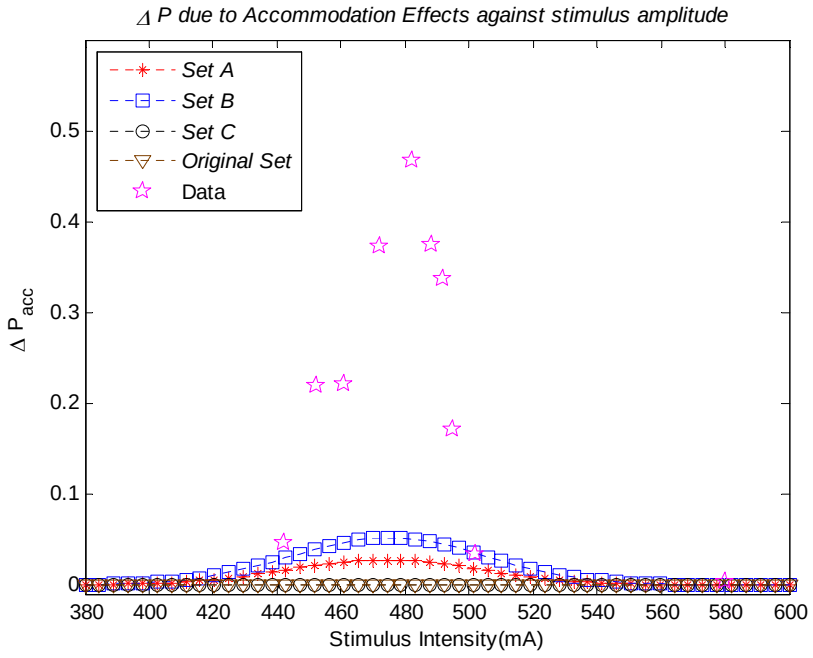

Figure 5-25 ΔP due to accommodation effects against stimulus amplitude. The dotted line with asterisk markers represents the result of Set A. The dotted line with square markers represents the result of Set B. The dotted line with circle markers represents the result of Set C. The dotted line with downward-pointing triangle markers represents the result of Original Set. The stars represent Δp observed from neurophysiological data.

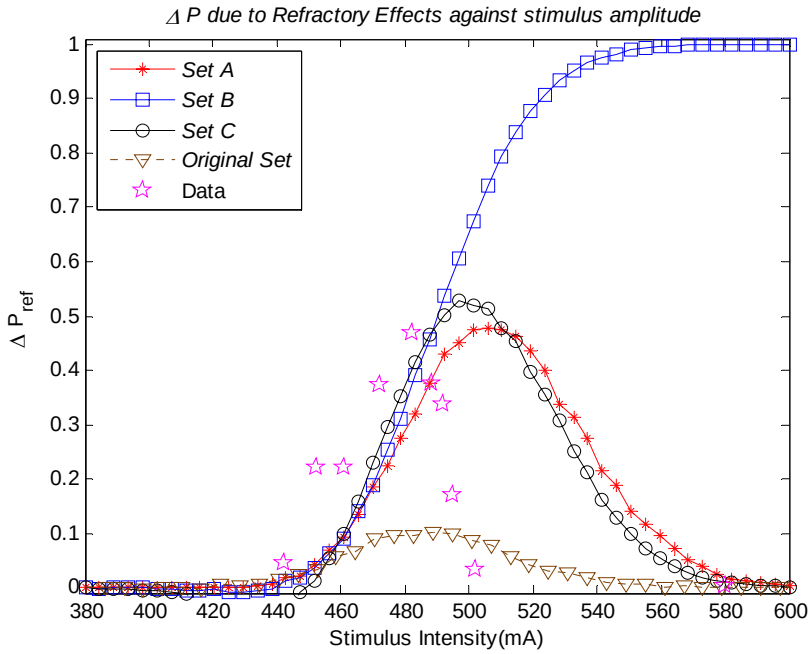

Figure 5-26 ΔP due to refractory effects against stimulus amplitude. The solid line with asterisk markers represents the result of Set A. The solid line with square markers represents the result of Set B. The solid line with circle markers represents the result of Set C. The solid line with downward-pointing triangle markers represents the result of Original Set. The stars represent Δp observed from neurophysiological data.

According to Figure 5-23, Figure 5-24, Figure 5-25 and Figure 5-26, the parameter selections have different impacts on the I/O curves and interpulse interactions.

The base value of the threshold, θ_0; and the threshold multiplier, θ_m: The parameter choice ($\theta_0 = 0$) is intended to calculate the maximum value of Δp_{acc} in conjunction with the modified function of $h_\infty(V)$. To investigate the impact of θ_0 and θ_m solely, we compare the results of *Set C* and the *Original Set*. In Figure 5-25, Δp_{acc} of *Set C* are almost zero like the results of the *Original Set*. But in Figure 5-26, Δp_{ref} of *Set C* are up to five times bigger than the results of *Original Set*. It indicates that increasing θ_m does not significantly improve accommodation effects; however, it makes a great impact on the firing

probabilities due to refractory effects. According to section 3.3.1, the absolute refractoriness in the LIFDT model is achieved by resetting h to zero, which instantaneously sets θ to infinity. Then the integration of h continues. Thus the larger the value of θ_m, the longer it takes for θ to approximate its steady state after an action potential. This may in part explain why the parameter P is fixed. Any small change in P or θ_m in order to increase accommodation effects will lead to greater refractory effects.

The offset for h_∞, μ_∞; and the standard deviation of h_∞, σ_∞: These two parameters control the shape of the function $h_\infty(V)$. The parameter choice in this section ($\mu_\infty = 8\,mV, \sigma_\infty = 0.1$) is intended to calculate the maximum value of Δh in conjunction with setting θ_0 to zero. To investigate the impact of μ_∞ and σ_∞, we compare the results of *Set A* and *Set C*. The theoretical predictions of the firing probabilities for the second pulse of *Set A* are 6.9% less than the predictions of *Set C* on average. The simulation results of *Set A* are consistent with the theoretical predictions for lower stimulus amplitudes ($A < 450mA$). It demonstrates that the modified function of $h_\infty(V)$ can improve the predictions of the firing probabilities for the second pulse for lower stimulus amplitudes ($A < 450mA$), but it is still above the slope of the neurophysiological data. For higher stimulus amplitudes ($A > 450mA$), firing probabilities for *Set A* and *Set C* are both under the slope of the neurophysiological data. Specifically, *Set A* increases Δp_{acc} up to 0.03 for stimulus amplitudes from $400mA$ to $550mA$. At the mean time, Δp_{ref} of *Set A* is about the same size of *Set C*. It indicates that the modified $h_\infty(V)$ can improve accommodation effects without adding extra refractory effects. As the aim of this section is to achieve the maximum

accommodation effects, refractory effects are not relevant in the parameter selection.

The recovery time-constant for h, τ_h: the effects of τ_h on Δh for the modified LIFDT model under subthreshold stimulus has been studied in Figure 5-21. And *Set B* is generated consequently to achieve the maximum Δh. To investigate the impact of τ_h, we compare the results of *Set A* and *Set B*. In Figure 5-24, *Set B* improves the theoretical predictions. However, the simulation results of *Set B* show that increasing the value of τ_h greatly influences the I/O curve. Specifically, Figure 5-25 shows that increasing the value of τ_h successfully enlarges Δp_{acc}. It reaches the first point of the neurophysiological data, but is still an order of magnitude lower than the following points of the neurophysiological data. Meanwhile Figure 5-26 shows that increasing τ_h also results in a large Δp_{ref}. As increasing τ_h actually slows down the permeability variable h, it takes more time for h to recover after an action potential rather than after a subthreshold stimulus. It suggests that the parameter choice of τ_h in *Set B* is not appropriate as refractory effects overwhelm the neural responses. However, this experiment is aimed at exploring the maximum Δp_{acc}, τ_h is only optimised for accommodation effects. The optimised τ_h improves the results of Δp_{acc} for lower stimulus amplitudes ($A < 440mA$), but does not change the slope of Δp_{acc} for stimulus amplitudes between $440mA$ and $460mA$, where the average firing probabilities are still under 0.2. Refraction contributes little to the response for such low stimulus amplitudes. Thus the overall I/O curve of *Set B* still cannot predict the neurophysiological data.

Given the above results, the LIFDT model cannot predict the neurophysiological data since:

1) By the initial assessment of the neurophysiological data, the LIFDT model cannot predict the data due to the strong accommodation effects. Accommodation effects in the LIFDT model are theoretically expressed by Eq.(4.5.4). In *Set B,* each parameter is optimised to achieve the maximum accommodation effects. Accommodation effects are effectively improved but are still smaller than the neurophysiological data, as in Figure 5-25.
2) Full optimization is not performed due to complexity. Alternative parameter selection may result in a better prediction, but none of the parameter selections can capture the strong accommodation effects in the neurophysiological data.

5.5 Conclusion

In this chapter, analytical descriptions have been developed of single-fibre responses to single-pulse and pulse-train (concerns accommodation effects only) stimuli. For single-pulse stimuli, it provides a computationally efficient method of simulating an auditory neuron. It predicts an almost accurate neural response without multiple iterations. For pulse-train stimuli, it quantifies firing probabilities due to accommodation effects. However, the analytical description of refractory effects was not investigated in this chapter. It cannot be directly used to derive a full neural response to pulse-train stimuli. Monte Carlo simulations of the LIFDT model can estimate the neural response instead. In addition, comparing the simulation results and analytical predictions provides an

approximation of firing probabilities due to refractory effects. In this way refractory effects and accommodation effects can be estimated separately. It improves the understanding of interpulse interactions, especially the accommodation effects.

The analytical approximation of the LIFDT model is derived based on several approximations and simplifications. For different parameter selections of σ_∞ and μ_∞, the simplification of the function $h_\infty(V)$ varies. In addition, the analytical approximation of the modified LIFDT model (section 5.4.1) is developed according to the pulse-train stimulus (presented in Figure 5-7). Application of this analytical model to other electrical stimulation should change accordingly.

With knowledge of how parameter selection influences the interpulse interactions, this chapter obtains the maximum accommodation effects in the LIFDT model. Although the parameter choice is not physiologically realistic, the LIFDT model still cannot predict the neurophysiological data. This may be due to:

- In Frankenhaeuser and Huxley model, τ_h is a Gaussian shape function of V with six parameters. The LIFDT model simplified the variable τ_h as a constant. This may degrad the dynamics.
- The LIFDT model ignores contributions from the potassium currents. The threshold is only related to the inactivation of sodium permeability, h. The time constant of h regulates both the accommodative mechanism and the refractory mechanism. The results of parameter selection demonstrate that a small change in Δp_{acc} will lead to great change in Δp_{ref}. On the contrary, the

neurophysiological data presented strong Δp_{acc} and relatively "normal" Δp_{ref}. The accommodation likely results from another voltage-dependent ionic channel. Hill [7] reviewed the excitation and accommodation in nerve fibres and suggested that accommodation is largely affected by the Ca-ion concentration. Sly *et al*. [17] suggested that the accommodation in auditory nerve might relate to a hyperpolarization-activated cation channel or a potassium channel.

- The analytical approximation of a pulse-train response is derived on the assumption that the standard deviation of noise remains constant. However, it is suggested that the variance of noise may increase with small, sustained depolarizations [120]. Paradoxically, the analysis in Chapter 4, Table 4-2 predicted just the opposite. It is suggested that both accommodation effects and refractory effects can influence the variance of noise.

To improve the LIFDT model, it requires a more thorough investigation of the behaviour of ionic channels during depolarizations that do not excite the auditory nerve. Improvement of the LIFDT model is possible by adding extra two or three parameters. This will make the LIFDT model contain more than ten parameters. Optimization of the new model will be more laborious unless more data are obtained. For large population of neurons, it will be more computationally expensive. In order to analyse accommodation in the limited neurophysiological data, a renewal process model using Markov Chains is applied in the next chapter.

Chapter6. *Markov Statistical Model*

6.1 Introduction

In the previous chapter, a theoretical analysis of the LIFDT model was given and efforts have been made in predicting a set of the neurophysiological data. However, the existing LIFDT model cannot capture the strong accommodation effects in the data because the time constant of h regulates both the accommodative mechanism and the refractory mechanism. Adding extra parameters and equations for the accommodative mechanism will make it more complicated for optimization but could be considered once the dynamics of the accommodation effects are better understood.

Another modelling approach is to utilize a statistical model to analyse the interpulse interactions in the neurophysiological data. Markov processes are widely used to model the spike activity in a peripheral auditory nerve fibre [121, 122], especially incorporating the refractory effects [45, 46, 69, 123, 124]. The statistical models usually study the time patterns of occurrences of the spikes, not the exact kinetics of ion channels. Therefore, statistical models have fewer parameters and require less data than conductance-based models. As there are only ten histograms of the neurophysiological data, it is more perhaps convenient to investigate the statistical characterization of the accommodation effects first and then refine the accommodation mechanism in the LIFDT model.

In studies of the spike activity of auditory nerve fibres, two statistics frequently used are the PST histograms and ISIH [27]. Poisson point processes, which are special cases of Markov processes, have been used to accurately model the ISIH of a single neuron to acoustic stimuli [125]. The Poisson process is a memoryless

process; however, neural responses are actually affected by their prior history. In order to incorporate the refractory effects, Poisson processes with dead-time have been developed [61, 63, 64, 126]. Miller *et al*. [45] argued that statistics measured experimentally had non-Poisson nature and a Markov process model predicted a better result than a Poisson process model. Markov renewal processes are frequently used to model the refractory effects of neural responses [46, 51, 58, 69, 70, 123, 124]. A Markov renewal process is a Markov process which has independent identically distributed inter-event times [122]. Unlike a Poisson process, the interval time in a renewal process takes on a more general distribution. Irlicht *et al*. [123] developed a self-exciting point process model and derived a closed-form solution for steady state neural responses for both acoustic stimulation and electric stimulation. Bruce *et al*. [51] developed a stochastic renewal process model and also derived a closed-form solution of steady state neural responses for electric stimulation. Those two models only studied the long term properties of neural responses. Xu *et al*. [69] developed a Markov renewal process model and provided the statistics associated with the neural response to each pulse. All the above models utilized a Markov chain to represent the refractory effects and the transition probabilities in the Markov chain were calculated according to a refractory function (a step-shaped function in [123], an exponential function in [46, 69]). None of the above models considered the accommodation effects and assumed that the firing probabilities are identical between pulses when no discharge occurred in previous firing history. Clearly this is not the case if accommodation effects are important because even subthreshold stimuli can change the firing probabilities.

The analysis in Chapter4 and Chapter 5 show that the accommodation effects is a much stronger factor than the refractory effects for low FE. Therefore, the aim of this chapter is to develop a Markov renewal process incorporating both the refractory effects and the accommodation effects.

Normally the refractory function is derived by modelling the ISIH which describes the time between consecutive discharges [27, 46, 58, 69]. For a renewal process, the interval distribution is referred to as the hazard function $\phi(k)$ where k is the length of the time interval since the last discharge and ϕ is the conditional probability. In this thesis, the neurophysiological data are only presented in the form of PST histogram and hence the refractory function cannot be developed directly. In Chapter 5, the LIFDT model failed to capture the strong accommodation effects in the neurophysiological data. As both accommodation and refractory mechanisms have an effects on the firing probability, the accuracy of refractory effects in the LIFDT model is uncertain. Consequently, we cannot derive a hazard function from the LIFDT model. For the accommodation effects, it is the same case.

Thus in this chapter we apply a conditional probability analysis [58] to the neurophysiological data and investigate the conditional probability distribution in the data. The conditional probability is actually the transition probability in the Markov Chain. The calculations involve estimates of the conditional probability of a firing for a specified pulse given that last firing occurred for some earlier pulse and the conditional probability of a firing for a specified pulse given that there is no firing for all previous pulses. Thus, it separates the accommodation effects and refractory effects and facilitates a direct comparison between those two interpulse interactions.

A general Markov process is outlined in section 6.2. A renewal method is applied to track the neural response using the conditional probability analysis. With the use of a stationary assumption, the general Markov model can be simplified to a linear system. Least-squares fitting is applied to the stationary Markov models in section 6.3. However, the results in section 6.4 demonstrate that the stationary Markov models can only fit the increments of the data because the conditional probability changes by pulse number. To take this time dependent effects into account a full non-stationary Markov model is presented in section 6.5. The non-stationary Markov model is fitted to the neurophysiological data by a trust-region dogleg algorithm in section 6.6. Results are presented in section 6.7. Finally discussion and conclusions are drawn in section 6.8.

6.2 A general Markov renewal process model

The neurophysiological data are presented in the form of a PST Histogram (Figure 3-15 and Figure 3-16), where histograms are displayed by pulse number instead of time. Within each pulse, spikes are summed from the start of the cathodic phase to the end of the anodic phase. As the duration of the biphasic pulse is short (50 μs for each phase), the neuron can only fire once per pulse at most. In other words, within each pulse there are only two states for a single neuron: “fire” or “not fire”. Therefore, the neural response qualifies as a discrete point process. Also this discrete point process qualifies as a renewal process, because after a firing the auditory nerve enters the refractory period and it has no “memory” of prior firings.

We derive a Markov renewal process model on the basis of a conditional probability analysis [58]. The conditional probability analysis has previously

only been applied to study the refractory effects by estimating the conditional probability of a firing in a specified time interval given that the last firing occurred during an earlier specified time interval. To incorporate the accommodation effects, we introduce the conditional probability of a firing in a specified time interval given no firing previously. Before we specify all the conditional probabilities, we first introduce the general Markov renewal process model.

As the data obtained are presented in the form of a PST Histogram rather than an ISIH, we describe the general Markov renewal process model in Table 6-1 rather than a Markov Chain. It facilitates the calculation of the firing probability at each pulse. Table 6-1 represents all the possible neural responses to an n-pulse stimulus given that it fires at the n'th pulse and only one firing has previously occured. Firing is denoted as "1" and not firing is denoted as "0".

Pulse Num	*1*	*2*	*…*	*n-3*	*n-2*	*n-1*	*n*
Firing Status						1	1
					1	0	1
				1	0	0	1
			…	…	…	…	…
		1	…	0	0	0	1
	1	0	…	0	0	0	1
	0	0	…	0	0	0	1

Table 6-1 The relationship between firing at the *n*'th pulse to the firing status of previous pulses. Each row shows one possible combination of neural responses. The table shows all permitted histories.

Each row presents one possible neural response. According to the renewal process, when a neuron fires, the membrane potential is reset to its resting potential. In other words, the 'neural memory' of history before firing is lost, and only the history after the last firing influence the current state of a neuron. In order to calculate the firing probability for the n'th pulse (the current pulse), we

only trace the firing history back to when it last fired. For example, if the neuron has fired at the *n-1*'th pulse, all the history from the 1st pulse to the *n*-2′th pulse is neglected.

Assume at each stimulus level, that the discharge rate ω_n is the probability that the neuron fires at the *n*'th pulse, i.e. $\omega_n \in [0, 1]$.

The probability of firing at the *n*'th pulse can be obtained by summing over all permitted histories in Table 6-1 as,

$$\omega_n = \sum_{H_{n-1}} P(n \mid H_{n-1}) f(H_{n-1}) \tag{6.2.1}$$

$$H_{n-1} = \{s_1, s_2, s_3, \ldots, s_{n-1}\} \qquad s_i \in \{0,1\} \qquad n \in [2,20]$$

where n is the pulse number, H_{n-1} is the history of status of the neuron from the 1st pulse to the *n*-1'th pulse, the neuron status at the *i*'th pulse is either "0" or "1", $P(n|H_{n-1})$ is the conditional probability of firing at the *n*'th pulse given previous history H_{n-1} , $f(H_{n-1})$ is the probability of the sequence H_{n-1} occurring.

Two types of conditional probabilities are involved in Eq.(6.2.1). One is the history that the neuron never fired until the *n*'th pulse, as stated in the last row in Table 6-1. This conditional probability will be dominated by the accommodation effects. Another is given the history that the neuron fired at a specified pulse and fires again at the *n*'th pulse. This conditional probability, [58], is dominated by refractory effects. Thus, estimating the conditional probabilities by this Markov renewal process model provides direct measure of the interpulse interactions.

In principle, the firing probability is dependent on the whole firing history. However, the analysis in Chapter 4 suggests otherwise. Figure 4-3 showed that

only the I/O curve of the first pulse is substantially different from those of subsequent pulses. I/O curves for the subsequent pulses are very close and many overlapped. This implies that although the firing probability varies in response to changes in stimulus amplitudes, it will converge to a stable state around 10 ms to 20 ms after the onset of the pulse sequence. The investigation of the refractory effects in the auditory nerve also demonstrates that the hazard function levels-off at a constant value after 20-25 ms [27, 58]. Also the investigation of the accommodation effects (also referred as the excitatory interpulse effects) observed from the auditory nerve of cats generally lasts for 0.5 ms [127]. Thus the general Markov renewal process model Eq.(6.2.1) can be simplified to a Markov model of lower order of approximately third order. In other words, the future firing status only depends on the firing probabilities of previous three pulses. It is not clear what order of the Markov model is sufficient to repredict the neurophysiological data. The following sections make a series of approximations and reduce the general Markov model to first order, second order and third order. Additionally, all the simplified Markov models are linear models, which facilitates the fitting of the data using a least-squares algorithm.

6.2.1 A stationary first order Markov model

First, assume only the last pulse influences the firing status at the current pulse, which is a simple way to start with the general model. In this case the firing probability resulting from the current pulse is only affected by whether or not it fires at previous pulse.

All the possible combinations of firing at the *n*'th pulse due to the *n-1'*th pulse are presented in Table 6-2. The probability of firing at the *n*'th pulse on the condition of firing at the *n-1*'th pulse is denoted as $P(n|1)$. The probability of

firing at the *n*'th pulse on the condition of not firing at the *n-1*'th pulse is denoted as $P(n|0)$.

Table 6-2 Firing status of the first order Markov model (discharge at the *n*'th pulse)

			Conditional Probability
Pulse Num	*n-1*	*n*	
Status	0	1	$P(2\|0)$
	1	1	$P(2\|1)$

However, these conditional probabilities are independent of pulse number because, in a renewal process, the conditional probability is only dependent on the interval between two consecutive discharges and does not therefore depend on the pulse number directly. Therefore, in general, we can denote $P(n|1)$ as $P(2|1)$ where the '2' denotes that we are considering the pulse after the *n-1'*th *(*in some sense this is pulse '2' in a sequence of two pulses).In otherwords we are assuming that the firing probabilities are stationary.

As it assumes that only previous two firing status affect ω_n, earlier status is ignored, e.g. the *n-2'*th status. The assumption implies neither the accommodation effects nor the refractory effects last for two-pulse intervals. In other words, if $s_{n-1} = 0$, whether the neuron fired or not at the *n-2'*th pulse, it somehow "recovers" to a steady state and starts a new memory at the *n-1'*th pulse. Thus to be consistent with the first assumption, we assume that the conditional probability $P(2|0)$ is constant regardless of the pulse number.

Then Eq.(6.2.1) can be simply written as a first order Markov model,

$$\omega_n = P(2\,|\,1)\cdot f(\{s_{n-1}=1\}) + P(2\,|\,0)\cdot f(\{s_{n-1}=0\}) \qquad (6.2.2)$$

where $f(\{s_{n-1}=1\})$ represents the firing probability at the *n*-1'th pulse, $f(\{s_{n-1}=0\})$ represents the probability of not firing at the *n*-1'th pulse. That is,

$$f(\{s_{n-1}=1\})=\omega_{n-1} \tag{6.2.3}$$

$$f(\{s_{n-1}=0\})=1-\omega_{n-1} \tag{6.2.4}$$

Therefore Eq.(6.2.2) can be re-written as,

$$\omega_n = P(2\,|\,1)\cdot\omega_{n-1} + P(2\,|\,0)\cdot(1-\omega_{n-1}) \tag{6.2.5}$$

Rearranging Eq.(6.2.5) gives,

$$\omega_n = \left[P(2\,|\,1)-P(2\,|\,0)\right]\cdot\omega_{n-1} + P(2\,|\,0) \tag{6.2.6}$$

Thus the first order Markov model is actually a linear difference equation of the firing probability ω_n as,

$$\omega_n = \alpha_1\cdot\omega_{n-1} + k \qquad n\in[2,20] \tag{6.2.7}$$

where

$$\alpha_1 = P(2\,|\,1)-P(2\,|\,0) \tag{6.2.8}$$

$$k = P(2\,|\,0) \tag{6.2.9}$$

6.2.2 A stationary second order Markov model

The first order Markov model is developed mainly on the assumption that the current neuron status is only dependent on the last status. As stated in section 6.2.1, it means that both the refractory effects and the accommodation effects last for 5 ms at most. However, based on the I/O curve analysis in Chapter 4 the refractory period may have a longer duration. Therefore, we derive a second

order Markov model which accounts for a 10 ms-history. The procedure is similar to that of the first order Markov model.

In this case, first we assume that the firing probability for the *n*'th pulse is affected by the spiking status of the *n-1*'th and *n-2*'th pulse. All the possible combinations of firing at the *n*'th pulse are listed in Table 6-3.

Table 6-3 Firing status of the second order Markov model (discharge at the *n*'th pulse)

				Conditional Probability
Pulse Num	n-2	n-1	n	
Status	0	0	1	P(3|0,0)
	1	0	1	P(3|1,0)
		1	1	P(2|1)

Second, the conditional probabilities $P(3|1,0)$and $P(2|1)$ are fixed in a renewal process and the '3' denotes the last of a sequence of three pulses. Third, $P(3|0,0)$ is assumed to be stationary. ω_n is calculated by summing all the permitted histories in Table 6-3. Then the general equation Eq.(6.2.1) can be written as,

$$\begin{aligned}\omega_n &= P(3\,|\,0,0)\cdot f\{H(s_{n-2}=0, s_{n-1}=0)\} \\ &+P(3\,|\,1,0)\cdot f\{H(s_{n-2}=1, s_{n-1}=0)\} + P(2\,|\,1)\cdot f\{H(s_{n-1}=1)\}\end{aligned} \tag{6.2.10}$$

where

$$f\{H(s_{n-2}=1, s_{n-1}=0)\} = \omega_{n-2}\cdot(1-P(2\,|\,1)) \tag{6.2.11}$$

As Table 6-3 lists all the possible histories,

$$\sum_{H_{n-1}} f(H_{n-1}) = 1 \tag{6.2.12}$$

Substituting Eq.(6.2.3), Eq.(6.2.11) into Eq.(6.2.12),

$$f\{H(s_{n-2}=0,s_{n-1}=0)\}=1-f\{H(s_{n-2}=1,s_{n-1}=0)\}-f\{H(s_{n-1}=1)\}$$
$$=1-\omega_{n-2}\cdot(1-P(2\,|\,1))-\omega_{n-1}$$

(6.2.13)

Substituting Eq.(6.2.3), Eq.(6.2.11) and Eq.(6.2.13) into Eq.(6.2.10) gives,

$$\omega_n=P(3\,|\,0,0)\cdot\left[1-\omega_{n-1}-\omega_{n-2}\cdot(1-P(2\,|\,1))\right]+P(3\,|\,1,0)\cdot\omega_{n-2}\cdot(1-P(2\,|\,1))+P(2\,|\,1)\cdot\omega_{n-1}$$
$$=\left[P(2\,|\,1)-P(3\,|\,0,0)\right]\cdot\omega_{n-1}+\left[P(3\,|\,1,0)-P(3\,|\,0,0)\right]\cdot\left[1-P(2\,|\,1)\right]\cdot\omega_{n-2}+P(3\,|\,0,0)$$

(6.2.14)

The second Markov model is also a linear difference equation of the firing probability ω_n,

$$\omega_n=\alpha_1\cdot\omega_{n-1}+\alpha_2\cdot\omega_{n-2}+k \qquad n\in[3,20] \tag{6.2.15}$$

where,

$$\alpha_1=P(2\,|\,1)-P(3\,|\,0,0) \tag{6.2.16}$$

$$\alpha_2=\left[P(3\,|\,1,0)-P(3\,|\,0,0)\right]\cdot\left[1-P(2\,|\,1)\right] \tag{6.2.17}$$

$$k=P(3\,|\,0,0) \tag{6.2.18}$$

6.2.3 A stationary third order Markov model

Now we have a Markov model that has a 10 ms history. It is not clear whether it is sufficient for the neurophysiological data so we developed a third order Markov model, which accounts for a 15 ms history. The procedure is similar to that of the first and second order Markov model.

In this case, first we assume that the firing probability for the *n*'th pulse is affected by the spiking status of the *n-1*'th, *n-2*'th and *n-3*'th pulse. All the possible combinations of spiking at the *n*'th pulse are listed in Table 6-4.

Table 6-4 Firing status of the third order Markov model (discharge at the *n*'th pulse)

					Conditional Probability
Pulse Num	*n-3*	*n-2*	*n-1*	*n*	
Status	0	0	0	1	P(4|0,0,0)
	1	0	0	1	P(4|1,0,0)
		1	0	1	P(3|1,0)
			1	1	P(2|1)

Second, the conditional probabilities $P(4|1,0,0), P(3|1,0)$ and $P(2|1)$ are fixed in a renewal process. Third, $P(4|0,0,0)$ is assumed stationary. Then the general equation (6.2.1) can be written as

$$\begin{aligned}\omega_n = {} & P(4\,|\,0,0,0)\cdot f\{H(s_{n-3}=0,s_{n-2}=0,s_{n-1}=0)\}\\ & +P4\,|\,1,0,0)\cdot f\{H(s_{n-3}=1,s_{n-2}=0,s_{n-1}=0)\}\\ & +P(3\,|\,1,0)\cdot f\{H(s_{n-2}=1,s_{n-1}=0)\}\\ & +P(2\,|\,1)\cdot f\{H(s_{n-1}=1)\}\end{aligned} \tag{6.2.19}$$

The calculations of Eq.(6.2.3), Eq.(6.2.11), Eq.(6.2.13) remain the same. Additionally,

$$f\{H(s_{n-3}=1,s_{n-2}=0,s_{n-1}=0)\}=\omega_{n-3}\cdot\left[1-P(2\,|\,1)\right]\cdot\left[1-P(3\,|\,1,0)\right] \tag{6.2.20}$$

and

$$\begin{aligned}& f\{H(s_{n-3}=0,s_{n-2}=0,s_{n-1}=0)\}\\ & =1-f\{H(s_{n-3}=0,s_{n-2}=0,s_{n-1}=0)\}\\ & -f\{H(s_{n-2}=1,s_{n-1}=0)\}-f\{H(s_{n-1}=1)\}\end{aligned} \tag{6.2.21}$$

Substituting Eq.(6.2.3), Eq.(6.2.11), Eq.(6.2.13), Eq.(6.2.20) and Eq.(6.2.21) into Eq.(6.2.19) gives,

$$\begin{aligned}\omega_n = {} & \left[P(2\,|\,1)-P(4\,|\,0,0,0)\right]\cdot\omega_{n-1}+\left[P(3\,|\,1,0)-P(4\,|\,0,0,0)\right]\cdot\left[1-P(2\,|\,1)\right]\cdot\omega_{n-2}\\ & +\left[P(4\,|\,1,0,0)-P(4\,|\,0,0,0)\right]\cdot\left[1-P(2\,|\,1)\right]\cdot\left[1-P(3\,|\,1,0)\right]\cdot\omega_{n-3}+P(4\,|\,0,0,0)\end{aligned} \tag{6.2.22}$$

Therefore the third order Markov model is also a linear difference equation of the firing probability ω_n,

$$\omega_n = \alpha_1 \cdot \omega_{n-1} + \alpha_2 \cdot \omega_{n-2} + \alpha_3 \cdot \omega_{n-3} + k \qquad n \in [4,20] \quad (6.2.23)$$

where

$$\alpha_1 = P(2\,|\,1) - P(4\,|\,0,0,0) \quad (6.2.24)$$

$$\alpha_2 = \left[P(3\,|\,1,0) - P(4\,|\,0,0,0)\right] \cdot \left[1 - P(2\,|\,1)\right] \quad (6.2.25)$$

$$\alpha_3 = \left[P(4\,|\,1,0,0) - P(4\,|\,0,0,0)\right] \cdot \left[1 - P(2\,|\,1)\right] \cdot \left[1 - P(3\,|\,1,0)\right] \quad (6.2.26)$$

$$k = P(4\,|\,0,0,0) \quad (6.2.27)$$

We are not presenting any higher order Markov model, because the fitting results (presented in section 6.4) suggest that the results of this third order Markov model do not improve much on those of the second order Markov model.

6.3 Fitting the stationary Markov model to the neurophysiological data

The general Markov renewal process model is simplified to three lower order stationary Markov models with parameters α_i and k. Each stationary Markov model is a linear difference equation of the firing probability. Thus a least-squares fitting method is applied to the neurophysiological data. Additionally, parameters of each linear equation can be interpreted as conditional probabilities with physiological meaning. However, it is not clear whether the model should extend and to which order. This leads to the problem of finding unique solutions to the Markov renewal process model.

6.3.1 The least-squares fitting

The method of linear least-squares is a standard approach to data fitting, especially for over-determined systems. The best fit in the least-squares finds the

overall solution that minimizes the sum of the squares of the errors made in solving each equation.

For example, to fit the third order Markov model Eq.(6.2.23). The data point $[\omega_1, \omega_2, \ldots \omega_{20}]$ is a set of firing probabilities in response of a twenty-pulse-train. The residual is the difference between the actual value of the dependent variable and the value predicted by the model. Take the data into the third order Markov model Eq.(6.2.23).

$$\begin{bmatrix} \omega_4 \\ \omega_5 \\ \vdots \\ \omega_{20} \end{bmatrix} = \begin{bmatrix} \omega_3 & \omega_2 & \omega_1 & 1 \\ \omega_4 & \omega_3 & \omega_2 & 1 \\ \vdots & \vdots & \vdots & \vdots \\ \omega_{19} & \omega_{18} & \omega_{17} & 1 \end{bmatrix} \cdot \begin{bmatrix} \alpha_1 \\ \alpha_2 \\ \alpha_3 \\ k \end{bmatrix} \tag{6.3.1}$$

Let x represent the independent variable and y represent the dependent variable. The value of the parameters are given by the physiological data. Let β represent the unknown parameters for the model.

$$y = \begin{bmatrix} \omega_4 \\ \omega_5 \\ \vdots \\ \omega_{20} \end{bmatrix} \qquad x = \begin{bmatrix} \omega_3 & \omega_2 & \omega_1 & 1 \\ \omega_4 & \omega_3 & \omega_2 & 1 \\ \vdots & \vdots & \vdots & \vdots \\ \omega_{19} & \omega_{18} & \omega_{17} & 1 \end{bmatrix} \qquad \beta = \begin{bmatrix} \alpha_1 \\ \alpha_2 \\ \alpha_3 \\ k \end{bmatrix} \tag{6.3.2}$$

$$y = x\beta$$

The residual is

$$r = y - x\beta \tag{6.3.3}$$

The object function is

$$S = r^2 = \|y - x\beta\|^2 = \sum_{n=4}^{20} (\omega_n - \alpha_1 \cdot \omega_{n-1} - \alpha_2 \cdot \omega_{n-2} - \alpha_3 \cdot \omega_{n-3} - k)^2 \tag{6.3.4}$$

The goal is to find the optimum parameter values for the model when the sum of the squared residuals is a minimum. S is minimized when its gradient vector is zero.

6.3.2 Uniqueness of the solution

In statistics, over-fitting occurs when a statistical model describes random error or noise instead of the underlying relationship. A model which has been over-fitted will show poor predictive performance, as it may exaggerate minor fluctuations in the data. The potential for over-fitting not only relies on the number of parameters but also the model structure and the error magnitude.

Although the first order, the second order and the third order Markov models are all over-determined systems, it is still possible that over-fitting with the data may occur. For example, if the first order Markov model can fit the data well enough

$$\omega_n = \hat{\alpha}\omega_{n-1} + \hat{k} \tag{6.3.5}$$

where $\hat{\alpha}$ and $\hat{k}$ are the optimum value, then

$$\omega_{n-1} = \hat{\alpha}\omega_{n-2} + \hat{k} \tag{6.3.6}$$

Substitute Eq.(6.3.6) into Eq.(6.3.5) gives,

$$\omega_n = \hat{\alpha}^2\omega_{n-2} + (\hat{\alpha}+1)\hat{k} \tag{6.3.7}$$

Then when we fit the second order Markov model with the same data

$$\omega_n = \alpha_1\omega_{n-1} + \alpha_2\omega_{n-2} + k \tag{6.3.8}$$

Substitute Eq.(6.3.5) in Eq.(6.3.8),

$$\omega_n = \alpha_1 \hat{\alpha} \omega_{n-2} + \alpha_2 \omega_{n-2} + \alpha_1 \hat{k} + k \tag{6.3.9}$$

Comparing Eq.(6.3.7) and Eq.(6.3.9), we get two quadratic equations,

$$\alpha_1 \hat{\alpha} + \alpha_2 - \hat{\alpha}^2 = 0 \tag{6.3.10}$$

$$k + \alpha_1 \hat{k} = \hat{k}(\hat{\alpha} + 1) \tag{6.3.11}$$

Solve for parameters α_1, α_2 and k. Because the number of unknown parameters is bigger than the number of quadratic equations, it is an underdetermined system. There are an infinite number of solutions to an underdetermined system. The values of α_1, α_2 and k are not unique. One root of the equations is

$$\begin{cases} \alpha_1 = \hat{\alpha} \\ \alpha_2 = 0 \\ k = \hat{k} \end{cases} \tag{6.3.12}$$

Other roots of the equations may fit to the noise in the data.

6.3.3 Least-squares fitting with constraints

In order to improve the accuracy of the fitting, it is necessary to use additional constraints. As all the parameters in the Markov model are interpreted into combinations of the conditional probabilities, additional constraints can be applied. For example, all the conditional probabilities range from 0 to 1.

The first order stationary Markov model as stated in Eq.(6.2.8) and Eq.(6.2.9),

$$k = P(2 \mid 0) \in [0,1] \tag{6.3.13}$$

Due to the refractory effects, the conditional probability $P(2 \mid 1) \le P(2 \mid 0)$, which implies that

$$\alpha_1 \le 0 \tag{6.3.14}$$

The second order stationary Markov model as stated in Eq.(6.2.15) -Eq.(6.2.18),

$$k = P(3 \mid 0,0) \in [0,1] \tag{6.3.15}$$

and

$$P(2 \mid 1) \in [0,1] \tag{6.3.16}$$

Due to refractory effects, $P(2 \mid 1) \le P(3 \mid 0,0)$ and $P(3 \mid 1,0) \le P(3 \mid 0,0)$.

Thus, according to Eq.(6.2.16) and Eq.(6.2.17),

$$\alpha_1 \le 0 \quad \alpha_2 \le 0 \tag{6.3.17}$$

The third order stationary Markov model as stated in Eq.(6.2.24)-Eq.(6.2.27),

$$k = P(4 \mid 0,0,0) \in [0,1] \tag{6.3.18}$$

$$P(2 \mid 1) \in [0,1] \tag{6.3.19}$$

$$P(3 \mid 1,0) \in [0,1] \tag{6.3.20}$$

Due to refractory effects, $P(2 \mid 1) \le P(4 \mid 0,0,0)$, $P(3 \mid 1,0) \le P(4 \mid 0,0,0)$ $P(4 \mid 1,0,0) \le P(4 \mid 0,0,0)$

Thus according to Eq.(6.2.24)-Eq.(6.2.26),

$$\alpha_1 \le 0 \quad \alpha_2 \le 0 \quad \alpha_3 \le 0 \tag{6.3.21}$$

6.4 Results of stationary Markov model

The least-squares fit with constraints is applied to fit the neurophysiological data to three stationary Markov models in Matlab. The fittings are performed with two different forms of the neurophysiological data: one is the gradient of the

neurophysiological data in section 6.4.1, another is the actual neurophysiological data in section 6.4.2. The gradient data $\Delta\omega_n$ are defined as,

$$\Delta\omega_n = \omega_{n+1} - \omega_n \tag{6.4.1}$$

By fitting the first difference of the data, the non-autonomous variable k in the linear equation (Eq.(6.2.7), Eq.(6.2.15) and Eq.(6.2.23)) is eliminated. Each system becomes a homogenous polynomial of degree one. It qualifies as a linear recurrence sequence[128].

The least-squares method is applied to both the gradient data and the whole data. The results of the fitting are shown by comparing the goodness of fit. In regression analysis, the goodness of fit includes the sum of squares error (SSE) and the coefficient of determination (the R squared measure of goodness of fit).

The SSE is defined as the sum of squared residuals [129],

$$SSE(y) = \|y - x\beta\|^2 \tag{6.4.2}$$

where y is the observed valued of data set, and $x\beta$ are the modelled values.

The R squared measure of goodness of fit is defined as

$$R^2 = 1 - \frac{SS_{err}}{SS_{tot}} = 1 - \frac{\|y - x\beta\|^2}{\|y - \bar{y}\|^2} \tag{6.4.3}$$

where SStot is defined as the total sum of squares of the data. It is the sum of squares due to pure error. It is proportional to the sample variance. The R^2 coefficient of determination is a statistical measure of how well the regression

line approximates the real data points. An R^2 of 1.0 indicates that the regression line perfectly fits the data.

6.4.1 Fitting gradient data set

Before fitting the gradient of the neurophysiological data, the stationary Markov models have to be transformed to the difference of the firing probability, $\Delta\omega_n$ and the constraints are changed consequently. As k is eliminated, the constraint on k is removed.

According to Eq.(6.4.1), the first order Markov model is written as,

$$\Delta\omega_n = \alpha_1 \cdot \Delta\omega_{n-1} \qquad \alpha_1 \le 0 \quad n \in [2,19] \tag{6.4.4}$$

And the second order Markov model is written as,

$$\Delta\omega_n = \alpha_1 \cdot \Delta\omega_{n-1} + \alpha_2 \cdot \Delta\omega_{n-2} \quad \alpha_1, \alpha_2 \le 0 \qquad n \in [3,19] \tag{6.4.5}$$

The third order Markov model,

$$\Delta\omega_n = \alpha_1 \cdot \Delta\omega_{n-1} + \alpha_2 \cdot \Delta\omega_{n-2} + \alpha_3 \cdot \Delta\omega_{n-3} \qquad \alpha_1, \alpha_2, \alpha_3 \le 0 \quad n \in [4,19]$$

(6.4.6)

The goodness of fit of three Markov models is presented in Table 6-5 and Table 6-6.

Table 6-5 *SSE* of fitting the gradient data with constraints

FE	0.02	0.05	0.1	0.2	0.3	0.4	0.5	0.6	0.7
1st order	0.0005	0.001	0.0012	0.0044	0.0033	0.0069	0.0193	0.0141	0.007
2nd order	0.0004	0.0008	0.0012	0.0024	0.0026	0.0046	0.0038	0.0126	0.0068
3rd order	0.0004	0.0007	0.0007	0.0011	0.0018	0.0018	0.0013	0.0063	0.0032

Table 6-6 R Squared measures of fitting the gradient data with constraints

FE	0.02	0.05	0.1	0.2	0.3	0.4	0.5	0.6	0.7
1st order	0	0.3353	0.0644	0.6354	0.9312	0.8466	0.8913	0.0554	0.1004
2nd order	0.065	0.2995	0.0021	0.6624	0.8398	0.8074	0.9755	0.159	0.1281
3rd order	0.0628	0.1943	0.3046	0.5865	0.7306	0.787	0.9889	0.275	0.3109

The SSE of the third order Markov model is the smallest among all three Markov models. For FE from 0.3 to 0.7, the SSE of the third order Markov model is reduced by at least half of the results of the second order Markov model.

The R Squared measures for all three Markov models for low FE (from 0.02 to 0.1) and high FE (0.6 and 0.7) were around zero. It is not the case that the fit does not work, but occurs because the gradient data are approx around zero. The best fit for those FE was roughly a horizontal line or a horizontal surface. Thus we focus on the results from FE of 0.2 to FE of 0.5. Although the SSE and R Squared measures for the third order Markov model are better than the result of either the first order Markov model or the second order Markov model, the results are not much improved compared to the second order Markov model.

The gradient data are fitted by the least-squares method. Thus the sum of squares of residuals is minimized. By adding extra variables, the SSE decreases as shown in Table 6-5. According to Eq.(6.4.3), the R Squared measures are weakly increased. As such, the R Squared measures are not sufficient to demonstrate the goodness of fit when choosing the number of variables. To investigate whether the third order Markov model with three variables is better than the second order Markov model with two variables, the adjusted R Squared measures are compared in Table 6-7. The adjusted R Squared measures is defined as unbiased R Squared measures [130],

$$\bar{R}^2 = 1-(1-R^2)\frac{N-1}{N-p-1} \tag{6.4.7}$$

where N is the sample size, p is the total number of regressors in the linear model. Unlike R squared measures, the adjusted R Squared measures increases only if the new term improves the model more than would be expected by chance. Also the adjusted R Squared measures does not have the same interpretation as R Squared measures. The adjusted R Squared measures can be negative.

Table 6-7 Adjusted R Squared measures of fitting the gradient of the data with constraints

FE	0.02	0.05	0.1	0.2	0.3	0.4	0.5	0.6	0.7
1st order	-0.0625	0.056951	-0.05809	0.366531	0.858888	0.69901	0.781498	-0.05924	-0.05179
2nd order	-0.13803	-0.04037	-0.14285	0.358657	0.663143	0.602134	0.944705	-0.11396	-0.12409
3rd order	-0.24507	-0.20281	-0.13405	0.179946	0.417204	0.524369	0.972432	-0.15548	-0.12919

The adjusted R Squared measures (FE from 0.2 to 0.5) of the second order Markov model is bigger than the result of the third order Markov model. It demonstrates that the second order Markov model fits the data better than the third order. The third order does not improve the fitting. It may over-fit the noise in the data. Therefore, only results of the gradient data fitted to the second order Markov model are presented in the following sections.

First, the PST histogram of increments of the firing probabilities is constructed by the estimated parameter $\hat{\alpha}_1, \hat{\alpha}_2$ and the initial values $\Delta\omega_1$ and $\Delta\omega_2$ (from data) as,

$$y_i = \hat{\alpha}_1 \cdot y_{i-1} + \hat{\alpha}_2 \cdot y_{i-2} \quad i \in [3,19] \tag{6.4.8}$$

where $y_1 = \Delta\omega_1$ and $y_2 = \Delta\omega_2$.

Each PST histogram is labelled by the number of its FE. The results of Eq.(6.4.8) are plotted as the solid line. The gradient data are plotted in asterisk markers. For purposes of comparison, all of the histograms in Figure 6-1 have the same vertical and horizontal scales.

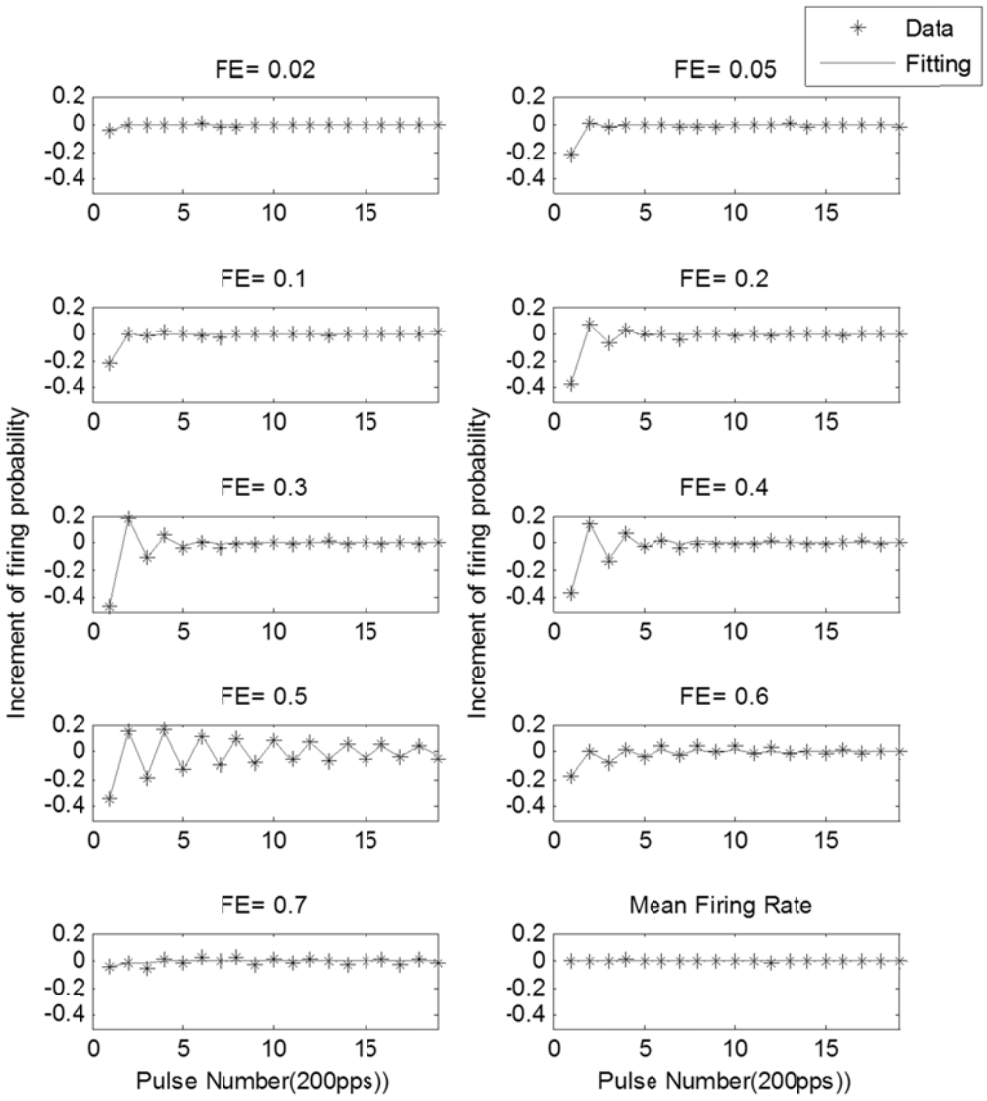

Figure 6-1 Increment of the firing probability histogram from fitting the second order Markov model

The second order Markov model can fit the gradient data. Especially for FE of 0.5, the second order Markov model almost accurately follows the oscillation in the data for all pulses.

Then the non-autonomous variable *k* in Eq.(6.2.15) can be calculated by its mean value,

$$\hat{k} = \frac{1}{18}\sum_{i=3}^{20} \omega_i - y_i \tag{6.4.9}$$

Thus the PST histogram is constructed by $\hat{\alpha}_1, \hat{\alpha}_2, \hat{k}$ with the initial value ω_1, ω_2,

$$\hat{\omega}_n = \hat{\alpha}_1 \cdot \hat{\omega}_{n-1} + \hat{\alpha}_2 \cdot \hat{\omega}_{n-2} + \hat{k} \quad n \in [3, 20] \tag{6.4.10}$$

where $\hat{\omega}_1 = \omega_1$ and $\hat{\omega}_2 = \omega_2$.

Rearranging Eq.(6.2.16), Eq.(6.2.17) and Eq.(6.2.18), the conditional probabilities can be calculated as

$$\begin{aligned} P(3 \mid 0,0) &= \hat{k} \\ P(2 \mid 1) &= \hat{\alpha}_1 + P(3 \mid 0,0) \\ P(3 \mid 1,0) &= \frac{\hat{\alpha}_2}{1 - P(2 \mid 1)} + P(3 \mid 0,0) \end{aligned} \tag{6.4.11}$$

The results are presented in Figure 6-2. The results of the fitting are plotted in a solid line, and the neurophysiological data are plotted in asterisk markers. For purposes of comparison, all of the histograms in Figure 6-2 have the same vertical and horizontal scales.

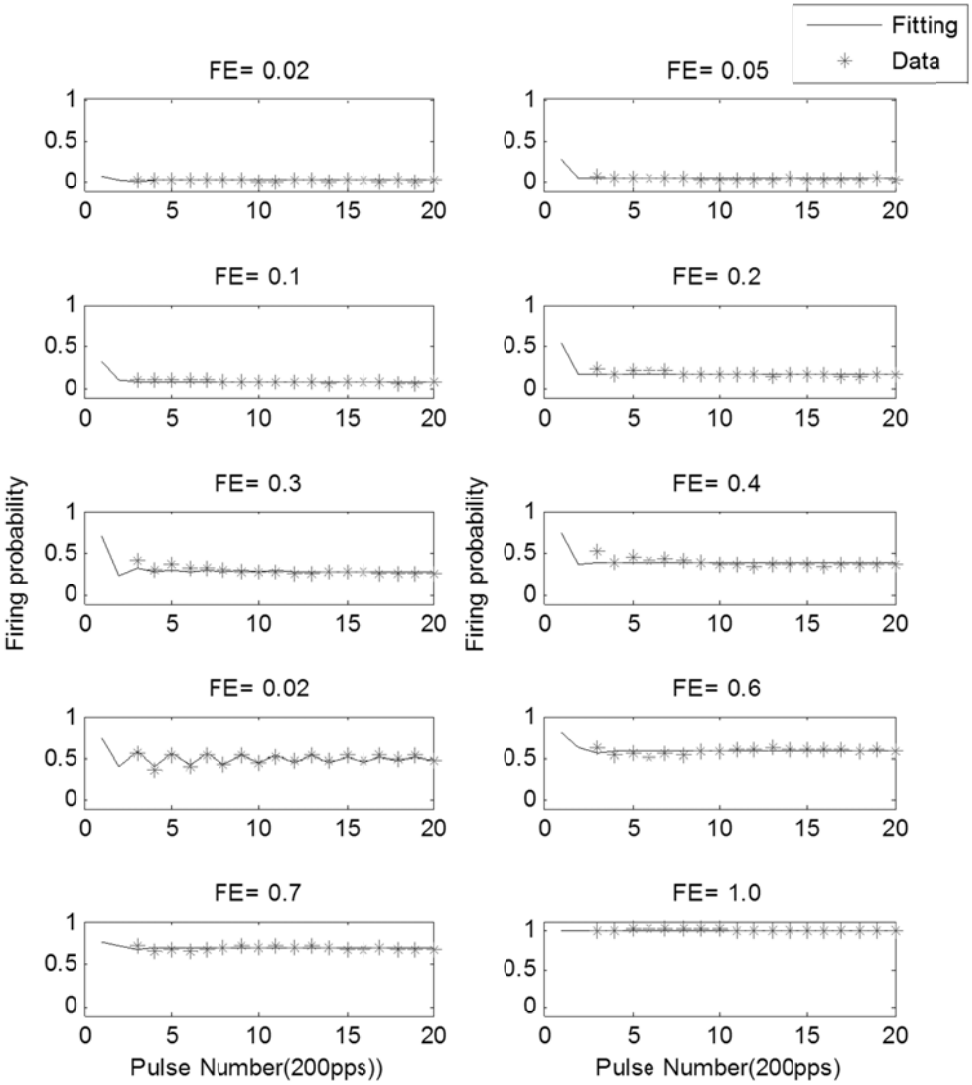

Figure 6-2 Firing probability histogram from fitting results for the second order Markov model to gradient data

All the conditional probabilities are listed in Table 6-8. The firing probabilities for the first pulse are also presented for comparison.

Table 6-8 Fitting the gradient data to the second order Markov model with constraints

FE	Conditional probabilities			ω_1
	$P(3\|0,0)$ /k	$P(3\|1,0)$	$P(2\|1)$	
0.02	0.021	-0.061	-0.121	0.070
0.05	0.057	0.057	-0.423	0.267
0.1	0.091	0.091	0.044	0.331
0.2	0.295	0.295	-0.328	0.554

0.3	0.431	0.431	-0.100	0.698
0.4	0.635	0.635	-0.023	0.744
0.5	0.946	0.946	0.016	0.740
0.6	0.822	0.822	0.423	0.803
0.7	0.946	0.946	0.586	0.763

The results for the whole data set are not as good as the results for the gradient data. Although the values of α_1 and α_2 are the same, the fitting results for the gradient data can capture the oscillations in the first five or six points then converge to a steady state value. When presenting the results for the PST histograms, the model only predicts the trend in the data. The firing probability converges to a steady state after the second or even the first point. The apparent discrepancy between these two curves relies on the variable *k*. It implies that the problem is caused by the assumed non-autonomous factor *k*. This phenomenon will be further discussed in section 6.4.3.

Although the accuracy of this conditional analysis is uncertain, Table 6-8 still presents some qualitative estimates of the accommodation effects and refractory effects. In the second order Markov model, the conditional probabilities $P(3|0,0)$ is related to the the accommodation effects; the conditional probability $P(3|1,0)$ and $P(2|1)$ are related to the refractory effects.

1. The probability $P(3|1,0)$ and $\omega(1)$, which is the firing probability at the first pulse, are always bigger than the probability $P(2|1)$. Some $P(2|1)$ are negative, which are out of the range of physiologically reasonable values. However, as $P(2|1)$ is smaller than $\omega(1)$, it suggests that the refractory effects lasts for at least 5 ms (the duration for one pulse). The increasing value of $P(3|1,0)$ suggests that the neuron "recovers" from

the refractory period. The "recover" here is an operational sense that refractory effects is removed from the neuron, it does not coincide with the actual physiological recovery processes.

2. For FE between 0.02 to 0.4, $\omega(1)$ is always bigger than $P(3|0,0)$. The conditional probability $P(3|0,0)$ is suppressed due to the accommodation effects only. The accommodation effects has significant influence on the neuron for low FE (from 0.02 to 0.4). This observation is consistent with the analysis in Chapter 5.
3. For all the FEs, the conditional probability $P(3|0,0)$ is almost identical to the conditional probability $P(3|1,0)$. It is not clear whether this indicates that after 10ms both refractory effects and accommodation effects "recover" to the same state or it is merely due to the constraint $\alpha_2 \leq 0$.

6.4.2 Fitting the whole data set

Fitting the gradient data without the parameter *k* may lead to some inaccuracy. We therefore now fit the stationary Markov models to the whole data directly. A least-squares fit with constraints is applied to three Markov models. The goodness of fit of the three Markov models is presented in Table 6-9,

Table 6-10 and

Table 6-11. The conditional probabilities are calculated according to Eq.(6.4.11).

Table 6-9 Fitting the whole data set to the first order Markov model with constraints (α1≤0 0≤k≤1)

FE	α_1	*k / P(2|0)*	*P(2|1)*	*SSE*	*R-squared*
0.02	0	0.017	0.017	0.0008	0
0.05	0	0.039	0.039	0.0021	0
0.1	0	0.088	0.088	0.0046	0

0.2	0	0.181	0.181	0.0102	0
0.3	-0.048	0.294	0.246	0.0351	0.0126
0.4	0	0.382	0.382	0.0313	0
0.5	-0.037	0.500	0.463	0.0501	0.0694
0.6	0	0.589	0.589	0.0188	0
0.7	0	0.697	0.697	0.0069	0

Table 6-10 Fitting the whole data set to the second order Markov model with constraints

FE	α_1	α_2	*k / (P3|00)*	*P(2|1)*	*P(3|10)*	*SSE*	*R-squared*
0.02	0	0	0.017	0.017	0.017	0.0008	0
0.05	0	0	0.038	0.038	0.038	0.002	0
0.1	0	0	0.087	0.087	0.087	0.0041	0
0.2	0	0	0.181	0.181	0.181	0.0102	0
0.3	0	0	0.282	0.282	0.282	0.0333	0
0.4	0	0	0.383	0.383	0.383	0.0311	0
0.5	-0.0247	0	0.500	0.475	0.500	0.044	0.0344
0.6	0	0	0.587	0.587	0.587	0.017	0
0.7	0	0	0.695	0.695	0.695	0.0058	0

Table 6-11 Fitting the whole data to the third order Markov model with constraints (α1≤0 α2≤0 α3≤0 0≤k≤1)

FE	α_1	α_2	α_3	*k/P(4|000)*	*P(2|1)*	*P(3|10)*	*P(4|100)*	*SSE*	*R-squared*
0.02	0	0	0	0.017	0.017	0.017	0.017	0.0008	0
0.05	0	0	0	0.037	0.037	0.037	0.037	0.0015	0
0.1	0	0	0	0.085	0.085	0.085	0.085	0.0031	0
0.2	0	0	0	0.177	0.177	0.177	0.177	0.0051	-0
0.3	0	0	0	0.274	0.274	0.274	0.274	0.0167	0
0.4	0	0	0	0.375	0.375	0.375	0.375	0.0142	0
0.5	0	0	-0.036	0.500	0.500	0.500	0.356	0.0381	0.0839
0.6	0	0	-0.027	0.600	0.600	0.600	0.433	0.0148	0.0253
0.7	0	0	-0.010	0.700	0.700	0.700	0.592	0.0051	0.0125

When fitting the first order Markov model to the whole data set, the optimal solution of α_1 at each FE is zero, except for FE of 0.3 and 0.5. When fitting the second order Markov model, the optimal solutions of α_1 and α_2 at each FE are zero, except for FE of 0.5. When fitting the third order Markov model, the

optimal solutions of α_1, α_2 and α_3 at each FE are still zero, except for FE of 0.5, 0.6 and 0.7. These results demonstrate that mostly the best fit to the whole data is simply a fixed number, as

$$\omega_n = k \tag{6.4.12}$$

Obviously, it does not describe any dynamics and hence is a poor description of the neural responses.

6.4.3 The shifting *k*

The stationary Markov model cannot fit the whole data. But it can almost accurately fit the gradient data. When constructing the PST histograms by adding the non-autonomous factor k, the firing probability quickly converges to a steady state. It cannot reproduce the dynamics of the neural response. The only difference between the increment of the firing probability histogram and the PST histogram relies on the non-autonomous factor k. One possible explanation for the poor quality of the fits is that k, and the conditional probabilities, are not stationary as assumed. This explanation would also suggest why the increments are fitted better – differentiating is used as a method to 'detrend' data yielding it more stationary – it might therefore be expected that stationary Markov models work better with detrended data.

To investigate whether nonstationarity is a problem, we now study how k depends on the pulse number.

First, we calculate the value of k at each pulse according to the data, denoted as k_n

$$k_n = \omega_n - \hat{\alpha}_1\omega_{n-1} - \hat{\alpha}_2\omega_{n-2} \qquad n \in [3, 20] \tag{6.4.13}$$

where $\hat{\alpha}_1, \hat{\alpha}_2$ are the least-squares estimates of α_1 and α_2 in the second Markov model to the gradient data. Results of k_n at FE of 0.05 are presented in Figure 6-3 for example.

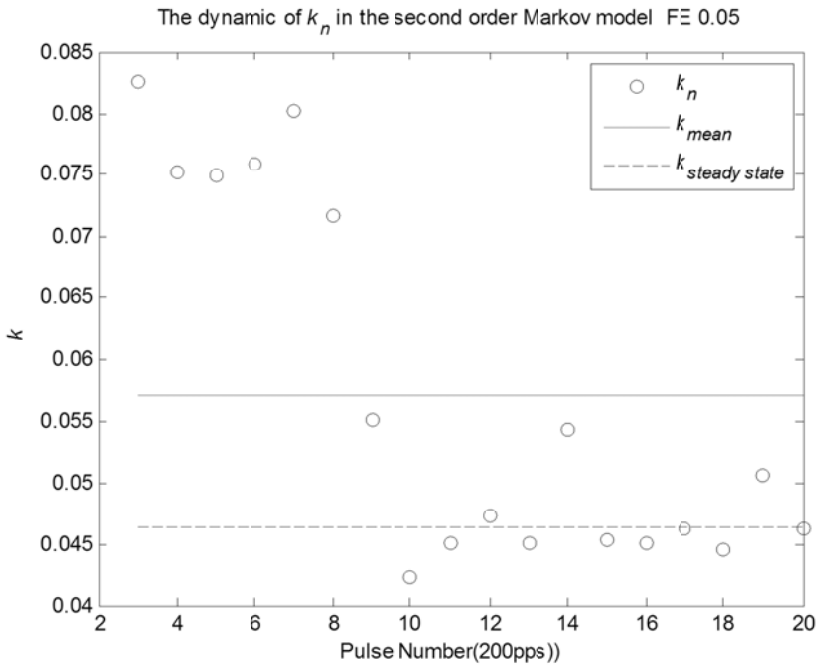

Figure 6-3 The dynamic of k_n in the second order Markov model at FE of 0.05. The k_ns are plotted in circle markers. The mean value of k_n, Eq.(6.4.9), is plotted in a solid line. The steady state of k_n is plotted in a dashed line, and it is discussed in the following text.

The results demonstrate that k_n slowly drifts from pulse to pulse. k_{mean} is the mean value of k_n, which is also defined as the estimated $\hat{k}$ in Eq.(6.4.9). In Figure 6-3, k_n is reduced by half after the 9th pulse, and remains at the number of 0.045 approximately. It suggests that maybe $\hat{k}$ should be estimated by its steady state value other than its mean value.

Then, we recalculated $\hat{k}$ by its steady state value, k_s. Assume after few pulses, the probability of firing converges to a steady state ω_s. Then Eq.(6.2.15) is written as,

$$\omega_s = \hat{\alpha}_1 \omega_s + \hat{\alpha}_2 \omega_s + k_s \tag{6.4.14}$$

where ω_s is calculated as the mean value of last ten firing probabilities,

$$\omega_s = \frac{1}{10} \times \sum_{i=10}^{20} \omega_i \tag{6.4.15}$$

Rearranging Eq.(6.4.14) gives,

$$k_s = (1 - \hat{\alpha}_1 - \hat{\alpha}_2) \cdot \omega_s \tag{6.4.16}$$

The results for k_s are compared to its mean value k_{mean} in Table 6-12. The standard deviation and the coefficient of variation of k_n are also presented for comparison. The coefficient of variation is defined as

$$C_v = \frac{\sigma}{\mu} \tag{6.4.17}$$

Table 6-12 Comparing the statistics of k_n

FE	0.02	0.05	0.1	0.2	0.3	0.4	0.5	0.6	0.7
k_{mean}	0.021	0.057	0.091	0.295	0.431	0.635	0.946	0.822	0.946
k_s	0.016	0.046	0.081	0.271	0.391	0.593	0.963	0.844	0.948
σ_{k_n}	0.008	0.015	0.016	0.034	0.056	0.057	0.034	0.041	0.022
$c_v(k_n)$	0.383	0.259	0.179	0.114	0.130	0.090	0.036	0.050	0.023

Then we construct a new PST histogram with k_s. Here we only present the figure of 0.05 FE as an example. The PST histogram constructed with k_{mean} is also plotted in this figure for comparsion.

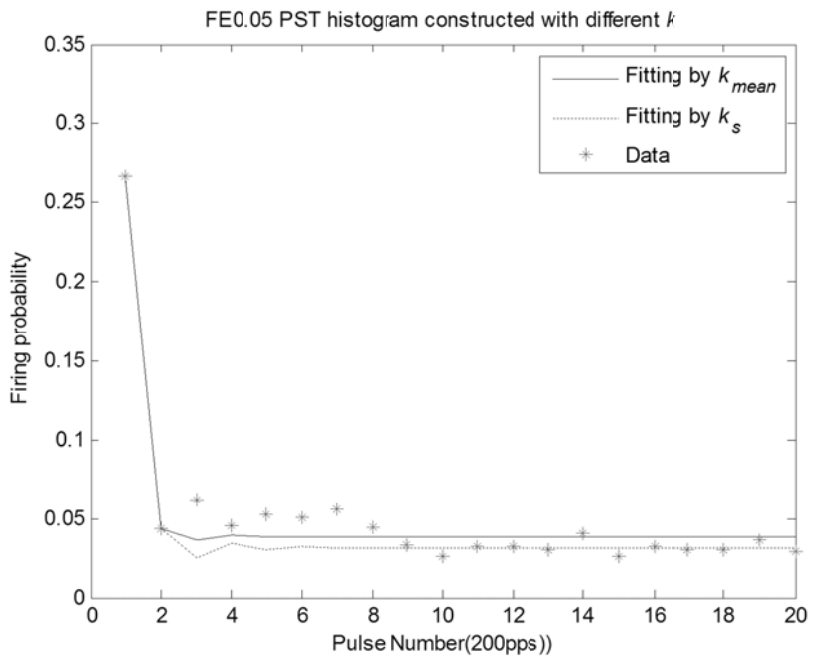

Figure 6-4 Comparing PST histograms constructed with different *k*. The results for k_{mean} are plotted in a solid line. The results for k_s are plotted in dotted line. The neurophysiological data are plotted in the asterisk markers for comparison.

Figure 6-4 indicates that although there is a difference between the value of $k_{mean}$and k_s, the PST histograms constructed by those two variables are similar. The firing probabilities estimated by k_s show a great agreement with last ten data points. On the other hand, the firing probabilities estimated by k_{mean} show an average agreement with all twenty data points. Still none of them can capture the dynamic in first few pulses.

In order to evaluate the dynamic of k_n, several statistics are presented in Table 6-12. To compare the dynamic of k_n between different FEs, the coefficient of variation of k_n is calculated according to Eq.(6.4.17). The coefficient of variation (C_v) is a normalized measure of dispersion of a distribution [119]. All the coefficients of variation of k_n in Table 6-12 are smaller than one. In statistical theory, the distribution of k_n is defined as low-variance. However, the figure of

k_n shows a large dispersion especially for FE of 0.02, 0.05 and 0.1. Take Figure 6-3 (FE of 0.05) for example. Although the coefficient of variation of k_n is 0.259 at 0.05 FE, k_n decreases by half after the ninth pulse. Also, the value of k_n monotonically increases at low FE and it monotonically decreases at high FE. It is not clear whether k_n has some certain trend or it is just sensitive to the noise in the data. Moreover, the I/O curve analysis in Chapter 4 suggest that the threshold in the neurophysiological data varies from pulse to pulse due to the accommodation effects and the refractory effects. It is possible that the fluctuations in threshold result in this drifting k_n.

Therefore, we applied some test data to the second order Markov model to investigate the main cause of this drifting in k_n. We adopt the LIFDT model (Eq.(3.3.1)-- Eq.(3.3.4)) to generate some test data, because first the LIFDT model is built with a noise factor; second although the LIFDT model only has little fluctuations in the threshold under the accommodation effects (presented in Figure 5-15), it can mimic the neurophysiological data by adding extra equation to the threshold Eq.(3.3.4).

The stimuli applied to the LIFDT model are the same as for the neurophysiological data, which are 100-ms duration 200-pps pulse trains shown in Figure 3-11. The LIFDT model consists of Eq.(3.2.9), Eq.(3.2.10), Eq.(3.2.11) and a threshold function as shown in the following text.

First the original threshold function in the LIFDT model is given by

$$\theta(t) = \frac{\theta_m}{h(t)^p} + \theta_0 \tag{6.4.18}$$

Second we modulate the threshold function Eq.(6.4.18) by adding a sine wave (within 100ms it is monotonically increasing over the time period),

$$\theta_1(t) = \frac{\theta_m}{h(t)^p} + \theta_0 + a \cdot \sin(2\pi t) \tag{6.4.19}$$

Third we modulate the threshold function Eq.(6.4.18) by adding a monotonically decreasing function

$$\theta_2(t) = \frac{\theta_m}{h(t)^p} + \theta_0 - a \cdot \sin(2\pi t) \tag{6.4.20}$$

The amplitudes of the sine wave in Eq.(6.4.19) and Eq.(6.4.20) are both a. It is defined as

$$a = 0.05 \times \theta(t)|_{t=0} \tag{6.4.21}$$

where 0.05 is obtained from I/O curve analysis of the neurophysiological data in Table 4-2.

Therefore, the LIFDT model is established with three different threshold functions. The parameter values in the LIFDT model are taken from Table 5-1, which are fitted to the I/O curve for the first pulse in the neurophysiological data. Like the neurophysiological data, the neural responses are generated by nine stimulus amplitudes, which is equivalent to FE from 0.02, 0.05, 0.1, 0.2, 0.3, 0.4, 0.5, 0.6 to 0.7 of the LIFDT model with unmodulated threshold θ. At each level of FE, the LIFDT model (Eq.(3.2.9)-Eq.(3.2.11)) with each threshold function (Eq.(6.4.18) or Eq.(6.4.19) or Eq.(6.4.20)) was simulated for a thousand iterations to a twenty-pulse stimulus, but with different noise at each iteration. Thus nine sets of test data are generated by the LIFDT model with each different

threshold function. For each data set (FE), the gradient test data are fitted to the second order Markov model by the constrained least- squared algorithm, and k_n is calculated according to Eq.(6.4.13). The results of k_n for $\overline{FE} = 0.05$ are presented in Figure 6-5 as an example.

In Figure 6-5, the modulated increasing threshold θ_1 drives k_n to decrease monotonically, which is the same trend in the neurophysiological data for high FE; on the other hand, the modulated decreasing threshold θ_2 drives k_n to increase monotonically, which is the same trend in the neurophysiological data for low FE. However, the results of the unmodulated threshold θ do not show such a trend. It indicates that the monotonical drifting in k_n is more likely related to the fluctuations in the threshold rather than the membrane noise.

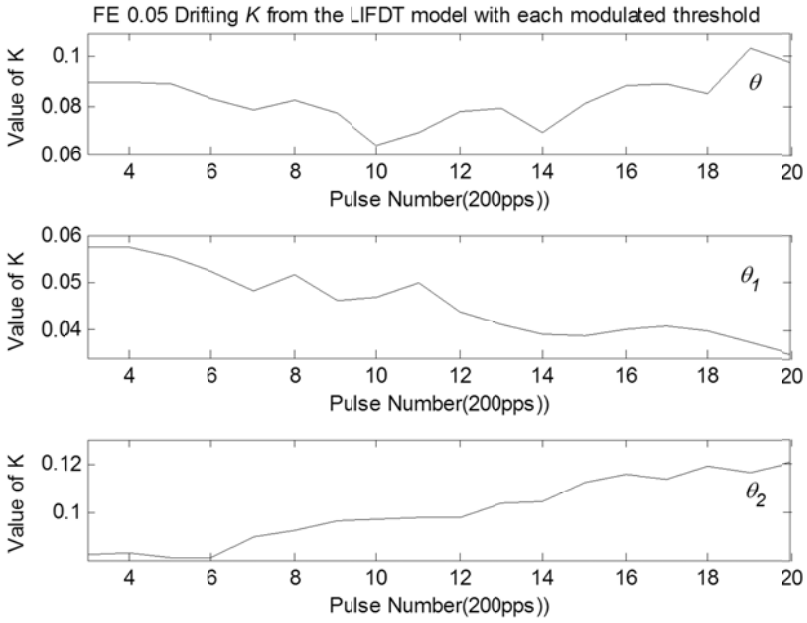

Figure 6-5 The drifting in *k* from the LIFDT model with each modulated threshold at FE=0.05.

Moreover, we compare the statistics of k_n in Table 6-13. The statistics of k_n include its mean value μ, the standard deviation σ and the coefficient of

variation C_v. Now to express those statistics in simple form we define the following notation. For the data set of the unmodulated threshold θ, the statistics are labelled as "k". For the data set of the modulated increasing threshold θ_1, the statistics are labelled as "k^+". For the data set of the modulated decreasing threshold θ_2, the statistics are labelled as "k^-".

Table 6-13 Statistics of the shifting k with original threshold, modulated threshold θ_1 and modulated threshold θ_2. For each circumstance, compare the mean value μ, the standard deviation σ and the coefficient of variation C_V.

	FE	0.02	0.05	0.1	0.2	0.3	0.4	0.5	0.6	0.7
θ	μ_k	0.033	0.083	0.137	0.304	0.420	0.597	0.968	1.105	1.225
	σ_k	0.007	0.010	0.011	0.014	0.013	0.013	0.012	0.015	0.015
	C_{V_k}	0.198	0.121	0.080	0.046	0.031	0.022	0.012	0.013	0.012
θ_1	μ_{k+}	0.016	0.046	0.102	0.226	0.229	0.374	0.537	0.756	0.876
	σ_{k+}	0.004	0.007	0.014	0.023	0.019	0.028	0.032	0.036	0.030
	C_{V_k}+	0.240	0.158	0.140	0.103	0.085	0.075	0.059	0.048	0.034
θ_2	μ_k-	0.033	0.101	0.120	0.276	0.396	0.622	0.691	0.708	0.704
	σ_k-	0.005	0.013	0.014	0.023	0.026	0.035	0.033	0.027	0.019
	C_{V_k}-	0.155	0.133	0.114	0.082	0.065	0.057	0.048	0.038	0.027

In Table 6-13, each column represents a fixed stimulus amplitude, in which the FE is calculated by the LIFDT model with unmodulated threshold θ. Therefore, for the LIFDT model with modulated threshold θ_1 or θ_2, the actual FEs are slightly different. Consequently the value of μ_k, μ_{k+} and μ_{k-} in the same column variy. Thus here we compare the coefficients of variation of the three data sets. At each FE, the coefficient of variation of the unmodulated threshold θ, C_{Vk}, is the smallest. For FE between 0.1 and 0.7, the coefficients of variation of the unmodulated thresholds are substantially smaller than those of a modulated thresholds (C_{Vk} is a half or even a fifth of C_{Vk^+} or C_{Vk^-}). It implies that the modulated threshold results in a much bigger dispersion than the membrane noise.

The test data of LIFDT with modulated threshold θ_1 or θ_2 are generated to resemble the neurophysiological data, for example they have the same level of membrane noise, fluctuations in the threshold under the accommodation effects etc. Additionally the results in Table 6-12 and Table 6-13 also provide the comparison of the test data to the neurophysiological data. The coefficients of variation of the test data are roughly the same level as those of the neurophysiological data. Therefore, observations from the test data are valid for the neurophysiological data.

This implies that the dispersion of k_n in the neurophysiological data is mainly caused by small variation in the threshold (approximately 5% fluctuations of the threshold). The stationary second order Markov model Eq.(6.2.15) is quite sensitive to such variation. Due to this sensitivity, the stationary second order Markov model can only fit the gradient data not the whole data set.

As k is interpreted as the conditional probabilities $P(3|0,0)$ according to equation(6.2.18), it implies that the conditional probabilities are slowly varying from pulse to pulse. We obtained good results for α_1 and α_2 in section 6.4.1. According to Eq.(6.2.16) and Eq.(6.2.17), α_1 and α_2 evolve as the difference of two conditional probabilities. It is possible that the first difference reduce the shifting trend in the conditional probabilities. Therefore, the stationary second order Markov model can still fit those two variables.

6.5 Non-stationary Markov renewal process model

Previous section discussed the fitting results of the stationary Markov model. The results demonstrated that the second order Markov model can only fit the gradient of the data, because the conditional probabilities are slowly varying in

time. In other words, they are non-stationary. Thus in this section we try to develop a Markov renewal process model without the stationary assumption.

In the stationary Markov model, all the conditional probabilities are assumed stationary, but the assumptions are made for different considerations. For those conditional probabilities related to the refractory effects, such as $P(3|1,0)$, they are stationary according to the renewal process. For those conditional probabilities related to the accommodation effects, such as $P(3|0,0)$, they are assumed stationary in consistency with the short history assumption.

The physiology of the neuron indicates that a neural response qualifies as a renewal process because if a neuron generates a spike, it would finally recover to its equilibrium state after the refractory period, the history before that spike can be neglected. Therefore, we keep the assumption based on the renewal process, and only modify the short history assumption.

Then the general Markov renewal process model Eq.(6.2.1) is still valid. The firing probability at each pulse can be calculated by summing up all the permitted histories. The probability of firing at the first pulse ω_1 is an initial condition. At the second pulse, ω_2 can be calculated from the first order Markov model. At the third pulse, ω_3 can be calculated from the second order Markov model. At the fourth pulse, ω_4 can be calculated from the third order Markov model. To simplify the form of the expressions, $f(H_{n-1})$ is simply denoted as $S(s_1, s_2, \dots, s_{n-1})$ where $s_{n-1} \in \{0,1\}$. Then ω_2 to ω_4 is,

$$\omega_2 = P(2|0)S(0) + P(2|1)S(1) \tag{6.5.1}$$

$$\omega_3 = P(3|0,0)S(0,0) + P(3|1,0)S(1,0) + P(2|1)S(1) \tag{6.5.2}$$

$$\begin{aligned}\omega_4 &= P(4\,|\,0,0,0)S(0,0,0) + P(4\,|\,1,0,0)S(1,0,0)\\ &+P(3\,|\,1,0)S(1,0) + P(3\,|\,0,0)S(0,0)\\ &+P(2\,|\,1)S(1)\end{aligned} \tag{6.5.3}$$

where

$$\begin{aligned}S(1) &= \omega_1\\ S(1,0) &= \omega_1(1-P(2\,|\,1))\\ S(1,0,0) &= \omega_1(1-P(2\,|\,1))(1-P(3\,|\,1,0))\\ S(0,0) &= (1-\omega_1)(1-P(2\,|\,0))\\ S(0,0,0) &= (1-\omega_1)(1-P(2\,|\,0))(1-P(3\,|\,0,0))\end{aligned}$$

When calculating ω_5, all the possible combinations of the permitted histories are listed in Table 6-14.

Table 6-14 The permitted histories at the fifth pulse

Pulse Num	1	2	3	4	5	Conditional probability
Status				1	1	*P(2|1)*
			1	0	1	*P(3|1,0)*
		1	0	0	1	*P(4|1,0,0)*
	1	0	0	0	1	*P(5|1,0,0,0)*
	0	0	0	0	1	*P(5|0,0,0,0)*

Then summing all the possible permitted histories in Table 6-14,

$$\begin{aligned}\omega_5 &= P(5\,|\,0,0,0,0)S(0,0,0,0) + P(5\,|\,1,0,0,0)S(1,0,0,0)\\ &+P(4\,|\,0,0,0)S(0,0,0) + P(4\,|\,1,0,0)S(1,0,0)\\ &+P(3\,|\,0,0)S(0,0) + P(3\,|\,1,0)S(1,0)\\ &+P(2\,|\,1)S(1)\end{aligned} \tag{6.5.4}$$

where
$$\begin{aligned}S(1,0,0,0) &= \omega_1(1-P(2\,|\,1))(1-P(3\,|\,1,0))(1-P(4\,|\,1,0,0))\\ S(0,0,0,0) &= (1-\omega_1)(1-P(2\,|\,0))(1-P(3\,|\,0,0)(1-P(4\,|\,0,0,0))\end{aligned}$$

When calculating the firing probability at one more pulse, two more conditional probabilities are introduced into the system. Now to express the general equation

in simple form we define the following notation for the conditional probability.

$$Q(n) = \Pr\left\{\text{next discharge occurs during pulse } n \mid \text{ last discharge occurred in the } 1^{st} \text{ pulse}\right\} \tag{6.5.5}$$

$$R(n) = \Pr\left\{\text{first discharge occurs during pulse } n \mid \text{ no discharge before}\right\} \tag{6.5.6}$$

Thus the conditional probabilities can be replaced by $Q(n)$and $R(n)$. For example,

$$P(5 \mid 1,0,0,0) = Q(5)$$
$$P(5 \mid 0,0,0,0) = R(5)$$

$Q(n)$ is related to the refractory effects and $R(n)$ is related to the accommodation effects. Then the general equation (6.2.1) can be expanded with $Q(n)$and $R(n)$,

$$\omega_n = \left\{ \begin{array}{c} R(1) \qquad n = 1 \\ R(2)[1-R(1)] + Q(2)\cdot R(1) \qquad n = 2 \\ \sum_{j=3}^{n}\left[R(j)\cdot\prod_{m=1}^{j-1}\left(1-R(m)\right)\right] + \sum_{j=3}^{n}\left[R(1)\cdot Q(j)\cdot\prod_{m=2}^{j-1}\left(1-Q(m)\right)\right] + Q(2)\cdot R(1) \qquad n \in [3,20] \end{array} \right\} \tag{6.5.7}$$

6.6 Fitting the full history Markov model to the neurophysiological data

The expanded form of the general Markov model Eq.(6.5.7) consists of multivariate polynomial equations. The neurophysiological data presented in Chapter 3 contain ten sets of data. For each set (FE), we try to solve the polynomial equations Eq.(6.5.7) for twenty data points by the trust-region dogleg algorithm [131, 132].

6.6.1 Fitting the full history Markov model by the trust-region dogleg algorithm

To establish an overdetermined system, the number of equations has to be bigger than the number of variables. For such overdetermined system, if the equations are not linearly independent, it yields a single solution. There are twenty equations based on the twenty data points. Therefore, Eq.(6.5.7) can only contain twenty variables in order to make an overdetermined system. Assume after the tenth pulse the conditional probabilities converge to a steady state as,

$$\begin{aligned} Q(n) &= Q(10) \quad n \in [11,20] \\ R(n) &= R(10) \quad n \in [11,20] \end{aligned} \tag{6.6.1}$$

From a physiological aspect, Eq.(6.6.1) suggests that if the neuron did not fire for at least nine pulses which is about 45 ms, the refractory effects is removed and the accommodation effects does not build up for over ten pulses. The influences of the interpulse interactions on subsequent pulses ($n \geq 11$) are identical. This is consistent with the observations of the I/O curve analysis to the neurophysiological data.

The general objective function is referred as $F_n(x)$,

$$F_n(x) = \left\{ \begin{array}{c} R(1) - \omega_1 \qquad n = 1 \\ R(2)[1 - R(1)] + Q(2)R(1) - \omega_2 \;\; n = 2 \\ \sum_{j=3}^{n} \left[R(j) \cdot \prod_{m=1}^{j-1} \left(1 - R(m)\right) \right] + \sum_{j=3}^{n} \left[R(1) \cdot Q(j) \cdot \prod_{m=2}^{j-1} \left(1 - Q(m)\right) \right] + Q(2) \cdot R(1) - \omega_n \\ n \in [3,20] \end{array} \right\} \tag{6.6.2}$$

where x is the vector of the variables $[Q(n), R(1), R(n)] \quad n \in [2,10]$, with constraint of Eq.(6.6.1).

The goal of solving Eq.(6.5.7) is to find a vector x that makes all $F_n(x) = 0$. For polynomial equations, Newton's Method [133] is normally used to find the roots. Newton's Method attempts to generates a sequence x_n from an initial guess x_0 that converges towards x_* such that $F_n(x_*) = 0$. The search direction Δx is given by solving

$$J(x_n)\Delta x = -F_n(x_n) \tag{6.6.3}$$

where $J(x_n)$ is the n-by-n Jacobian matrix

$$J(x_n) = \begin{bmatrix} \nabla F_1(x_n)^T \\ \nabla F_2(x_n)^T \\ \vdots \\ \nabla F_n(x_n)^T \end{bmatrix} \tag{6.6.4}$$

Thus the next guess of x_{n+1} is given by

$$x_{n+1} = x_n - J(x_n) \setminus F_n(x_n) \tag{6.6.5}$$

where \ is the matrix left division in MATLAB .

It will converge towards a root of $F_n(x)$. Newton's Method can run into difficulties, when the matrix of $J(x_n)$ may be singular. Also Newton's method may not converge if the starting point is far from the solution.

For the multivariate polynomial equations, trust-region techniques (also known as the restricted step method) [134] are frequently used. Trust-region is a term to denote the subset of the region of the objective function $F_n(x_n)$. If an adequate model of the objective is found within the trust region then the region is expanded. Otherwise, the region is contracted. A merit function is developed to

decide if x_{n+1} is better or worse than x_n. The merit function $m(\Delta x)$ is modified from Newton's Method.

$$\min_{\Delta x} m(\Delta x) = \frac{1}{2} F_n(x_n)^T F_n(x_n) + \Delta x^T J(x_n)^T F_n(x_n) + \frac{1}{2} \Delta x^T J(x_n)^T J(x_n) \Delta x \tag{6.6.6}$$

The powell dogleg procedure [132] has been applied when computing the step Δx to minimize equation(6.6.6). The step Δx is constructed from a convex combination of a Cauchy step and a Gauss-Newton step for $F_n(x)$. The Cauchy step is calculated as

$$\Delta x_C = -\beta J(x_n)^T F_n(x_n) \tag{6.6.7}$$

where β is chosen to minimize(6.6.6).

The Gauss-Newton step is calculated by

$$\Delta x_{GN} = -J(x_n) \backslash F_n(x_n) \tag{6.6.8}$$

The step Δx is chosen such that

$$\Delta x = \Delta x_C + \lambda(\Delta x_{GN} - \Delta x_C) \tag{6.6.9}$$

where λ is the largest value in the interval [0,1] so that Δx is within the trust-region dimension. The trust-region dogleg algorithm is more robust than using the Gauss-Newton Method with a line search.

6.6.2 Validation of the trust-region dogleg algorithm: noise effects

To investigate the accuracy of the trust-region dogleg algorithm, another statistical data set is generated to validate this algorithm. First, we examine how

noise affects the accuracy. The statistical data is generated by the twenty-pulse-history Markov model Eq.(6.5.7) with a Gaussian noise,

$$T_n = \begin{Bmatrix} R(1) + D\cdot\xi(n) & n = 1 \\ R(2)[1-R(1)] + Q(2)\cdot R(1) + D\cdot\xi(n) & n = 2 \\ \sum_{j=3}^{n}\left[R(j)\cdot\prod_{m=1}^{j-1}\left(1-R(m)\right)\right] + \sum_{j=3}^{n}\left[R(1)\cdot Q(j)\cdot\prod_{m=2}^{j-1}\left(1-Q(m)\right)\right] & \\ +Q(2)\cdot R(1) + D\cdot\xi(n) & n\in[3,20] \end{Bmatrix} \tag{6.6.10}$$

where D is the intensity of noise, ξ is a Gaussian white noise source. In the test data, we simply assume that the conditional probabilities converges to a steady state after the third pulse, which is

$$\begin{aligned} Q(n) &= Q(3) \quad n\in[4,20] \\ R(n) &= R(3) \quad n\in[4,20] \end{aligned} \tag{6.6.11}$$

The Gaussian noise is added to mimic the variations in the neurophysiological data. The parameter values are given in Table 6-15. Three sets of test data are generated with different noise intensity e.

Table 6-15 Parameter values of the test data

$R(1)$	$R(2)$	$Q(2)$	$R(3)$	$Q(3)$
0.5	0.30	0.05	0.35	0.10

The first data set T_n^1 is generated without noise; the second data set T_n^2 is generated with noise intensity D_2, which is 5% of the mean value of T_n^1; the third data set T_n^3 is generated with noise intensity D_3, which is 10% of the mean value of T_n^1. Three data sets are fitted to the Eq.(6.5.7) with the constraint Eq.(6.6.11) by the trust-region dogleg algorithm. The fitting results are plotted in Figure 6-6,Figure 6-7 and Figure 6-8. The results are presented in Table 6-16. As $R(1)$ is the initial value T_1, only four variables are compared.

Table 6-16 Fitting results of the test data with different noise intensity by the trust-region dogleg algorithm

Noise intensity	$R(2)$	$Q(2)$	$R(3)$	$Q(3)$
0	0.30	0.05	0.35	0.10
5%	0.25	0.09	0.33	0.10
10%	0.34	0.01	0.39	0.11

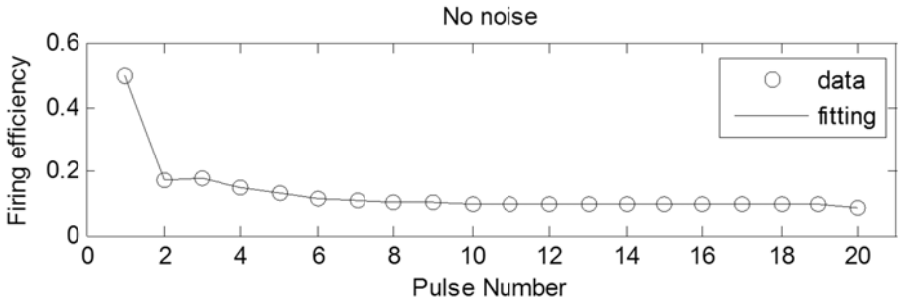

Figure 6-6 Fitting the noise free test data T_n^1 by the trust-region dogleg algorithm

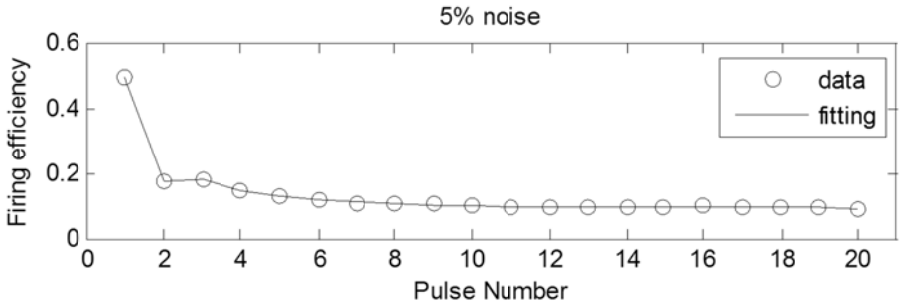

Figure 6-7 Fitting the 5% noise test data T_n^2 by the trust-region dogleg algorithm

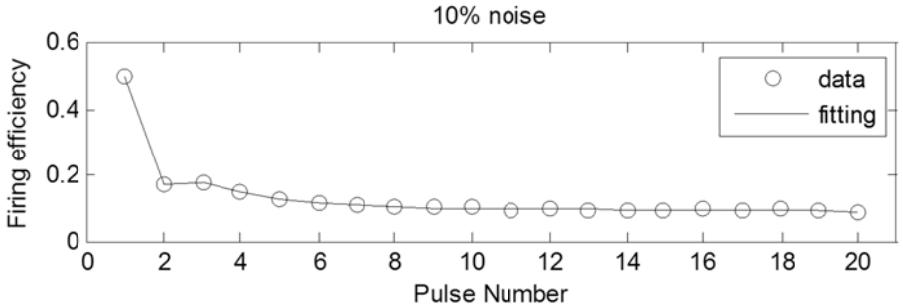

Figure 6-8 Fitting the 10% noise test data T_n^3 by the trust-region dogleg algorithm

In Table 6-16, the trust-region dogleg algorithm can find the exact solution to those four variables by fitting the noise free test data. Increasing the intensity of

the noise to 5%, the accuracy of the solution for $R(2), Q(2)$ and $R(3)$ degraded, but it still finds the exact solution for $Q(3)$. When the noise intensity is increased to 10%, the trust-region dogleg algorithm cannot find any exact solution. Although even the solutions to the third data set provide a good fit as shown in Figure 6-8, the solution can only provide a qualitative estimation of the conditional firing probability. The fitting results are greatly influenced by the intensity of the noise, especially for the conditional probabilities of small value, such as $Q(2)$.

6.6.3 Validation of the trust-region dogleg algorithm: convergence time effects

The fitting results for the test data T_n^1 are accurate. However, it is not clear after what period the conditional probabilities in the neurophysiological data will converge. Thus we try to examine how the convergence time affects the accuracy of fitting. In practice, the convergence time is actually the added constraints.

We still use the test data set T_n^1 (noise free), in which the conditional probabilities converge after three pulses. But we fit this test data to Eq.(6.5.7) with different constraints. For example, if the convergence time is assumed as m pulses time, then the constraint is

$$\begin{matrix} R(n) = R(m) \\ Q(n) = Q(m) \end{matrix} \quad n \in [m+1, 20] \tag{6.6.12}$$

The test data set T_n^1 is fitted to Eq.(6.5.7) with convergence time from three pulses to six pulses. In each row, the conditional probabilities are omitted after it has converged.

Table 6-17 Fitting results of the test data to Eq.(6.5.7) with different convergence time by the trust-region dogleg algorithm

Converg-ence time	$R(2)$	$Q(2)$	$R(3)$	$Q(3)$	$R(4)$	$Q(4)$	$R(5)$	$Q(5)$	$R(6)$	$Q(6)$
3 pulses	0.300	0.050	0.350	0.100						
4 pulses	0.300	0.050	0.350	0.100	0.350	0.100				
5 pulses	0.300	0.050	-0.157	0.473	0.090	0.096	0.056	0.056		
6 pulses	0.300	0.050	0.070	0.306	0.022	0.246	0.074	0.073	0.062	0.062

The results in Table 6-17 indicate that the trust-region dogleg algorithm successfully finds the solution for the convergence time of three pulses and four pulses. When the convergence time is two-pulse time longer than the actual time in the test data T_n^1, the trust-region dogleg algorithm over fits. The converged conditional firing probabilities, $R(5)|_{5\ pulses}$, $Q(5)|_{5\ pulses}$, $R(6)|_{6\ pulses}$ and $Q(6)|_{6\ pulses}$, are not even close to their values in the test data. Interpreting such conditional probabilities may be misleading. This experiment suggests that the convergence time is crucial to the fitting.

Therefore, the trust-region dogleg algorithm can accurately find the solution of Eq. (6.5.7) for noise free data with accurate convergence time. The accuracy of fitting degraded as noise intensity in the data increased. The accuracy of the fitting also depends on the accuracy of the convergence time.

The I/O curve analysis in Figure 4-3 suggests that firing probability converges to a steady state after three or four pulses. Therefore, the full history Markov renewal process model Eq.(6.5.7) is fitted with four different convergence time: 3 pulses, 4 pulses, 5 pulses and 6 pulses.

6.7 Results of the full history Markov renewal process model

The full history Markov renewal process model Eq.(6.5.7) is fitted to the neurophysiological data by the trust-region dogleg algorithm. The fitting results for convergence times of 3, 4 and 5 pulses are almost identical. The results successfully represent the neurophysiological data, especially the dynamics in the first few pulses which are not captured by the stationary Markov model. However, the results for a convergence time of 6 pulses may over fit to the noise. The PST histogram of FE=0.4 are presented in Figure 6-9 as an example.

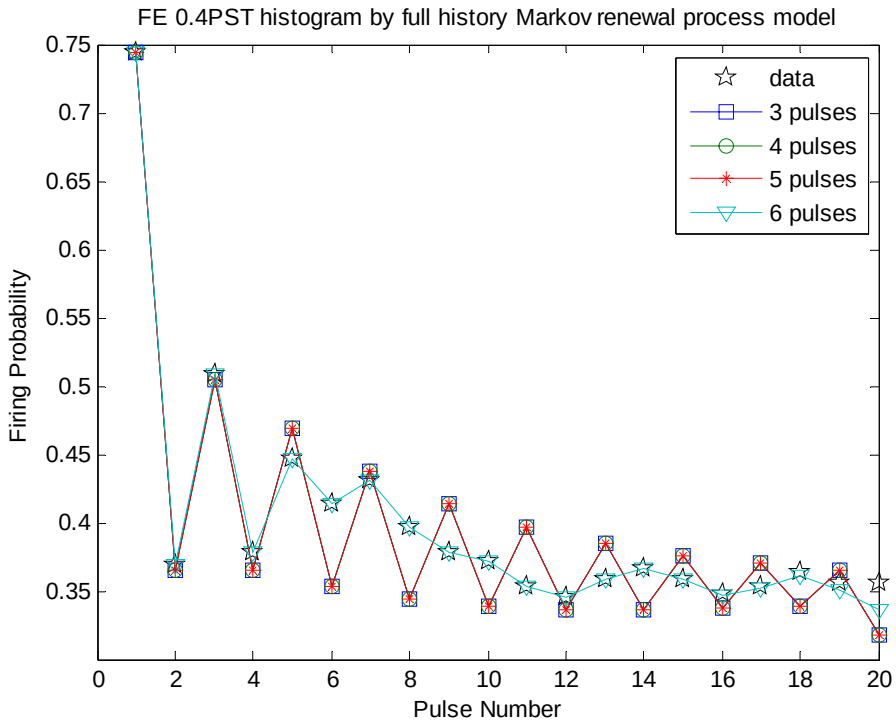

Figure 6-9 PST histogram calculated by the fitted full history Markov renewal process model. The neurophysiological data are plotted in pentagrams. The results for convergence time of 3 pulses is plotted in a solid line with square markers; the results for convergence time of 4 pulses is plotted in a solid line with circle markers; the results for convergence time of 5 pulses is plotted in a solid line with asterisk markers and the results for convergence time of 6 pulses is plotted in a solid line with downward-pointing triangle markers.

Moreover, the conditional probabilities at each FE are plotted in the following figures, where $R(n)$ is plotted in a solid line with asterisk markers and $Q(n)$ is plotted in a dotted line with square markers, ω_1 is plotted in stars markers for comparison. As the fitting results of convergence time of 3 pulses, 4 pulses and 5 pulses completely overlap, only one result is drawn in the figure.

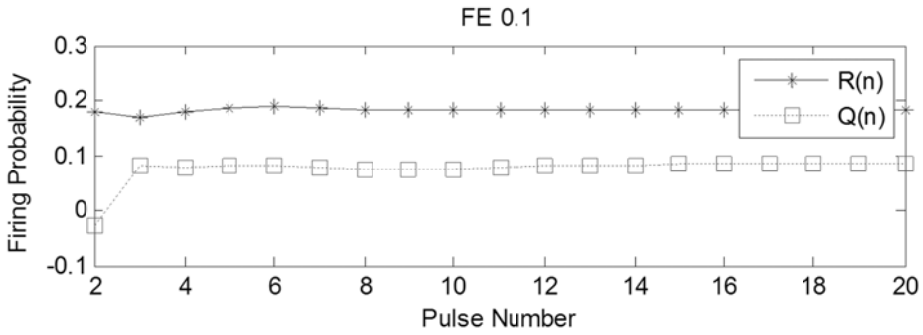

Figure 6-10 Fitted conditional probability of Eq.(6.5.7) at FE 0.1

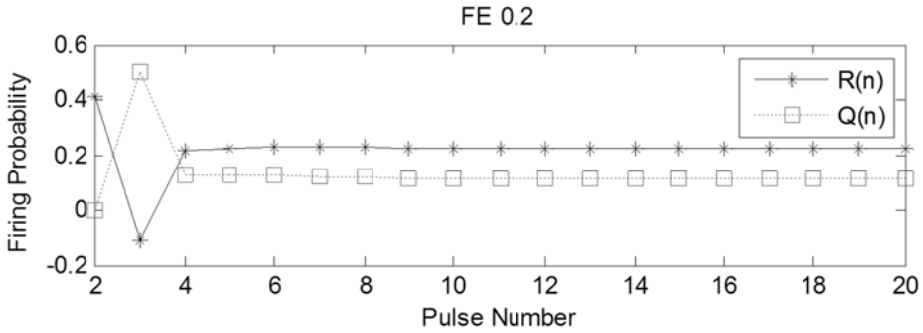

Figure 6-11 Fitted conditional probability of Eq.(6.5.7) at FE 0.2

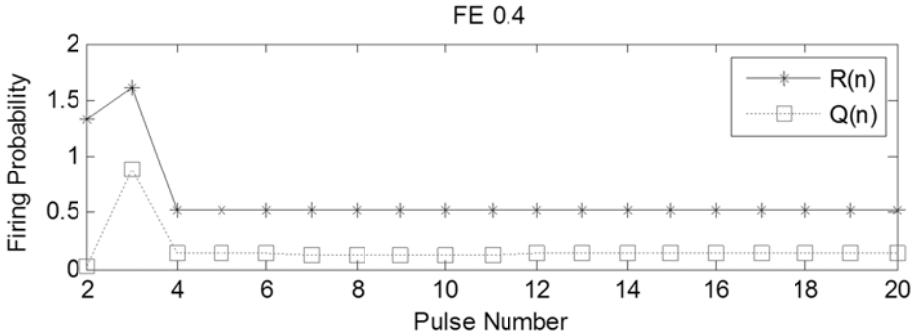

Figure 6-12 Fitted conditional probability of Eq.(6.5.7) at FE 0.4

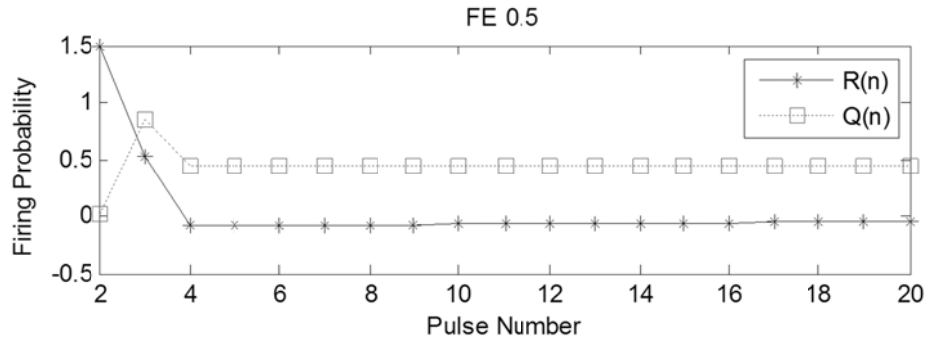

Figure 6-13 Fitted conditional probability of Eq.(6.5.7) at FE 0.5

The results for $Q(n)$ show how the refractory effects influence the firing and the results for $R(n)$ show how the accommodation effects influence the firing. Although some of the conditional probabilities are out of the physiological reasonable range, observations from these results can still provide a qualitative analysis on the interpulse interactions:

1. The fitted conditional probabilities $R(2)$ for high FE ($FE \geq 0.5$) are out of the physiological reasonable range. $R(2) = P(2|0)$. It suggests at high FE the probability of firing at the second pulse given it did not fire at the first pulse is so high that it seems inevitable, which has a probability of 1 or even more.
2. The fitted conditional probabilities $R(n)$ of low FE ($FE < 0.4$) decrease after the first pulse. As $R(n)$ is removed from the refractory effects, the suppression is only related to the accommodation effects. The suppression starts from the first pulse, lasts for two-pulses, slowly recovers from the third pulse and finally converges to a steady state at the fourth pulse.
3. The fitted conditional probabilities $Q(2)$ for all FE are close to zero. Then there is a boost in $Q(3)$, even for 0.05 FE. It can be partly explained as: for high FE the neuron enters the refractory effects after being discharged

on the first pulse; and it is still in the refractory period when the second pulse is applied; on the third pulse the firing probabilities are increased due to the undershoot after the refractory period; and it recovers to a steady state at the fourth pulse. For Low FE, the shape of $Q(n)$ is similar to that for high FE. It is not clear whether there is a significant overshoot pattern in the refractory function or the probability $Q(n)$ is messed by the variations in the neurophysiological data.

4. Stable recordings from single auditory nerve fibres are viable for short periods of time. It is suggested that the error of measurement is greater at low FE. It may in part explain the variations in the conditional probabilities at low FE. To overcome the firing stability of one nerve fibre, the data were pooled across the auditory nerve fibres within defined ranges of FE. This may partly explain the shifting phenomena in the conditional probabilities. As the Markov renewal process models are sensitive to the noise and fluctuations in the threshold, this pooling approach degraded the accuracy of the conditional probability analysis, especially for low FEs ($\mathrm{FE} < 0.4$).

These observations are basically consistent with the observations of Table 6-8. The difference between those two observations relies on the convergence time and the level of the steady state. The convergence time is actually defined by the model itself. Further experimental work on direct study of the ISI histogram would be helpful in refining the constraint of the convergence time and even the refractory function and accommodation function.

6.8 Conclusion

This chapter studied the interpulse interactions in the neural response to pulse-train stimuli by a Markov renewal process model. Previous statistical models have predicted good results for the refractory effects only [45, 46, 69, 123, 124], however, they did not concern the accommodation effects in the interpulse interactions. The proposed Markov renewal process model gives a direct measure of the conditional probabilities that are related to the accommodation effects or the refractory effects.

Both the stationary second order Markov model and the full history Markov model are fitted to the neurophysiological data. The stationary second order Markov model can only fit the gradient data due to drifting in the parameter k. By comparison with some test data, the drifting phenomenon is found to be related to the variations in the threshold rather than the membrane noise. Moreover, it also proves that the LIFDT model cannot capture the neurophysiological data due to the lack of such variations. The full history Markov model is successfully fitted to the neurophysiological data. The investigation of the conditional probabilities provides a separate estimation of the accommodation effects and the refractory effects.

Chapter7. *Conclusion*

7.1 Summary

The phenomenological LIFDT model (Eq.(3.3.1)—Eq.(3.3.4)) was presented in Chapter 3. This LIFDT model had previously been validated by neural responses of the sciatic nerve of the toad *Xenopus laevis* to sinusoidal electrical stimulation. In this thesis, we have further investigated the use of the LIFDT model to pulsatile electrical stimulation. Specifically, the LIFDT model was fitted to neurophysiological data (presented in Chapter 3). Extracellular recordings were made from the central axon of single auditory nerve fibres of the adult guinea pig, which is a physiological model of the electrically simulated cochlea nerve. Four models were fitted to these neurophysiological data in this thesis.

First, a simple I/O curve model was developed in Chapter 4 to constrain the parameters. As the simple I/O curve model avoided the complication of interpulse interactions, it only provided approximate ranges of the parameters which controls the membrane potential in the LIFDT model, such as τ_m and D. Other unknown parameters were fitted "by hand". The initial assessment of fitting only predicted the equilibrium firing rate but not the dynamics due to accommodation effects.

Second, in order to investigate whether the LIFDT model is sufficient to capture the dynamics in the neurophysiological data, analytical approximations of the LIFDT model to electrical pulsatile stimuli were developed in Chapter 5.

Comparisons were made between predictions by the theoretical LIFDT model and Monte Carlo simulations of the LIFDT model. The predictions of the

theoretical models to single pulse stimuli agree with the simulation results, which can predict accurate firing probabilities for the first pulse from the neurophysiological data. The results indicated that the auditory nerve response to single electrical pulses can be described by a simple, computationally efficient theoretical model.

Then the analytical version of LIFDT model was extended to describe the firing probabilities in response to pulse-train stimuli. In this thesis, the analytical version of LIFDT model only incorporated the accommodation effects and excluded the refractory effects. In other words, it was assumed that if the neuron had fired, the refractory effects was fully recovered when the next pulse was applied. The application of these analytical models permits direct measurement of suppression of firings due to accommodation effects. Then suppression of firings due to the refractory effects can be calculated by comparing the theoretical predictions and the simulation results. Furthermore, the impacts of parameter selections on I/O curves and interpulse interactions were fully studied.

The results showed that although the parameter values were optimized to achieve the maximum accommodation effects, to the extent that it led to physiological unreasonable refractory effects in the simulation result, it was still smaller than the accommodation in the neurophysiological data. Hence the LIFDT model cannot capture the dynamics in the neurophysiological data.

Finally, the interpulse interactions were modelled by a statistical Markov renewal process model in Chapter 6. As was investigated in section 6.1, most statistical models of auditory nerve responses to pulse-train electrical stimulations exclude the accommodation effects and only study the neural response of the steady state

stationary and non-stationary Markov renewal process models were considered. Conditional probabilities can be calculated and compared directly. The second order stationary Markov model accurately predicted the increment of firing probabilities between consecutive pulses to the 200 pps pulse trains. The results also indicated that the conditional firing probabilities slowly vary over time (by pulse number) and hence the stationary Markov model cannot predict the firing probabilities. The non-stationary Markov model sustantially predicted the dynamics in the neurophysiological data. And the fitted conditional firing probabilities provide a description of the accommodation and refractory effects.

7.2 Implications for computational modelling of auditory neurons

7.2.1 Accommodation effects on auditory nerve response

In Chapter 4 the I/O curve analysis revealed that both accommodation effects and refractory effects contributed to the neural response to pulse train stimuli from the neurophysiological data. It indicated that accommodative mechanisms dominate the temporal response at lower firing probabilities ($\mathrm{FE} < 0.2$). The accommodation mechanisms were also observed from the tuning curves in the electrophysiological data [17, 38] and loudness and perceptual threshold in the psychophysical data [20]. Therefore, the accommodation mechanisms are crucial when modelling the firing pattern to low stimulus amplitudes.

Computational auditory models which do not include accommodation mechanisms, such as [27, 46, 70], cannot predict these neurophysiological data. The LIFDT model is investigated to fit the experimental data, as it incorporates both accommodation effects and refractory effects. In the LIFDT model the time constant of h, which loosely equates to the inactivation of sodium permeability in

the FH model, regulates both the accommodative mechanism and the refractory mechanism. However, the results in Chapter 5 suggested that those two interpulse interactions have similar but different time constants. Therefore, the existing LIFDT model cannot capture accommodation effects in the data.

In Chapter 6, these two interpulse interactions were investigated by two Markov renewal process models. The Markov renewal process models are sensitive to the noise in the data and the convergence time of conditional probabilities. The consistent fitting results of the I/O curve model, the stationary Markov model and the non-stationary Markov model provided a better understanding of the accommodation:

1. The size of the accommodation effects is dependent on the amplitude of the stimulus.
2. Under subthreshold stimuli, the accommodation effects suppresses the firing probability of the auditory nerve. And it has great influence on the threshold.
3. The accommodative behaviour recovers after around 15ms.
4. As the PST histograms in the neurophysiological data were presented by the discrete pulse number, the results only gave a qualitative description of the dynamics due to accommodation effects.

The results of this thesis indicate the LIFDT model is applicable for pulsatile electrical stimulation when investigating the long term property of the auditory nerve. When investigating the short term property, the non-stationary Markov renewal process model is more efficient.

7.3 Future work

The usefulness of the LIFDT model to pulsatile electrical stimulation is limited. It is desirable to apply more experimental data to further modify the accommodation mechanisms by adding extra variables and equations. In particular, experimental data which reveal accommodation effects in the form of ISIHs or PST histograms from a single auditory nerve fibre may help to validate the model or suggest improvements to it.

The results of this thesis indicate the utility of analytical versions of the LIFDT model and statistical Markov models in investigating the interpulse interactions of the auditory nerve fibre. The analytical version of the LIFDT model only considers the accommodation effects and excludes the refractory effects. This has been done in order to demonstrate that the LIFDT model is insufficient to produce reasonable predictions of neurophysiological data. However, the analytical version may be extended to incorporate refractory effects. The full neural response can be modelled by statistical Markov models, in which the conditional firing probabilities can be calculated by the analytical version of the LIFDT model accordingly. This would complete the analytical predictions of the LIFDT model for pulse-train response and provide more quantitative evaluations of the interpulse interactions. Also it would further facilitate the fitting to other experimental data instead of exhaustive simulations.

The next step would be to extend the LIFDT model to fit psychophysical data. As the analytical version of the LIFDT model is computationally efficient, it can be easily applied to psychophysical tasks which require simulating a large population of nerve fibres. Psychophysical data may further assist in

understanding the relationship between the perception of stimuli generated by cochlear implants and the underlying temporal pattern of auditory nerve responses.

Appendix A Code for LIFDT model with two –step Heun scheme:

```
clear all
close all
%load stimulus,
load I2001N.mat

%define n ,t,v,v',w,
N=1e6;M=1;NN=28000;u=4000;
t=linspace(0,1,N);
tlap=t(1:N)-u/N;
hh=1/N;
num=zeros(1,NN);
spike=zeros(M,NN);
pp=zeros(1,N);

%initial value
Abs=1000;
a=zeros(1,NN);st=zeros(1,NN);th=zeros(1,NN);
III=[I(1:14000),zeros(1,NN-14000)];
tor=0.0007;
htor=0.0019;
D=0.01;
tabs=0.000284;
mu=-4.5;sigma=100;
thm=32.2;th0=0;p=1.3;f=200;

for j=1:M

v=zeros(1,NN);V1=zeros(1,NN);vprime=zeros(1,NN);vprime1=zeros(1,N
N);a=zeros(1,NN);es=randn(1,NN);st=zeros(1,NN);h=zeros(1,NN);h1=z
eros(1,NN);hprime=zeros(1,NN);hprime1=zeros(1,NN);hinf=zeros(1,NN
);
        th=zeros(1,NN);
        v(1)=0;v1(1)=0;
        h(1)=1/(1+exp((v(1)-mu)/sigma));
        h1(1)=h(1);
        th(1)=thm/(h(1)^p)+th0;
        hinf(1)=h(1);
        %Heunse Method
        for i=2:NN
            vprime(i)=(III(i)*Abs-v(i-1))/tor;
            v1(i)=v(i-1)+sqrt(2*D*hh)*es(i)/tor+vprime(i)*hh;
            vprime1(i)=(III(i)*Abs-v1(i-1))/tor;
            v(i)=v(i-
1)+sqrt(2*D*hh)*es(i)/tor+hh*(vprime(i)+vprime1(i))/2;
            hinf(i)=(1+exp((v(i)-mu)/sigma))^(-1);
            hprime(i)=(-h(i-1)+hinf(i-1))/htor;
            h1(i)=h(i-1)+hprime(i)*hh;
            hprime1(i)=(-h1(i-1)+hinf(i-1))/htor;
            h(i)=h(i-1)+hh*(hprime(i)+hprime1(i))/2;
            th(i)=thm/(h(i)^p)+th0;
```

```
            if a(i)> tabs
                st(i)=0;
                st(i+1)=0;
                a(i+1)=a(i)+1/N;
            end

                if st(i)==1
                    if a(i)<tabs
                       st(i+1)=st(i);
                       a(i+1)=a(i)+1/N;
                    end
                end

                if st(i)==0
                    if v(i)> th(i)
                        spike(j,i)=1;
                        h(i)=0;
                        v(i)=0;
                        num(j)=num(j)+1;
                        st(i+1)=1;
                        a(i+1)=0;
                    end
                end
                i=i+1;
            end
            j=j+1;
end
```

Appendix B Proofs for Chapter 5

Proof of analytical approximation of LIFDT model to a subthreshold pulse-train stimulus

For 200pps pulse-train stimulus, the second pulse is delivered 5ms after the first pulse. Thus the stimulus second can be described as

$$S(t)=\begin{Bmatrix} A & 0<t<T_1 \\ 0 & T_1\le t\le T_1+T_2 \\ -A & T_1+T_2<t<2T_1+T_2 \\ 0 & 2T_1+T_2<t<t_2 \\ A & t_2<t<t_2+T_1 \\ 0 & t_2+T_1\le t\le t_2+T_1+T_2 \\ -A & t_2+T_1+T_2<t<t_2+2T_1+T_2 \\ 0 & t\ge t_2+2T_1+T \end{Bmatrix}$$

$$\begin{aligned} &= A\cdot[u(t)-u(t-T_1)-u(t-T_1-T_2)+u(t-2T_1-T_2)] \\ &+A\cdot[u(t-t_2)-u(t-t_2-T_1)-u(t-t_2-T_1-T_2)+u(t-t_2-2T_1-T_2)] \end{aligned} \tag{8.1.1}$$

Then the differential equation of the membrane potential Eq.(5.2.2) can be solved as

$$\begin{aligned} V(t) &= A(1-e^{-t/\tau_m})\cdot u(t) \\ &-A(1-e^{-(t-T_1)/\tau_m})\cdot u(t-T_1) \\ &-A(1-e^{-(t-T_1-T_2)/\tau_m})\cdot u(t-T_1-T_2) \\ &+A(1-e^{-(t-2T_1-T_2)/\tau_m})\cdot u(t-2T_1-T_2) \\ &+A(1-e^{-(t-t_2)/\tau_m})]\cdot u(t-t_2) \\ &-A(1-e^{-(t-T_1-t_2)/\tau_m})\cdot u(t-T_1-t_2) \\ &-A(1-e^{-(t-T_1-T_2-t_2)/\tau_m})\cdot u(t-T_1-T_2-t_2) \\ &+A(1-e^{-(t-2T_1-T_2-t_2)/\tau_m})\cdot u(t-2T_1-T_2-t_2) \end{aligned} \tag{8.1.2}$$

The linear approximation, Eq.(5.2.7), is still valid for $h_\infty(t)$. Substituting the linear equation, Eq.(8.1.2), into Eq.(3.3.2) to give,

$$\tau_h\dot{h}(t)=-h(t)+b\cdot V(t)+c \tag{8.1.3}$$

and applying Laplace transforms to both sides of Eq.(4.3.29), still using the standard over bar to denote the Laplace Transform, yields

$$\tau_h\cdot\mathcal{L}\{\dot{h}(t)\}=-\mathcal{L}\{h(t)\}+b\cdot\mathcal{L}\{V(t)\}+\mathcal{L}\{c\} \tag{8.1.4}$$

which implies that

$$\tau_h\cdot[s\cdot\bar{h}(s)-h(0)]=-\bar{h}(s)+b\cdot\bar{V}(s)+\frac{c}{s} \tag{8.1.5}$$

Solving for $\bar{h}(s)$ gives

$$\bar{h}(s) = \frac{h(0)}{s + 1/\tau_h} + \frac{b \cdot \bar{V}(s)/\tau_h}{s + 1/\tau_h} + \frac{c/\tau_h}{s^2 + s/\tau_h} \tag{8.1.6}$$

The second part of Eq.(4.3.32) is in the form of the product of two known Laplace Transforms which are

$$\mathcal{L}^{-1}\left\{\frac{b/\tau_h}{s + 1/\tau_h}\right\} = \frac{b}{\tau_h} \cdot e^{-t/\tau_h} \cdot u(t) \tag{8.1.7}$$

$$\mathcal{L}^{-1}\left\{\bar{V}(s)\right\} = V(t) \tag{8.1.8}$$

According to the convolution theorem,

$$\mathcal{L}^{-1}\left\{\bar{V}(s) \cdot \frac{b/\tau_h}{s + 1/\tau_h}\right\} = V(t) \otimes \frac{b}{\tau_h} \cdot e^{-t/\tau_h} = \frac{Ab}{\tau_h} \int_0^t V(q) \cdot e^{-(t-q)/\tau_h} dq \tag{8.1.9}$$

Taking the inverse Laplace transform of Eq.(4.3.32) to get the general solution,

$$h(t)=\mathcal{L}^{-1}\left\{\frac{h(0)}{s+1/\tau_h}\right\}+\mathcal{L}^{-1}\left\{\frac{b\cdot\bar{V}(s)/\tau_h}{s+1/\tau_h}\right\}+\mathcal{L}^{-1}\left\{\frac{c/\tau_h}{s^2+s/\tau_h}\right\}$$

$$=h(0)\cdot e^{-t/\tau_h}+\frac{Ab}{\tau_h}\int_0^t V(q)\cdot e^{-(t-q)/\tau_h}dq+h(0)\cdot[1-e^{-t/\tau_h}]$$

$$=h(0)+Ab\cdot(1-e^{-t/\tau_h}-\frac{\tau_m}{\tau_m-\tau_h}e^{-t/\tau_m}+\frac{\tau_m}{\tau_m-\tau_h}e^{-t/\tau_h})\cdot u(t)$$

$$-Ab\cdot(1-e^{-(t-T_1)/\tau_h}-\frac{\tau_m}{\tau_m-\tau_h}e^{-(t-T_1)/\tau_m}+\frac{\tau_m}{\tau_m-\tau_h}e^{-(t-T_1)/\tau_h})\cdot u(t-T_1)$$

$$-Ab\cdot(1-e^{-(t-T_1-T_2)/\tau_h}-\frac{\tau_m}{\tau_m-\tau_h}e^{-(t-T_1-T_2)/\tau_m}+\frac{\tau_m}{\tau_m-\tau_h}e^{-(t-T_1-T_2)/\tau_h})\cdot u(t-T_1-T_2)$$

$$+Ab\cdot(1-e^{-(t-2T_1-T_2)/\tau_h}-\frac{\tau_m}{\tau_m-\tau_h}e^{-(t-2T_1-T_2)/\tau_m}+\frac{\tau_m}{\tau_m-\tau_h}e^{-(t-2T_1-T_2)/\tau_h})\cdot u(t-2T_1-T_2)$$

$$+Ab\cdot(1-e^{-(t-t_2)/\tau_h}-\frac{\tau_m}{\tau_m-\tau_h}e^{-(t-t_2)/\tau_m}+\frac{\tau_m}{\tau_m-\tau_h}e^{-(t-t_2)/\tau_h})]\cdot u(t-t_2)$$

$$-Ab\cdot(1-e^{-(t-t_2-T_1)/\tau_h}-\frac{\tau_m}{\tau_m-\tau_h}e^{-(t-t_2-T_1)/\tau_m}+\frac{\tau_m}{\tau_m-\tau_h}e^{-(t-t_2-T_1)/\tau_h})\cdot u(t-t_2-T_1)$$

$$-Ab\cdot(1-e^{-(t-t_2-T_1-T_2)/\tau_h}-\frac{\tau_m}{\tau_m-\tau_h}e^{-(t-t_2-T_1-T_2)/\tau_m}+\frac{\tau_m}{\tau_m-\tau_h}e^{-(t-t_2-T_1-T_2)/\tau_h})\cdot u(t-t_2-T_1-T_2)$$

$$+Ab\cdot(1-e^{-(t-t_2-2T_1-T_2)/\tau_h}-\frac{\tau_m}{\tau_m-\tau_h}e^{-(t-t_2-2T_1-T_2)/\tau_m}+\frac{\tau_m}{\tau_m-\tau_h}e^{-(t-t_2-2T_1-T_2)/\tau_h})\cdot u(t-t_2-2T_1-T_2)$$

(8.1.10)

The response of $\theta(t)$ is calculated by taking Eq.(4.3.36) into Eq.(3.3.4).

The result at the first pulse is identical to section 5.2.1. Therefore, we only interested in the response at the second pulse. In order to investigate the accuracy of the theoretical response to the second pulse of pulse train 200pps (Eq.(8.1.2) and Eq.**Error! Reference source not found.**), the theoretical results are compared with simulation results in the following figures. In each figure, the response predicted by the theoretical model is plotted in the solid line with square markers, and the simulation result is plotted in dotted line with asterisk markers. To improve the visibility of these figures, only one out of every four data points is shown in each line. In addition, four timelines are displayed to distinguish the responses to different phases of the second pulse, which are $t=t_2$(start of the anodic phase), $t=t_2+T_1$ (end of the anodic phase), $t=t_2+T_1+T_2$ (start of the cathodic phase) and $t=t_2+2T_1+T_2$ (end of the cathodic phase).

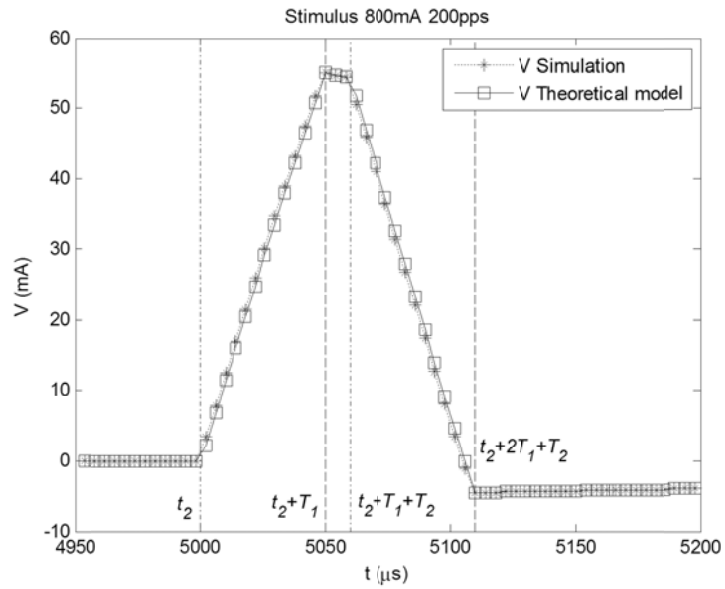

Figure-1 Membrane potential $\boldsymbol{V(t)}$ response to the second pulse of pulse train 200pps, Eq.(8.1.2).

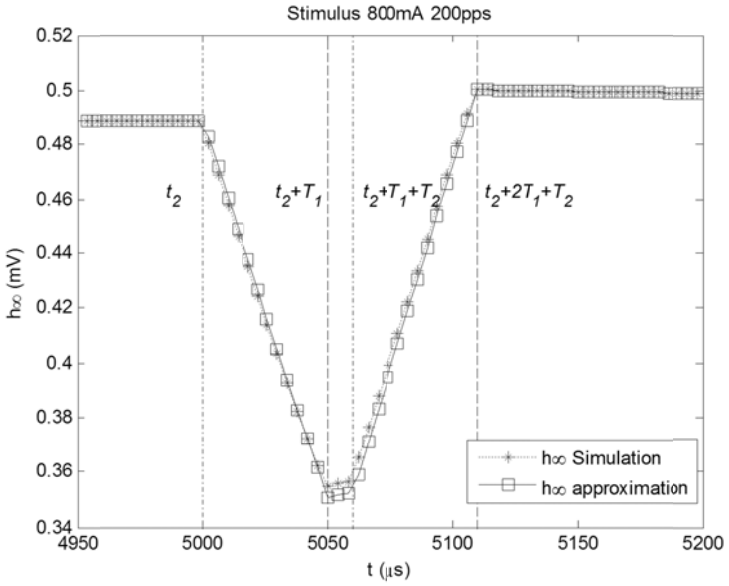

Figure-2 $\boldsymbol{h_\infty(t)}$ response to the second pulse of pulse train 200pps,

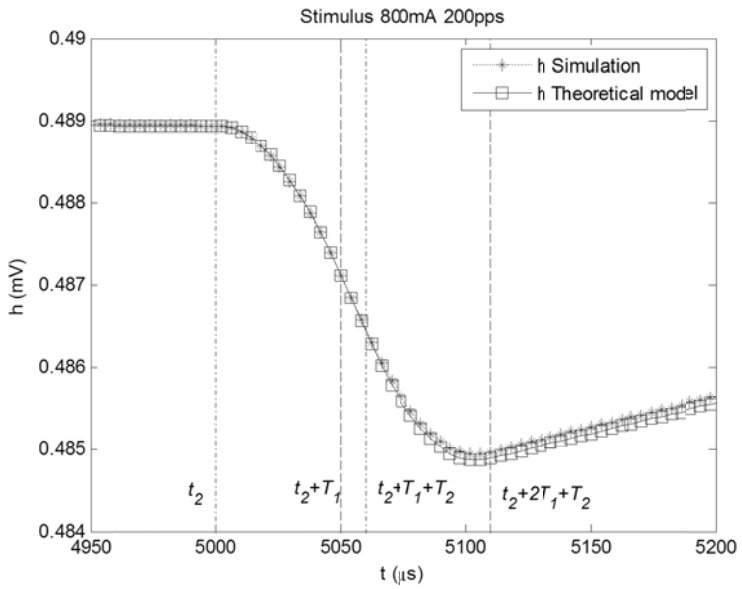

Figure -3 $\boldsymbol{h(t)}$ response to the second pulse of pulse train 200pps,

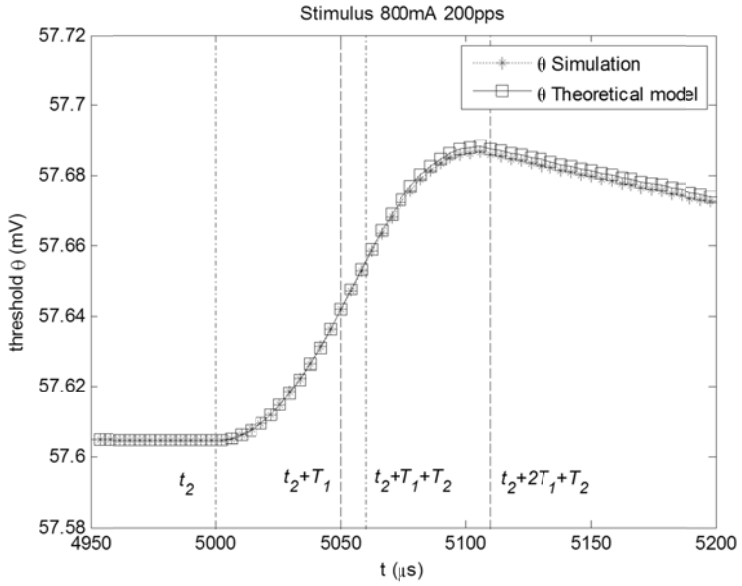

Figure -4 $\boldsymbol{\theta(t)}$ response to the second pulse of pulse train 200pps, Eq.(3.2.12).

The trends in the neural responses to the second pulse are similar to the first pulse responses. The membrane potential $V(t)$ increases monotonically during the anodic phase of each pulse (shown in Figure-1). It reaches the maximum voltage at the end of the anodic phase. Then $V(t)$ decreases monotonically and reaches the minimum voltage at the end of the cathodic phase. $V(t)$ slowly recovers to zero afterwards. The threshold $\theta(t)$ increases monotonically during the second pulse (shown in Figure -4). At the end of the cathodic phase, $\theta(t)$ obtains its maximum value. Then $\theta(t)$ recovers to its equilibrium value $\boldsymbol{\theta_{eq}}$, which is defined as

$$\theta_{eq} = \frac{\theta_m}{(h_\infty|_{V=0})^p} + \theta_0 \tag{8.1.11}$$

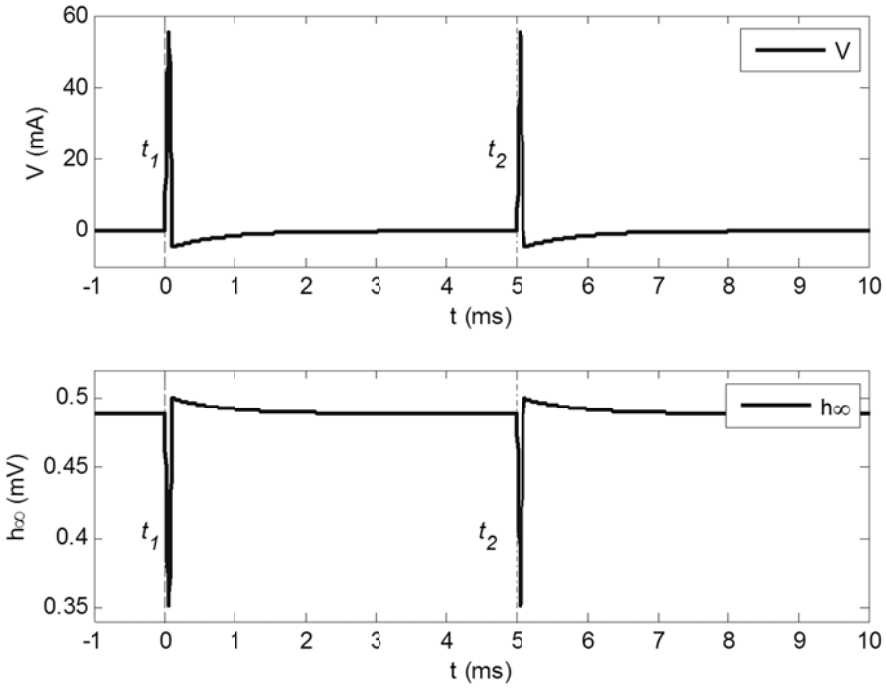

Figure-5 Theoretical predictions of $\boldsymbol{V(t)}$ and $\boldsymbol{h_\infty(t)}$ responses to a two-pulse stimulus (200pps), the dashed lines displays the time t= $\boldsymbol{t_1}$ and dash-dot line displays the time t= $\boldsymbol{t_2}$.

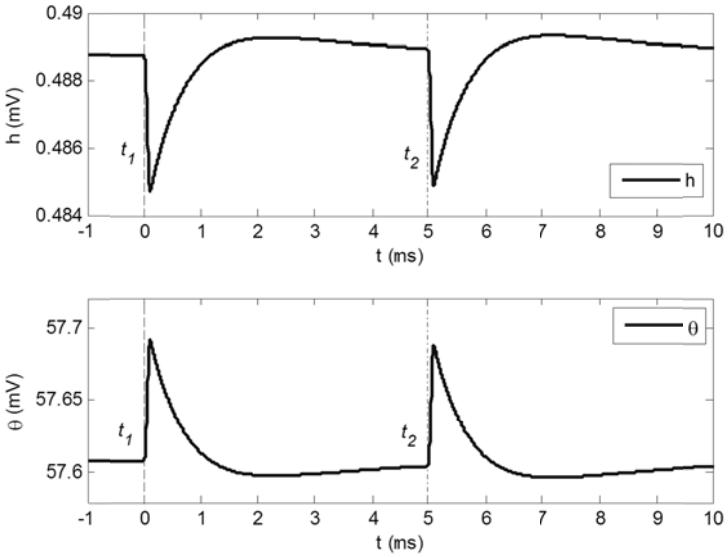

Figure-6 Theoretical predictions of $\boldsymbol{h(t)}$ and $\boldsymbol{\theta(t)}$ responses to a two-pulse stimulus (200pps). The dashed lines displays the time t= $\boldsymbol{t_1}$ and dash-dot line displays the time t= $\boldsymbol{t_2}$.

Thus, the only chance of firing on the second pulse is still at the end of the anodic phase. It depends on whether the maximum membrane potential, $V(t_2+T_1)$, crosses the threshold, $\theta(t_2+T_1)$.

Next, add the Gaussian noise to the deterministic LIFDT model for the second pulse. The noise is considered uncorrelated between pulses. However, it is suggested that the variance of the noise may increase with small, sustained depolarizations [120]. Due to the uncertainty about the noise, the standard deviation of noise remains constant as for the stochastic auditory nerve model [46] during interpulse interactions.

The probability of firing on the second pulse, $p(2)$, can be expressed on the basis of the theoretical model for a single-pulse stimulus as,

$$p(2) = \int_{\theta\big|_{t=t_2+T_1} - V\big|_{t=t_2+T_1}}^{\infty} \frac{1}{\sqrt{2\pi\sigma^2}} e^{-\frac{x^2}{2\sigma^2}} dx \tag{8.1.12}$$

where σ^2 is variance of the noise,

$$\begin{aligned} V\Big|_{t=t_2+T_1} = A(1 - e^{-T_1/\tau_m} - e^{-(t_2-T_1-T_2)/\tau_m} + e^{-(t_2-T_2)/\tau_m} \\ + e^{-t_2/\tau_m} - e^{-(T_1+t_2)/\tau_m}) \end{aligned} \tag{8.1.13}$$

and

$$\theta(t_2+T_1) = \frac{\theta_m}{h(t_2+T_1)^p} + \theta_0 \tag{8.1.14}$$

where $h(t_2+T_1)$ is calculated by Eq.(4.3.36)

Thus, Eq.(4.3.46) can be written as

$$p(2) = \frac{1}{2}(1 + erf\frac{V(t_2+T_1) - \theta(t_2+T_1)}{\sqrt{2}\sigma}) \tag{8.1.15}$$

References

1. Clark, G., *Cochlear Implants: Fundamentals and Applications*. Modern Acoustics and Signal Processing2003: Physics Today. 830.
2. Moore, D.R., et al., *The Oxford handbook of auditory science*. The Ear2010, Oxford: Oxford University Press.
3. Evans, E.F., *Auditory processing of complex sounds: an overview.* Philos Trans R Soc Lond B Biol Sci, 1992. **336**(1278): p. 295-306.
4. Kim, D.O., S.O. Chang, and J.G. Sirianni, *A population study of auditory-nerve fibers in unanesthetized decerebrate cats: response to pure tones.* J Acoust Soc Am, 1990. **87**(4): p. 1648-55.
5. Kim, D.O. and K. Parham, *Auditory nerve spatial encoding of high-frequency pure tones: population response profiles derived from d' measure associated with nearby places along the cochlea.* Hear Res, 1991. **52**(1): p. 167-79.
6. Nicholls, J.G., et al., *From neuron to brain : a cellular and molecular approach to the function of the nervous system*. 3rd ed1992, Sunderland, Mass.: Sinauer Associates. 92, 807 p.
7. Hill, A.V. *Excitation and Accommodation in Nerve*. in *Proceedings of the Royal Society* 1936. London.
8. Lucas, K., *Quantitative researches on the summation of inadequate stimuli in muscle and nerve, with observations on the time-factor in electric excitation.* J Physiol, 1910. **39**(6): p. 461-75.
9. Baker, M. and H. Bostock, *Depolarization changes the mechanism of accommodation in rat and human motor axons.* J Physiol, 1989. **411**: p. 545-61.
10. Vallbo, A.B., *Accommodation Related to Inactivation of the Sodium Permeability in Single Myelinated Nerve Fibres from Xenopus Laevis.* Acta Physiol Scand, 1964. **61**: p. 429-44.

11. Vallbo, A.B., *Accommodation of Single Myelinated Nerve Fibres from Xenopus Laevis Related to Type of End Organ.* Acta Physiol Scand, 1964. **61**: p. 413-28.
12. Krylov, B.V. and V.S. Makovsky, *Spike frequency adaptation in amphibian sensory fibres is probably due to slow K channels.* Nature, 1978. **275**(5680): p. 549-51.
13. Sachs, M.B. and E.D. Young, *Encoding of steady-state vowels in the auditory nerve: representation in terms of discharge rate.* J Acoust Soc Am, 1979. **66**(2): p. 470-9.
14. Clark, G.M., et al., *Temporal coding of frequency: neuron firing probabilities for acoustic and electric stimulation of the auditory nerve.* Ann Otol Rhinol Laryngol Suppl, 1995. **166**: p. 109-11.
15. Rose, J.E., et al., *Phase-locked response to low-frequency tones in single auditory nerve fibers of the squirrel monkey.* J Neurophysiol, 1967. **30**(4): p. 769-93.
16. Sly, D., et al., *The response of the auditory nerve to electrical stimulation following deafness*, in *Asilomar Cochlear Implant Conference*2005.
17. Sly, D.J., et al., *Deafness alters auditory nerve fibre responses to cochlear implant stimulation.* Eur J Neurosci, 2007. **26**(2): p. 510-22.
18. O'Leary, S.J., Y.C. Tong, and G.M. Clark, *Responses of dorsal cochlear nucleus single units to electrical pulse train stimulation of the auditory nerve with a cochlear implant electrode.* J Acoust Soc Am, 1995. **97**(4): p. 2378-93.
19. Allingham, D., N.G. Stocks, and R.P. Morse, *A phenomenological model of myelinated nerve with a dynamic threshold*: Coventry
20. White, M.W., M.M. Merzenich, and J.N. Gardi, *Multichannel cochlear implants. Channel interactions and processor design.* Arch Otolaryngol, 1984. **110**(8): p. 493-501.
21. Hinojosa, R. and J.R. Lindsay, *Profound Deafness: Associated Sensory and Neural Degeneration.* Arch Otolaryngol, 1980. **106**(4): p. 193-209.
22. Hinojosa, R. and M. Marion, *Histopathology of profound sensorineural deafness.* Ann N Y Acad Sci, 1983. **405**: p. 459-84.

23. Colombo, J. and C.W. Parkins, *A model of electrical excitation of the mammalian auditory-nerve neuron.* Hearing Research, 1987. **31**(3): p. 287-311.
24. !!! INVALID CITATION !!!
25. Wever, E.G. and C.W. Bray, *Action Currents in the Auditory Nerve in Response to Acoustical Stimulation.* Proc Natl Acad Sci U S A, 1930. **16**(5): p. 344-50.
26. Tasaki, I., *Nerve impulses in individual auditory nerve fibers of guinea pig.* J Neurophysiol, 1954. **17**(2): p. 97-122.
27. Kiang, N.Y., et al., *Stimulus Coding in the Cochlear Nucleus.* Ann Otol Rhinol Laryngol, 1965. **74**: p. 463-85.
28. Doyle, J.B., Jr., et al., *Electrical Stimulation in Eighth Nerve Deafness. A Preliminary Report.* Bull Los Angel Neuro Soc, 1963. **28**: p. 148-50.
29. Doyle, J.H., J.B. Doyle, Jr., and F.M. Turnbull, Jr., *Electrical Stimulation of Eight Cranial Nerve.* Arch Otolaryngol, 1964. **80**: p. 388-91.
30. Tong, Y.C., et al., *Psychophysical studies evaluating the feasibility of a speech processing strategy for a multiple-channel cochlear implant.* J Acoust Soc Am, 1983. **74**(1): p. 73-80.
31. Simmons, F.B., *Electrical stimulation of the auditory nerve in man.* Arch Otolaryngol, 1966. **84**(1): p. 2-54.
32. Clark, G.M., et al., *The University of Melbourne--nucleus multi-electrode cochlear implant.* Adv Otorhinolaryngol, 1987. **38**: p. V-IX, 1-181.
33. Evans, E.F., J.P. Wilson, and T.A. Borerwe, *Animal models of tinnitus.* Ciba Found Symp, 1981. **85**: p. 108-38.
34. Eddington, D.K., *Speech discrimination in deaf subjects with cochlear implants.* J Acoust Soc Am, 1980. **68**(3): p. 885-91.
35. Møller, A.R., *Hearing : anatomy, physiology, and disorders of the auditory system*. 2nd ed2006, Amsterdam, NE ; Boston, MA: Elsevier/Academic Press. xiv, 309 p.
36. Moller, A.R., *Review of the roles of temporal and place coding of frequency in speech discrimination.* Acta Otolaryngol, 1999. **119**(4): p. 424-30.

37. Frankenhaeuser, B. and A.F. Huxley, *The Action Potential in the Myelinated Nerve Fiber of Xenopus Laevis as Computed on the Basis of Voltage Clamp Data.* J Physiol, 1964. **171**: p. 302-15.
38. Morse, R.P. and E.F. Evans, *The sciatic nerve of the toad Xenopus laevis as a physiological model of the human cochlear nerve.* Hearing Research, 2003. **182**(1-2): p. 97-118.
39. Schwarz, J.R. and G. Eikhof, *Na currents and action potentials in rat myelinated nerve fibres at 20 and 37 degrees C.* Pflugers Arch, 1987. **409**(6): p. 569-77.
40. Chiu, S.Y., et al., *A quantitative description of membrane currents in rabbit myelinated nerve.* J Physiol, 1979. **292**: p. 149-66.
41. Kiang, N.Y. and E.C. Moxon, *Physiological considerations in artificial stimulation of the inner ear.* Ann Otol Rhinol Laryngol, 1972. **81**(5): p. 714-30.
42. Pfingst, B.E., *Operating ranges and intensity psychophysics for cochlear implants. Implications for speech processing strategies.* Arch Otolaryngol, 1984. **110**(3): p. 140-4.
43. Hodgkin, A.L. and A.F. Huxley, *A quantitative description of membrane current and its application to conduction and excitation in nerve.* J Physiol, 1952. **117**(4): p. 500-44.
44. Kiang, N.Y., et al., *A block model of the cat cochlear nucleus.* J Comp Neurol, 1975. **162**(2): p. 221-45.
45. Miller, M.I. and K.E. Mark, *A statistical study of cochlear nerve discharge patterns in response to complex speech stimuli.* J Acoust Soc Am, 1992. **92**(1): p. 202-9.
46. Bruce, I.C., et al., *A stochastic model of the electrically stimulated auditory nerve: pulse-train response.* IEEE Trans Biomed Eng, 1999. **46**(6): p. 630-7.
47. Bruce, I.C., et al., *A stochastic model of the electrically stimulated auditory nerve: single-pulse response.* IEEE Trans Biomed Eng, 1999. **46**(6): p. 617-29.

48. Rubinstein, J.T., et al., *Pseudospontaneous activity: stochastic independence of auditory nerve fibers with electrical stimulation.* Hearing Research, 1999. **127**(1-2): p. 108-118.
49. Miller, C.A., P.J. Abbas, and J.T. Rubinstein, *An empirically based model of the electrically evoked compound action potential.* Hearing Research, 1999. **135**(1-2): p. 1-18.
50. Matsuoka, A.J., et al., *The neuronal response to electrical constant-amplitude pulse train stimulation: additive Gaussian noise.* Hearing Research, 2000. **149**(1-2): p. 129-137.
51. Bruce, I.C., et al., *Renewal-process approximation of a stochastic threshold model for electrical neural stimulation.* J Comput Neurosci, 2000. **9**(2): p. 119-32.
52. Rattay, F., P. Lutter, and H. Felix, *A model of the electrically excited human cochlear neuron. I. Contribution of neural substructures to the generation and propagation of spikes.* Hear Res, 2001. **153**(1-2): p. 43-63.
53. Allingham, D., et al., *Noise enhanced information transmission in a model of multichannel cochlear implantation*, in *Proc. SPIE Fluctuations and Noise in Biological, Biophysical, and Biomedical Systems II*, D.a.B. Abbott, SM and Der, A and Sanchez, A, Editor 2004, SPIE-INT SOC OPTICAL ENGINEERING. p. 139-148.
54. Woo, J., C.A. Miller, and P.J. Abbas, *Biophysical model of an auditory nerve fiber with a novel adaptation component.* IEEE Trans Biomed Eng, 2009. **56**(9): p. 2177-80.
55. Frijns, J.H.M., J. Mooij, and J.H. ten Kate, *A quantitative approach to modeling mammalian myelinated nerve fibers for electrical prosthesis design.* Biomedical Engineering, IEEE Transactions on, 1994. **41**(6): p. 556-566.
56. Hille, B., *Ionic channels of excitable membranes*1984, Sunderland, Mass: Sinauer Associates. 426 p.
57. Viemeister, N.F. and G.H. Wakefield, *Temporal integration and multiple looks.* J Acoust Soc Am, 1991. **90**(2 Pt 1): p. 858-65.

58. Gray, P.R., *Conditional probability analyses of the spike activity of single neurons.* Biophys J, 1967. **7**(6): p. 759-77.

59. Horikawa, Y., *Noise effects on spike propagation during the refractory period in the FitzHugh-Nagumo model.* J Theor Biol, 1993. **162**(1): p. 41-59.

60. Miller, C.A., P.J. Abbas, and B.K. Robinson, *Response properties of the refractory auditory nerve fiber.* J Assoc Res Otolaryngol, 2001. **2**(3): p. 216-32.

61. Lowen, S.B. and M.C. Teich, *Auditory-nerve action potentials form a nonrenewal point process over short as well as long time scales.* J Acoust Soc Am, 1992. **92**(2 Pt 1): p. 803-6.

62. Parzen, E. and Society for Industrial and Applied Mathematics., *Stochastic processes*, in *Classics in applied mathematics 24*1999, Society for Industrial and Applied Mathematics (SIAM, 3600 Market Street, Floor 6, Philadelphia, PA 19104): Philadelphia, Pa.

63. Schaette, R., T. Gollisch, and A.V. Herz, *Spike-train variability of auditory neurons in vivo: dynamic responses follow predictions from constant stimuli.* J Neurophysiol, 2005. **93**(6): p. 3270-81.

64. Deger, M., et al., *Nonequilibrium dynamics of stochastic point processes with refractoriness.* Phys Rev E Stat Nonlin Soft Matter Phys, 2010. **82**(2 Pt 1): p. 021129.

65. Tuckwell, H.C., *Introduction to theoretical neurobiology*. Cambridge studies in mathematical biology 81988, Cambridge [Cambridgeshire] ; New York: Cambridge University Press.

66. Bruce, I.C., et al., *The effects of stochastic neural activity in a model predicting intensity perception with cochlear implants: low-rate stimulation.* IEEE Trans Biomed Eng, 1999. **46**(12): p. 1393-404.

67. Morse, R.P. and E.F. Evans, *Enhancement of vowel coding for cochlear implants by addition of noise.* Nat Med, 1996. **2**(8): p. 928-932.

68. Morse, R.P. and E.F. Evans, *Additive noise can enhance temporal coding in a computational model of analogue cochlear implant stimulation.* Hearing Research, 1999. **133**(1-2): p. 107-119.

69. Yifang, X. and L.M. Collins, *Predicting the threshold of pulse-train electrical stimuli using a stochastic auditory nerve model: the effects of stimulus noise.* Biomedical Engineering, IEEE Transactions on, 2004. **51**(4): p. 590-603.

70. Yifang, X. and L.M. Collins, *Predicting dynamic range and intensity discrimination for electrical pulse-train stimuli using a stochastic auditory nerve model: the effects of stimulus noise.* Biomedical Engineering, IEEE Transactions on, 2005. **52**(6): p. 1040-1049.

71. Loizou, P.C., *Introduction to cochlear implants.* IEEE Eng Med Biol Mag, 1999. **18**(1): p. 32-42.

72. Loizou, P.C., et al., *Comparison of speech processing strategies used in the Clarion implant processor.* Ear Hear, 2003. **24**(1): p. 12-9.

73. Fitzhugh, R., *Impulses and Physiological States in Theoretical Models of Nerve Membrane.* Biophys J, 1961. **1**(6): p. 445-66.

74. Sigworth, F.J., *The variance of sodium current fluctuations at the node of Ranvier.* J Physiol, 1980. **307**: p. 97-129.

75. Ohmori, H., *Studies of ionic currents in the isolated vestibular hair cell of the chick.* J Physiol, 1984. **350**: p. 561-81.

76. Motz, H. and F. Rattay, *A study of the application of the Hodgkin-Huxley and the Frankenhaeuser-Huxley model for electrostimulation of the acoustic nerve.* Neuroscience, 1986. **18**(3): p. 699-712.

77. Horikawa, Y., *Noise effects on spike propagation in the stochastic Hodgkin-Huxley models.* Biol Cybern, 1991. **66**(1): p. 19-25.

78. Horikawa, Y., *Simulation study on effects of channel noise on differential conduction at an axon branch.* Biophys J, 1993. **65**(2): p. 680-6.

79. Lewis, E.R. and B.R. Parnas, *Theoretical bases of short-latency spike volleys in the peripheral vestibular system.* J Vestib Res, 1994. **4**(3): p. 189-202.

80. Zidanic, M. and P.A. Fuchs, *Kinetic analysis of barium currents in chick cochlear hair cells.* Biophys J, 1995. **68**(4): p. 1323-36.

81. Chow, C.C. and J.A. White, *Spontaneous action potentials due to channel fluctuations.* Biophys J, 1996. **71**(6): p. 3013-21.

82. Kistler, W.M., W. Gerstner, and J.L.v. Hemmen, *Reduction of the Hodgkin-Huxley Equations to a Single-Variable Threshold Model.* Neural Computation, 1997. **9**(5): p. 1015-1045.

83. Fox, R.F., *Stochastic versions of the Hodgkin-Huxley equations.* Biophys J, 1997. **72**(5): p. 2068-74.

84. Marsalek, P., *Coincidence detection in the Hodgkin-Huxley equations.* Biosystems, 2000. **58**(1-3): p. 83-91.

85. Rattay, F. and M. Aberham, *Modeling axon membranes for functional electrical stimulation.* Biomedical Engineering, IEEE Transactions on, 1993. **40**(12): p. 1201-1209.

86. Cartee, L.A., *Evaluation of a model of the cochlear neural membrane. II: comparison of model and physiological measures of membrane properties measured in response to intrameatal electrical stimulation.* Hear Res, 2000. **146**(1-2): p. 153-66.

87. Negm, M.H. and I.C. Bruce, *Effects of I(h) and I(KLT) on the response of the auditory nerve to electrical stimulation in a stochastic Hodgkin-Huxley model.* Conf Proc IEEE Eng Med Biol Soc, 2008. **2008**: p. 5539-42.

88. Woo, J., C.A. Miller, and P.J. Abbas, *Simulation of the electrically stimulated cochlear neuron: modeling adaptation to trains of electric pulses.* IEEE Trans Biomed Eng, 2009. **56**(5): p. 1348-59.

89. Fohlmeister, J.F., *Adaptation and accommodation in the squid axon.* Biol Cybern, 1975. **18**(1): p. 49-60.

90. Hagiwara, S. and Y. Oomura, *The critical depolarization for the spike in the squid giant axon.* Jpn J Physiol, 1958. **8**(3): p. 234-45.

91. Frankenhaeuser, B. and L.E. Moore, *The Effect of Temperature on the Sodium and Potassium Permeability Changes in Myelinated Nerve Fibres of Xenopus Laevis.* J Physiol, 1963. **169**: p. 431-7.

92. Frankenhaeuser, B., *Accommodation in single nerve fibres.* Acta Physiol Scand, 1953. **29**(1): p. 126-7.

93. Frankenhaeuser, B. and A.B. Vallbo, *Accommodation in Myelinated Nerve Fibres of Xenopus Laevis as Computed on the Basis of Voltage Clamp Data.* Acta Physiol Scand, 1965. **63**: p. 1-20.

94. Hartmann, R., G. Topp, and R. Klinke, *Discharge patterns of cat primary auditory fibers with electrical stimulation of the cochlea.* Hear Res, 1984. **13**(1): p. 47-62.

95. Dobie, R.A. and N. Dillier, *Some aspects of temporal coding for single-channel electrical stimulation of the cochlea.* Hearing Research, 1985. **18**(1): p. 41-55.

96. Derksen, H.E. and A.A. Verveen, *Fluctuations of resting neural membrane potential.* Science, 1966. **151**(716): p. 1388-9.

97. Morse, R.P. and P. Roper, *Enhanced coding in a cochlear-implant model using additive noise: Aperiodic stochastic resonance with tuning.* Physical Review E, 2000. **61**(5): p. 5683.

98. Rubinstein, J.T., *Threshold fluctuations in an N sodium channel model of the node of Ranvier.* Biophys J, 1995. **68**(3): p. 779-85.

99. Verveen, A.A., *Axon diameter and fluctuation in excitability.* Acta Morphol Neerl Scand, 1962. **5**: p. 79-85.

100. Mino, H., J.T. Rubinstein, and J.A. White, *Comparison of Algorithms for the Simulation of Action Potentials with Stochastic Sodium Channels.* Annals of Biomedical Engineering, 2002. **30**(4): p. 578-587.

101. Fox, R.F. and Y. Lu, *Emergent collective behavior in large numbers of globally coupled independently stochastic ion channels.* Phys Rev E Stat Phys Plasmas Fluids Relat Interdiscip Topics, 1994. **49**(4): p. 3421-3431.

102. Bruce, I.C., *Implementation issues in approximate methods for stochastic Hodgkin-Huxley models.* Ann Biomed Eng, 2007. **35**(2): p. 315-8; author reply 319.

103. Bruce, I.C., *Evaluation of stochastic differential equation approximation of ion channel gating models.* Ann Biomed Eng, 2009. **37**(4): p. 824-38.

104. Imennov, N.S. and J.T. Rubinstein, *Stochastic Population Model for Electrical Stimulation of the Auditory Nerve.* Biomedical Engineering, IEEE Transactions on, 2009. **56**(10): p. 2493-2501.

105. Mino, H., et al., *Effects of electrode-to-fiber distance on temporal neural response with electrical stimulation.* IEEE Trans Biomed Eng, 2004. **51**(1): p. 13-20.

106. Miller, C.A., et al., *Neural masking by sub-threshold electric stimuli: animal and computer model results.* J Assoc Res Otolaryngol, 2011. **12**(2): p. 219-32.

107. Lapicque, L., *Recherches quantitatives sur l'excitation électrique des nerfs traitée comme une polarisation.* J. Physiol. Pathol. Gen., 1907(9): p. 620-635.

108. Collins, L.M., R.L. Miller, and W.D. Ferguson, *On the relationship between noise and speech recognition in cochlear implant subject: a theoretical and psychophysical study,*, 2000, 9th DSP Workshop, Waldemar Ranch Resort, TX.

109. Pfingst, B.E. and D.J. Morris, *Stimulus features affecting psychophysical detection thresholds for electrical stimulation of the cochlea. II: Frequency and interpulse interval.* J Acoust Soc Am, 1993. **94**(3 Pt 1): p. 1287-94.

110. Stocks, N.G., *Suprathreshold stochastic resonance in multilevel threshold systems.* Phys Rev Lett, 2000. **84**(11): p. 2310-3.

111. Verveen, A.A. and H.E. Derksen, *Amplitude distribution of axon membrane noise voltage.* Acta Physiol Pharmacol Neerl, 1969. **15**(3): p. 353-79.

112. Verveen, A.A., H.E. Derksen, and K.L. Schick, *Voltage fluctuations of neural membrane.* Nature, 1967. **216**(5115): p. 588-9.

113. Feller, W., *An introduction to probability theory and its applications*. 3d ed. Wiley series in probability and mathematical statistics1967, New York,: Wiley. 303.

114. MacGregor, R.J. and E.R. Lewis, *Neural modeling : electrical signal processing in the nervous system*1977, New York: Plenum Press. xiv, 414 p.

115. Mannella, R., *Integration of Stochastic Differential Equations on a Computer.* International Journal of Modern Physics C, 2002. **13**(09).

116. Gerstner, W. and W.M. Kistler, *Spiking neuron models : single neuron, populations, plasticity*2002: Cambridge, U.K. New Yourk : Cambridge University Press. 480.

117. Gerstein, G.L. and N.Y. Kiang, *An approach to the quantitative analysis of electrophysiological data from single neurons.* Biophys J, 1960. **1**: p. 15-28.

118. Press, W.H., *Numerical recipes in FORTRAN : the art of scientific computing*. 2nd ed1992, Cambridge [England] ; New York, NY, USA: Cambridge University Press. xxvi, 963 p.

119. Evans, M. and J.S. Rosenthal, *Probability and statistics : the science of uncertainty*2004, New York: W.H. Freeman and Co. 202.

120. Siebenga, E., A.W. Meyer, and A.A. Verveen, *Membrane shot-noise in electrically depolarized nodes of Ranvier.* Pflugers Arch, 1973. **341**(2): p. 87-96.

121. Parzen, E., *Stochastic processes*. Holden-Day series in probability and statistics1962, San Francisco,: Holden-Day. xi, 324 p.

122. Papoulis, A. and S.U. Pillai, *Probability, random variables, and stochastic processes*. 4th ed2002, Boston: McGraw-Hill. x, 852 p.

123. Irlicht, L. and G.M. Clark, *Control strategies for nerves modeled by self-exciting point processes.* Ann Otol Rhinol Laryngol Suppl, 1995. **166**: p. 361-3.

124. Gaumond, R.P., C.E. Molnar, and D.O. Kim, *Stimulus and recovery dependence of cat cochlear nerve fiber spike discharge probability.* J Neurophysiol, 1982. **48**(3): p. 856-73.

125. Siebert, W.M., *Some implications of the stochastic behavior of primary auditory neurons.* Kybernetik, 1965. **2**(5): p. 206-15.

126. Turcott, R.G., et al., *A nonstationary Poisson point process describes the sequence of action potentials over long time scales in lateral-superior-olive auditory neurons.* Biol Cybern, 1994. **70**(3): p. 209-17.

127. Frijns, J.H., S.L. de Snoo, and R. Schoonhoven, *Potential distributions and neural excitation patterns in a rotationally symmetric model of the electrically stimulated cochlea.* Hear Res, 1995. **87**(1-2): p. 170-86.

128. Cormen, T.H., *Introduction to algorithms, second edition*, 2001, MIT Press: Cambridge, Mass.

129. Draper, N.R. and H. Smith, *Applied Regression Analysis*1998: Wiley-Interscience.
130. Steel, R.G.D., J.H. Torrie, and D.A. Dickey, *Principles and Procedures of Statistics*1960, New York: McGraw-Hill Companies. 187,287.
131. Nocedal, J. and S.J. Wright, *Numerical optimization*. Springer series in operations research1999, New York: Springer. xx, 636 p.
132. Powell, M.J.D., *A Fortran Subroutine for Solving Systems of Nonlinear Algebraic Equations*. Numerical methods for nonlinear algebraic equations, ed. P. Rabinowitz1970: Gordon and Breach Science Publishers. Ch.7.
133. Avriel, M., *Nonlinear Programming: Analysis and Methods.* 2003: p. 216.
134. Conn, A.R., N.I.M. Gould, and P.L. Toint, *Trust-Region Methods* Optimization2000: Society for Industrial Mathematics. 50.